FERMILAB-THESIS-2021-18

First Muon Neutrino on Argon Cross Section Measurements with an Off-Axis Beam

by

Christopher R. Barnes

A dissertation submitted in partial fulfillment
of the requirements for the degree of
Doctor of Philosophy
(Physics)
in the University of Michigan
2021

Doctoral Committee:

Assistant Professor Joshua Spitz, Chair
Professor Christine Aidala
Professor Henriette Elvang
Associate Professor Christopher Miller
Professor Jianming Qian

Christopher R. Barnes

barnchri@umich.edu

ORCID ID: 0000-0002-8782-6774

Dedicated to Mom, Dad, Maddy, and Bridget. Also, to the Batavia River Walk, for offering me a respite from physics research at all times of the year.

ACKNOWLEDGEMENTS

Any success that I've had in graduate school would not have been possible without love and support from a large group of people. I would like to acknowledge them here.

First, thank you to my fellow graduate students in the Spitz group who were there with me almost from the start to the end: Rory Fitzpatrick and Johnathon Jordan. I have never ceased to be astounded by your incredible physics acumen, professionalism, and collegiality. In fact, by comparison it was sometimes difficult to be in the same research group in graduate school simultaneously with such outstanding physicists.

Thank you to Joel Mousseau for your guidance, sense of humor, and for navigating the ups and downs of space charge and SBND readout electronics with me. See you at the 2033 Notre Dame - Michigan game. Thank you to Eric Marzec for giving such useful comments on my work at Spitz Group meetings.

Thank you to the undergraduates in the Spitz group for making summers at Fermilab and in Ann Arbor more fun: Polina Abratenko, T.J. Borucki, Claire Savard, Billy Warner, and Alexis Metzler. A special shoutout goes to Daniel Mishins, without whom most of progress on X-ARAPUCA electronics presented in this thesis would not have been possible.

Thank you to Jon Ameel, Sten Hansen, and Terry Kiper for the electronics help. Thank you to Bill Badgett for guidance on SBND-related items.

Thank you to my fellow physics graduate students in physics at the University of Michigan for all of the good times we had together: Brian McPeak, Rachel Hyneman, Callum Jones, Michael Viray, Taylor Baildon, Liuxing Shen, Joseph Kleinhenz, Max De Jong, Felicity Hills, and Dmitri

Mihaliov. Thank you especially to Alexa (Rakoski) Mihaliov for your friendship this past decade, [redacted]

Thank you to the members of the NuMI and Cross Section groups at Fermilab who have helped see the analysis in this thesis through to the end: Kirsty Duffy, Steven Gardiner, Andy Furmanski, Elena Gramellini, and Katrina Miller. Thank you especially to Krishan Mistry for indulging my every last request for anything NuMI flux-related.

Thank you to the Deep Learning group at Fermilab for introducing me to neutrino physics and helping me get acquainted to the MicroBooNE Experiment: Kazuhiro Terao, Vic Genty, Lauren Yates, Rui An, Adrien Hourlier, and Jarrett Moon.

I would especially like to thank two MicroBooNE collaborators who were instrumental in teaching me about LArTPCs and getting me up to speed with graduate school-level research: Taritree Wongjirad and David Caratelli. I would not have developed into the physicist I am today without help from the two of you, and for that I am forever grateful. I can't wait to read someday about the fantastic careers you two are having in the field.

Thank you to Sam Zeller, Bonnie Fleming, Matt Toups, and Michele Weber for your outstanding leadership on the MicroBooNE collaboration. Thank you to Wes Ketchum for your insight and perspective on all things MicroBooNE-related. The analysis in this thesis would not have been nearly as strong without the oversight and wisdom that you provided each week for many years. Thank you to Herb Greenlee for endless computing help over the years and for onboarding me well for my role as Release Manager.

Thank you to my friends at Fermilab for making Batavia and St. Charles feel like home: Gray Putnam, Varuna Meddage, Adam Lister, and Alex Diaz. Thank you to the staff and patrons at Mark's 2nd Street Tavern and Cindy Jarchow for always making Indiana St. a welcoming place to come back to after a long day. Thank you for the residents and volunteers [redacted] in Aurora, IL for giving me a sense of perspective and always reminding me of what's most important.

Thank you to my Notre Dame friends for plenty of non-intellectual stimulation over the past decade: Brian Hartnett, Trevor Bonventre, Patrick Meade, Daniel Wiegandt, Chris Reiche, Alex

Carter, Nikki Reyes, Maddie Daly, Megan Daly, Meaghan Hannon, Jessica Goston, Anastasia Fay, Caroline Fullam, Boyoung Yoo, and Jenny Wittenberg. Thank you to Will Raaf, Jesus Mendoza, and Phillip Kim for your friendship from Carroll Hall to the present day.

Thank you to John Walawender and Bob Miller for your companionship from the very beginning (band camp and the crib, respectively). I wouldn't have many great memories I cherish without the two of you, and I'm looking forward to making many more in the years to come. Thank you to Pete Ferguson for many laughs and good conversations shared over breakfasts during the past seven years. You made OLQM what it was during my five wonderful years there in the early 2000s.

Thank you to Mom, Dad, Maddy, and Bridget. [redacted] (no matter where you move, Mom and Dad!) will forever be home, and I will always be proud to be a member of the Barnes family. The four of you have made me into the person who I am today, and you're a part of me until the very end.

Lastly, thank you to my wonderful advisor, Associate (as of Sept. 2021) Prof. Joshua Spitz. Words cannot describe the gratitude I have to you for offering me a position in your group my first year and for being there for me through good times and bad. I'm completely certain that I would never have reached this moment without you, and I will never quite be able to thank you for all you have done for me. Being your first graduate student has been one of the great honors of my life, and I look forward to seeing everything that you (and the members of your group) accomplish in the years and decades to come.

PREFACE

This thesis presents work done with the Short Baseline Neutrino (SBN) program at Fermilab on the MicroBooNE and SBND experiments. My contribution to the research described herein consists of performing studies with cosmic rays (the reconstruction work in Chapter 5), isolating pure samples of cosmic rays (the ACPT track sample in Chapter 6), using those samples for calibration purposes (the space charge effect analysis in Chapter 7), isolating and measuring $\nu_\mu/\overline{\nu}_\mu$ interactions (the low-energy neutrino isolation and inclusive analysis in Chapters 9 and 10), and building the data acquisition system for X-ARAPUCA light detectors (Chapter 3).

Chapter 1 gives an overview of neutrino physics, highlighting distinct qualities of neutrinos, the central anomaly for which MicroBooNE was conceived, and other important research questions that neutrinos could help answer. Chapter 2 covers the Short Baseline Neutrino (SBN) Program at Fermilab at large and Chapter 4 pertains to the MicroBooNE experiment, the experiment on which the analysis in this thesis was done, in depth. Chapter 3 gives detail on a new light detection technology that will be used in the Short Baseline Near Detector (SBND), another experiment on the SBN. Chapter 5 provides an introduction into cosmic rays in the MicroBooNE detector and Chapter 6 goes into depth about how cosmic rays and other samples can be used to calibrate the detector. Chapter 7 contains the details of one calibration that can be performed using cosmic rays, that of the space charge effect (SCE). Chapter 8 reports an attempt to isolate a low-energy, monoenergetic sample of muon neutrino events for study. Chapter 9 lays the foundation for the primary result of this thesis, inclusive single-differential cross sections of ν_μ and $\overline{\nu}_\mu$ events from the NuMI beam target, and Chapter 10 presents the analysis results. Finally, Chapter 11 interprets the meaning of the result and places it into context.

TABLE OF CONTENTS

LIST OF FIGURES

FIGURE

LIST OF TABLES

TABLE

LIST OF ABBREVIATIONS

BNB Booster Neutrino Beam
NuMI NeUtrinos at the Main Injector
POT Protons On Target
LArTPC Liquid Argon Time Projection Chamber
CC Charged-Current
NC Neutral-Current
MicroBooNE Micro BOOster Neutrino Experiment
MiniBooNE Mini BOOster Neutrino Experiment
SBND Short-Baseline Near Detector
ICARUS Imaging Cosmic And Rare Underground Signals
DUNE Deep Underground Neutrino Experiment
PMT PhotoMultiplier Tubes
PDS Photon Detection System
A/C Crossing Anode/Cathode Crossing
ACPT Anode/Cathode-Piercing Track
SCE Space Charge Effect
KDAR Kaon Decay-At-Rest
NuMuCCInclusive ν_μ Charged-Current Inclusive
PPFX Package to Predict the FluX
CCQE Charged-Current QuasiElastic
RPA Random Phase Approximation
MEC Meson Exchange Current

ABSTRACT

While over ninety years have passed since neutrinos were first predicted in 1930 by Wolfgang Pauli, much about them is still unknown [20]. How many types of neutrinos there are, how precisely neutrinos change flavor, and how neutrinos interact with various types of matter are largely unanswered questions that have implications for fields beyond particle physics, such as cosmology and astrophysics. The final question can be answered partially by differential cross section measurements, two of which constitute the primary result of this thesis.

The NeUtrinos at the Main Injector (NuMI) Beam at Fermilab in Batavia, IL provides a source of $\nu_\mu/\overline{\nu}_\mu$ neutrinos to the MicroBooNE experiment, an 85 ton liquid argon time projection chamber (LArTPC). The technology allows for high precision particle tracking and energy reconstruction that can be used to make cross section measurements. Necessary work for making these measurements for which the author of this thesis made an essential contribution is presented in detail in References [21] [22] [11] [23]. The measurement presented in this thesis is made with 2.187×10^{20} Protons on Target (POT), the standard metric for an amount of beam exposure, of data when the beam was in forward horn current mode. Single-differential cross section measurements in terms of muon candidate kinetic energy and direction are made, and their χ^2 fits with simulation are 5.8 (12 d.o.f.) and 11.4 (10 d.o.f.), respectively. This indicates that the muon kinematics for ν_μ and $\overline{\nu}_\mu$ CC events primarily in the energy range [0-3] GeV can be trusted for oscillation experiments, including DUNE, because of the agreement to within the associated systematic and statistical uncertainties between the measurement and the model in every bin of both single-differential cross sections.

This result adds to the corresponding result for the Booster Neutrino Beam (BNB) because it covers a completely different energy region than that measurement, a double-differential cross

section in terms of muon momentum and direction [14]. This result contributes to reducing the uncertainty in near-far event rate comparisons in long baseline neutrino experiments and also adds to existing knowledge of the neutrino-nucleus interaction by describing the outgoing muon kinematics in $\nu_\mu/\overline{\nu}_\mu$ interactions. This result is the first-ever measurement of $\nu_\mu/\overline{\nu}_\mu$ differential cross sections in liquid argon made with an off-axis beam.

CHAPTER 1

Introduction to Neutrino Physics

In particle physics, the smallest components of the universe can help explain the behavior of the largest. Questions about the formation of galaxies, stellar evolution, and the matter/antimatter asymmetry can be answered by how particles interact on a subatomic level. Theories about the rate and nature of large-scale processes must be compared against the known behaviors of their constituent particles. The bedrock of particle physics lies within a set of fundamental particles and their interactions known as the Standard Model.

1.1 The Standard Model

The foundation of particle physics lies within the Standard Model, which contains fundamental particles and the forces that they exert upon one another. A graphic of the Standard Model is shown in Figure 1.1.

There are three types of particles in the Standard Model: leptons, quarks, and bosons. The quarks come in six varieties: up, charm, and top (all with charge +2/3e) and down, strange, and bottom (all with charge -1/3e). All of the quarks have spin +1/2. Single quarks are not found in nature; in fact, the force between quarks gets stronger the further that they get from one another. Bosons are the force-carrying particles; photons transmit the electromagnetic force, gluons transmit the strong nuclear force and the W^+, W^-, and Z^0 particles transmit the weak nuclear force. The Higgs boson, discovered in 2012, has a corresponding field which gives the other particles in the Standard Model their mass. Theorists have speculated about a particle called the graviton which transmits the gravitional force, but it has never been detected experimentally. In order of increasing strength, the four fundamental forces of nature are gravity, the weak nuclear force, electromagnetism, and the strong nuclear force. Because gravity is so much weaker (by a factor of 10^{24}) than the weak nuclear force, theoretical physicists have struggled to make sense of its quantum aspects and find a place for it in their models.

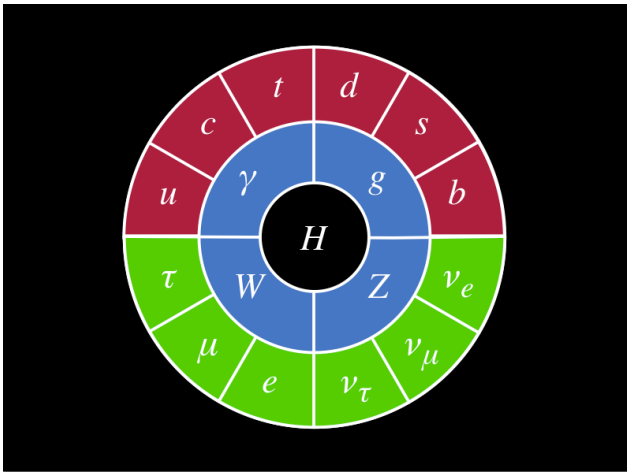

Figure 1.1: The Standard Model of particle physics. It consists of three types of particles: leptons, quarks, and bosons [1].

Leptons form the final class of fundamental particles, and they come in two varieties: electrically charged with relatively plentiful mass and electrically neutral with relatively little mass. Each relatively massive, charged lepton has a corresponding relatively light, neutral partner, with each pair coming with in three varieties: the electron (e), the muon (μ) and the tau (τ). The relatively light, neutral partners are the neutrinos, research of which constitutes the entirety of this thesis.

1.2 Prediction

In December of 1930, Wolfgang Pauli first predicted the existence of neutrinos in order to explain the energy that was missing in beta decays [20]. This is the decay of a neutron to a proton, an electron, and an electron antineutrino:

$$n \rightarrow p + e^- + \overline{\nu}_e \tag{1.1}$$

Pauli's theory was partially based on the observation that the energies of electrons emitted in beta decays was continuous rather than discrete, as was proved in an experiment by Otto Hahn and Lise Meitner in 1911 [20]. The existence of neutrinos explains why this is the case, because the neutrino can share energy with the charged lepton within a range.

Enrico Fermi named the neutrino in 1931 by making a play on the Italian word for neutron, 'neutrone', which means large and neutral. Neutrino means small and neutral in Italian. By 1934, Fermi had developed a theory of beta decay which included the neutrino. He developed a principle called 'Fermi's Golden Rule', which states that the probability of a beta decay is proportional to

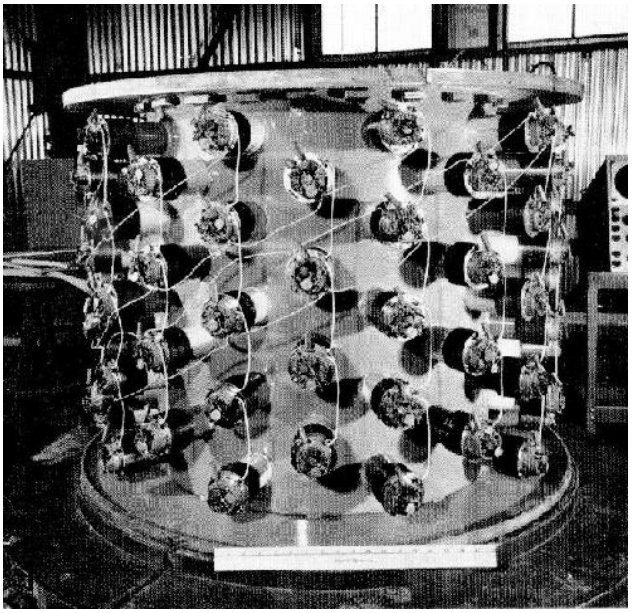

Figure 1.2: The water tank that Cowan and Reines used to detect antineutrinos, the first detection of those particles [2].

the coupling between the initial and final states of the process, factored by the density of final states available to the system.

1.3 Discovery

Neutrinos are extraordinarily difficult to detect in comparison to larger particles with greater mass and charge, so their existence was not proven until over 20 years after they were first proposed by Pauli. Clyde Cowan and Frederick Reines detected electron antineutrinos in 1956 at a nuclear reactor. The detector they built, a tank of water in which electron antineutrinos from the reactor would interact with protons and release neutrons and positrons, contained cadmium chloride, which releases a gamma ray when it absorbs a neutron [20]. Scintillator material present in the setup would detect the gamma ray from the cadmium 5 μs after the one from the positron when an antineutrino had interacted in the tank according to the principles of inverse β-decay.

On average, Cowan and Reines had detected approximately three antineutrino interactions per hour in their detector after they had been taking data for months. As a test, they ensured that they had been detecting antineutrinos in the tank by taking data when the reactor was off. They received the Nobel Prize in Physics in 1995 for their work. A picture of their detector, which they used near the nuclear plant at Savannah River in South Carolina, is shown in Figure 1.2.

1.4 Neutrino Properties

Neutrinos are distinguished by several unique properties:

- Neutrinos have very little mass (certainly less than several eV).
- Neutrinos interact via the weak force only.
- Neutrinos very rarely interact.
- Neutrinos oscillate between different flavor eigenstates as they propagate through space.

These idiosyncratic qualities are described in more detail in the sections that follow.

1.4.1 Neutrino Mass

The finding that neutrinos have mass was the first shortcoming of the Standard Model to completely describe the state and behavior of particle physics. The Standard Model predicts that neutrinos travel at the speed of light, and to do so they must necessarily be massless. However, it was proven that a neutrino's wave function is time-dependent, which means that it must travel at less than the speed of light and have mass. Sufficient evidence to support this claim was collected by the SuperKamiokande experiment in Japan, which consists of water and PMTs and is the world's largest underground neutrino detector [24]. It reported the first evidence of neutrino oscillations in 1998. The result had a statistical significance of more than 5 standard deviations, which is the general standard for discoveries in particle physics [20].

The mass of a neutrino is not precisely known, but it is constrained by experimental limits. The Karlsruhe Tritium Neutrino (KATRIN) experiment in Germany found in 2019 that the most mass that an electron antineutrino can have is 1.1 eV at 90% confidence level [25]. Previously, this limit was 2.3 eV at 95% confidence level in 2005 and 2.05 eV at 95% confidence level in 2011. The limit found by KATRIN is less than the mass of an electron (511 keV) by more than a factor of 450,000 and less than the mass of a muon (106 MeV) by more than a factor of 95,000,000. The most stringent limit on neutrino masses comes from cosmology, which compares data from a satellite to models for the development of structure in the early universe to yield a sum of all three neutrino masses of 0.17 eV.

1.4.2 Neutrino Interactions

Neutrinos are the most abundant known particles with mass in the universe, yet they rarely interact when they propagate through space. More than a trillion neutrinos pass through a person's body

every second, but maybe a single one will interact within their body in their entire lifetime. Quantitatively, the cross section of a single muon neutrino with an an argon nucleus is O(10^{-38} cm^2) for the energy range of most neutrinos under study in this thesis, 0 GeV - 3 GeV.

For neutrinos in the energy range 100 MeV - 20 GeV, there are three main channels in which the neutrino can interact:

- elastic and quasi-elastic scattering: a neutrino scatters off of an entire nucleon and frees one or more nucleons in the target. For CC interactions (like the signal under study in this thesis), the process is referred to as 'quasi-elastic scattering', while for NC interactions it is referred to as 'elastic scattering'.
- resonance production: a neutrino excites the nucleon target to a resonance state, and the baryonic resonance that results decays to a number of different hadronic final states which produce mesons and nucleons.
- deep inelastic scattering: a neutrino resolves the constituent quarks of the nucleon and produces a hadronic shower.

The plot shown in Figure 1.3 compares the total neutrino cross section from a number of different experiments to the prediction from NUANCE, a neutrino event generator, for each channel [3]. This quantity can be expressed in terms of a variable (or multiple) involved in the neutrino interaction in a quantity called a differential cross section. The results of this thesis are differential cross section measurements as well as total cross sections, calculated by summing the contents of the bins in the differential cross sections.

1.4.3 Neutrino Oscillation and Mixing

The three flavors of neutrinos are composed of at least three mass eigenstates: ν_1, ν_2, and ν_3. In a two-neutrino framework, the probability that a neutrino of flavor a oscillates to one of flavor b as it moves through space is determined by the following equation [26]:

$$P(\nu_a \rightarrow \nu_b) = \sin^2(2\theta_{ab}) \sin^2(\Delta m^2 \frac{L}{4E}) \tag{1.2}$$

In this equation, θ_{ab} is known as the mixing angle between neutrino flavor a and neutrino flavor b, Δm^2 is the mass splitting between the two mass eigenstates that make up the two flavor eigenstates, L is length that the neutrino propagates, and E is the energy of the neutrino. The mass splitting is the difference between the squares of the masses of the two neutrino mass eigenstates, m_1^2 - m_2^2, and θ is a quantity that can be determined experimentally.

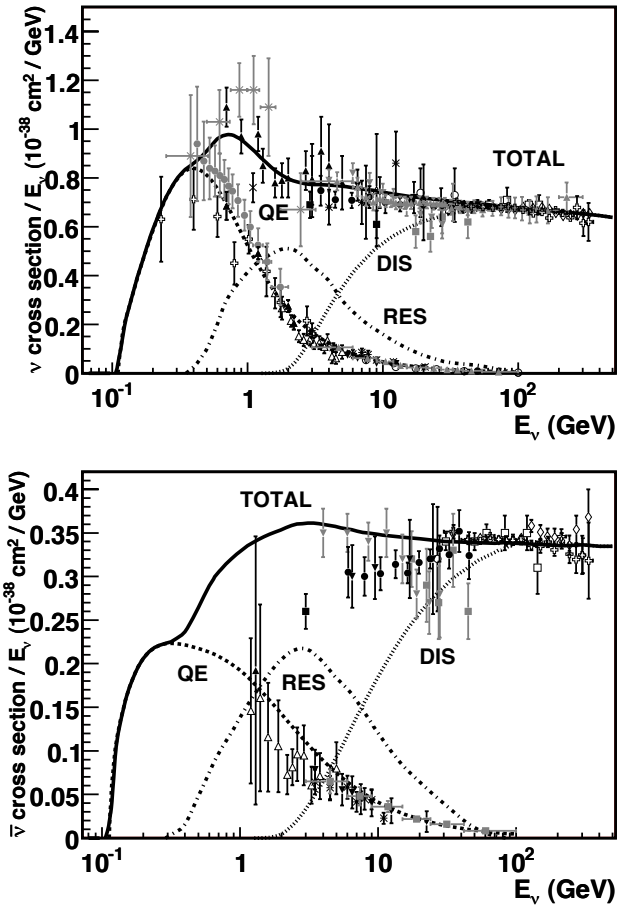

Figure 1.3: A plot showing the total CC cross section per nucleon for (top) ν and (bottom) $\overline{\nu}$ events for an isoscalar target [3]. The three main interaction channels, quasi-elastic scattering (QE), resonance production (RES), and deep inelastic scattering (DIS), are also shown. One of the interaction channels not shown is coherent pion production, which according to simulation contributes to a small percentage ($< 1\%$) of signal events passing the selection in the analysis in Chapter 9 of this thesis. The predictions for each are provided by NUANCE, a neutrino event generator, in comparison to the results from a number of different neutrino experiments, such as MiniBooNE, NuTeV, and NOMAD, for the QE channel and the total cross section per nucleon.

In a three-neutrino paradigm, the neutrino mass eigenstates can be expressed in terms of the 3×3 Pontecorvo-Maki-Nakagawa-Sakata (PMNS) matrix multiplied by each of the flavor eigenstates [27]. The PMNS matrix is:

$$U = \begin{bmatrix} 1 & 0 & 0 \\ 0 & \cos(\theta_{23}) & \sin(\theta_{23}) \\ 0 & -\sin(\theta_{23}) & \cos(\theta_{23}) \end{bmatrix} \begin{bmatrix} \cos(\theta_{13}) & 0 & \sin(\theta_{13})\mathrm{e}^{-\mathrm{i}\delta} \\ 0 & 1 & 0 \\ -\sin(\theta_{13})\mathrm{e}^{\mathrm{i}\delta} & 0 & \cos(\theta_{13}) \end{bmatrix} \begin{bmatrix} \cos(\theta_{12}) & \sin(\theta_{12}) & 0 \\ -\sin(\theta_{12}) & \cos(\theta_{12}) & 0 \\ 0 & 0 & 1 \end{bmatrix} \tag{1.3}$$

A neutrino oscillation experiment typically takes one of two forms: an appearance measure-

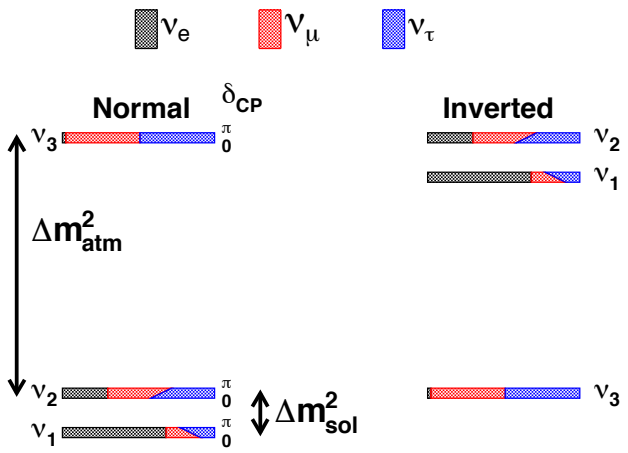

Figure 1.4: An image of the (left) normal and (right) inverted neutrino mass hierarchy. The colors that make up each neutrino mass eigenstate correspond to the amount of each flavor eigenstate that it corresponds to [4].

ment or a disappearance measurement. In an appearance measurement, one flavor of neutrino oscillates into a second flavor of neutrino over a distance, and the number of the first flavor of neutrino at the start of the neutrinos' trajectory is compared to the number of the second flavor at the end. In a disappearance measurement, the numbers of a single flavor of neutrino are compared both at the start and at the end of the neutrinos' trajectory to determine if any have oscillated to another flavor and, if they have, how many have done so.

There are at least three neutrino mass eigenstates. The mass splitting between two of them, ν_1 and ν_2, is experimentally measured to be $(7.37^{+0.20}_{-0.15}) \times 10^{-5}\text{eV}^2$ [28]. The third mass eigenstate, ν_3, is either much heavier or much lighter than the other two mass eigenstates. Its splitting with ν_2, Δm^2_{23}, is experimentally measured to be $(2.54 \pm 0.04) \times 10^{-3}\text{eV}^2$ [28]. The situation in which ν_3 is much heavier than the other two mass states is known as the normal hierarchy, and the case in which it is much lighter is known as the inverted hierarchy. Figure 1.4 shows (left) the normal hierarchy and (right) the inverted hierarchy, with the composition of each mass eigenstate colored the proportion of each flavor eigenstate that it is made up of [4].

In 1985, a Russian team found that flavor oscillations are modified as neutrinos propagate through matter. This was a first-time observation implying that neutrinos must have mass [20]. Unfortunately, attempts to reproduce the experiment were unsuccessful. The Liquid Scintillator Neutrino Detector (LSND) experiment at Los Alamos National Laboratory in Los Alamos, New Mexico consisted of mineral oil, scintillator material, and photomultiplier (PMT) tubes and detects neutrino interactions by means of the light that they deposit into the PMTs. It operated by shooting a beam of muon antineutrinos of up to a couple of hundred MeV at a target 30 m away and looking for electron antineutrinos. In 1998, it found that muon antineutrinos have a nonzero probability

to oscillate into electron antineutrinos at these energies over this distance [29]. The results are controversial, because the excess cannot be explained by the Standard Model and points to physics beyond it. As discussed earlier in this chapter, Super-Kamiokande reported the first definitive evidence of neutrino oscillations, also in 1998.

A number of different neutrino experiments today are designed to study oscillations. A measurement that can be performed with a nuclear reactor is that of θ_{13}, the mixing angle between the first and the third neutrino mass states. The Double Chooz experiment, using two detectors containing scintillator fluid doped with gadolinium to study the products of neutrino interactions, measured θ_{13} at the Chooz Reactor Complex in France with three years of data-taking [30]. This value was later measured for the first time by the Daya Bay Experiment, a set of eight gadolinium-doped organic liquid scintillators, at the Daya Bay Nuclear Power Complex in China [31]. Their measurement was improved in 2015 [32].

Accelerator neutrino experiments can also be used to study neutrino oscillations. One example is the T2K (Tokai to Kamioka) experiment in Japan. T2K shoots neutrinos underground from the eastern coast of Japan to the western coast, sending them to the same facility at which the Super-K experiment is located [33]. T2K was designed to study neutrino oscillations, which it does by using a near detector (located at Tokai in Japan) and a far detector (Super-K serves as the far detector for this experiment). MicroBooNE and The Short Baseline Near Detector (SBND), the two experiments with which the work in this thesis was done, are also accelerator neutrino experiments. They are described in more detail in Chapters 2 and 4.

Neutrino oscillations can also point to new beyond-the-Standard-Model physics beyond revealing that neutrinos have mass. The MiniBooNE experiment at Fermilab recognized an excess of electron neutrino-like events at neutrino energies < 600 MeV. The results are not compatible with the current understanding of neutrino oscillations in the three-neutrino model. They could point to the existence of a fourth type of neutrino, a 'sterile' neutrino, which interacts only via the gravitational force [5]. The plot shown in Figure 1.5 displays the disagreement between prediction (shown in the stacked histograms) and data (the data points). MicroBooNE can improve upon this result because of its ability to distinguish electron interactions from photon interactions, which is key to being able to fully characterize the excess of events in data.

An excess of electron antineutrinos was seen by LSND as well, and the result cannot be compatible with the three-neutrino model [6]. It could indicate $\overline{\nu}_\mu \longrightarrow \overline{\nu}_e$ oscillations over a distance of 30 m. A plot of the excess events plotted vs. the length that the neutrinos propagated divided by the neutrino energy is shown in Figure 1.6.

The results of this thesis will help to inform neutrino oscillation measurements by providing differential cross sections expressed in terms of muon kinematics, which will help to limit systematic uncertainty in those efforts. The cross section systematics in oscillation measurements, which

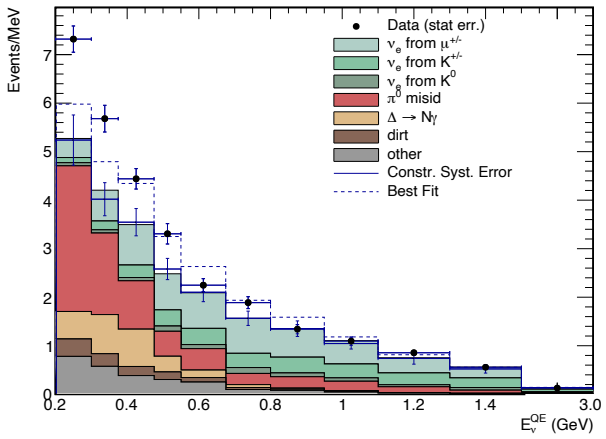

Figure 1.5: A plot showing the excess discovered by the MiniBooNE experiment for electron neutrino-like events. There is an excess of data events observed in the neutrino energy region $<$ 600 MeV [5].

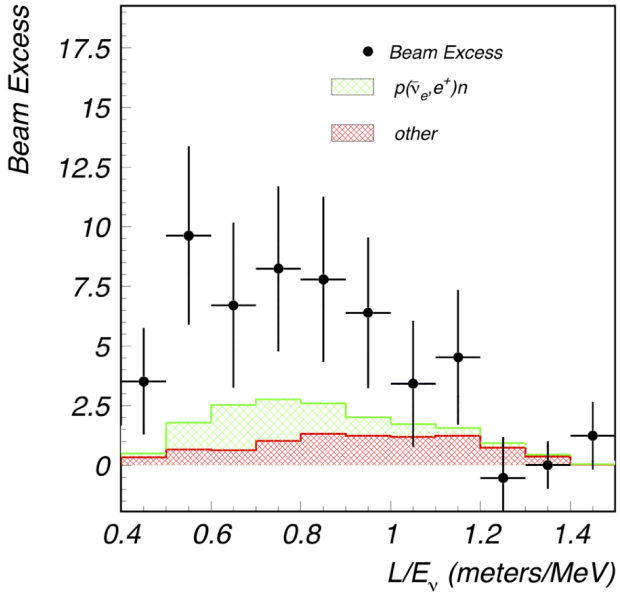

Figure 1.6: A plot showing an excess of events in data in comparison to simulation in the kinematic variable propagation length divided by neutrino energy, discovered by the LSND experiment [6].

tend to dominate the systematic uncertainty budget, will be reduced directly by this [34].

1.5 Open Questions Concerning Neutrinos

Neutrinos can answer a number of questions about the nature of matter and the structure of the universe, most notably:

- Are matter neutrinos different from antimatter neutrinos?
- How many types of neutrinos are there?
- What is the nature of the interaction of neutrinos with matter?
- How often do muon neutrinos oscillate into electron neutrinos?

If matter neutrinos are identical to antimatter neutrinos, then neutrinos are a particle species named 'Majorana', meaning that they are their own antiparticles. If this is true, this can help explain why there was more matter than antimatter in the early universe, which explains why the universe is not entirely empty. Additional neutrinos can help explain anomalies observed by the MiniBooNE and LSND experiments (Section 1.4.3) and would represent an additional shortcoming of the Standard Model beyond the finding that neutrinos have mass. The nature of the interaction of neutrinos with matter is described by means of differential cross section and total cross section measurements, several of which are the result of this thesis (Chapters 10 and 11). The interactions of neutrinos with atomic nuclei can help explain nuclear structure (particularly if the neutrinos are monoenergetic, like the signal in Chapter 8 is) and can help constrain systematic uncertainties in oscillation measurements (discussed in Section 1.4.3). The work done to answer the first three questions is central to answering the final question in the list. If the number of neutrinos predicted by theory can be verified by experiment and the interaction of neutrinos with matter is well-described, then the frequency with which muon neutrinos oscillate into electron neutrinos should match up accurately between theory and experiment. If it does not, that is evidence of additional physics not described by the Standard Model.

Building on the work of the past, future experiments will provide insight into these questions beyond what is currently known. The mu2e experiment at Fermilab is designed to study the conversion of a muon into an electron. If this process is observed to occur without any accompanying neutrinos, that exists as evidence that lepton number conservation can be violated, a further shortcoming of the Standard Model [35]. The Deep Underground Neutrino Experiment (DUNE), a future neutrino experiment that consists of LArTPCs, will shoot neutrinos from Fermilab to the Sanford Underground Research Facility (SURF) in Lead, South Dakota, 1,300 kilometers away. DUNE will study several topics relevant to answering the questions above by studying neutrino oscillations, searching for signs of proton decay, and probing supernova by means of neutrinos that they release from their collapse [36].

CHAPTER 2

LArTPC Technology and The Short Baseline Neutrino (SBN) Program at Fermilab

In order to measure neutrinos with an accelerator, at least one detector is needed. The MicroBooNE experiment is a Liquid Argon Time Projection Chamber (LArTPC), which is a tank of liquid argon that is placed in a neutrino beam. Such a detector measures neutrino interactions by means of deposited charge, scintillation light, a cosmic ray tagger system, and beam timing information. MicroBooNE is part of the Short Baseline Neutrino (SBN) Program at Fermilab in Batavia, IL along with the Short Baseline Near Detector, SBND (the near detector) and Imaging Cosmic And Rare Underground Signals, ICARUS (the far detector). MicroBooNE is the intermediate detector in the SBN.

2.1 LArTPC Motivation and Evolution

A LArTPC is an advantageous way to study neutrinos because of its high resolution of particle charge and energy, which allows for the energy (with limited resolution) and flavor of incoming neutrinos to be determined. The LArTPC concept for neutrinos was first proposed in the late 1970s by Carlo Rubbia and was first built into a detector in the 2000s with the commissioning of the ICARUS experiment at Gran Sasso in Italy and the ArgoNeuT experiment at Fermilab. The SBN represents the next generation of LArTPC detectors to be followed by the Deep Underground Neutrino Experiment (DUNE), described in Section 1.5, which will consist of two detectors located 1,300 km apart. DUNE is expected to have first beam in the mid-2020s and is benefiting from the research and development and analysis techniques under development by the SBN.

A LArTPC consists of at least one anode and a cathode kept at different voltages to allow the ionization electrons from charged particles that result from the neutrino interactions to flow to the anode to be recorded. One of the reasons that argon is used is because it has a high electron mobility, meaning that electrons can drift long distances without being reabsorbed by argon

ions. Furthermore, argon has a relatively high boiling point (87.3 K), allowing the detector to be maintained at an achievable temperature (89 K for MicroBooNE). The argon remains in liquid form because it is appropriately pressurized. Argon is abundant in nature (the Earth's atmosphere is 0.93% argon) so it is cheap [37]. It has a density of 1.4 g/cm^3, which means that neutrinos will interact at a rate that allows for events for study over a timescale of days of data-taking. Argon scintillates light at an intensity of 40,000 γ/MeV when muons, the most copiously produced charged particle, propagate, which can be detected by a light detection system. It is transparent to this scintillation light, which means that there is no quenching before the light is detected. Finally, the liquid argon in MicroBooNE was not observed to suffer a dielectric breakdown until an electric field value of 38 kV/cm, over two orders of magnitude greater than the MicroBooNE electric field value of 273.9 V/cm [38].

2.2 Types of Detector Information

The types of information that a LArTPC uses to study neutrino interactions are described in this section. A graphic of a LArTPC is shown in Figure 2.1, displaying how light and charge information are collected (the CRT panels are not shown) [7].

2.2.1 Deposited Charge

In a liquid argon time projection chamber, neutrinos enter into the detector and interact with the nuclei of argon atoms. Charged particles, primarily muons, protons, pions, and electrons, emanate from the point of interaction, called the 'vertex', ionizing the argon atoms in their paths. The resulting ionization electrons flow towards the anode wire planes under the influence of an electric field, which allows for the trajectories of the outgoing charged particles to be reconstructed. There are three wire planes with adjacent wires separated by 3 mm which read out the charge: two, oriented at $\pm$ 60 degrees with respect to the horizontal, read out charge by means of induction, and one, oriented vertically, reads out charge by means of collection. The three wire planes are located 3 mm from one another to avoid charge quenching between them. The charge takes O(ms) to flow from the point of argon ionization to the wire planes, with the maximum drift time of ~2.3 ms in MicroBooNE and ~1.25 ms in SBND.

2.2.2 Collected Light

When charged particles pass through the liquid argon, the argon atoms release light in addition to ionization electrons. This light takes two forms, Cherenkov and scintillation. The Cherenkov light is emitted in a cone in the direction in which the particle is traveling and is released over a duration

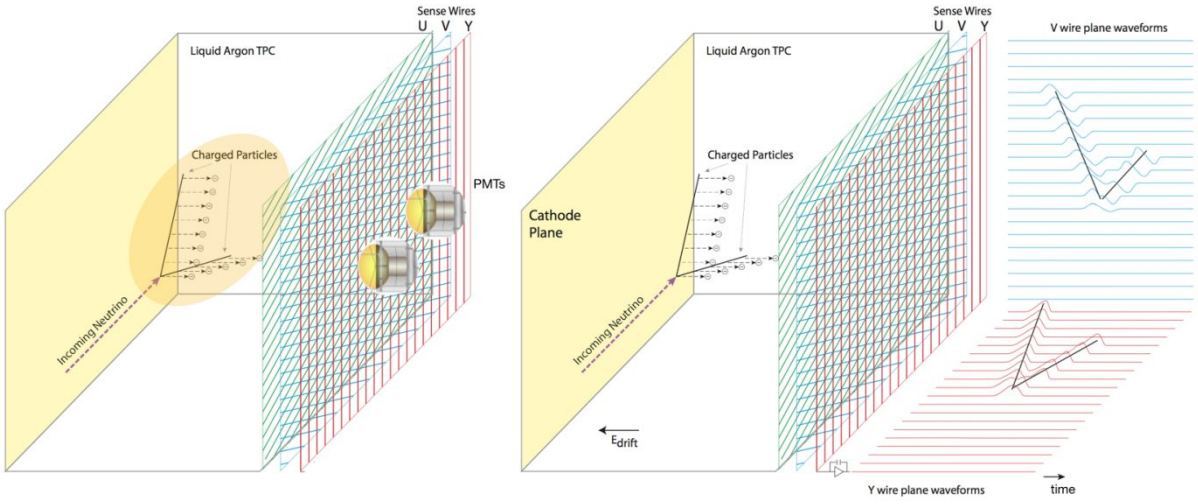

Figure 2.1: A description of how light (in PMTs, shown on the left) and charge (on three wire-planes, shown on the right) are collected [7]. The CRT panels are not included in these diagrams.

of picoseconds. The scintillation light escapes from an argon excimer (a Rydberg state with an Ar_2^+ core and a bound electron) over a period of nanoseconds and is emitted isotropically. Both sources of light are collected by a system of 32 PhotoMultiplier Tubes (PMTs), which have O(ns) resolution. Amounts of the light are reconstructed in the PMTs in units of PhotoElectrons (PEs), with higher values corresponding to more intense flashes. In addition to providing light information for the timing of neutrino interactions, PMTs allow for the matching of flash information to the charge in the directions transverse to the drift of ionization electrons.

2.2.3 Cosmic Ray Tagger (CRT) Information

Several meters outside of the cryostat, there are scintillator panels that record particle hits, particularly from cosmic ray muons [39]. These are primarily intended to match activity from cosmic rays in the TPC to recorded hits in an attempt to reject cosmic ray backgrounds - this is discussed in more detail in its use in the low-energy neutrino selection (see Section 8.7). MicroBooNE consists of four scintillator panels situated on the detector sides corresponding to the top, bottom, anode, and cathode; this is discussed in more detail in the description of MicroBooNE (see Section 4.1).

2.2.4 Beam Timing Information

For an event to be considered for a neutrino analysis in MicroBooNE, there must be a flash reconstructed within the beam window. For the Booster Neutrino Beamline (BNB) datastream (data from the on-axis beamline), there must be a flash reconstructed in the time window [3.2 μs, 4.8

μs] with respect to the beam trigger. For data from the NeUtrinos from the Main Injector (NuMI) beamline, which is the datastream used for the analysis in this thesis, there must be a flash reconstructed in the time window [5.74 μs, 15.34 μs]. A set of algorithms perform what is known as 'flash-matching': comparing a flash of light to a TPC object to determine if the object could potentially belong to a neutrino. The flash-matching algorithm used to select events for the analyses in this thesis uses a χ^2 fit to compare a reconstructed flash to the predicted flash spectrum of a TPC object (the number of degrees of freedom in the fit is the number of PMTs in data which have a nonzero amount of light).

2.3 Advantages of LArTPCs

2.3.1 High Resolution Particle Tracking

Because MicroBooNE consists of three wire planes, it can track the trajectories of particles with millimeter precision. ArgoNeuT contained only two wire planes with which to study the paths of particles. The third wire plane in MicroBooNE provides more information with which to track the positions of particles within the detector. There is ambiguity on the drift coordinate within MicroBooNE because of its offset with respect to the trigger time, but that is something that can be measured for in-time tracks and a specific class of cosmic ray muon tracks (see Section 6.1).

Once the trajectory and species (found using the technique described in Section 2.3.2) of a particle have been determined, the momentum of a particle contained in the detector can be determined based on how long its extent is. The relationship between track length and momentum has been well-studied for liquid argon by the Particle Data Group for muons and other particle species in what is called the 'range' momentum reconstruction technique [40] [41]. This method would obviously fail for non-contained muon candidates because not all of those tracks' energy is deposited in the TPC, but another technique takes advantage of the scattering of those tracks to reconstruct their momentum with worse resolution (~14%) than the range method (~2-4%) [42]. With the output from either technique, the kinetic energy of the track can be determined from the momentum of the track.

2.3.2 High-Precision Calorimetry For Particle Identification

The primary advantage of using a LArTPC for a neutrino experiment is the calorimetry information, the charge deposited per unit length, which can be calibrated to provide accurate discrimination between different particle species in the MicroBooNE detector. Different particle types ionize different numbers of argon ions as a function of the distance from the end of the track,

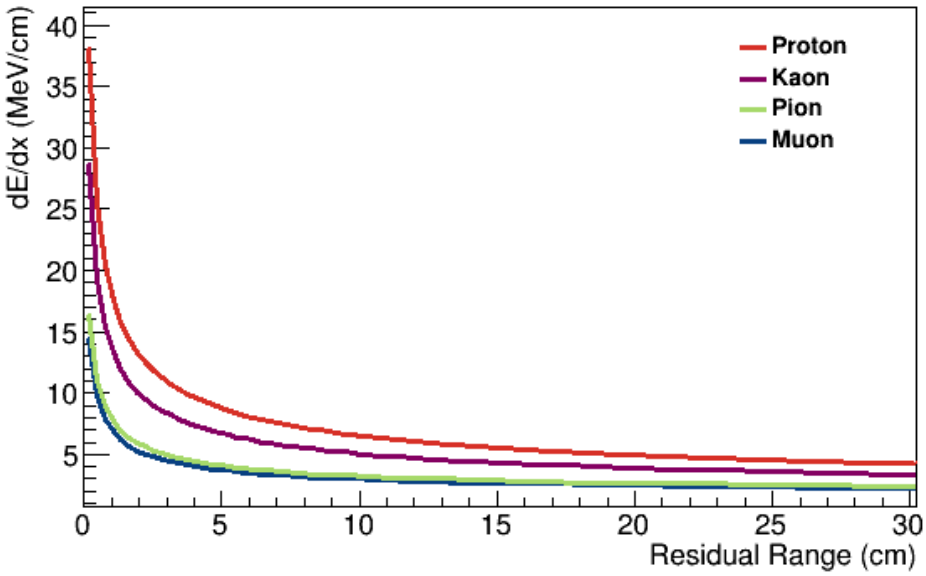

Figure 2.2: A plot showing the dE/dx as a function of the residual range for different particle species in MicroBooNE as theoretical models predict. These particles typically deposit tens to hundreds of MeV of energy in the detector, and their behavior asymptotically approaches constant charge deposit in the limit of infinite track length.

a variable called the residual range. Figure 2.2 shows this information from a theoretical model for the four main particle species in MicroBooNE: muons, pions, kaons, and protons. Minimum ionizing particles (MIPs) ionize argon atoms at a constant rate of ~2 MeV/cm, with the increase shown here only taking place within the last few centimeters of a track's trajectory. Low-energy electrons travel through liquid argon as tracks as well, but they manifest themselves as showers at higher energy. This is why they are not contained within Figure 2.2.

There are two types of neutrino interactions in LArTPCs: charged-current (CC) and neutral-current (NC). In CC interactions, a W boson acts as mediator between the initial and final products

Figure 2.3: A diagram of (left) a charged-current (CC) and (right) a neutral-current (NC) interaction [8]. Note that the CC interaction reveals information about neutrino flavor based on the species of outgoing particle but the NC interaction does not.

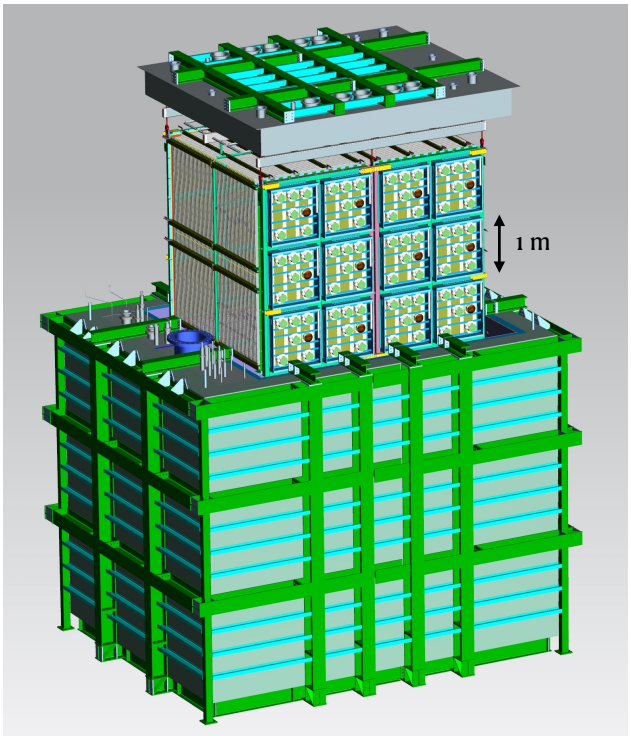

Figure 2.4: A simulated graphic of the SBND detector. The top portion is the lid, the middle is the TPC, and the bottom is the cryostat exterior.

in the interaction. A charged particle of the same flavor as the neutrino is released, allowing information about the neutrino flavor to be deduced. In NC interactions, a Z boson is the mediator, and there is only a hadronic particle (a proton or several) of the interaction which is released. This does not allow for any information about neutrino flavor to be deduced from the outgoing particles. Figure 2.3 shows a diagram of CC and NC interactions, the former of which is the classification of the signal under study in the analysis in this thesis.

2.4 Other Experiments in the Short Baseline Neutrino Program

2.4.1 Short Baseline Near Detector

The near detector in the Short Baseline Neutrino Program, SBND, is located 110 m from the Booster Neutrino Beam (BNB) source. SNBD has a larger active mass than MicroBooNE of 112 tons. It consists of two anodes with a cathode located in the middle of both of them. In addition to a set of PMTs to detect light from neutrino interactions, SBND will also include X-ARAPUCAs for this purpose as well (discussed in more detail in Chapter 3). The X-ARAPUCAs will be located behind each of the anodes, which are each divided into 12 panels which contain 8 X-ARAPUCAs

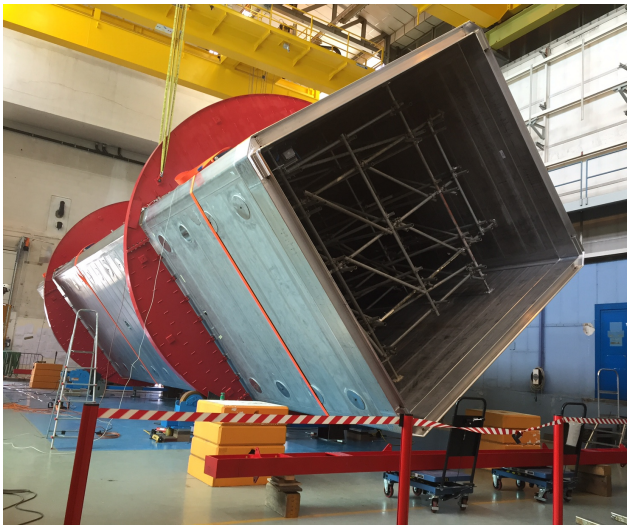

Figure 2.5: A graphic of the ICARUS detector. ICARUS consists of two modules, shown in this image (front and back).

each. As of this writing, SBND is expected to take beam in the year 2022. An image of the SBND detector is shown in Figure 2.4.

2.4.2 ICARUS

ICARUS, the SBN far detector, was previously located in Gran Sasso, Italy, where it was located underground and took data from 2010 to 2014. It was moved to Fermilab in 2017 and was placed in the detector hall in 2018. It contains 480 tons of liquid argon. It contains two symmetric modules which are 3.6 m high, 3.9 m wide, and 19.9 m long. Like SBND, each of the modules contain two anodes and one cathode located between them. ICARUS is located 600 m from the Booster Neutrino Beam source. Like MicroBooNE, ICARUS also consists of three wire planes at each anode. An image of the SBND detector is shown in Figure 2.5.

2.5 The Neutrino Beams For the SBN

There are two beams that deliver neutrinos to MicroBooNE: the Booster Neutrino Beam (BNB) and the NeUtrinos at the Main Injector (NuMI) beam. Figure 2.6 shows the angles at which neutrinos exit at different points along the NuMI beam to reach MicroBooNE as well as the orientations of both beams with respect to MicroBooNE [9].

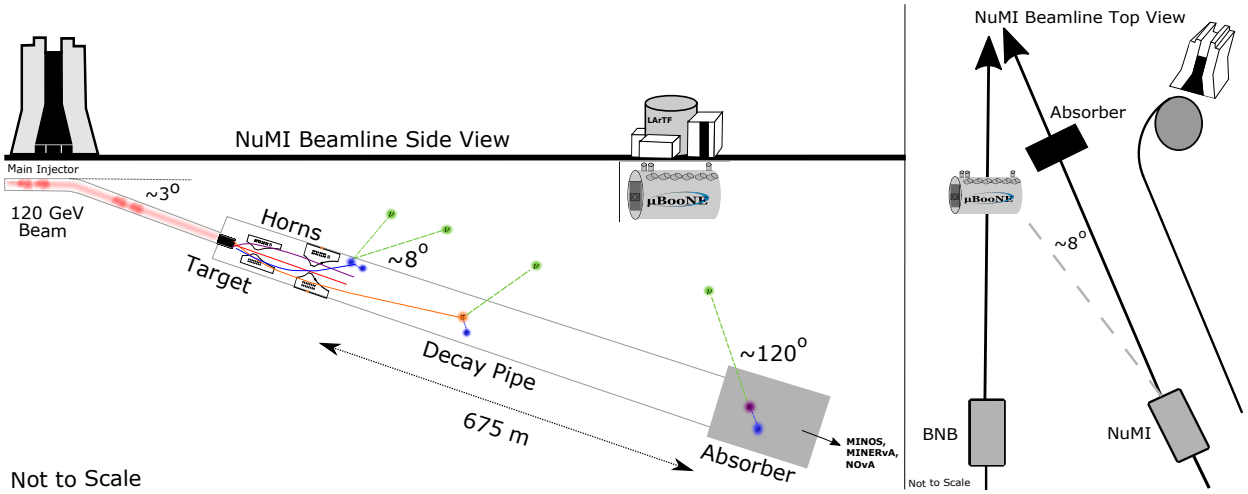

Figure 2.6: A graphic showing (left) the angles at which neutrinos exit at different points along the NuMI beam to reach MicroBooNE and (right) the relative orientations of both the BNB and NuMI beams with respect to MicroBooNE [9].

2.5.1 The Booster Neutrino Beam (BNB)

The BNB is the on-axis beam for the SBN. The beamline delivers an 8 GeV source of protons to collide with a proton target. It delivers neutrinos with a peak energy of 0.8 GeV to MicroBooNE as part of a ν_μ-enriched beamline. The neutrinos delivered by this beam are the ones used to study the low-energy excess (LEE) observed by the MiniBooNE and LSND experiments. Because the neutrino analyses presented in this thesis focus on signal neutrinos delivered by NuMI, the primary focus of this section will be on that beamline.

2.5.2 The NeUtrinos at the Main Intector (NuMI) Beam

The NeUtrinos at the Main Injector (NuMI) beam is the off-axis beam for the SBN. It delivers off-axis neutrinos to both MicroBooNE and ICARUS in the SBN and on-axis neutrinos to MINERνA, MINOS, and NOνA. For the NuMI beamline, protons collide with a carbon target at 120 GeV, producing pions and kaons that travel into a set of horns. The horns direct currents in one direction or another to create a ν_μ or $\overline{\nu}_\mu$ enriched beam. Because of the energies used in the NuMI beamline, there is a much higher content of ν_e neutrinos than there are for the BNB.

For NuMI, the neutrino energy spectrum would cover the range of energies from 1 GeV to 16 GeV. The 120 GeV proton beam is extracted from the Main Injector ring at Fermilab and sent through an area called the Main Injector MI-60 extraction enclosure, an area known as the NuMI stub, and an inclined pipe which carries the protons to the vicinity of the target underground [43].

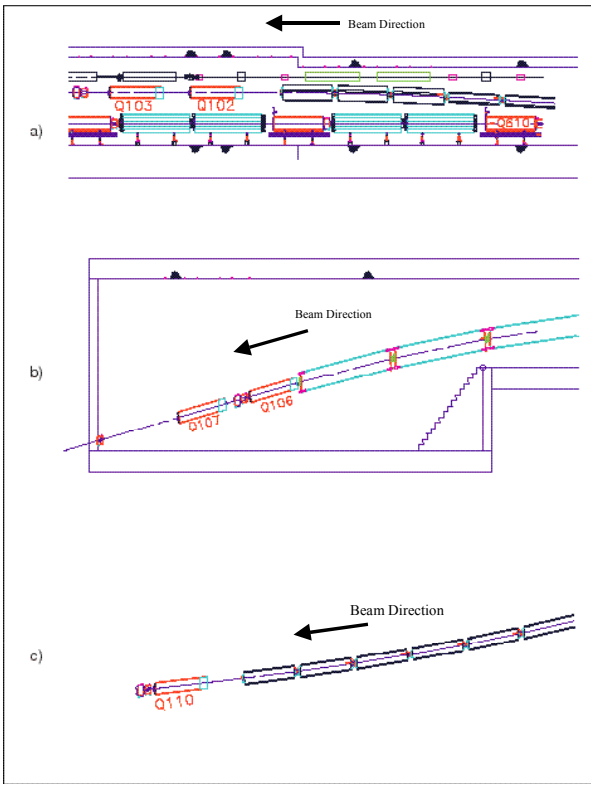

Figure 2.7: The three stages of passage to the vicinity of the NuMI target: (a) the Main Injector MI-60 extraction enclosure, (b) the NuMI stub, and (c) the inclined pipe which leads underground.

A graphic of this is shown in Figure 2.7. The protons are transported in pulses which contain at least 2.5×10^{13} protons each. A set of quadrupoles and bending magnets direct the proton beam towards the NuMI target.

The protons strike the proton target in a beam pointed directly at the MINOS far detector in an attempt to maximize the event rate there. The target is shaped so that most of the primary protons from the Main Injector interact but so that a minimum of the pions and kaons interact as well. This is achieved by making the target long and thin so that the pions and kaons can escape through the sides. The effects of the field from the focusing horns is what determines the length of the target. The radius of the target is determined by striking a balance between the flux of pions and kaons (which decreases with increasing radius) and the heat from the incidence of the proton beam (which also decreases with increasing radius).

There are two focusing horns, which are meant to focus the secondary particles of a given sign down the axis of the decay pipe. The horns have a parabolic shape, which is meant to make their magnetic fields act as lenses. Particles that are more or less focused by the first horn are more focused by the second horn so that they continue down the beam direction.

The focused neutrinos of a given sign pass 50 m to the start of the decay pipe, which is focused in the direction of the MINOS cavern in the Soudan mine in Minnesota. The length of the decay pipe, 675 m, was chosen to maximize the neutrino flux at the far detectors for the studies to be performed while also minimizing the associated costs. The radius of the decay pipe was chosen to be 1 m to minimize the kaon and pion interactions with the walls of the pipe while keeping the cost of manufacturing the pipe low.

A hadron absorber is located at the end of the decay pipe. All hadrons, including the protons that did not interact in the target, are stopped by this device. The concentration of incident particles is much less than it is at the NuMI target. A muon shield in the form of 240 m of dolomite rock is also located at the end of the decay pipe to remove all muons that emerge from the decay pipe before they enter the MINOS near detector.

CHAPTER 3

X-ARAPUCA Light Detectors

As mentioned in Chapter 2, the SBND experiment will include photomultiplier tubes (PMTs), ARAPUCAs, and X-ARAPUCAs in its photon detection system (PDS). The X-ARAPUCAs and ARAPUCAs, a word which means 'trap to catch birds' in Portuguese, are meant to improve the timing sensitivity and efficiency of a PMT-only photon detection system. Its timing has a faster response than PMTs, and it also operates on less voltage than PMTs do. SBND will demonstrate how these devices will work in preparation for the DUNE experiment. Light collection is essential for a surface LArTPC like SBND to reject cosmogenic backgrounds in order to select neutrino interactions. In DUNE, information from the PDS is important to study nucleon decay as well as supernova neutrinos if such an event would occur during data-taking.

3.1 X-ARAPUCA Structure and Operation

The X-ARAPUCA is valuable to the SBND experiment because they cover large detection areas (of approximately 1 m^2) with efficiencies at the several percent level. It is based on the idea that photons from light collected in the SBND TPC can be trapped in a box and used to study the neutrino interactions.

Physically, the X-ARAPUCA is a box which consists of a dichroic filter (located below a layer of p-TherPhenyl (pTP) when detecting VUV light, which shifts the 127 nm wavelength up to 350 nm) and an acrylic slab made of PolyVinyl Toluene (PVT) which shifts the wavelength close to the wavelength of green light (~550 nm). A picture is shown in Figure 3.1. A dichroic filter is a device which is almost completely ($> 95\%$) transparent to wavelengths below a specific value and almost completely ($> 98\%$) reflective to wavelengths above that same value. The slab adjusts the wavelength of light that passes through to a specific value. An image of the components of an X-ARAPUCA is shown in Figure 3.1 [10].

There are three mechanisms by which X-ARAPUCAs will detect scintillation light in liquid argon. First, a photon may come in and be wavelength-shifted to a greater wavelength by the slab

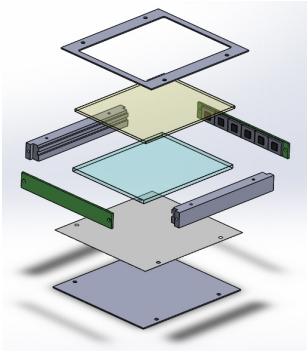

Figure 3.1: The structure of an X-ARAPUCA in SBND. It consists of (from top to bottom) a filter holder, a dichroic filter, a wavelength-shifting acrylic slab, a 3M VIKUITI foil, and a G-10 backplane [10].

before being prevented from leaving the X-ARAPUCA by the dichroic filter. Second, a photon that is converted by the filter and the slab can be trapped in the slab by total internal reflection. The sides of the filter that do not contain the photosensors will be coated with a reflective layer to keep the photon trapped. Lastly, a photon that arrives at a high angle of incidence will be reflected off the slab and directed to the photosensors. An image of these process is shown in Fig. 3.2 [10].

There are two types of X-ARAPUCAs that will be used in SBND. One detects direct scintillation light from the neutrino interactions and one which detects light which is wavelength-shifted from the UV spectrum to the visible spectrum by using TPB. There are 96 direct light X-ARAPUCAs and 96 reflected-light X-ARAPUCAs in SBND for a total of 192.

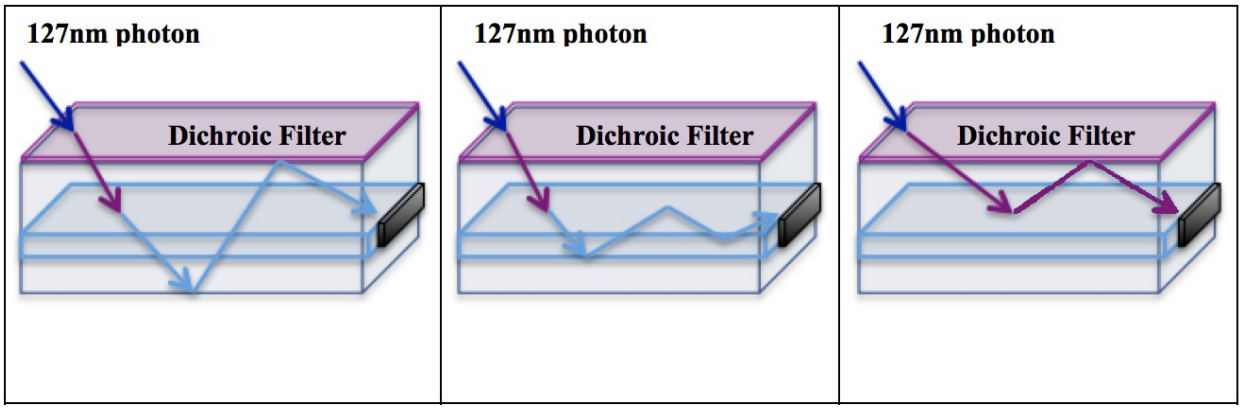

Figure 3.2: A graphic showing the three ways that an X-ARAPUCA detects emitted light in liquid argon [10].

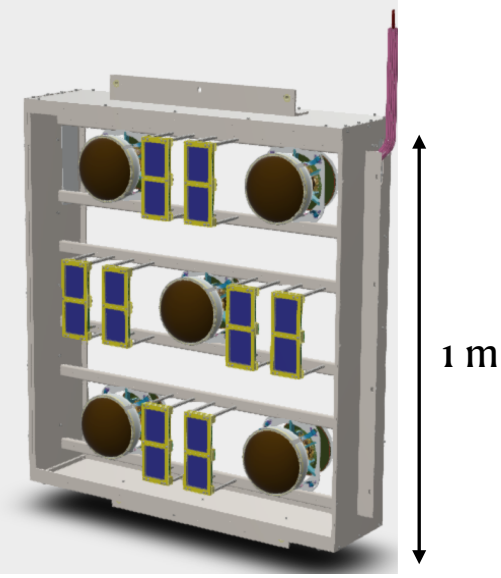

Figure 3.3: A graphic of the panel that contains the X-ARAPUCAs and the PMTs. Twelve of these will be placed behind each of the anodes in SBND.

3.2 Position in SBND

The X-ARAPUCAs in SBND will be located on panels with the PMTs on each side of the detector (behind each of the anodes in the detector). An image of one of these panels is shown in Figure 3.3. Twelve of these panels will be located behind each of the anodes. Figure 3.4 contains an image of the X-ARAPUCA and each of the SiPMs used to read it out. Along with the X-ARAPUCAs in the detector, there will be 120 PMTs.

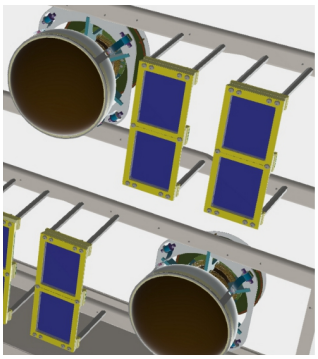

Figure 3.4: A zoomed-in image of the X-ARAPUCAs in SBND with the two SiPMs which read out the X-ARAPUCA shown in maize and blue.

3.3 DAPHNE Readout System

The readout for the X-ARAPUCAs, named Detector electronics for Acquiring PHotons from NEutrinos (DAPHNE), is adapted from a system designed for the mu2e experiment (described in Section 1.5). The readout system consists of a front-end board (FEB) which collects an analog signal from the SiPMs attached to the X-ARAPUCA. The analog signal is converted to a digital one and is stored in a Random Access Memory (RAM) chip on the FEB before being sent to a controller, which combines the signals from each of the FEBs. Each FEB consists of four Field Programmable Gate Arrays (FPGAs), an integrated circuit which is programmed for customizable use, each of which reads in four channels of data. Each channel reads data in from four SiPMs. There are three lower-level FPGAs on the controller which collect the data from the FEBs and one higher-level FPGA which combines the information from the lower-level FPGAs. The OrangeTree card on the controller sends information to the Data Acquisition System (DAQ) over an ethernet connection. There are twelve FEBs total in the experiment, and they will feed into two controllers (six will feed into each controller). The system will read out a total of 176 X-ARAPUCAs.

3.3.1 Front-End Board (FEB)

An image of the FEB is shown in Figure 3.5. Data is read in to the FEB by means of HDMI cords which plug into the ports shown at the bottom of the image. The data is converted from an analog to a digital signal in 12 bit words at 80 MHz. Logic written to the FPGA determines the quantity of data at each point in the pipeline within the FEB. Data from each FEB is fed into the controller over ethernet.

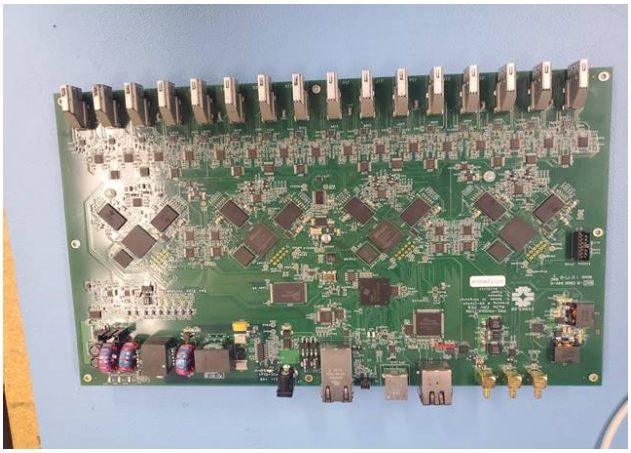

Figure 3.5: A graphic of the FEB used in DAPHNE. The FEB is connected to the SiPMs by means of the HDMI ports on the part of the FEB at the top of the image.

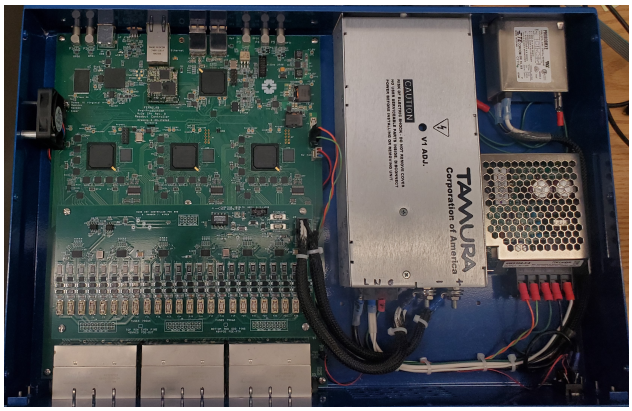

Figure 3.6: A graphic of the controller used in DAPHNE. The three lower-level FPGAs are shown along with the higher-level ones. The FEBs connect by means of ethernet cords to the side of the controller chassis at the bottom of the image. The controller connects to the DAQ by means of the ethernet connection at the top of the image.

3.3.2 Controller

An image of the controller is shown in Figure 3.6. The controller consists of four FPGAs, a microcontroller chip, and an OrangeTree card (OrangeTree is the name of the manufacturer). The OrangeTree card determines the flow of data from the top-level FPGA to the DAQ. As of this writing, the code controlling the interface between top-level FPGA and the OrangeTree is under development.

3.3.3 Readout Rate and Suppressing Samples

Because of the data rates that are expected in the experiment, it is possible that the readout cannot keep up with the amount of samples streaming through the system from the X-ARAPUCA. The bottleneck upstream of the controller (the part of the system that determines the limitations of a system, in this case in the context of processing data) is the rate at which the controller can read data from each of the FEBs, which is 10 MB/s.

As a first-order calculation of how much data collected by the SBND triggering system that will have to be suppressed, the expression below is used. This is a balance of the rate at which data is read out of the board to the ethernet (lefthand side) to the rate at which data is read onto the board (righthand side).

$$\mathrm{B} \;=\; \mathrm{WfSZ} \tag{3.1}$$

The variables in Equation 3.1 have the following definitions:

Variable	Definition
B	Bandwidth for Reading Data From the FEB To the Controller [$\frac{\text{MB}}{\text{s}}$]
W	Length of Readout Window for One Cosmic [s]
f	Frequency of Cosmic Readouts [s^{-1}]
S	ADC data rate [$\frac{\text{GB}}{\text{s}}$]
Z	Suppression Rate [Unitless]

This equation must be inverted to solve for Z, the percentage of information that will have to be suppressed in order to balance the input and output rates of data onto the front-end board (FEB). You can break this equation down even further, defining the frequency of cosmic readouts using the following equation:

$$\text{f} = \text{CTN} \tag{3.2}$$

The variables in 3.2 have the following definitions:

Variable	Definition
C	Rate of Cosmic Ray Muons [s^{-1}]
T	TPC Windows [s]
N	Trigger Rate [s^{-1}]

The values that are plugged in for these quantities have the following values:

Variable	Value
B	10 $\frac{\text{MB}}{\text{s}}$
W	7 μs
S	7.68 $\frac{\text{GB}}{\text{s}}$
C	5.208e3 s^{-1}
T	4.8 ms
N	10 s^{-1}

The value for the readout window length (W) was selected by considering the muon rest frame lifetime of 2.2 μs and picking a time of several times this value to detect light from most muon decays to Michel electrons in the detector. The value for the ADC data rate (S) was selected by considering the sampling rate, the number of channels, and the size of each of the samples. The cosmic rate (C) considers 25 cosmic rays in a readout window of 4.8 ms, the appropriate values for MicroBooNE.

If Equation 3.2 is inserted into Equation 3.1 and the resultant equation is inverted to solve for Z, the value is found to be 0.74. This means that 26% of the information collected will have to be eliminated at a sampling rate of 80 million samples per second to keep up with the bandwidth of 10 MB/s.

If the entire system is considered together, then the process that serves as the limiting one of its entire operation is the readout of data from the OrangeTree Card to the DAQ. As of this writing, a similar calculation has not been performed for that process.

3.3.4 Readout Modifications

Several major modifications were made to the readout to adapt it to SBND's needs from its original form with mu2e. First, the amount of data to be read out for each pulse was adjusted to include the full amount of the pulse above threshold to include full pulses. This is important to reconstruct entire flashes, especially the late part that may belong to light belonging to a Michel electron. Secondly, the firmware for the controller was changed so that the controller reads data out over an ethernet connection. Lastly, the algorithm for the top-level FPGA is being modified so that data is read out from the top-level FPGA to the DAQ. Previously, the microcontroller was used to send commands to the OrangeTree via the top-level FPGA, but that step has been removed to speed up the data rates that the system can handle.

3.3.5 Simulation Study

A study was perfomed using data from a teststand with X-ARAPUCAs to learn the nature of the waveforms in practice. These waveforms were taken from some X-ARAPUCAs that detect direct light and some that detect reflected light. The waveforms were taken over an entire event readout, which for SBND lasts for 3.75 ms: 1.25 ms (one drift length) before the trigger time and 2.50 ms (two drift lengths) after. The study found that if a window of 2 μs is opened around every pulse, then $> 98\%$ of pulses above a modest threshold can be read out.

3.3.6 Current Status

To complete the DAQ for the X-ARAPUCA light detectors, the following steps have to be taken in the following order:

1. The top-level controller firmware must be adapted to accomodate the OrangeTree only. This would take the microcontroller completely out of use in delivering data to the DAQ.

2. The controller firmware must be made to work with the BoardReader, which takes information from the controller to deliver to the DAQ.

3. The BoardReader must be designed to deliver data to the DAQ in the appropriate way to be used in analysis with the SBND experiment.

As of this writing, the first step is underway, but steps 2-3 have yet to commence.

CHAPTER 4

The MicroBooNE Experiment

MicroBooNE is an 85 active ton liquid argon time projection chamber located 470 m from the Booster Neutrino Beam (BNB) target at Fermilab in Batavia, IL, USA. It has been taking data since October 2015, and it is the first experiment in the Short Baseline Neutrino Program (SBN) at Fermilab to do so. The other two experiments are the SBND experiment, scheduled to take data in 2022, located 110 m from the target, and ICARUS, scheduled to take data in 2021, located 600 m from the target, both described in Chapter 2. The peak neutrino energy for the Booster Neutrino Beamline (BNB), the on-axis beam that delivers neutrinos to MicroBooNE, is 0.8 GeV. MicroBooNE is also exposed to neutrinos from the Neutrinos at the Main Injector (NuMI) beamline, which delivers the signals under study within Chapter 8, ν_μ neutrinos from the two-body decay of a kaon at the NuMI beam dump, and Chapter 9, $\nu_\mu/\overline{\nu}_\mu$ neutrinos from the NuMI beam target.

The primary physics goal of MicroBooNE is to investigate the low-energy excess of electron neutrino-like events observed first by the LSND experiment at Los Alamos National Laboratory and later by the MiniBooNE experiment at Fermilab. A plot showing the disagreements between data and simulation for the electron neutrino-like events is shown in Chapter 1 in Fig. 1.5. MicroBooNE can distinguish electron events from photon events much better than MiniBooNE can, which is crucial to resolving what is causing this discrepancy. Potentially, the discrepancy can be explained by a fourth type of neutrino, called a 'sterile' neutrino, which interacts only by means of the gravitational force. This is described in detail in Chapter 1.

MicroBooNE has made significant contributions to the understanding of LArTPCs and the associated physics. The first study of the space charge effect (SCE) in liquid argon, both in simulation and in data, has been performed with MicroBooNE [23] [11], described in detail in Chapter 7. Furthermore, the liquid argon in MicroBooNE has been shown to be quite pure, corresponding to an electron lifetime of 18 ms during periods of stable data-taking [44]. Along with the other experiments in the SBN, MicroBooNE has been an important step in preparations for DUNE (described in Section 1.5).

MicroBooNE's periods of data-taking, called 'runs', take place from the fall of one year to the

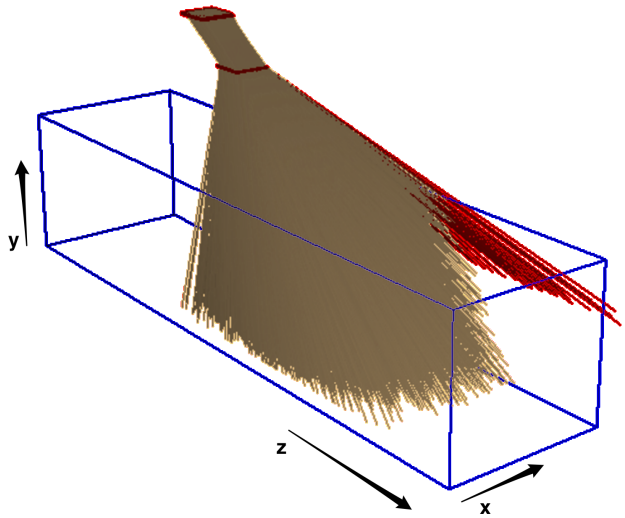

Figure 4.1: A graphic of the MUon Counter System (MuCS) in MicroBooNE [11]. This is a configuration in which the tracks that intersect both boxes may pierce the top and the cathode. The brown tracks are those which intersect the TPC and the red tracks are those which miss the TPC.

summer of the next. On-beam data, the sets of data which may include neutrino interactions, are taken in the fall to the spring, while off-beam data is taken in the summer. Off-beam data is also taken during the fall to the spring during the periods when the beam is off.

MicroBooNE performs its calibrations primarily with cosmic muons. Isolating a sample of muons for this purpose is described in Chapter 6 and the calibration for the largest analysis systematic, the space charge effect (SCE), is described in Chapter 7. There is also a UV laser calibration system available for providing higher precision calibrations than what cosmic muons can provide in addition to performing calibrations on the timescale of several seconds as well. MicroBooNE also used an external tagger called the MUon Counting System, MuCS, which tagged cosmic muons with specific trajectories for detector physics studies. A graphic of the MuCS system is shown in Figure 4.1 [11].

MicroBooNE's first cross section result arrived in 2018 in the form of a charged-current π_0 total cross section; this was also MicroBooNE's first-ever non-detector physics measurement published [13]. The muon neutrino charged-current inclusive result with BNB data was published in 2019 [14]. Two other cross section results, the charged-current quasi-elastic-like muon neutrino differential cross section and the differential cross section of ν_μ charged-current events with protons and no pions, are presented in Section 4.7 as well.

4.1 Detector Structure

MicroBooNE is a single-phase LArTPC, meaning that the argon is only in one state (liquid). Also, unlike SBND, it only contains a single anode. The electric field within the TPC is set to 273.9 V/cm, and the liquid argon is kept at a temperature of 89 K.

MicroBooNE readout consists of three wire planes which collect charge at the anode of the detector. The wire planes are named the U, V, and Y. The U and V collect charge by means of induction, and the Y plane collects charge by means of collection. The U and V planes are oriented at 60° with respect to one another, and the Y plane wires are parallel to the y-axis.

The origin for the detector coordinate system is located at the upstream end of the detector, on the anode side, midway up the full height of the detector. The x-coordinate extends from [0 cm, 256.35 cm], the y coordinate, from [-116.5 cm, 116.5 cm], and the z-coordinate, [0 cm, 1036.8 cm]. A graphic of the detector is shown in Figure 4.2.

The MicroBooNE optical detection system consists of 32 photomultiplier tubes (PMTs). These are arranged as in the diagram shown in Figure 4.3 and have a resolution on the order of nanoseconds. They are designed to detect light of wavelength 400-500 nm, not the UV light which is produced in the detector of wavelength of 125 nm. Therefore, there is a plate coated with Tetraphenyl Butadiene (TPB) and polystyrene. TPB is a molecule which absorbs scintillation light and reemits it with a wavelength of ~425 nm.

MicroBooNE also consists of a CRT, with four panels placed behind the top, bottom, anode,

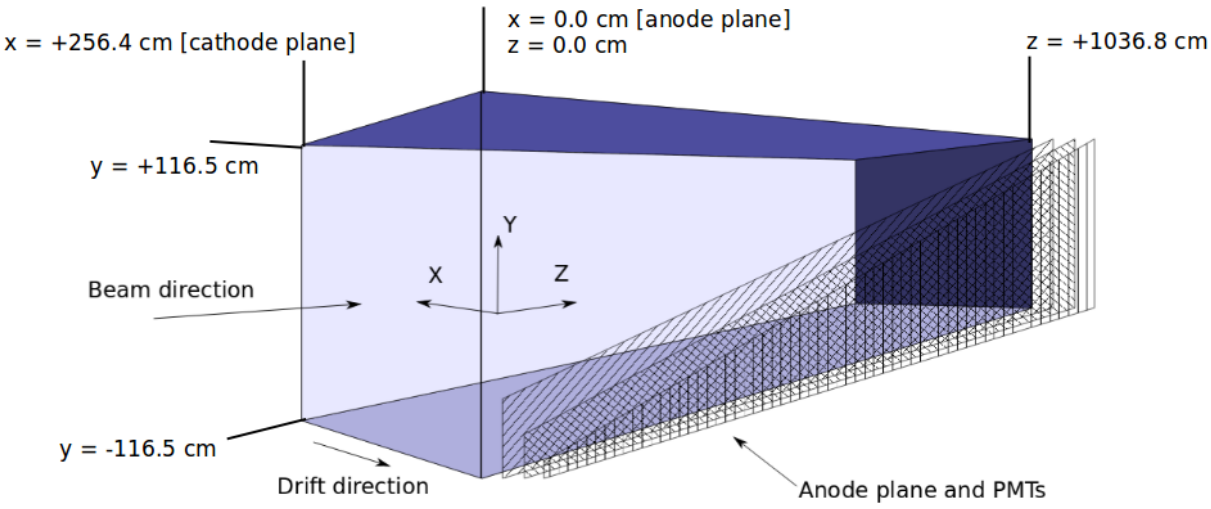

Figure 4.2: A graphic of the MicroBooNE detector. The Booster Neutrino Beam source comes in from the front of the detector, shown on the left side of the image.

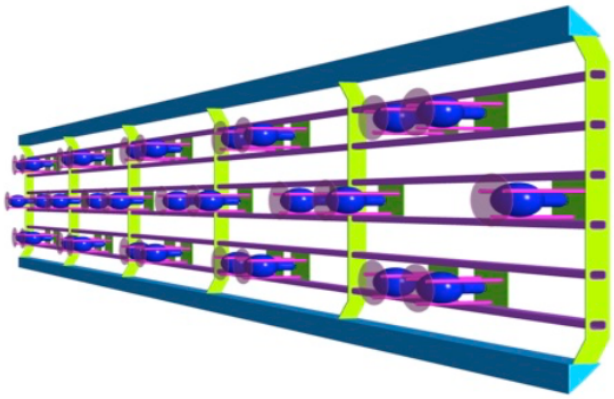

Figure 4.3: A graphic of the MicroBooNE PMTs. There are 32 of them in the detector in total, and they are each 8 inches.

and cathode faces of the detector. The top panel is placed 5.4 m above the TPC, the bottom panel is located 1.4 m below, and the anode and cathode side panels are located 1.4 m from the TPC on either side. The panels consist of scintillator strips, with sixteen scintillator strips 10.8 cm wide and 2 cm thick. Each scintillating strip is equipped with two WLS fibers which detect the light signals. The fibers are read out by one SiPM installed at the fiber edge. A total of 32 photosensors are deployed in each module. All modules have the same width of 1.75 m and their lengths depend on their position inside the detector. The CRT is currently used in analyses of a time period in which the system was fully operational, which was any time period starting in November 2017 or later. It is currently used to reject cosmic backgrounds by using timing and position, the strategies of which are described in Chapter 8.

4.2 Detector Electronics

There are two systems of detector electronics, the TPC electronics and the PMT electronics. The TPC electronics consist of both cold electronics, which are located in the TPC and are responsible for the shaping and pre-amplification of the signals on the wire planes, and the warm electronics, which are located in the cryostat and are responsible for the digitization, processing, and readout of the signals passed from the cold electronics. These are then transmitted to the ADC and Front-End readout modules (FEMs), which are contained in approximately equal amounts in nine readout crates. The PMT electronics control the amplification, shaping, digitization, and formatting of the signals from the light detection system.

4.2.1 TPC Electronics

The main part of the TPC cold electronics are Application Specific Integrated Circuits (ASICs), each of which is connected to 16 anode wires, that number 516 in total. They operate with a gain of 14 mV/fC and a shaping time of 2 μs. They are located in the liquid argon close to the wires so to optimize the signal-to-background ratio. The warm electronics consist of three parts: (1) the intermediate preamplifier, which amplifies the signal as it travels from the cold electronics, (2) service boards, which regulate and monitor the signals from the front-end ASICs, and (3) the readout electronics, which digitize and compress the data before it is sent to the DAQ. The readout electronics digitize the data at 64 MHz with 12 bit resolution, and the data is downsampled by an FPGA chip to 2 MHz. They consist of 130 ADC/FEMs which are housed in the nine readout crates, synchronized together by a 16 MHz clock. The data passes from there to the XMIT modules, where it is stored temporarily.

4.2.2 PMT Electronics

The PMT signal is processed with a unipolar shape that has a 60 ns rise time and takes 200 ns to return to baseline. These waveforms are digitized at 64 MHz with 16-bit resolution at 4095 dynamic range at 4 V/4095 ADC. They are collected on both low-gain (LG) and high-gain (HG) channels to capture the waveforms with both good dynamic range and full characterization. One cold cable carries in the high voltage to the system and transmits the read-back signals for each PMT. The system consists of 3 ADC/FEM boards which also connect to the XMIT modules which carry the signals to the DAQ crates.

4.3 Data Structure and Capacity

The MicroBooNE PMT and TPC systems acquire data separately from one another, which is combined offline to form events for the detector. The TPC window consists of 1.6 μs frames which are stitched together around each external trigger, with one frame coming before the trigger time and two frames coming after the trigger time. The purpose of this is to collect the charge from interactions that occur close to the cathode and properly reject cosmic ray events. The drift time of the detector is 2.3 ms, so that allows interactions that occur in time with the beam more than enough time allowance to reach the anode of the experiment.

While the TPC system just receives triggers and collects data with the static readout, the PMT system issues and receives triggers. The PMT system collects 23.4 μs of unbiased readout immediately following a trigger in an attempt to collect all of the light information associated with a neutrino interaction. Additionally, 0.6 μs of data is collected when a PMT waveform passes a

specific threshold. This data-taking, referred to as the cosmic discriminator readout, collects data anytime a waveform passes a threshold of 9.5 PEs. Because very few events contain a neutrino interaction of the entire set taken by the detector, an offline software trigger is applied to filter out events in which there is not a minimum amount of light recorded in the beamspill.

Altogether, the data rates in the detector are approximately 150 MB/event for the TPC information, which is scaled down to 30 MB/event after using Huffman encoding, which is a method of lossless data compression. The sofware trigger reduces the amount of events for which it is necessary to save this amount of information.

4.4 Detector Non-Idealizations

In an idealized detector, the number of ionization electrons that arrive at the anode wire planes is equal to the number that were released from the original argon atom upon ionization. These electrons flow towards the anode wire plane under only the influence of the TPC electric field, arriving at the detector at the same y and z coordinates at which ionization occurred. The x coordinate is equal to the true x position inside the detector with an offset proportional to the time at which ionization occurred with respect to the trigger. There are four main detector effects that contribute to the impracticality of this scenario: SCE, recombination, electron lifetime, and diffusion. SCE is discussed in detail in Chapter 7, so it is not covered here. A declining light yield in the detector over time also represents a detector non-idealization, but that does not affect what is happening in the TPC.

4.4.1 Recombination

Recombination is the absorption of a drifting ionization electron with an argon ion. This is a form of 'charge quenching' in the detector, which occurs when the charge reconstructed at the anode wire planes is less than what was deposited in the detector. The equation for recombination is given below:

$$\frac{dQ}{dx} = \frac{dE}{dx} \times R \times \frac{LC}{W} \tag{4.1}$$

In this expression, R is the recombination factor, $\frac{dQ}{dx}$ is the charge deposited per unit length, $\frac{dE}{dx}$ is the energy deposited per unit length, L is the lifetime purity, C is a calibration constant to convert units, and W is the electron ionization energy, 23.6 eV. R can be described by two models: the Birks Model and the Modified Box Model. They are described by the following equations:

$$R_{\text{Birks}} = \frac{A_B}{1 + \frac{k_B}{\rho} \times \frac{dE}{dx} \times \frac{1}{\epsilon}} \tag{4.2}$$

$$R_{\mathrm{ModifiedBox}} = \frac{\log(\alpha + \frac{\beta_P}{\rho\epsilon} \times \frac{dE}{dx})}{\frac{\beta_P}{\rho\epsilon} \times \frac{dE}{dx}} \tag{4.3}$$

In the Birks model equation, using an electric field of ϵ = 0.5 kV/cm and a liquid argon density ρ = 1.383 g/cm^3, ICARUS measured the two fit parameters A_{B} and k_{B} to be 0.800 $\pm$ 0.003 and 0.0486 $\pm$ 0.0006 (kV/cm)(g/cm^2)/MeV, respectively. In the Modified Box model equation, using an electric field of ϵ = 0.481 kV/cm and a liquid argon density ρ = 1.383 g/cm^3, ArgoNeuT measured the two fit parameters α and β_{p} to be 0.93 $\pm$ 0.02 and 0.212 $\pm$ 0.002 (kV/cm)(g/cm^2)/MeV, respectively. Previous experiments have used these two models in fitting their data for the recombination effect. ArgoNeuT has fit its data with both the modified box model and the Birks model, while ICARUS has fit its data with the Birks model.

4.4.2 Diffusion

Diffusion is the spreading-out of the ionization electron cloud as it flows towards the anode wire planes. This occurs due to forces between the ionization electrons themselves. Diffusion is calculated in terms of a longitudinal coefficient, which pertains to the drift direction, and the transverse coefficient, which is calculated in the wire coordinate direction. The equation for longitudinal diffusion is given in terms of the width of an electron cloud arriving at the wire planes by the following equation:

$$\sigma_{\mathrm{t}}^2(\mathrm{t}) = \sigma_0^2 + (\frac{2\mathrm{D_L}}{\mathrm{v_d^2}})\mathrm{t} \tag{4.4}$$

In this equation, $\sigma_{\mathrm{t}}^2(\mathrm{t})$ is the width of the electron cloud at time t in units of s^2, σ_0^2 is the initial width of the electron cloud in units of s^2, $\mathrm{D_L}$ is the diffusion constant with units of cm^2/s, $\mathrm{v_d}$ is the drift velocity of ionization electrons in the detector, and t is the time that the electron cloud has been drifting in units of s. MicroBooNE has measured the diffusion value using ACPT muon tracks, but has currently switched over to using CRT tracks for improved coverage. Both are described in Chapter 6. The measurement is performed by fitting track waveforms to a Gaussian and using the standard deviation to estimate the the longitudinal coefficient. As of this writing, there is a new analysis underway for measuring the transverse diffusion coefficient.

4.4.3 Electron Lifetime

Electron lifetime is defined as the half-life of an ionization electron in the MicroBooNE TPC. The electron lifetime could be lower if there are elements within the detector which absorb the ionization electrons as they flow towards the anode wire planes, such as oxygen. A measurement to extract this quantity was found by taking AC-crossing tracks and finding the ratio between the

amount of charge at the anode to the amount of charge at the cathode with the following equation, where τ is the variable representing the electron lifetime:

$$\frac{Q_A}{Q_C} = \exp(\frac{-\mathrm{t}_{\mathrm{drift}}}{\tau}) \tag{4.5}$$

In the selection for the tracks, there were also angular cuts and a cut on the number of collection plane hits to ensure that a pure sample of tracks was used.

The amount of time that it takes for an ionization electron to flow from the cathode to the anode, detector effects nonwithstanding, is 2.3 ms. It was found that during periods of stable data taking, MicroBooNE has an electron lifetime of 18 ms, which is more than seven times the drift time of the detector. Even during times of lower-purity data-taking, the electron lifetime value is 6.3 ms, which is more than 2.5 times the drift time of the detector.

4.4.4 Light Yield Decline

The light yield in MicroBooNE has been declining over the first four years of data-taking, an effect that is still under study. The light deposited in the PMTs from anode-piercing tracks and cathode-piercing tracks has declined by 25-30% and 45%, respectively, between April 2016 and July 2018. The amount of light in reconstructed flashes is lower as a result, and flash-matching has suffered as well.

4.5 Issues With MicroBooNE

There are two issues with MicroBooNE that cause the operation of the experiment to differ from the way that it was designed to run: malfunctioning wires and excess light in the detector.

4.5.1 Malfunctioning Wires

Approximately 10% of the wires in MicroBooNE are either shorted, noisy or misconfigured. There are two main regions of the detector with shorted wires: on the U plane, there is a region of shorted wires located approximately at z = 200 cm, and on the Y plane, there is a region of dead wires located approximately at z = 700 cm. Misconfigured wires are those which have an incorrect shaping time of 1 μs instead of the standard 2 μs. That variety and noisy wires alike are located throughout the three wire planes.

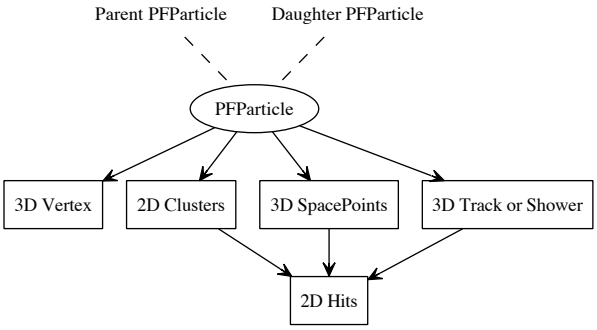

Figure 4.4: The Pandora output data products [12]. The Pandora PFParticle hierarchy is indicated by the dashed lines and the associations between the PFParticles and their associated products are denoted by the solid lines.

4.5.2 Excess Light

There is an excess of 'late light', light that occurs in the 0.5 ms following a PMT flash, that occurs in MicroBooNE. This is scintillation light, because the Cherenkov light that occurs in a LArTPC is prompt. This can potentially be studied with a teststand setup.

4.6 Pandora Reconstruction Framework

All of the reconstructed objects in MicroBooNE that are described in Chapters 8 and 9 are constructed using the Pandora framework, which generates a particle hierarchy according to clustering of the charge on the wire planes [12]. Within this hierarchy, particles are linked to their daughters (the particles that they produced through an interaction) or their parents (the particles that generated them through an interaction), as shown in Figure 4.4. The particles are classified as either 'track-like' (like a muon, proton, charged pion, kaon, or lower-energy electron) or 'shower-like' (like a higher-energy electron or photon). These particles are formed from lower-level objects called 'hits', clusters of charge on one of the wire planes close in time. The 'tracks', or paths that the particles took within the detector, are input to the algorithms described in the later chapters and are associated with the neutrino vertex, the location in the detector where a neutrino interacted. Novel algorithms described in Chapters 8 and 9 are used to precisely find the location of the vertex within the interactions, so Pandora is not used for that purpose.

An additional challenge handled by the Pandora framework is selecting the part of an event which is most likely to contain a neutrino interaction. Pandora contains all potential neutrino candidates into a quantity known as a 'neutrino slice', which is described in more detail in Chapter 8. For most events, a set of binary requirements comparing the location and time of the flash

in-time with the beam to each neutrino slice will eliminate every neutrino slice but one. For the others, a flash-matching procedure that compares the amount of light in each PMT similar to the one described in Section 5.2.5, a topological score that uses TPC-only information to assess the probability that this neutrino slice is a neutrino (the NuScore variable in Section 9.2), and a comparison of the in-time flash to obvious cosmic tracks in the event are also used. For ν_μ CC events from the BNB datastream, this algorithm identifies a neutrino slice corresponding to the correct neutrino 93% of the time.

4.7 MicroBooNE Results

MicroBooNE has released a number of results so far pertaining to detector physics (most of which are discussed in Chapters 6 and 7), reconstruction, exotic and rare physics, and cross section physics. There are four cross section results to date which have been published: the total cross section of a charged-current π_0 interaction and differential cross sections of the inclusive charged-current ν_μ signal, charged-current quasi-elastic-like muon neutrino events, and muon neutrino events with protons and no pions in the final state. All of these results were produced using BNB data. Another cross section result, the flux-averaged cross section of inclusive ν_e and $\overline{\nu}_e$ events with NuMI data, has been accepted for publication but has not yet been published. All of the published cross section results are described in more detail below.

4.7.1 Charged-Current π^0 Total Cross Section

MicroBooNE's charged-current π^0 total cross section is the first automated selection of this signal in liquid argon. There is no cut placed on the invariant mass of the π^0 in the event, which informs how well shower energy is reconstructed in MicroBooNE. For the selection, shower identification and the distance between the vertex and a track allow for tagging the signal events. The result is also expressed while including nuclear scaling of the event rates with a target, which is shown in Figure 4.5 for deuterium (measured at Argonne National Laboratory), carbon (measured with MiniBooNE), and argon (measured within this work) [13].

4.7.2 ν_μ Inclusive Differential Cross Section

This is the first-ever double differential cross section ν_μ cross section on liquid argon. It measures the differential cross section as a function of the muon candidate momentum and the scattering angle with respect to the BNB beam direction, which allows for comparison between the neutrino-argon data and neutrino models over an expansive range of these variables. The result is shown in reconstructed space by translating the efficiencies from truth space through a process called

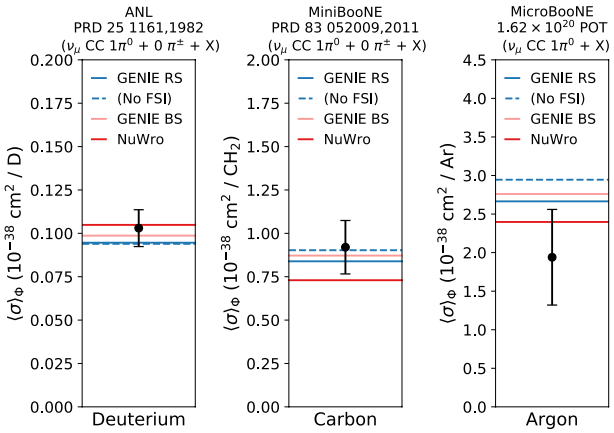

Figure 4.5: The result of the MicroBooNE charged-current π^0 total cross section (far right) compared to results for ANL (far left) and MiniBooNE (middle) [13]. The bars denote the total uncertainty.

'forward-folding'. The results are shown in Figure 4.6, where it can be seen that the greatest disagreements in the phase space occur in the most extreme backwards-going direction (top-left) and the most extreme forwards-going direction (bottom-right)[14].

4.7.3 Charged-Current Quasi-elastic-like Muon Neutrino Differential Cross Section

The differential cross section of charged-current quasi-elastic-like (CCQE-like) muon neutrino events requires that there is one muon, one proton, and no pions in the final state. For kinematic requirements in the analysis, the muon must have momentum $0.1 < p_\mu < 1.5$ GeV/c and an angle corresponding to -0.65 $< \cos(\theta_\mu) <$ 0.95 and the proton must have momentum $0.3 < p_p < 1.0$ GeV/c and an angle corresponding to $\cos(\theta_p) > 0.15$. The angles are calculated the same way that they are for the inclusive analysis described in Section 4.7.2. This is the part of the phase space region where the detector response to the signal is well-understood and the detection efficiency is appropriately high. One of the differential cross section results is shown in Figure 4.7 for (from left to right) the muon momentum, the proton angle, and the proton momentum for (top) the full phase space and (bottom) the part of the phase space with $\cos(\theta_\mu) > 0.8$ excluded. The efficiencies are calculated as the ratio of reconstructed events in a bin to the number of truth events in the same bin, which accounts for bin migrations. The cross section is expressed in terms of real variables. Removing the part of the phase space at high values of muon candidate $\cos(\theta_\mu)$ significantly improves the agreement between the theoretical models and the data.

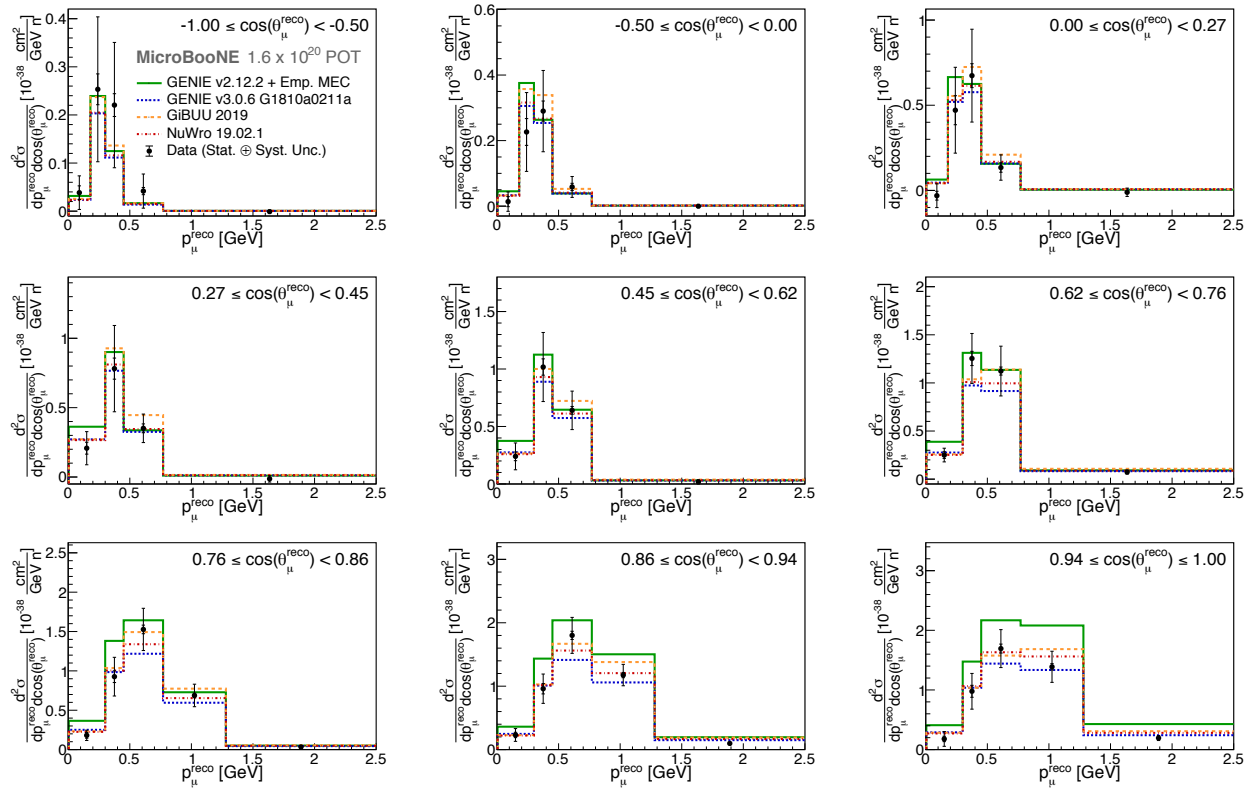

Figure 4.6: The result for the BNB charged-current inclusive differential cross section. The plots are for different values of the cosine of the scattering angle with respect to the BNB neutrino beam direction (the MicroBooNE detector z-direction) [14].

4.7.4 Differential Cross Section of ν_μ Charged-Current Events with Protons and No Pions

This analysis measures the differential cross section of events from the BNB datastream with a muon with momentum $p_\mu > 100$ MeV/c, no pions, and the most-energetic proton must have momentum in the range 300 MeV/c $< p_p <$ 1.0 GeV/c. This cutoff for the proton was chosen to improve sensitivity to nuclear effects in comparison to an inclusive measurement while also retaining high-enough statistics for a significant measurement relative to other exclusive final proton states. Two of the differential cross section results from this analysis are shown in Figures 4.8 and 4.9 for the muon momentum and the cosine of the muon angle with respect to the BNB beamline (the same definion as in Section 4.7.2), respectively. The same forward-folding technique that was used on the inclusive result in Section 4.7.2 was used for this analysis as well. The muon momentum plot has relatively high χ^2 per degree of freedom values driven primarily due to the highest-momentum bin, which is in tension with the theoretical models. Agreement in the differ-

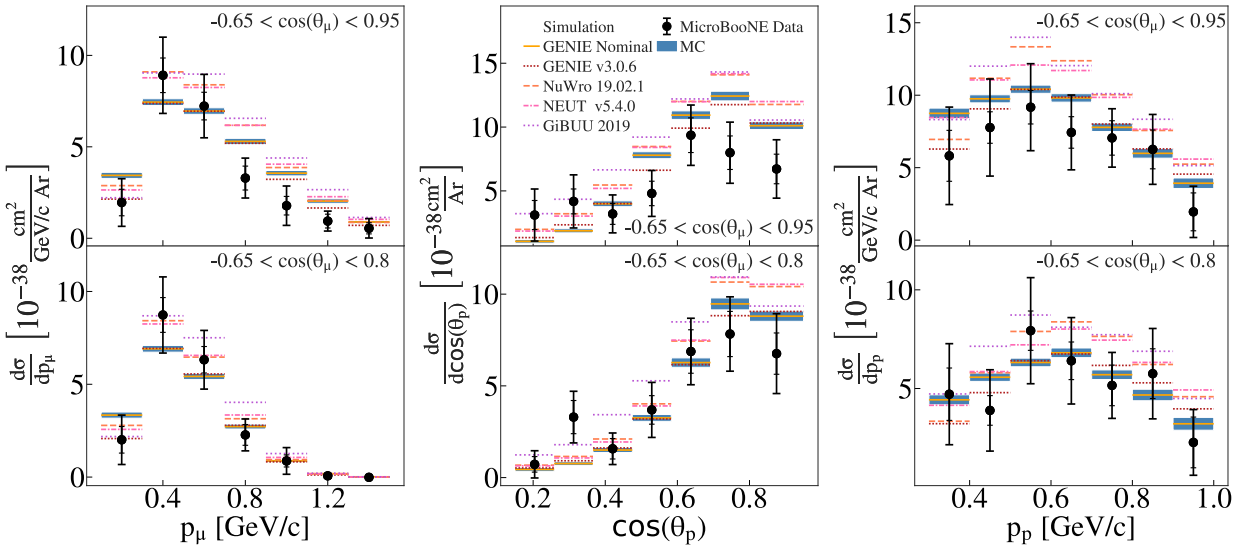

Figure 4.7: The result for the differential cross section of CCQE-like ν_μ events [15]. The differential cross section is shown as functions of (from left to right) the muon momentum, the proton angle, and the proton momentum for (top) the full phase space and (bottom) the part of the phase space with $\cos(\theta_\mu) > 0.8$ excluded.

ential cross section expressed in terms of muon candidate $\cos(\theta)$ (in reconstructed space) plot is good except in the most forward-going bin (most in the neutrino direction), where a deficit of data

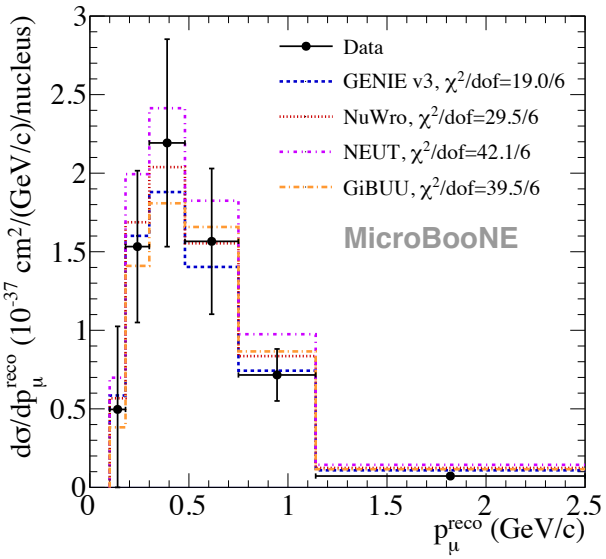

Figure 4.8: The differential cross section of ν_μ charged-current events with one proton and no pions in the final state, expressed in terms of muon momentum [16].

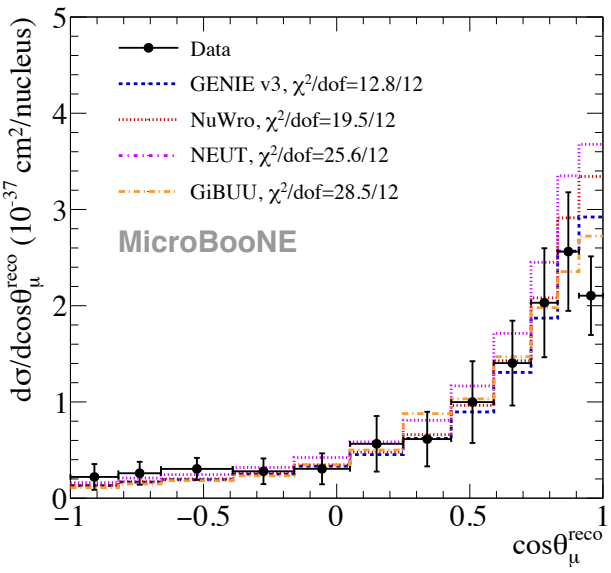

Figure 4.9: The differential cross section of ν_μ charged-current events with one proton and no pions in the final state, expressed in terms of muon candidate cos(θ) (in reconstructed space) [16].

is seen.

4.8 MicroBooNE Low-Energy Excess Analyses

To study the low-energy excess (LEE) of electron neutrino-like events observed by the MiniBooNE experiment (described in Section 1.4.3), MicroBooNE has launched four analyses which collectively use three frameworks: Pandora, Deep Learning, and Wirecell. These are the names with which they are referred to internally on the collaboration.

4.8.1 Pandora Analyses

There are two analyses on MicroBooNE which use the Pandora framework: the electron analysis and the single-photon analysis. They both make use of the Pandora reconstruction framework, which is described in Section 4.6. The electron analysis is tasked with reconstructing electron neutrinos in the Booster Neutrino Beamline (BNB) in an attempt to constrain the electron neutrino content of the beam's flux. The single-photon analysis is designed to test the hypothesis that the LEE is an anomalously large rate of neutral-current Δ resonant production on argon followed by Δ radiative decay. As of this writing, the Pandora electron LEE analysis has been approved to proceed to a sideband region closer to the signal region, and the single-photon analysis is currently being reviewed to make this same step.

4.8.2 Deep-Learning Analysis

The deep learning analysis uses convolutional neural networks (CNNs) to reject background, primarily cosmic rays, and select neutrino interactions. A first generation of the LEE analysis was completed that used the semantic-segmentation method to separate track-like pixels from shower-like pixels in an event display image. Their reconstruction utilizes the method of tagging cosmic rays described in Section 5.2. The reconstruction relies on identification of a neutrino vertex to then identify the particles that were produced by the neutrino and emanate from that point. The analysis is still working on getting approval to move into the sideband region closer to the signal region. A second iteration of the analysis, currently scheduled to be released in spring 2022, will utilize deep-learning techniques in more aspects of the analysis than currently use them.

4.8.3 Wirecell Analysis

The Wirecell analysis works by matching clusters of charge in 3D. Relative to the other two analyses, it has excellent cosmic rejection, which allows for better sensitivity to the LEE signal region. It works by applying successive filters designed to remove cosmic background, ν_μ charged-current background, and NC background. Wirecell is currently developing its analysis in the sideband region further from the LEE signal region.

4.9 MicroBooNE Data-Taking

MicroBooNE first recorded neutrino interactions in October 2015. Since then, it has taken five periods of neutrino data (known as Runs 1-5) as of the writing of this thesis. These periods begin in the fall of each year and conclude in the following summer. The data corresponding to the NuMI beamline can be split into those collected when the beam was in neutrino mode (with the beam consisting of ~55% more neutrinos than antineutrinos) and those generated when the beam was in antineutrino mode (with the beam consisting of an approximately equal amount of neutrinos and antineutrinos). The flux of neutrinos for NuMI running in neutrino mode and antineutrino mode are shown in Figures 4.10 and 4.11, respectively. For the purposes of having a well-defined flux for the measurement of the ν_μ charged-current differential cross section presented in this thesis, all of the 'good' (as determined by the beam, the DAQ, and the detector quality measures) Run 1 neutrino-mode data (February 2016 - June 2016) is used. The NuMI beamline was in neutrino mode for part of Run 2 and switched to neutrino mode at the end of Run 4 (Spring 2019), but enough statistics are available for Run 1 to make the single-differential cross section measurements. The amount of systematic error in the analysis (discussed in Chapter 10) prevents more statistics from being beneficial for the analysis.

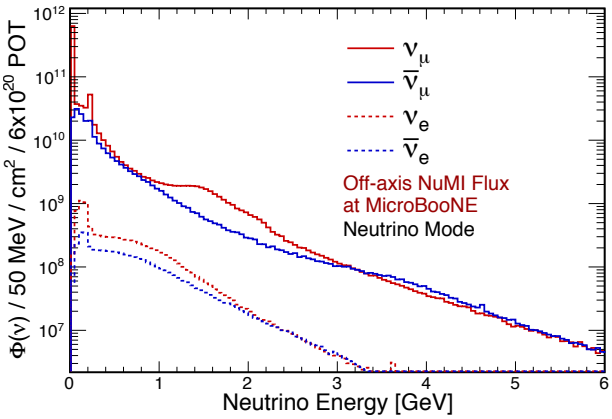

Figure 4.10: The flux of the NuMI beamline when it is in neutrino mode.

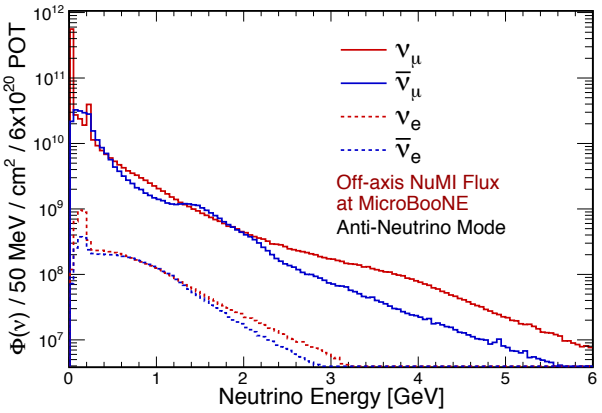

Figure 4.11: The flux of the NuMI beamline when it is in antineutrino mode.

CHAPTER 5

Cosmic Rays in MicroBooNE

5.1 Introduction

Cosmic rays are a background to every MicroBooNE neutrino analysis. In a typical readout window of 4.8 ms, there can be an expected ~25 cosmic rays that are incident within the detector. An example MicroBooNE event display with simulated cosmic rays is shown in Figure 5.1. In SBND, an experiment with an active volume ~32% larger than MicroBooNE's, there are expected to be ~50 cosmic rays per readout window. It is important to tag and remove cosmic rays from neutrino analyses. However, cosmic rays can also perform important purposes on the experiment, such as in a calibration of the detector (Chapter 6) and in attempts to detect latent physics effects.

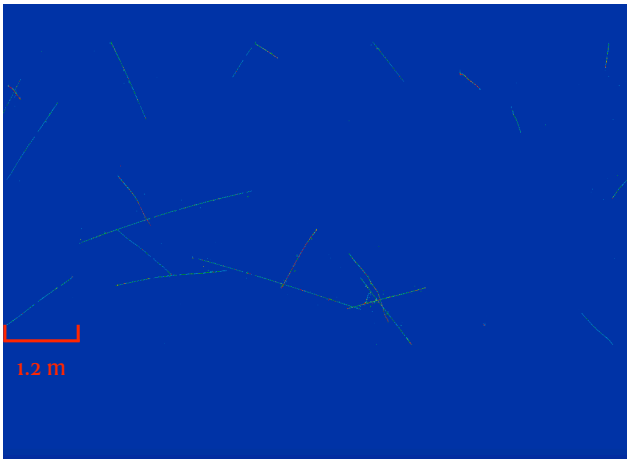

Figure 5.1: An event display with cosmic rays from the MicroBooNE collection plane. Cosmic rays, as shown in this image, are randomly distributed in position in the detector (the x-axis represents the detector z-axis direction) and time (the y-axis) in an event.

5.2 Tagging Cosmic Rays

When identifying the tracks of cosmic ray muons, it is important to recognize that the majority of them are 'through-going', meaning that they both enter and exit the detector. A tool designed to tag them for the MicroBooNE Deep Learning Low-Energy Excess analysis leveraged that fact by tagging the track endpoints first. The tracks, to within the distortions caused by detector non-uniformities, take largely straight-line behavior between the two endpoints, so the track's charge is almost entirely contained between them.

After identifying the through-going muons, the 'stopping' muons are identified. These enter the detector but then come to a halt within the detector. They are more difficult to reconstruct because they take a more curved path as they lose their energy close to the end of their trajectory and they may have a Michel electron at the end of their track. The through-going pixels are masked to make this process easier.

Finally, contained clusters of charge are tagged. These could be residue from neutral cosmic particles or they may be from neutrino interactions. These are passed to the next stage of reconstruction to determine whether they are from a neutrino interaction or not.

5.2.1 Through-Going Cosmic Ray Reconstruction

The first of the three stages of tagging cosmic rays, the reconstruction of through-going cosmic rays, starts by finding charge deposited on the boundary of the detector. The geometry of MicroBooNE's three wireplanes, discussed in Chapter 4, is designed so that wires from the three planes overlap in the same y and z coordinate locations at top, bottom, upstream, and downstream faces of the detector, as shown in Figure 5.2 for the top. When charge appears on these three wires, a boundary crossing can be declared.

There are two effects that make the process of matching charge to a wire crossing difficult. First, ~10% of the wires in the detector are unresponsive or produce bad signals. Second, the space charge effect (SCE) distorts the position of charge in the detector because the electric field within the detector is affected by the presence of positive ions. A discussion of SCE and its associated calibration takes place in Chapter 7.

Although this technique cannot be used to find boundary crossings for anode and cathode crossing points, those points can be identified by their coincidence with a flash recorded by the PMTs. Tracks that pierce the anode will have a drift coordinate proportional to the time that the flash was reconstructed in the PMTs at the trajectory point at which the track pierced the anode. Tracks that pierce the cathode will obey the same relationship but their drift coordinate will be offset by a constant proportional to the drift time of the detector (~2.3 ms). The proportionality

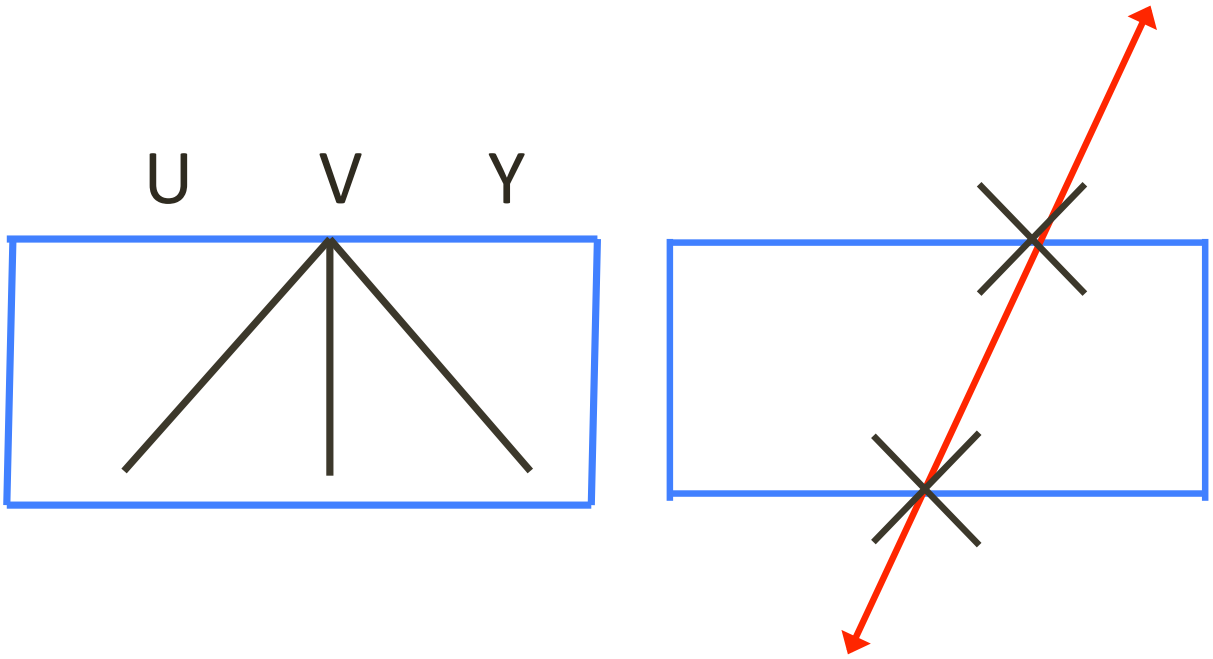

Figure 5.2: A descriptive image of the method used to tag boundary crossings at the top, bottom, upstream, and downstream ends of the detector. Wire crossings on the three planes (left) near to the detector boundary where cosmic muons entered or exited the detector (right) are used to find the endpoints of the cosmic muon track.

constant between the offsets on the drift coordinate and the times of the reconstructed flashes is the drift velocity of the detector. These geometric circumstances form the basis of isolating the ACPT calibration sample described in Section 6.2.

This technique was developed before the SCE calibration described in Chapter 7 was completed. To account for SCE, non-uniformities in the TPC electric field, in finding crossing wires on different planes, there are two distances from the wire planes at which wires on the planes which overlap with one another are identified: 3 cm and 16 cm. As you move further into the detector from the wire planes, there are more combinations of wires which overlap with one another. There is allowance that the wire with charge on it just be located in the neighborhood of the match, the value of which used was 20% for the studies shown here. This is a fairly relaxed requirement, as there are usually multiple wires satisfying this condition for a given crossing point. A nearest-neighbors clustering is used to identify the crossing point from a set of neighboring wires with charge. For the anode and cathode crossing points, this clustering algorithm is used to combine pixels on the same plane which have in-time charge. Two-plane combinations are used to allow for a bad channel on the third plane: the two planes with charge are used to identify the wire on the third plane which should have charge.

Using these techniques, ~85% of crossing points are found. This value remains largely constant

as the amount of cosmogenic activity in the image increases.

Once the crossing points are found, a straight-line fitter is used to determine if a track can be formed between a set of crossing points. For each set of crossing points, the algorithm moves in a straight line, looking at each set of five pixels in the vicinity of a central pixel in each step for charge that is above threshold. At each point, there must be charge above threshold on at least one of the pixels on each plane or two planes must contain charge and the third plane must be in a dead region. If 95% of steps contain pixels above threshold, then the pixels are tagged as belonging to a through-going track.

If between 20% and 95% of pixels are above threshold, then a second algorithm, called the A* algorithm, is used to reconstruct tracks [45]. It operates by finding points in 3D detector space either within a spherical radius or within a forward cone from previously found points. Because the algorithm is iterative by relying on previously reconstructed track points to find new ones, the images are compressed so that each pixel is 4 wires by 24 time ticks to reduce computation time. In the new image, therefore, a set of 4 wires in the original image must be dead for the new pixel to be classified as dead. This limits the amount of time that the algorithm will take to run for each event. After the algorithm is run, a set of (x, y, z) detector points are provided to a track and the image is returned to its former resolution.

The performance of the through-going track reconstruction algorithm is dependent on the endpoints that are given to it, since those serve as the seeds to the linear charge tagger and the A* algorithm. If the truth endpoints are provided to the through-going muon tagger, then 90% of the through-going muon pixels are tagged.

5.2.2 Stopping Muon Tagger

The stopping muon tagger takes as input the boundary points and pixels which were not tagged by the through-going muon tagger. It operates by following each input boundary point into the detector in steps of a defined length and looking for connecting charge, using the following constraints:

- The path covered by a step should project back into all three planes to a region with charge.
- If more than one step is possible, it should be the one most along the direction of the previous step.

A 3D path for a candidate stopping muon is constructed by following these criteria.

5.2.3 Contained Charge Tagger

After the stopping muon tagger is run, its algorithm is used to cluster the remaining pixels into clusters on each plane. Next, clusters of charge that occurs over the same time interval and within

the same (y, z) region of the detector are grouped together.

Once a common time interval is found for the charge slices across the different planes, the time interval is divided into sets of 24 pixels. After it is ensured that all three planes have charge, tests are done to make sure that the wires for the three planes overlap inside the TPC. If the boundary formed by the intersections of the wires overlaps inside the TPC for this time interval, then the cluster is classified as 'good'. If the boundary formed by the intersections of the wires does not overlap anywhere inside the active volume of the TPC, then the time interval is classified as 'bad'. If one or more of the planes does not have charge within this time interval, then the time slice is not kept. The (y, z) boundary is projected back into the wire planes for any good slice. This is done because the 3D overlap information to split up two tracks that may have been merged together in one of the views. The time slices are then combined to form clusters if enough in the same vicinity are classified as 'good'.

One concern is that this method includes too many charge hits which are clustered together because they occur within the same time interval. However, because the through-going muon tagger and stopping muon tagger are run before this, that problem is reduced. Also, only clusters with a 'good' time-interval fraction of 0.75 are kept, which reduces this problem and also limits the number of clusters which occur in a bad channel region of the detector.

5.2.4 Pixel-Tagging Performance

To judge the performance of the cosmic tagger, one can consider the number of pixels that are tagged in an off-beam event by each stage of the tagger's performance. For pixels above a threshold, it is found that ~75% of pixels are tagged in the through-going stage of the tagger. This fraction does not change significantly after the stopping muon tagger is run, which could be due to an increased number of dead channels in a simulation upgrade. Once the the contained cluster tagger is run, the average fraction of pixels tagged is $> 90\%$. The distribution for the fraction of pixels tagged in each stage is shown in Figure 5.3.

5.2.5 Flash-Matching Reconstructed Objects in the TPC

Once an object of charge in the TPC has been reconstructed, whether it is a track, shower, or a cluster, it can be compared to a flash of light recorded in the PMTs. This serves two purposes:

- It can be compared to the in-time flash to see if it could belong to a neutrino interaction.
- It can be compared to flashes out-of-time with the beamspill to confirm that it corresponds to cosmogenic activity rather than a possible neutrino interaction.

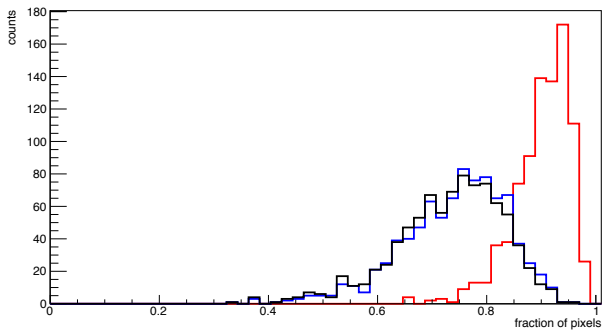

Figure 5.3: The fraction of pixels tagged in each stage of the cosmic ray tagger's performance: through-going (black), stopping (blue), contained (red).

The flash-matching procedure takes the following steps:

- Reconstructed track and shower objects are converted into clusters of charge, called 'qclusters', which contain information for how many photons are deposited in the PMTs at each point along the object's trajectory. The resolution between points on the QCluster is 0.5 cm and the amount of energy deposited in the TPC per unit length is particle-specific (2.07 MeV/cm for muons). The number of photons is obtained by multiplying the distance between two points and the amount of energy deposited per unit length by the 'light yield', which is the amount of light deposited in the PMTs per unit energy. The value is 40000 $\frac{\gamma}{\text{MeV}}$ for simulation and 52360 $\frac{\gamma}{\text{MeV}}$ for data, the latter quantity stemming from the total light yield fit. The results of this are shown in Figure 5.6.

- The information is converted into a 'flash hypothesis' by using values from the MicroBooNE photon library. The number of photons deposited by each point in the track's trajectory is multiplied by the global quantum efficiency and by the probability that a given photon will reach one of the PMTs. The CCV corrections, which are the quantum efficiencies of the individual PMTs, can also be applied, but those are not used in this study.

- The number of expected PEs in each PMT is fit to the number of reconstructed PEs in a PMT flash using equation 5.1. For this χ^2 calculation, the number of degrees of freedom is equal to the number of PMTs showing light in the data flash. If the flash was reconstructed using the 'simpleFlashCosmic' module instead of the 'simpleFlashBeam' module, meaning that it was reconstructed outside of the 23.4 μs time window immediately following the trigger, then the number of PEs in each PMT is multiplied by a correction to account for the biased waveform collected in the cosmic discriminated readout window.

$$\chi^2 = \frac{1}{\mathrm{N}_{\text{Data PEs} > 0}} \sum_{\text{Data PEs} > 0} 2(\mathrm{O} - \mathrm{E})(\log \mathrm{O} - \log \mathrm{E}) \tag{5.1}$$

An additional feature that was placed into the flash-matching procedure was extending tracks that terminate close to the boundary of the TPC to the edge of the cryostat. This was considered because tracks deposit light in the PMTs as they pass through the cryostat. All tracks that terminate less than 10 cm from the boundary of the active volume of the TPC (without accounting for space charge effects) are extended into the cryostat.

To use this flash-matching framework, there are two corrections that have to be calculated: a correction for the cosmic discriminator and also a correction for the different light yield for events in data vs. those in simulation. For the former, a sample of ACPT tracks (discussed in more detail in Chapter 6) were used, because they have full 3D trajectory information available. The correction factor at low PE values (< 60 PEs) was calculated to be 0.424; at higher PE values, it was calculated to be 0.354. The two-dimensional distribution used to obtain the cosmic discriminator correction factors is shown in Figure 5.4. The χ^2 is shown before and after applying the cosmic track extensions and the cosmic discriminator corrections in Figure 5.5.

The data light yield was tuned by using only cathode-piercing tracks in data. This is because forming a flash hypothesis for tracks located close to the anode is difficult because of their proximity to the PMTs, which renders anode-piercing tracks less useful in doing this. The correction factor between the two was formed by performing a fit between the total amount of light for each track both in the hypothesis flash and in the data flash. The correction factor was found to be 1.309. The resulting distributions are shown in Figure 5.6.

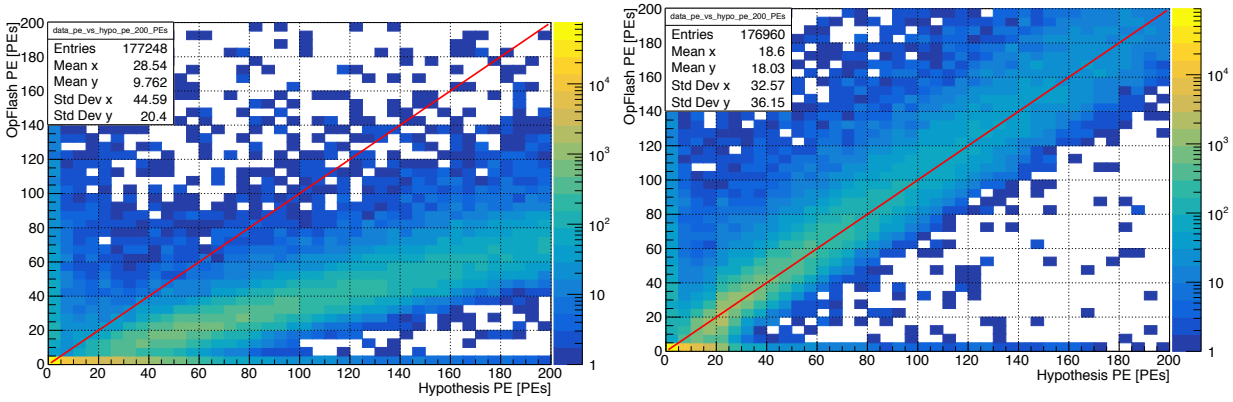

Figure 5.4: The number of PEs in the reconstructed flash (OpFlash PEs) vs. the number of PEs in the hypothesis flash (Hypothesis PEs) shown before (left) and after (right) applying the cosmic discriminator and extension corrections. There are 32 entries in both heatmaps for each track with each corresponding to one PMT.

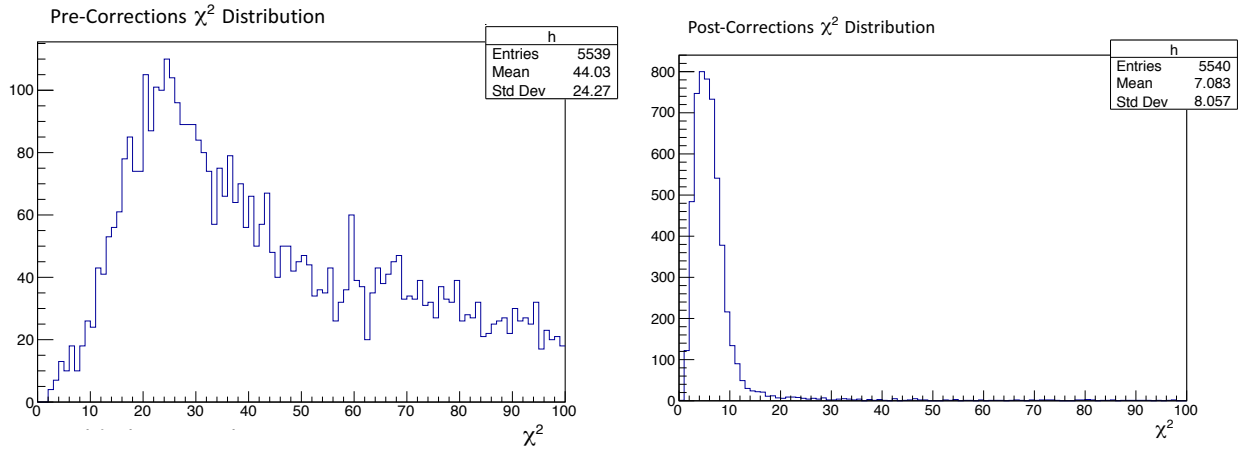

Figure 5.5: The χ^2 distributions for truth-only tracks matched to a 'truth' flash before (left) and after (right) applying cosmic discriminator and extension corrections. In the lefthand plot, only 1.9% of entries have a χ^2 value less than 10, while 86.7% of entries in the righthand plot have a χ^2 value less than 10.

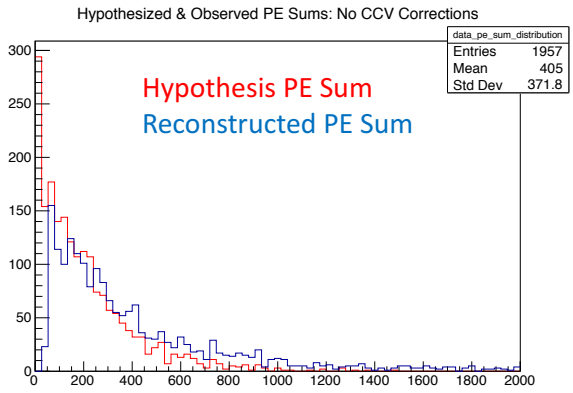

Figure 5.6: The distributions for the hypothesized PE spectrum (shown in red) and the reconstructed data spectrum (shown in black) for off-beam, cathode-piercing tracks after applying the correction. There is a peak in the first bin of the hypothesized PE spectrum but not in the reconstructed spectrum because of a $>$ 50 PEs cut placed on the events of the cathode-piercing tracks.

Because of issues with forming a flash hypothesis by using the photon library, there are not currently cuts in place that are used in reconstructing through-going muon tracks within the cosmic ray tagger of the Deep Learning Low-Energy Excess Analysis.

CHAPTER 6

Types of Calibration Samples and Their Uses

'Calibration' of a detector is setting the scale for a measureable quantity using a detectable sample with a known value of this quantity. Another term for this type of sample is 'standard candle'. There are seven samples that serve this purpose within MicroBooNE: (1) Anode/Cathode-Piercing Cosmic Ray muon tracks (ACPT tracks), (2) Anode/Cathode-crossing (A/C-crossing) tracks, (3) stopping muon tracks, (4) Michel electron tracks, (5) photon showers from a π^0 decay-at-rest, (6) CRT-tagged tracks, and (7) Kaon-Decay-At-Rest (KDAR) muonic and hadronic products [46].

6.1 Anode/Cathode-Piercing Cosmic Ray Muon Tracks

6.1.1 Introduction

As discussed in Chapter 5, cosmic rays bombard MicroBooNE, occurring at a rate of ~25 per each 4.8 ms event. Because they are randomly distributed in position and orientation in the detector and time in an event, well-reconstructed cosmic ray muon tracks serve as an effective calibration sample for LArTPCs. In order to use cosmic rays as a calibration sample, full 3D information of a track is needed.

The y and the z information of a trajectory point on a cosmic ray muon track is provided by the wire plane information. Other than offsets caused by detector effects, such as the space charge effect (SCE), it represents the position of the track at that point along its trajectory for those two Cartesian coordinates. The x-coordinate, however, is offset by an amount proportional to the time with respect to the event trigger time at which the cosmic ray muon track passed through the detector. For most tracks, that coordinate can only be found through the flash-matching process such as the one described in Chapter 5 or by means of tagging the track with a CRT hit as described in this chapter. For tracks that pierce the anode or the cathode, however, knowledge of the true x-position of the track at that point allows for full 3D information to be provided.

6.1.2 Algorithm Description

The algorithm for t_0 reconstruction makes the following assumptions about the tracks of cosmic-ray muons:

- The tracks are downwards-going.
- The tracks are through-going.

Because of the assumption that the tracks are through-going, a cosmic ray muon track tagged by this algorithm is assumed to pierce two faces of the TPC, and at least one must be the anode or the cathode. Tracks that pierce both the anode and the cathode are referred to as 'A/C-crossing tracks' and are discussed in Section 6.2.

A track is assumed to enter/exit a y or z face of the TPC if its endpoint comes within a certain distance from that face. In results published in a public note on this technique, the distance is set to 13 cm, but for the sample used for the SCE analysis with cosmic muons described in Chapter 7 the distance was 20 cm [21]. The initial result was intended to demonstrate this technique, while the value of 20 cm had to be used to fully demonstrate the effects that SCE had upon track reconstruction in the detector.

A track is considered to be anode-piercing or cathode-piercing if:

- the entering point is found to be entering through the top, upstream, or downstream faces

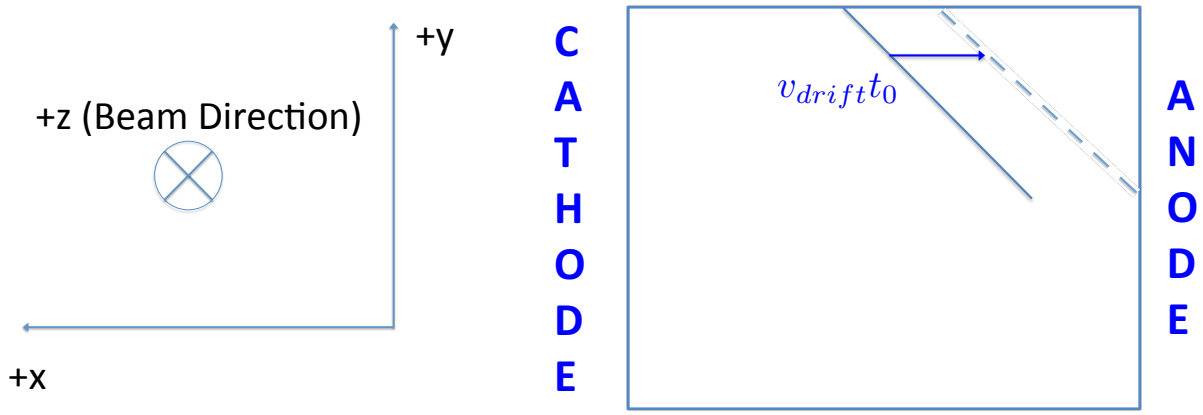

Figure 6.1: A schematic of an example side-piercing track t_0-tagged with this algorithm as shown for the xy plane. This track enters the top of the TPC and exits through the anode. The solid line represents the reconstructed track and the dotted line represents the reconstructed track with the t_0 correction applied. This correction consists of a product of the drift velocity of electrons in liquid argon, v_{drift}, and reconstructed track t_0.

of the TPC, and the exiting point is found to not exit through the bottom, upstream, or downstream faces of the TPC, or

- the entering point is found not to be entering through the top, upstream, or downstream faces of the TPC, and the exiting point is found to exit through the bottom, upstream, or downstream faces of the TPC.

Because of the downwards-going assumption, the vanishingly rare cases in which a muon enters through the bottom of the TPC or exits through the top are not considered. A background of short tracks in which both of a track's trajectory points in y and z are found within resolution on the same TPC face were considered a background and not included in the analysis.

For anode-piercing tracks, the charge will require no time to drift to the readout wires. Therefore, the t_0 can be reconstructed by using the following equation in which v_{drift} is the drift velocity of electrons in liquid argon, to 0.1114 cm/μs (a value that was later corrected with the use of the laser calibration system described in Chapter 4 by means of a procedure described in Chapter 7):

$$t_0 = \frac{x_A}{v_{\text{drift}}} \tag{6.1}$$

For cathode-piercing tracks, charge associated with the cathode-piercing x-coordinate x_C will have to drift through the full TPC drift-length. Therefore, the t_0 value is given by the following equation in which T_{drift} is the time needed for ionization electrons to drift the full length of the TPC, 2300 μs [47]:

$$t_0 = \frac{x_C}{v_{\text{drift}}} - T_{\text{drift}} \tag{6.2}$$

In the above equations, both time and drift-distance are measured with respect to the event trigger time. Charge arriving at the anode-plane at the trigger-time will have a reconstructed x-coordinate of 0 cm. Figure 6.1 displays the technique of offsetting the track for a top-piercing, anode-piercing track.

6.1.3 Purifying the Sample

Tracks which stop within the detector volume may mistakenly be tagged by the algorithm leading to an incorrectly reconstructed t_0. This is because the track end-point will be consistent with neither exiting from the bottom nor the front or end of the TPC and will therefore pass the selection cuts. Backgrounds in this category arise from stopping cosmic-ray muons and also broken tracks which should be through-going but are not fully reconstructed. Shorter tracks stitched together into longer ones can also result from reconstruction failures. In order to limit such backgrounds a simple

matching of TPC and PMT information to determine if a track's t_0 was correctly reconstructed or not is used. Because scintillation light produced in the detector reaches the PMT system virtually instantaneously on the time scale of the track charge deposition measurements (O(ns) vs. O(μs to ms)), each cosmic-ray muon will lead to a flash of light in the PMT system at time t_0. If no flash was recorded at a time in a given window around the reconstructed t_0, it is assumed the track's t_0 was reconstructed incorrectly and the track is discarded. The fact that there is sufficient pre-trigger and post-trigger digitized charge data recorded allows this technique to be executed.

In order to enhance the purity of the selected tracks a scan over three parameters is conducted:

- the difference in time between reconstructed t_0 and a flash of scintillation light recorded by the PMTs (encapsulated in a quantity called the flash window, described in Section 6.1.4);
- the number of photoelectrons (PEs) in the flash recorded by the PMTs; and
- the reconstructed track length (L_{track}).

In evaluating the ACPT t_0-tagging method, the purity and the efficiency are defined as follows:

$$\text{Purity} = \frac{\text{Number of Tracks Passing Cuts With a Well-Reconstructed } t_0}{\text{Number of Tracks Passing Cuts}} \tag{6.3}$$

$$\text{Efficiency} = \frac{\text{Number of Tracks Passing Cuts}}{\text{Total Number of Tracks in Sample}} \tag{6.4}$$

Enacting these cuts enhances the purity of the sample while decreasing the yield of the sample. To use a sample for calibration purposes, the purity of the sample should be as close to unity as possible.

6.1.4 Results

Here the results from scans of the cut parameters and values are displayed in the form of heatmaps. The x-axis displays the cut on track length [cm] and the y-axis displays the cut on the number of PEs required in a flash within the range specified at the top of the plot.

In simulation it is found that the anode-piercing sample maintains a higher purity than the cathode-piercing sample when both are subject to the same set of cuts. This comparison, displayed in Figure 6.2, is due to the better resolution in the difference in time between reconstructed track t_0 and the time of the flash of light in the PMTs, a result of the location of the PMTs behind the anode. The track length cut has very little effect on the anode-piercing sample, which essentially reaches purity values of unity past a modest (~40 PEs) cut on the y-axis. The vertical bands seen in both plots are the result of the low statistics of the sample: a sample becomes more pure when one of the very few tracks with poorly reconstructed t_0 is removed by an increment in the track length

cut, causing the purity to increase to a higher value in that single interval. A tighter cut on the flash window increased sample purity across the heatmap for identical cuts on track length and number of flash PEs, as shown in Figure 6.3 for anode-piercing tracks and Figure 6.4 for cathode-piercing tracks.

The purity values for the externally tagged data events, shown in Figure 6.5, are not as high as for the simulated anode-piercing and cathode-piercing events. This is due to several reasons: first, impurities in the external muon tagger render the maximum purity that this reconstruction method can achieve less than unity in spite of the cuts applied to mitigate this effect. Second, the presence of any distortions of track positions due to variations in the electric field [11] and other impurities in the TPC worsen track reconstruction and also lower the maximum purity values that can be achieved. The decrease in purity at high values of the track length cut ($>$ 170 cm) and low values of the cut on the number of PEs (in the range [10 PEs, 40 PEs]) in a flash is partially a result of dead wires on the anode wire planes [48]. The cosmic tagger system has limited coverage in the detector, so tagged tracks with a greater length will be reconstructed with information from some of the same wires. When the sample is subject to cut values of $>$ 200 cm on track length and $>$ 10 PEs on the number of PEs, dead wires could explain up to a 5% deficiency in the purity at these values. Another possibility is the presence of short, cathode-grazing cosmic ray muon tracks that are coincidentally in time with a flash of light recorded in the PMTs.

By enforcing cuts of $>$ 80 cm on track length and $>$ 50 PEs with a flash window of $\pm$ 1 μs, purity values of 99% for the simulated top-piercing/bottom-piercing and anode-piercing sample, 98% for the simulated top-piercing/bottom-piercing and cathode-piercing sample, and 97% for the externally tagged top-piercing/bottom-piercing and cathode-piercing sample are achieved. The

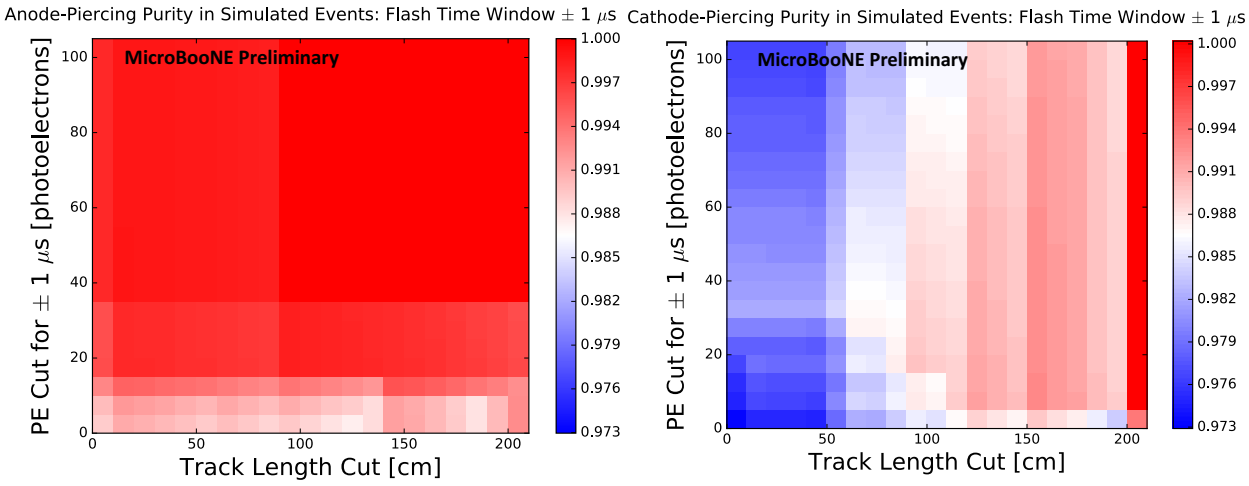

Figure 6.2: Heatmaps for the simulated anode-piercing (left) and cathode-piercing (right) purities for a PE cut range of 0-100 PEs with a $\pm$ 1 μs flash window.

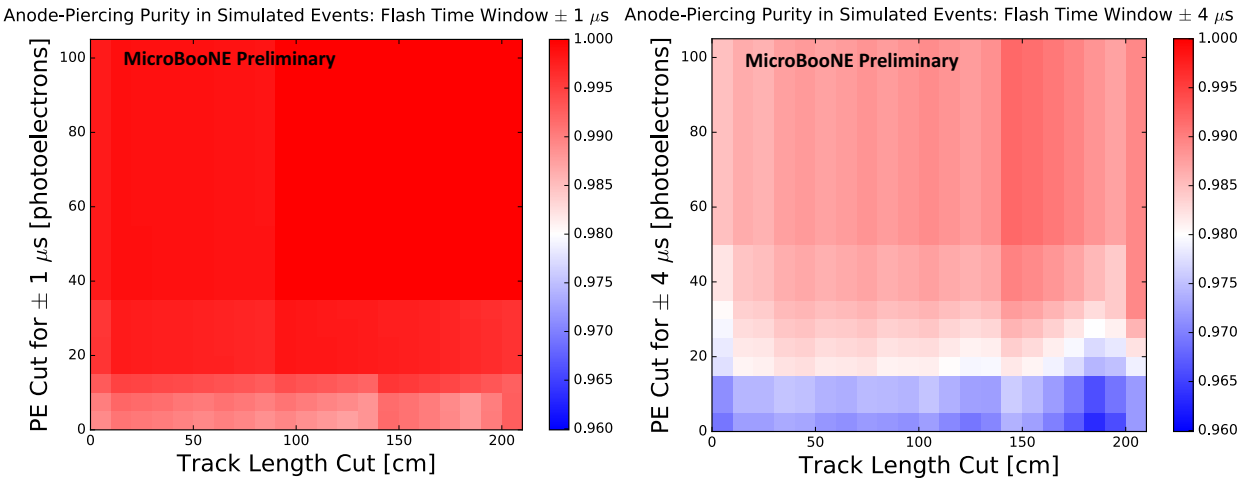

Figure 6.3: Heatmaps for the simulated anode-piercing purity for a PE cut range of 0-100 PEs with $\pm$ 1 μs and $\pm$ 4 μs flash windows. The higher purity values in the plot with the tighter flash window indicates that tracks closer in time to a flash of light recorded in the PMTs is more likely to have well-reconstructed t_0.

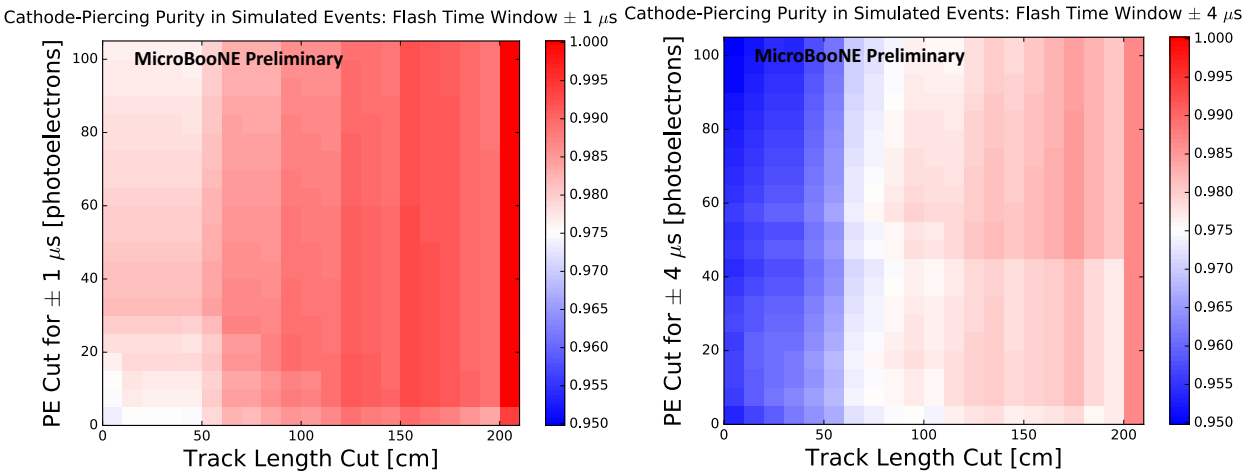

Figure 6.4: Heatmaps for the simulated cathode-piercing purity for a PE cut range of 0-100 PEs with $\pm$ 1 μs and $\pm$ 4 μs flash windows. The higher purity values in the plot with the tighter flash window indicates that tracks closer in time to a flash of light recorded in the PMTs is more likely to have well-reconstructed t_0.

upstream-piercing/downstream-piercing tracks are not included in this generation of the study, which was published in Ref. [21].

6.1.5 Application to Cosmics Data and Simulated Events

With samples of tracks produced with these optimal cuts, coverage maps are presented here showing which areas of the TPC tracks tagged with this algorithm travel through most frequently.

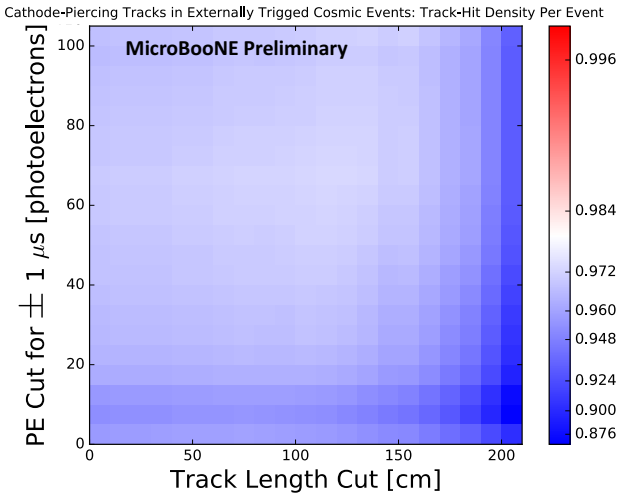

Figure 6.5: A heatmap for the externally tagged cosmic-ray muon sample for a PE cut range of 0-100 PEs with a $\pm$ 1 μs flash window. This plot is shown with a logarithmic color scale to show the range of the quantity for this range of cuts.

The two samples of tracks used in this study are simulated events and off-beam cosmic-ray data events triggered by an external pulser. Tracks in the latter sample are not required to have triggered the MuCS system but instead represent cosmic events of all orientations in the TPC. No cuts were placed on the latter sample before the cuts on the scanning parameters were enacted, but the same cuts from Section 6.1.4 are applied to the simulated sample. The number of top-piercing/bottom-piercing and anode-piercing are shown along with top-piercing/bottom-piercing and cathode-piercing tracks in Table 6.1.

Sample	Total Tracks
Anode-Piercing Tracks	3303
Cathode-Piercing Tracks	1868
All Tracks	5171

Table 6.1: The number of each denomination of tracks used in simulation to produce coverage maps after the optimal set of cuts presented in Section 6.1.4.

6.1.6 Coverage of ACPT t_0-tagged Tracks

6.1.6.1 Simulated Events

Table 6.1 shows the number of each denomination of tracks that survive the optimal set of cuts from 2000 events. The yield values for these two samples are 1.7 tracks/event for the top-piercing/bottom-

piercing and anode-piercing case and 0.9 tracks/event for the top-piercing/bottom-piercing and cathode-piercing case.

Coverage maps for simulated events in detector y vs. z coordinates are shown in Figure 6.6. These maps show very little bias between the anode-piercing and cathode-piercing cases. The less densely populated center of the TPC in the cathode-piercing case as compared to the anode-piercing case is a result of fewer tracks passing the optimal set of cuts in the former vs. the latter. There is better coverage near the center of the TPC than near the edge for both samples, because a greater portion of reconstructed track trajectories will be contained in the TPC in the region with intermediate-z values, from 300 cm - 700 cm, than in the regions on either side of the TPC.

A strong bias is instead visible in a y vs. x coverage map of the same sample. The anode-piercing tracks necessarily must pierce the TPC face at x = 0 cm and the cathode-piercing tracks, the face at x = 256.4 cm, which explains that these distributions are concentrated within different regions in x.

Note that top-entering tracks will pierce the side while exiting the TPC and the bottom-exiting tracks will pierce the side while entering. As in Figure 6.6, the highest coverage values in the anode-piercing coverage map as compared to the cathode-piercing coverage map is, again, due to greater statistics in the anode-piercing sample. These results are shown in Figure 6.7.

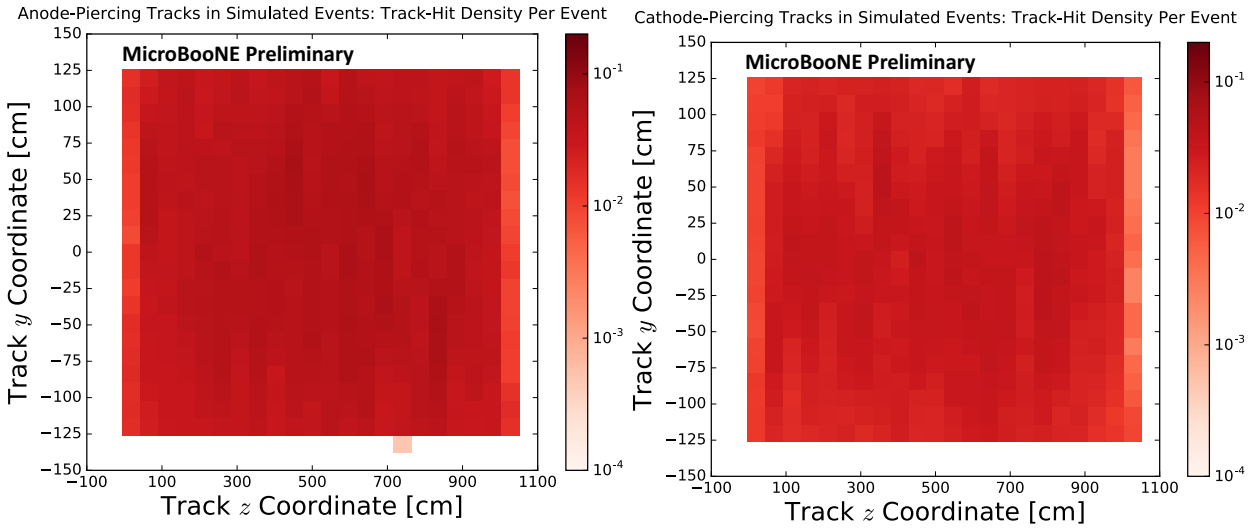

Figure 6.6: Coverage maps for anode-piercing (left) and cathode-piercing (right) track-hit densities per event of y vs. z for the optimal set of cuts for a simulated sample. These distributions are very similar.

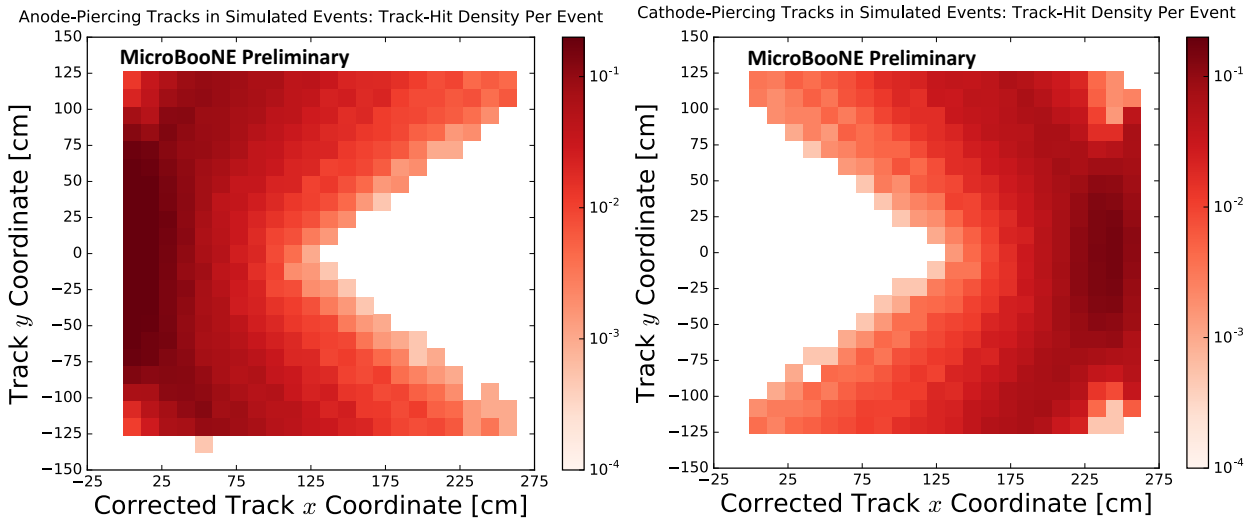

Figure 6.7: Coverage maps for the anode-piercing (left) and cathode-piercing (right) track-hit densities per event of y vs. x for the optimal set of cuts for a simulated sample. The x-coordinate axis is labelled as 'corrected' because the constant proportional to the t_0 correction is applied to every x-coordinate.

6.1.6.2 Data Events

Table 6.2 shows the number of each denomination of tracks that survive the optimal set of cuts from 5084 events. The yield values for these two samples are 0.73 tracks/event for the anode-piercing case and 0.18 tracks/event for the cathode-piercing case. These numbers are lower than those in the simulated events sample due to obstacles to wire plane charge collection and SCE, which is present in data but not included in simulation. This study was completed before SCE was included in MicroBooNE simulation. The numbers of upstream-piercing/downstream-piercing tracks are not included in this same generation of studies, but typically those efficiencies are 10-20 times lower than the ones for top-piercing/bottom-piercing studies.

Sample	Number of Tracks
Anode-Piercing Tracks	3702
Cathode-Piercing Tracks	916
All Tracks	4618

Table 6.2: The number of each denomination of tracks used in the off-beam cosmic data to produce coverage maps after the optimal set of cuts presented in Section 6.1.4.

The coverage maps for the off-beam cosmic data sample with y plotted vs. z are shown in Figure 6.8. These plots show greater coverage values in the anode-piercing case as compared to the cathode-piercing case in all areas of the TPC, because over four times as many tracks survive

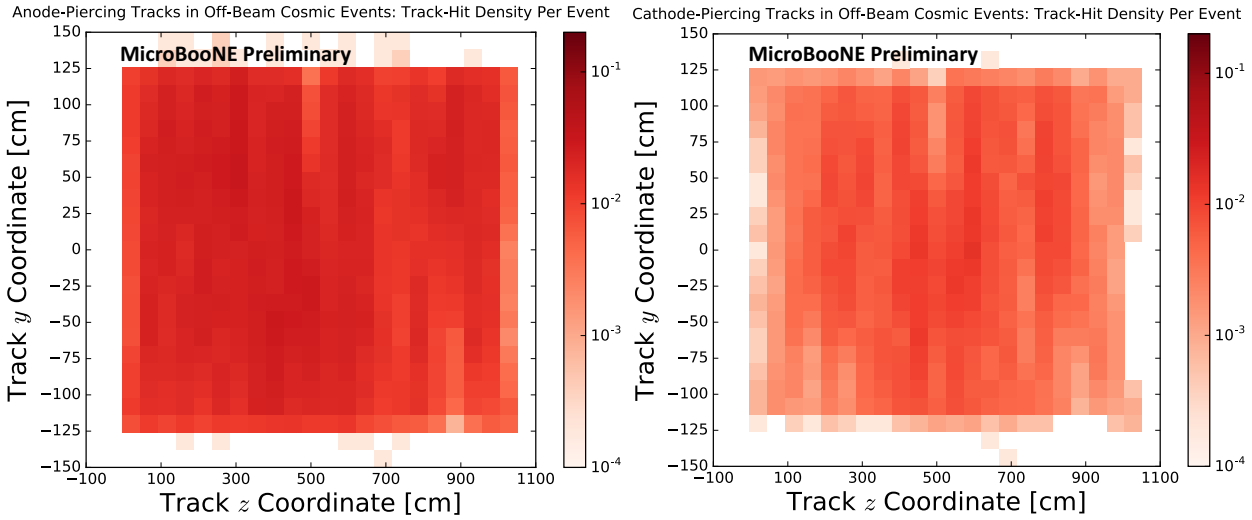

Figure 6.8: Coverage maps anode-piercing (left) and cathode-piercing (right) track-hit densities per event of y vs. z for the optimal set of cuts for the off-beam cosmic data events.

the optimal set of cuts in the anode-piercing case as do in the cathode-piercing case, as shown in Table 6.2. In both plots, however, the coverage is greatest in the TPC bulk between z = 200 cm - 700 cm. There is a dropoff in coverage in the vertical area close to z = 700 cm because this is a dead wire region of the TPC. Some voxels in the heatmaps representing regions located outside of the TPC volume are populated because these are filled on the occasion that track reconstruction begins outside the TPC.

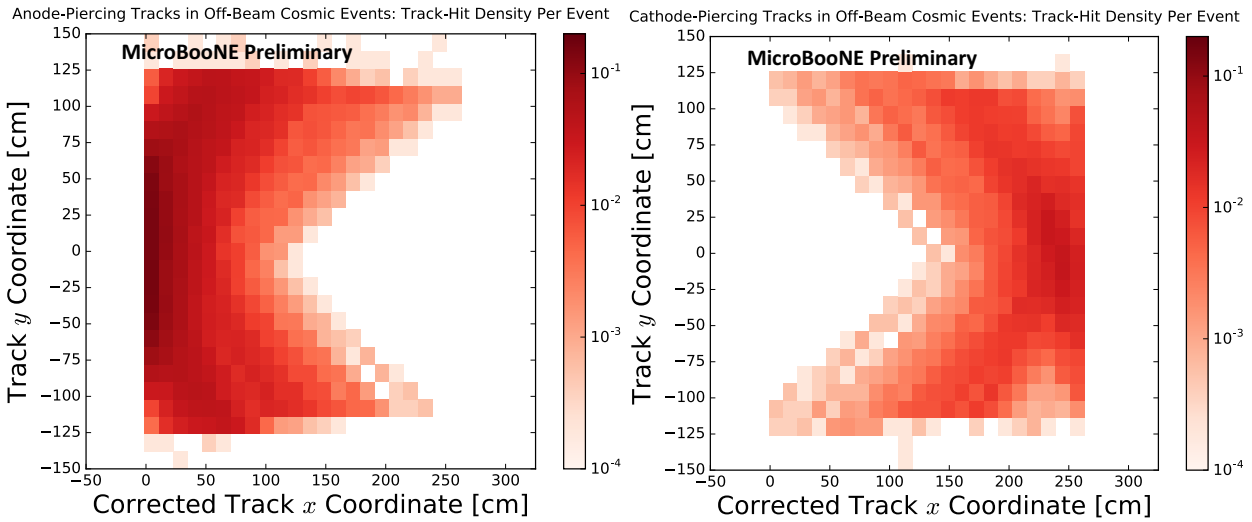

Figure 6.9: Coverage maps for anode-piercing (left) and cathode-piercing (right) track-hit densities per event of y vs. x for the optimal set of cuts for the off-beam cosmic data events. The x-coordinate axis is labelled as 'corrected' because the constant proportional to the t_0 correction is applied to every x-coordinate.

Coverage maps for y vs. x are shown in Figure 6.9. The same bias that was present in the analogous coverage maps for simulation in Figure 6.7 can be seen in this one. The coverage values are also lower in the corners of the TPC in the y vs. x plane in the cathode-piercing case because of any distortions of track positions due to SCE, which pushes ionization electrons away from the negatively charged cathode.

6.2 A/C-crossing Tracks

Tracks that pierce both the anode and the cathode, referred to as 'A/C-crossing tracks', can be used as a calibration sample after they have full 3D information available, just like the sample in Section 6.1. They must have their t_0 provided in order to have full 3D information available, and the way that this happens is by taking the point on the track closest to the anode and dividing by the drift velocity (Equation 6.1). These tracks are selected by requiring that they have an x-projected track length within the range [250, 270] cm, meaning that they traversed the entire detector x-length of 256.35 cm. It is estimated that 0.13% of tracks are A/C-crossing tracks [49]. These tracks are ideal for studying the purity of liquid argon and for correcting the charge yield of the TPC due to their extent across the entire drift direction of the detector [44].

To improve the calorimetry of the events selected for an electron lifetime study on MicroBooNE, cuts on track angle and on the minimum number of hits on the collection plane can also be used. When the MicroBooNE charge yield throughout the detector was corrected, the following angular cuts were used:

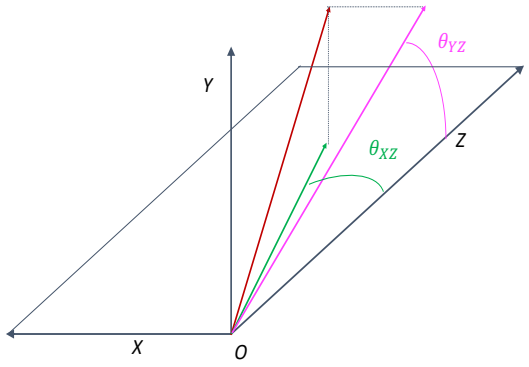

Figure 6.10: This diagram defines the angular variables, θ_{XZ} and θ_{YZ}, that are used within MicroBooNE.

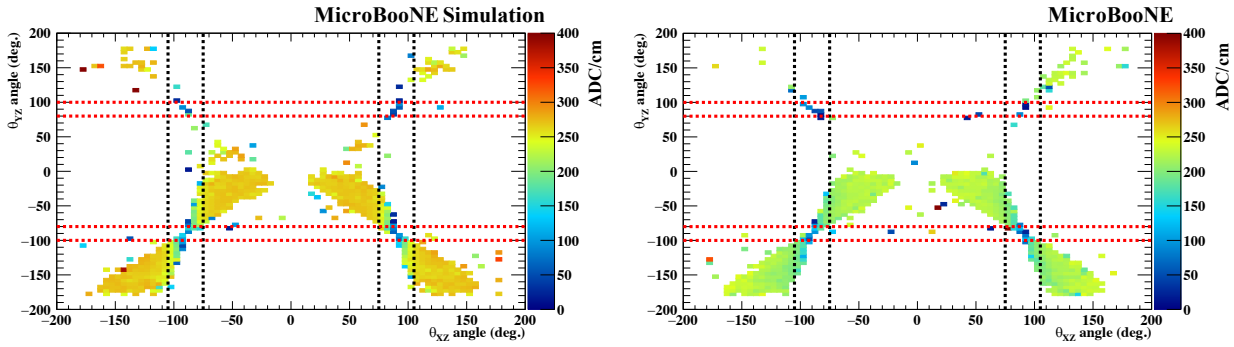

Figure 6.11: A plot showing the distribution of hits in the two angular variables, θ_{XZ} (x-axis) and θ_{YZ} (y-axis) for (left) simulation and (right) data. The z-axis represents the intensity of each hit.

- θ_{XZ} must not be in the range of 75° to 105°, because tracks in this region are nearly orthogonal to the wire planes and are likely to be misreconstructed.
- θ_{YZ} must not be in the range of 80° to 100°, because tracks in this region are nearly parallel to the collection plane wires and a large amount of their charge could be reconstructed on the same wire.

These angles are defined in Figure 6.10 and plots showing the distribution of hits as a function of these two angles are shown in Figure 6.11.

A cut on the number of hits on the collection plane is intended to promote a number of hits

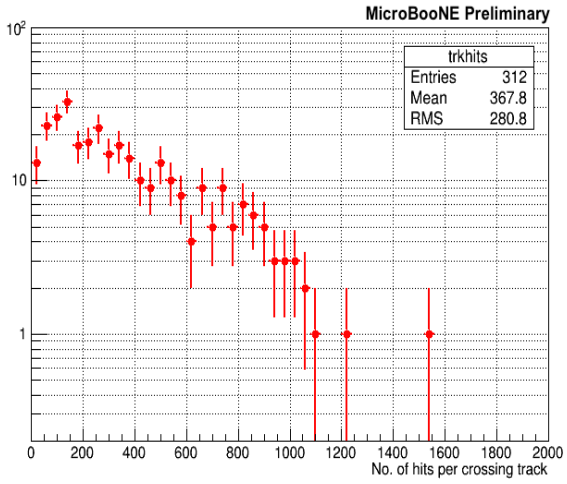

Figure 6.12: The distribution of collection plane hits for tracks having an x-projected length in the range [250, 270] cm.

along the detector x-direction for liquid argon purity studies. A distribution on this variable for A/C-crossing tracks is shown in in Figure 6.12.

6.3 Stopping Muons

As mentioned in Chapter 4, charged particles deposit energy in a distinct way in liquid argon, a process that has been thoroughly studied in other contexts. This process can be used to calibrate LArTPCs, which it was to allow for uniform charge deposition throughout the entire detector. In particular, stopping muons can be used to convert between $\frac{dQ}{dx}$, the amount of charge deposited per unit distance, and $\frac{dE}{dx}$, the amount of energy deposited per unit distance, in the detector [49]. The comparison between the predicted most probable energy loss and the fitted most probable energy loss for a sample of stopping muons is shown in Figure 6.13 as a function of the stopping muon kinetic energy. The disagreement at low values of kinetic energy is due to shortcomings of the recombination model in that region.

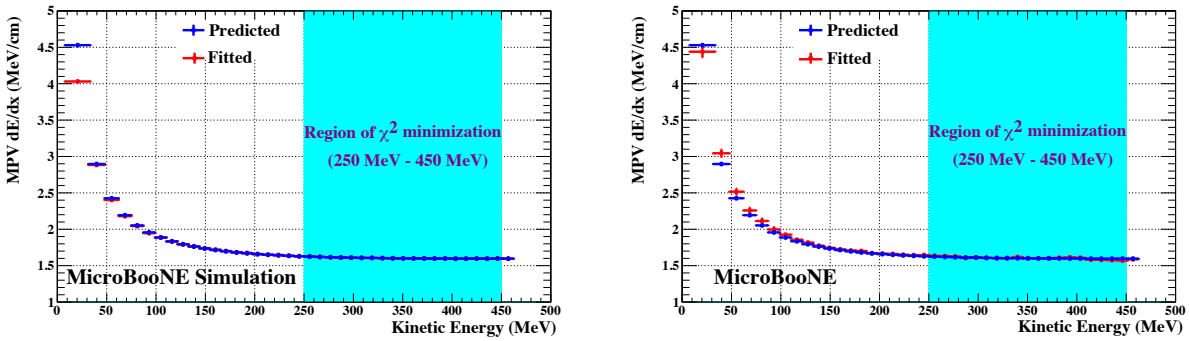

Figure 6.13: A comparison between the predicted most probably energy loss and the fitted most probable energy loss for a sample of stopping muons in the MicroBooNE experiment as a function of the stopping muon kinetic energy. The region with the best χ^2 agreement is highlighted. Here, the number of hits along the reconstructed tracks serves as the number of degrees of freedom in the χ^2 fit.

6.4 Michel Electrons

6.4.1 Description

When a muon track terminates within the MicroBooNE detector, it is because one of two things happens:

- The muon is captured by an argon ion. This occurs 74% of the time for μ^- and never for μ^+, which repel the positively charged argon ions.
- The muon decays (typically at rest) into a Michel electron. This occurs 26% of the time for μ^- and 100% of the time for μ^+.

A muon decays to a Michel electron through the following process:

$$\mu^{\pm} \rightarrow e^{\pm} + \nu \backslash \bar{\nu} \tag{6.5}$$

The muon typically decays at rest, meaning that the energy of the Michel electron is constrained to be within the range [0 - 52.8] MeV due to conservation of energy. This energy can be dissipated through collision energy with the argon in the detector or through radiative energy loss (the release of photons). The stopping power of liquid argon is shown in Figure 6.14. Based on this plot, a Michel electron with greater energy will release more energy in the form of photons than one with lesser energy will.

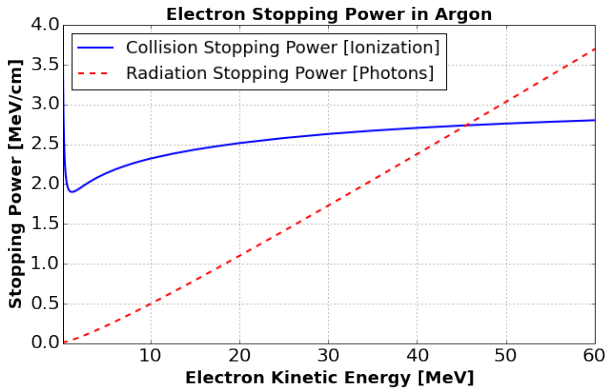

Figure 6.14: The stopping power of LAr as a function of track kinetic energy for ionization (collision) and radiation (photon release).

6.4.2 Selection

To isolate a sample of Michel electrons, the following procedure is used for the ionization energy that is released in the TPC [50]:

- The truncated mean charge is taken for each hit along a particle track. It is calculated by finding the distribution of 8 hits on either side of the hit in question, removing 25% of the charge of the hits at the lower/higher ends of the distribution, and calculating the mean from the remaining values. The hit with the greatest amount of charge located within ~5 cm of the truncated mean charge maximum is denoted the muon stopping point.

- The average local linearity, or a measure of the linearity of the neighboring points, is calculated for the five hits surrounding the muon stopping point. A local linearity of one for a hit indicates a completely straight track in the vicinity of that hit. This average value for the five surrounding points is required to be less than 0.8, indicative of a 'kink' at the muon stopping point which is characteristic of the start of the Michel electron track.
- Cuts requiring that at least 70% of hits have a local linearity > 0.9 and that the track have length > 10 cm are applied to eliminate short tracks which tend to scatter more, making Michel electron identification more difficult.

Once the tracks are selected, all hits within 80 cm (corresponding to ~3 radiation lengths of liquid argon) and within a 30% angle of the reconstructed muon direction are grouped into clusters to reconstruct radiative photons. A cluster must have at least 1 MeV of energy to be considered. The following cuts are applied to the reconstructed photons before the energy is reconstructed:

- Photons with greater than 20 hits (corresponding to ~10 MeV) are not considered.
- Photons with between 5 and 20 hits must have a local linearity less than 0.8.
- Photons must not contain charge within a 2 cm distance from any charge not reconstructed as belonging to the Michel electron.

With these cuts, Michel electrons are reconstructed with a purity of 80%-90% and an efficiency of 2%. The efficiency was found by comparing the number of selected Michel electrons to the number of true Michel electrons in a Monte Carlo event sample. The purity was found by comparing the reconstructed wire and tick values for a Michel electron to the true values. Because of the plentiful amount of off-beam data available with MicroBooNE, this permits there to be thousands of Michel electron candidates available for this study.

6.4.3 Energy Reconstruction

When reconstructing the energy of selected Michel electrons, the ratio between the number of reconstructed electrons and the number of electrons collected on the wires must be accounted for. This was found by comparing the energy deposited per unit length ($\frac{dE}{dx}$) vs. residual range (distance from the end of the muon track) to known values for liquid argon. The relationship between the two variables that was derived is the following:

$$\frac{e^-}{e^-_{\text{reco}}} = 1.01 \tag{6.6}$$

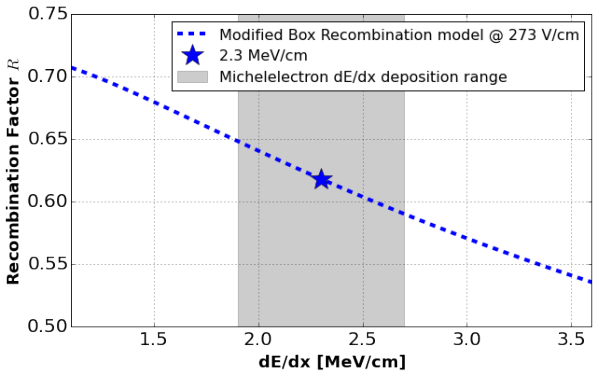

Figure 6.15: The recombination coefficient in liquid argon as a function of $\frac{dE}{dx}$ at the operating electric field value of MicroBooNE 273.9 V/cm. The region typical of stopping muons is shaded in gray.

It is also important to know the recombination coefficient for the detector to accurately relate the amount of charge reconstructed in the detector to the amount collected at the wire planes. The modified box model was used for this analysis, meaning that the relationship between the recombination coefficient and $\frac{dE}{dx}$ is the following:

$$\mathrm{R} \;=\; \ln \frac{\frac{dE}{dx} \;\times\; \beta \;+\; \alpha}{\frac{dE}{dx} \;\times\; \beta} \tag{6.7}$$

where:

$$\alpha \;=\; 0.93 \;\pm\; 0.02, \tag{6.8}$$

$$k_b \;=\; 0.212 \;\pm\; 0.002 \;[\frac{\mathrm{g} \;\times\; \mathrm{kV}}{\mathrm{MeV} \;\times\; \mathrm{cm}^3}], \tag{6.9}$$

$$\beta = \frac{k_b}{\rho \;\times\; E_{\mathrm{field}}} \;=\; 0.562\;[\mathrm{cm/MeV}]. \tag{6.10}$$

The recombination value used in the analysis is derived using a constant $\frac{dE}{dx}$ value of 2.3 MeV/cm, which gives a recombination coefficient of 0.62. This value was chosen because it is the mean value of the range 1.9 MeV/cm - 2.7 MeV/cm which is characteristic of stopping muons in liquid argon. The recombination coefficient as a function of $\frac{dE}{dx}$ is shown in Figure 6.15.

6.4.4 Results

The selection and energy reconstruction algorithms were run over a set of $5.44 \;\times\; 10^5$ off-beam events, identifying 1.4×10^4 Michel electron candidates. The ionization-only reconstructed energy

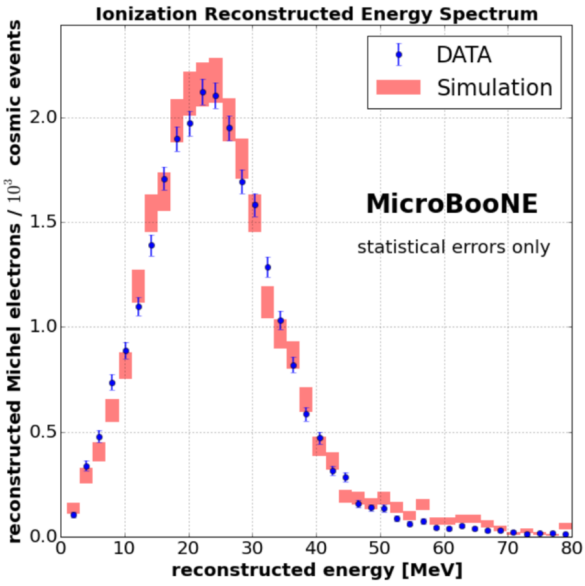

Figure 6.16: The ionization-only Michel electron energy spectrum for data (blue) and simulation (red). The error bars represent the statistical uncertainties only for both the simulation and the data.

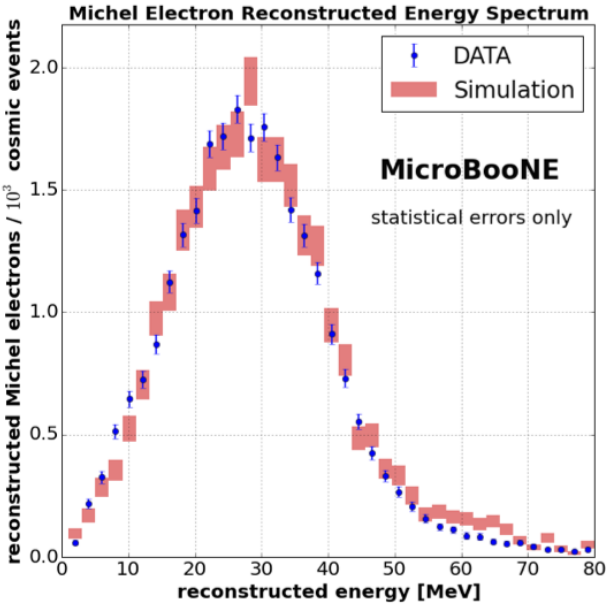

Figure 6.17: The full Michel electron energy spectrum for data (blue) and simulation (red) formed by including the energy from radiative photons. The error bars represent the statistical uncertainties only for both the simulation and the data.

spectrum is shown in Figure 6.16 and the full reconstructed energy spectrum is shown in Figure 6.17. Data and simulation are shown in both plots. By including radiative photons in Figure 6.17,

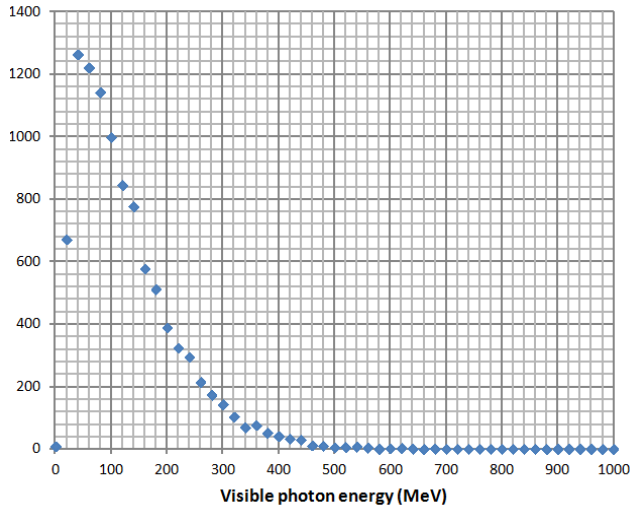

Figure 6.18: The amount of visible energy deposited by the photons from a π^0 decay-at-rest in a LArTPC detector in simulation.

the peak is ~30 MeV, while it is ~21 MeV in Figure 6.16. The energy resolution is greater than 30% when using ionization energy only, but this improves to ~20% when radiative photons are included.

6.5 Photon Tracks From a π^0 Decay-at-Rest

In a LArTPC, one of the processes that can take place is the decay-at-rest of a π^0 to two photons, which leave a shower in the detector that begins depositing charge a distance of several centimeters from the interaction vertex. Because the mass of a π^0 is known exactly to be 135 MeV, if this particular signature can be identified from others in the detector, the reconstructed energy of the two photons can be compared to this mass as a map. The calibration procedure for using this sample is to take the amount of visible energy of the photons that is reconstructed in the detector (shown in simulation in Figure 6.18) and calculate the residual of its most probable value with respect to half the mass of the π^0. As of this writing, this calibration sample has not been constructed or used with MicroBooNE.

6.6 CRT-Tagged Tracks

In addition to providing a means of tagging cosmics and removing them from neutrino interactions, the CRT panels can provide a cosmic calibration sample for detector physics work. Because of the requirement that the tracks be anode-piercing or cathode-piercing, the ACPT sample does not

provide the best coverage across the detector, particularly close to the center. Likewise, the A/C-crossing sample has too low of an event rate to provide a calibration sample that can accurately capture time dependence in detector effects.

Because of gaps in coverage, the CRT-tagging algorithm relies only on matching tracks to a single CRT hit in performing the matching. The way that it works is the following:

- The TPC track has its t_0 corrected using the time of the CRT hit. This offset is applied to the x-coordinates of the track's endpoints.
- The TPC track's endpoints are extrapolated to the CRT hit plane.
- The distance of closest approach (DCA) is calculated between the track's trajectory extrapolated to that plane and the location of the CRT hit. If the DCA is less than 40 cm for the top CRT panel or less than 20 cm for the other CRT panels, the hit and the track are declared matches. The ratio of ACPT tracks matched to a hit as a function of DCA is shown in Figure 6.19 for each CRT plane.

The efficiency of track-hit matching is ~54% and the purity is ~93%. As of this writing, this track sample is being used in the MicroBooNE diffusion analysis, albeit with several additional cuts. The tracks must:

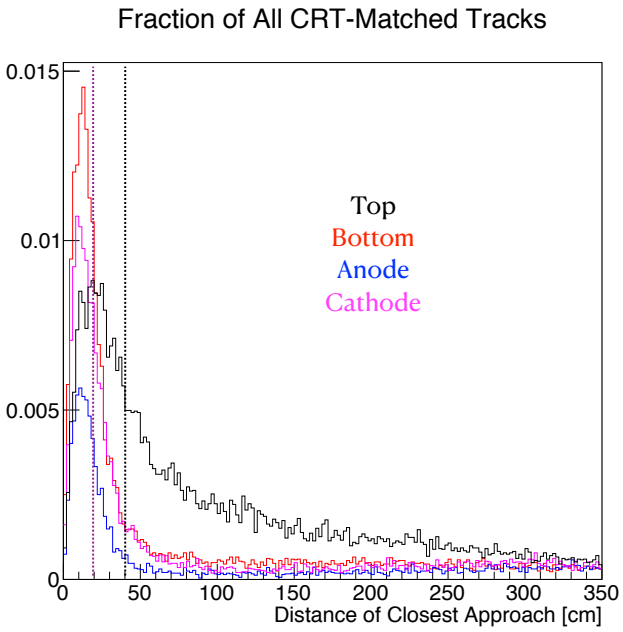

Figure 6.19: The fraction of TPC tracks matched to a CRT hit on a specific plane. To declare a match, DCA cut values of 20 cm (for the anode, cathode, and bottom, shown in blue, magenta, and red, respectively) and 40 cm (for the top) are used.

- be greater than 50 cm in length.
- have a transverse distance less than 6 cm.
- be through-going.
- have a value of θ_{xz} in the range [-6°, 6°].
- have a value of θ_{yz} in the range [-40°, 40°].

6.7 KDAR Events

A K^+ decays to a muon (μ^+) and a muon neutrino (ν_μ) 64% of the time to produce a Kaon Decay-At-Rest (KDAR) muon neutrino. Because this is a two-body decay-at-rest, the energy of the neutrino is known to be exactly 236 MeV. Protons that do not interact within NuMI beam target travel 720 m through the NuMI decay pipe to the beam dump, where they interact [51]. Some of them form kaons there, which serves as a source of neutrinos to be studied with MicroBooNE. It is expected that there will be ~970 KDAR events from the NuMI beam dump assuming a cross section of 1.25×10^{-39} cm^2/neutron for 8.3×10^{20} POT, which corresponds to ~16 months of data-taking with the NuMI beam in reverse horn current mode.

The length of the muon track in KDAR interactions is tightly constrained, because all of the events have energy 236 MeV. 40 cm serves as a loose upper limit of this quantity. Typically, the topologies of KDAR interactions in the MicroBooNE LArTPC consist of a muon track with high ionization at its start corresponding to the hadronic portion. This flux would serve as a 'standard candle' for neutrino energy reconstruction, demonstrating how well MicroBooNE analyses can reconstruct that variable given the current reconstruction tools. An attempt to isolate these low-energy, monoenergetic events is described in Chapter 8. Unfortunately, due to large flux and cross section uncertainties, the analysis is impossible to perform as of this writing.

CHAPTER 7

The Space Charge Effect

The space charge effect (SCE) is caused by distortions in the electric field of a LArTPC detector due to positively-charged argon ions flowing towards the cathode of the detector in the direction of the electric field, opposite the direction of the flow of ionization electrons. By using anode-piercing/cathode-piercing muon tracks, a calibration was derived for MicroBooNE to calculate the magnitude of the electric field distortions and to correct track trajectories for SCE. It is found that the effects are largely constant over time, with temporal variations of $< 5\%$ over the time periods of several days considered in this study. Along with recombination, SCE is the most dominant detector systematic in MicroBooNE neutrino analyses. Constraining it will allow for more precise measurements to be made with the experiment.

7.1 Introduction

The electric field within a TPC is designed to be uniform, a characteristic determined by the anode, the cathode, and the wire plane geometry. However, modifications to the electric field, such as those due to SCE, cause changes to the trajectories of charged-particle clusters of ionization electrons as they drift towards the anode wire planes.

A study of SCE in MicroBooNE was previously performed by using through-going tracks tagged by the MuCS system, described in Chapter 4 [11]. For the runs of the MuCS used for this study, the tracks were projected into the x-y plane and directed specifically at the cathode. Figure 7.1 indicates the effects of SCE on track reconstruction. Instead of outlining the boundaries of the detector, the tracks endpoints are located closer to the middle of the TPC the further along the x-axis the track was incident in the TPC. This is the result of ionization electrons being more affected by SCE the closer to the cathode they pass through the detector.

SCE in a LArTPC is the result of the buildup of positive ions at the cathode as a result of the ionization of argon atoms when charged particles pass through the detector. The ~25 cosmic rays that pass through the detector per 4.8 ms readout create a significant amount of charge buildup.

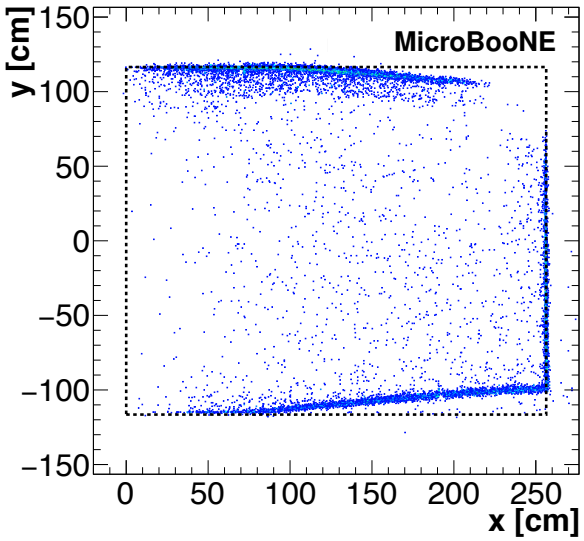

Figure 7.1: A graphic of the track endpoints of cosmic ray muon tracks that pass through the MuCS system [11]. In the absence of SCE, the track endpoints would outline the edges of the box, which represent the boundaries of the detector active volume. The anode is located at x = 0 cm and the cathode is located at x = 256 cm.

This affects the electric field within the TPC, as the drift velocity of argon ions, at ~4 mm/s, is approximately five orders of magnitude smaller than the ionization electron drift velocity of ~1.1 mm/μs. The resulting distortions in the electric field lead to different drift times and positions of ionization electrons. Additionally, the electron-ion recombination rate is different, because that depends on the electric field in different parts of the detector. If this effect was not accounted for, then there would be biases in the amount of deposited energy and track reconstruction.

The work presented in this chapter highlights a calibration of SCE in the detector that was derived using cosmic ray muons. The calibration is compared to a dedicated simulation of the effect. This work complements work done to extract the electric field distortions throughout the detector by using the laser system. The calibration uses crossing points of cosmic muons to unambiguously correct the track distortions due to SCE in three dimensions. The estimated spatial distortions of the track can be used to find the electric field distortions in that area of the TPC, which allows for the correcting of the electron-ion recombination throughout the detector. This quantity is important for both particle identification and the energy measurements of particles.

7.2 Simulation

To account for SCE in the MicroBooNE LArTPC, there is a dedicated simulation to model the effect. It simulates both the impacts of space charge on the electric field as well as the distortions in the positions of ionization electron clusters at different points within the TPC volume. The simulation uses a Fourier series solution to the boundary value problem to solve for the electric field on a three-dimensional grid. Interpolation between the grid points using radial basis functions is used to find the electric field everywhere inside the TPC. Range tracking using the RFK45 method is used to simulate the expected position in ionization electron position. The simulation uses a drift velocity measurement that is derived using a fifth-order polynomial fit to ICARUS T600 drift velocity measurements which are performed at several different electric fields and at the same temperature as MicroBooNE. The data-driven calibration presented in this chapter uses a drift velocity measurement made at MicroBooNE.

For the simulation, it is assumed that charge deposition rate of cosmic muons is uniform across the detector. Through the known angular spectrum of cosmic rays, which produce ~50,000 electron-ion pairs per centimeter, it is known that there are 1.6×10^{-10} C/m^3/s at a drift electric field of 273.9 V/cm. This calculation accounts for the effects of electron-ion recombination. The space charge density is approximated as linear with respect to the anode plane and independent of y and z if higher-order effects of the electric field distortions on SCE itself. The linear space

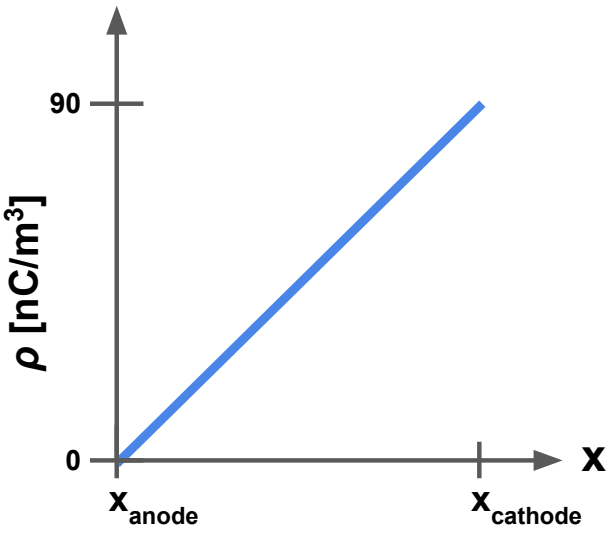

Figure 7.2: Space charge density ρ as a function of the x position assumed in the simulation. The maximum space charge density (the value at the cathode), 90 nC/m^3, takes into account both the expected rate of charge deposition by cosmic rays and the amount of electron-ion recombination within the detector. This quantity is modeled as independent of y and z.

charge density profile is shown in Figure 7.2 for a drift electric field of 273.9 V/cm.

Some examples of the electric field distortions and of ionization electron cluster distortions are shown in Figures 7.3 and 7.4, respectively. The maximum electric field distortions are estimated to be 10-15% in both the x (drift) and y/z (wire) directions at MicroBooNE's electric field of 273.9 V/cm.

While the simulation provides a comparison from first principles for the SCE in MicroBooNE and contains simple features that may be expected in data, there are several shortcomings in its formation that make a data-driven calibration important. First, the flow of liquid argon is not simulated. Second, while the rate of charge deposition by cosmic rays throughout the detector is assumed to be uniform, that may not be true due to more charge deposition closer to the top of the detector. Lastly, the linear space charge density assumed in the simulation approximates the ion drift speed (4 mm/s at an electric field of 273.9 V/cm) as constant throughout the detector, when in reality SCE affects this and renders this assumption incorrect.

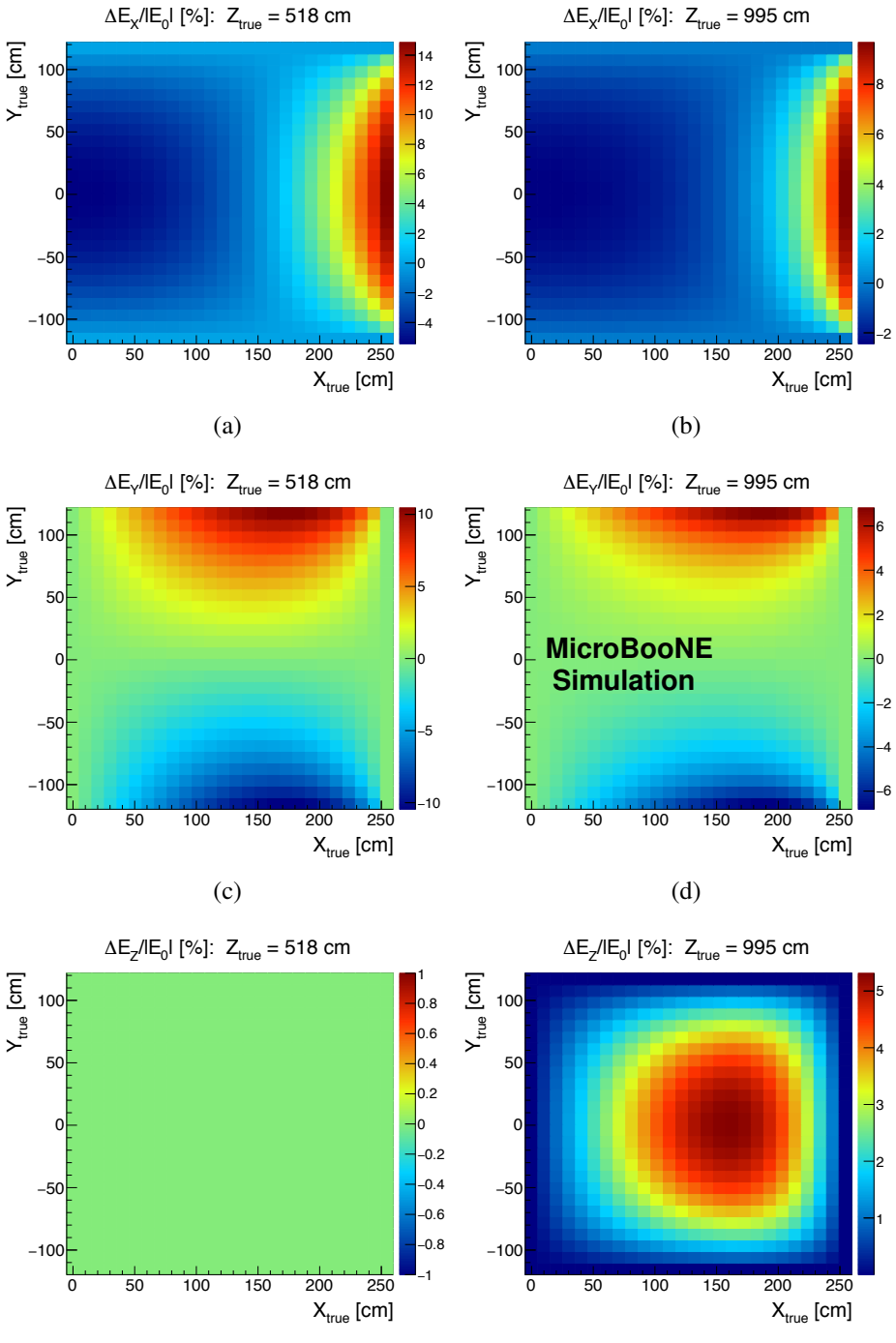

Figure 7.3: A visualization of the effects of SCE on the electric field in the TPC for the x-component (a,b), the y-component (c,d), and the z-component (e,f). These results are shown for the nominal electric field value of 273.9 V/cm and are shown as a function of true position inside the TPC. These results are shown for both a central slice in z in (a, c, e) and for a slice closer the downstream end of the detector for (b, d, f).

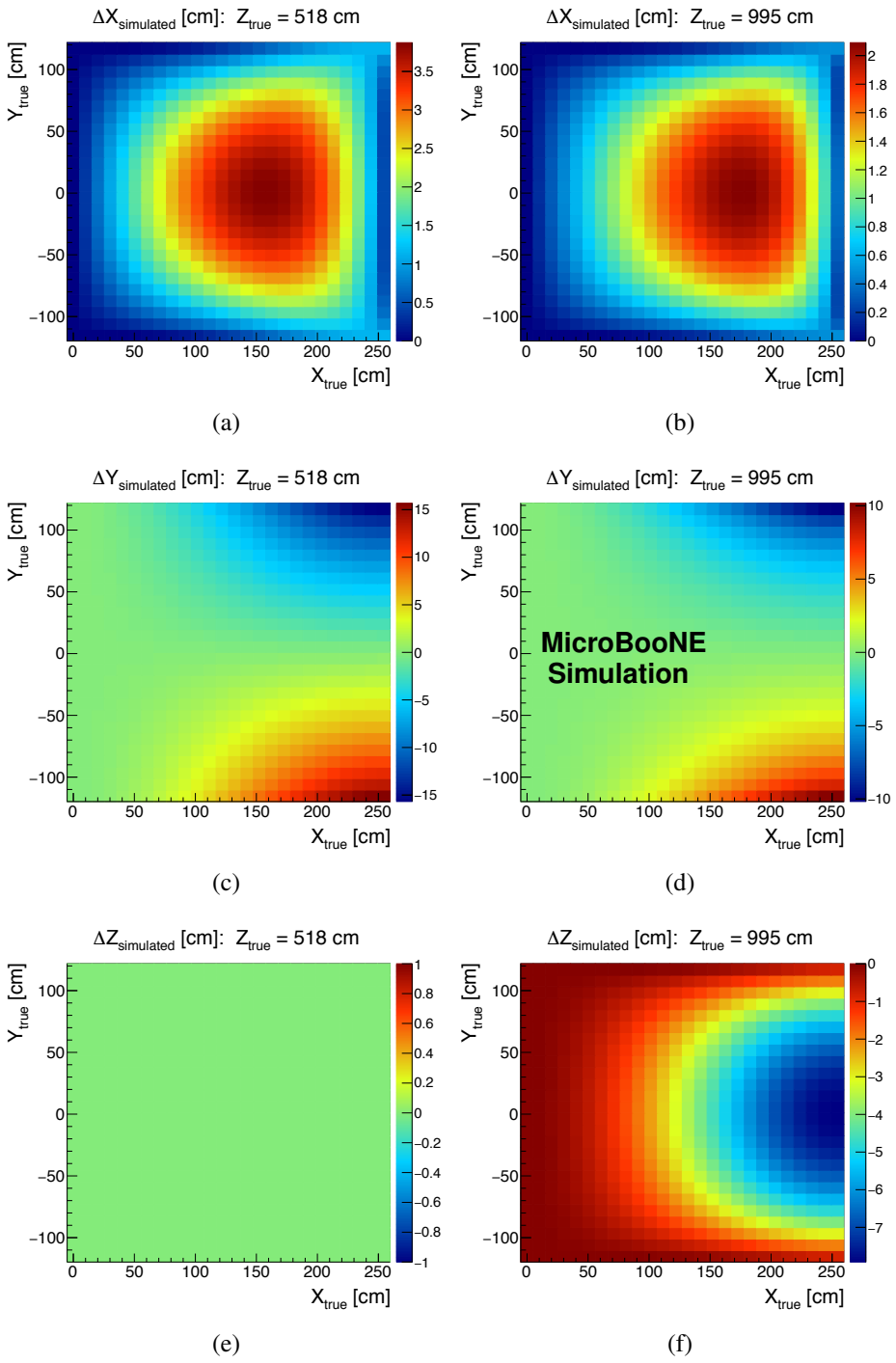

Figure 7.4: A visualization of the effects of SCE on the locations of clusters of ionization electrons in the TPC for the x-component (a,b), the y-component (c,d), and the z-component (e,f). These results are shown for the nominal electric field value of 273.9 V/cm and are shown as a function of true position inside the TPC. These results are shown for both a central slice in z in (a, c, e) and for a slice closer the downstream end of the detector for (b, d, f).

7.3 Track Samples

To perform these studies, the ACPT and A/C crossing track samples described in Chapter 6 are used. There are three important changes to the preparation of the ACPT sample described there, however: first, there is a cut to eliminate tracks that may have been reconstructed partially outside of the event readout window, meaning that the track is not well-reconstructed and likely has a poorly reconstructed t_0. Second, there is a cut on tracks not exceeding a specific length that is variable depending on the faces of the TPC that the track pierced, which is because these shorter tracks are likelier to have a poorly reconstructed t_0 than others. Third, the resolution value on the boundary of the detector used is 20 cm to fully capture the impact that SCE has on track reconstruction in these regions of the TPC. The A/C crossing track sample is reconstructed with an x-projected track length in the range [254, 258] cm (different from the [250, 270] cm interval as presented in Chapter 6) and requires that the tracks do not come within 20 cm of any y or z face of the detector. There are no cuts on calorimetry used in preparing the A/C crossing track sample.

For these studies, approximately 5M events in data are collected. Only 200k are used for the spatial distortion studies to allow for shorter computing time, but all of the statistics are used for the time-dependence studies, which require statistics from all different time intervals. For Monte Carlo, 1M events from CORSIKA, a cosmic ray simulator, are used.

7.4 Drift Velocity Measurement

To calculate the drift velocity in MicroBooNE, a sample of A/C crossing tracks was used to find how long it took the ionization charge on the cathode side of these tracks to flow to the anode wire planes. The sample of ACPT tracks was taken from the full set of 5M data events and amounted to 27k tracks in total. The distribution of drift times formed by these crossing tracks peaks at 2.321 ms. The measured distance between the cathode and the anode within the detector is 254.4 cm at 89 K, the operating temperature of the detector. There is an additional 0.5 cm added to the measurement to account for cumulative SCE in the drift direction of charge that originates at the cathode, which is predicted by the SCE simulation. This leads to a calculated drift velocity value of 1.098 ± 0.004 mm/μs. The uncertainty associated with this measurement stems from an uncertainty associated with variations in the cathode-anode drift distance across the detector, the SCE correction, statistics in the timing measurement, and the reconstruction of muon tracks.

The results of MicroBooNE's nominal drift velocity measurement are shown in Figure 7.5 along with previous measurements made in the ICARUS T600 detector [52]. The results used in this paper are formed from using a drift velocity model that is formed by fitting a fifth-order polynomial to ICARUS T600 data combined with the MicroBooNE nominal drift velocity mea-

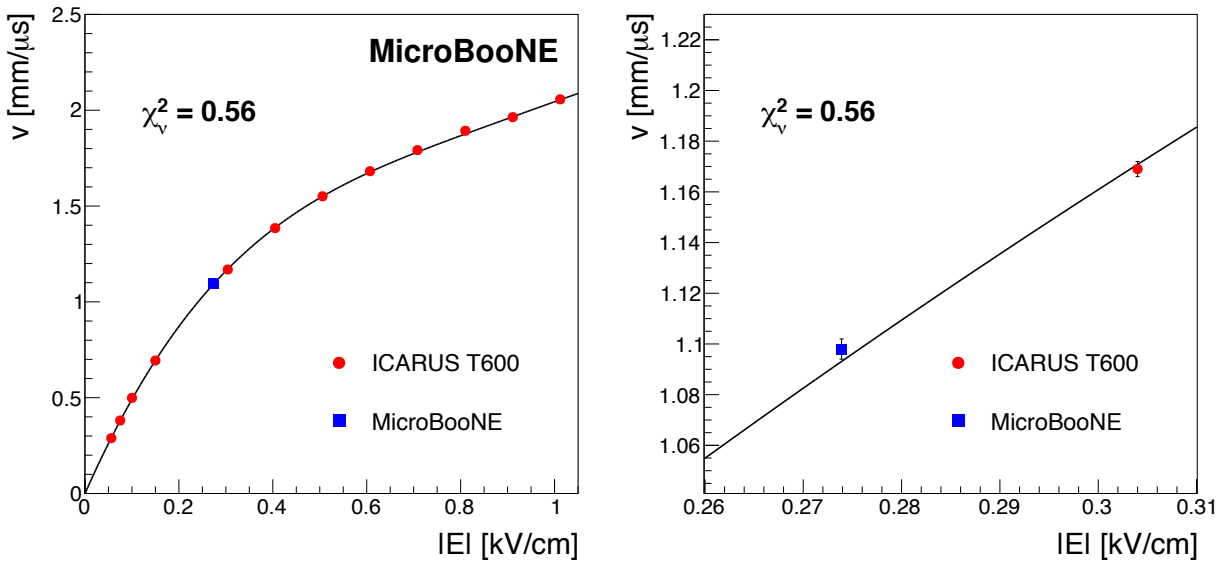

(a) (b)

Figure 7.5: MicroBooNE drift velocity measurement ($\nu_0 = 1.098 \pm 0.004$ mm/μs measured at $|E_0| = 0.2739$ kV/cm) compared to drift velocity measurements made at various electric field values at the ICARUS T600 experiment [12]; shown are both (a) the full electric field range and (b) the region of parameter space near the MicroBooNE electric field and the closest ICARUS T600 measurement. The combined dataset is fitted to a fifth-order polynomial function (solid curve), resulting in an excellent fit (χ^2_ν = 0.56, where χ^2_ν is the reduced chi-square statistic associated with the fit). All measurements shown were made at an operating temperature of 89 K.

surement. The results of this fit are shown in Table 7.1.

Fit Parameter	Value
p_0	0.0
p_1	5.534
p_2	-6.531
p_3	3.208
p_4	0.3897
p_5	-0.5562

Table 7.1: Parameters used in the fit for the drift velocity model used in the SCE calibration procedure. The equation is fifth-order: $\nu(E) = p_0 + p_1 E + p_2 E^2 + p_3 E^3 + p_4 E^4 + p_5 E^5$. Here, E is in units of kV/cm and ν is in units of mm/μs. In the fit, p_0 is forced to 0.

7.5 Ionization Electron Position Distortion Correction Technique

In order to measure the track offsets due to SCE within the detector, the procedure in Figure 7.6 is used. First, the y and z faces of the TPC are calibrated using tracks that pierce the anode. Because the tracks piercing the anode have a minimal distortion due to SCE, their endpoints on the anode side of the detector are approximately located where they would be in the absence of SCE. Using the results of the anode-piercing face calibration, tracks that pierce the top, bottom, upstream, and downstream faces of the detector as well as the cathode are used to calibrate that face. Finally, once all the faces of the detector are calibrated, crossing tracks are used to calibrate the TPC bulk using unambiguous point-to-point matching.

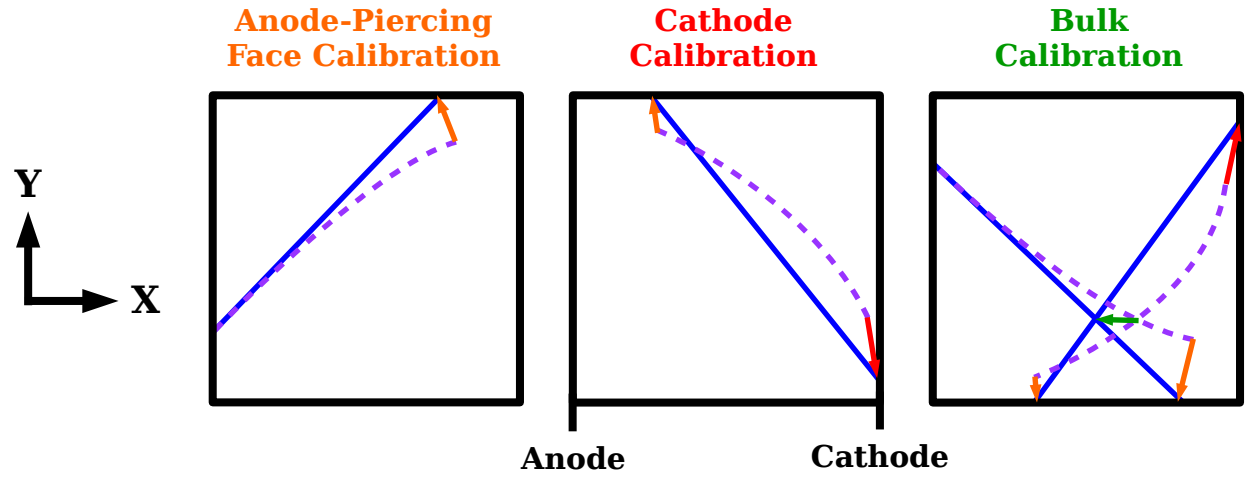

Figure 7.6: Shown here are the three steps for calibrating the detector for SCE. The anode-piercing face calibration (left) and cathode calibration (center) are meant to calibrate the endpoint of tracks, while the bulk calibration (right) calibrates the body of the detector.

7.5.1 Anode-Piercing Face Calibration

Because the ionization electrons do not need to drift to reach the anode plane, no calibration is needed to correct ionization electron cluster positional distortions at this face of the TPC. However, the other five faces of the TPC require a calibration to obtain the true point of entry or exit on a given track.

As part of this calibration stage, a 5 cm gap between the field cage and the instrumented TPC volume impacts the true position of ionization charge before it drifts. This offset is shown in Figure 7.7 and it affects the calibration at the y and z faces that the anode-piercing face calibration

is intended for. The diameter of the field cage tubes is 1 cm, there is an average offset of 4.5 cm in the true location of the ionization charge position in the y and z directions. Because this affects the calibration of the y and z faces, it has to be accounted for in this stage of the calibration procedure so that the correction calibration is propagated downstream. This correction must only be applied to events in data, because in simulation it is assumed that the instrumented TPC volume ends at the field cage.

The calibration of the y and z faces of the TPC uses the endpoint of the track that does not terminate at the anode plane to determine the offset due to SCE in three dimensions. The component of the correction vector that is orthogonal to the TPC face (y for the top and bottom and z for the upstream and downstream ends) is projected to that face of the TPC. The transverse components are corrected by using the simulation described in Section 7.2. The way that this is done is by utilizing the component of the correction vector perpendicular to the TPC face with the components of the simulation for that Cartesian direction and the direction that is being calibrated,

$$\Delta x_{\text{reco}} = \Delta y_{\text{reco}} \times \Delta x_{\text{sim}}(x,z)/\Delta y_{\text{sim}}(x,z) \tag{7.1}$$

and

$$\Delta z_{\text{reco}} = \Delta y_{\text{reco}} \times \Delta z_{\text{sim}}(x,z)/\Delta y_{\text{sim}}(x,z) \tag{7.2}$$

where Δx_{reco}, Δy_{reco}, and Δz_{reco} are the reconstructed spatial offsets in the x, y, and z di-

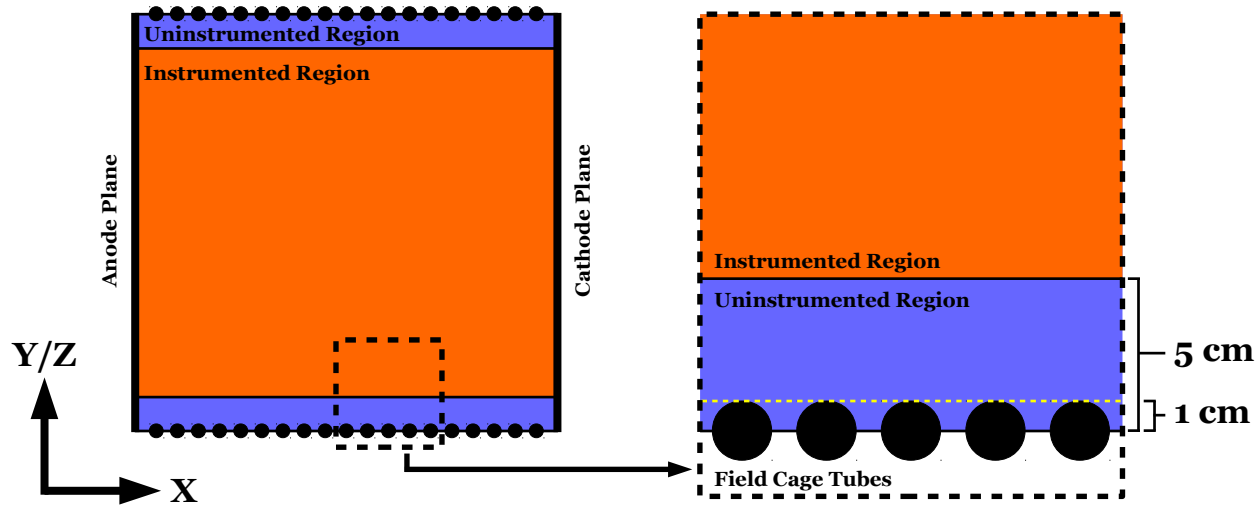

Figure 7.7: Image depicting the 5 cm offset between the field cage and the instrumented TPC volume in the MicroBooNE TPC. Because the diameter of the field cage tubes is approximately 1 cm, there is an approximately 4.5 cm offset on average from the assumed true charge position at the TPC boundary in the y and z directions. This image is not drawn to scale.

mensions, respectively, and $x_{\mathrm{sim}}(x,z)/\Delta y_{\mathrm{sim}}(x,z)$ are the ratio of the x and y spatial offsets in the simulation. This procedure uses two-dimensional voxels that are approximately 10 cm in both dimensions for each TPC face. Although this part of the calibration procedure relies on the simulation, the magnitude of the correction vector is dominated by the component orthogonal to the TPC face, which is determined independently of the simulation.

Because of the 4.5 cm offset in the location of the position of a true ionization electron cluster at the y and z boundaries of the TPC, this procedure cannot be applied in regions of the TPC in which the orthogonal offset from the detector face is greater than this amount ($x > 100$ cm). Therefore, in regions where the procedure cannot be applied, the offsets due to simulation are used instead, scaled according to data-driven values at which this technique is possible.

7.5.2 Cathode Calibration

Once the offsets due to SCE have been determined at the y and z faces of the detector, the cathode can be calibrated by using tracks that pierce one of those faces and the cathode itself. This step aims to calibrate the true entry or exit point of a track at the cathode plane. To do this, the SCE simulation is used in addition to the results from the anode-piercing face calibration. An interpolation is performed between the top and bottom of the TPC to 'weight' the SCE simulation such that the spatial offsets at the cathode match those obtained from the anode-piercing face calibration where the cathode intersects with the y TPC faces. This is done in the following way:

$$F(y) \;=\; (y - y_{\mathrm{bottom}})/(y_{\mathrm{top}} - y_{\mathrm{bottom}}), \tag{7.3}$$

$$S(y,z) \;=\; F(y)\Delta y_{\mathrm{reco}}(y_{\mathrm{top}},z)/\Delta y_{\mathrm{sim}}(y_{\mathrm{top}},z) + (1-F(y))\Delta y_{\mathrm{reco}}(y_{\mathrm{bottom}},z)/\Delta y_{\mathrm{sim}}(y_{\mathrm{bottom}},z), \tag{7.4}$$

$$\Delta x_{\mathrm{reco}}(y,z) = S(y,z) \;\times\; \Delta x_{\mathrm{sim}}(y,z), \tag{7.5}$$

$$\Delta y_{\mathrm{reco}}(y,z) = S(y,z) \;\times\; \Delta y_{\mathrm{sim}}(y,z), \tag{7.6}$$

and

$$\Delta z_{\mathrm{reco}}(y,z) = S(y,z) \;\times\; \Delta z_{\mathrm{sim}}(y,z), \tag{7.7}$$

where y_{top} (y_{bottom}) is the vertical position at the top (bottom) of the detector, x_{reco}, y_{reco}, and z_{reco} are the reconstructed spatial offsets at the cathode plane in the x, y, and z dimensions, respectively, x_{sim}, y_{sim}, and z_{sim} are the simulated spatial offsets at the cathode plane in the x, y, and z dimensions, respectively, $F(y)$ is the interpolation function, and $S(y,z)$ is the scale factor

used to modify the simulated spatial offsets used at the cathode for the calibration. Like the anode-piercing face calibration, this procedure uses two-dimensional voxels that are approximately 10 cm in both dimensions for each TPC face.

7.5.3 TPC Bulk Calibration

The last step in the calibration procedure uses the results from the anode-piercing face calibration and the cathode calibration to calibrate the bulk of the TPC. By drawing a straight line through the true endpoints of the tracks, the true trajectory of the track through the detector can be approximated. This alone cannot provide a correction for the trajectories of the tracks through the TPC, because it is ambiguous which point on the reconstructed track corresponds to which part of the truth track. This problem is solved by using pairs of crossing muon tracks. By comparing the locations of where pairs of reconstructed tracks cross to where the corresponding truth tracks cross, a 3D correction map for the bulk of the TPC is derived. It is required that pairs of tracks come within 1 cm of each to be used in this process. Pairs of tracks do not have to be reconstructed in the same event because SCE does not vary significantly over periods of time (see Section 7.8). Using voxels that are approximately 10 cm in each TPC dimension, the spatial offsets are determined on a voxel-by-voxel basis by taking the median offset associated with the distribution of offsets from the near crossing-track pairs that populate a given voxel.

Enough statistics for this procedure are achieved by using 200k cosmic ray muon tracks. Multiple coulomb scattering (MCS) causes deviations between the straight-line approximation that is used for truth tracks and its true trajectory through the TPC, but this is mitigated by taking the median of the distribution in each voxel.

Because there are parts of the TPC in which the coverage of cosmic muons is lacking, particularly in the middle of the TPC, gaps in the spatial distortion maps are expected. The laser system can provide coverage to fill in these gaps in the distortion map. Also, because the spatial offsets are continuous and vary gradually as a function of position, gaps in the map can be removed by using interpolation: in these studies, a cubic spline followed by a median filter is applied (using a $3 \times 3 \times 3$ voxel window for the latter) to fill in these gaps.

7.5.4 Calculation of Electric Field Distortions

After the spatial distortions due to SCE have been determined throughout the entire TPC volume, the electric field distortions associated with SCE can be computed. Using the drift velocity model presented earlier, the local drift velocity must be calculated by using the spatial distortion map. Next, the electric field throughout the TPC can be found by solving the equation $\nu(E) = \nu(x, y, z)$ for each voxel in the TPC, with $\nu(x, y, z)$ representing the local drift velocity.

7.6 Calibration Results

7.6.1 Measurements at TPC Faces

The measurements of the offsets at the TPC faces in simulation and in data are shown in Figures 7.9 and 7.10, respectively. For the data events in Figure 7.10, the offset of 4.5 cm to account for the gap between the field cage and the instrumented TPC volume is not included; it is added at a later stage of the calibration. Included for comparison are the predictions for the track offsets for SCE from simulation in Figure 7.8, which are largely reproduced in Figure 7.9 when the calibration is applied. There is a region of relatively large Δy located at the top of the detector close to $z = 5$ m. This is because of two overlapping dead channels from two wire planes at the top of the TPC, which makes charge appear to look displaced from the top of the detector. By comparing Figure 7.9 to Figure 7.10, the difference in track offsets due to SCE can be recognized. Compared to simulation, the offsets are less at the top, upstream, and downstream ends of the detector in data. When the 4.5 cm gap between the field cage and instrumented TPC volume is accounted for, there is an increase in the spatial offsets in data. At the top of the TPC, the track distortions are lesser close to the upstream end of the detector than they are close to the downstream end. Additionally, there is a reduction in track distortions at the upstream end of the TPC at approximately 0.5 m. Although the cause of these effects has not been identified, liquid argon flow patterns could be responsible because they remove SCE from the TPC active volume.

7.6.2 Measurements in TPC Bulk

The calibration in the TPC bulk leads to a distortion map throughout the TPC volume away from the boundaries. It is difficult to show the full distortion map, but included here are distortion maps for slices of the detector located at $z = 5.18$ m (close to the center of the detector) and $z = 9.95$ m (downstream in the detector).

In Figures 7.11 and 7.12, the results of the data-driven calibration on simulation are compared to the truth offsets in the simulation for the two slices of the detector in z. The data-driven calibration nearly reproduces the truth offsets.

Figures 7.13 and 7.14 show the results of the data-driven calibration on data and a comparison to the same results for simulation. The results from simulation are altogether very similar to the results generated for the data, but there are some features of the data that cannot be reproduced from the simulation derived from first principles.

The performance of the data-driven calibration is shown in Figure 7.15 for all three dimensions throughout the entire detector, comparing the spatial offsets in the simulation to those that are recovered in the data-driven calibration of the simulation. Each entry in the plot is a voxel that

is approximately 10 cm in each dimension in the detector. A comparison is shown for the x and y dimensions, averaged over the entire z extent of the detector, in Figure 7.16. The resolution and bias, calculated using the standard deviation and mean of the distributions in Figure 7.15, respectively, are shown in Table 7.2. The resolution is < 4 mm and the bias is < 1 mm in all dimensions.

In order to evaluate the performance of the calibration procedure on data, the laser system is used. Because the true trajectories of the laser tracks are known, the reconstructed laser tracks can be corrected with the SCE calibration and then compared to the truth tracks. The comparison is carried out by comparing the 'laser track residuals', the distance between points on the reconstructed track to points on the truth track, both before and after the SCE corrections are applied. This calculation is applied on a point-by-point basis along the entire extent of the reconstructed laser track, and for each laser track associated with a full scan throughout the entire TPC volume. An effective SCE calibration should produce straighter reconstructed laser tracks with smaller residuals.

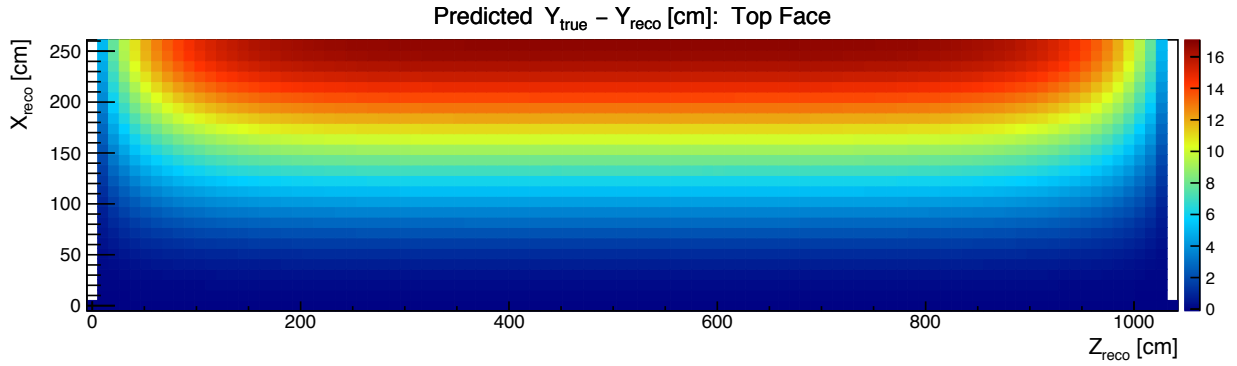

(a)

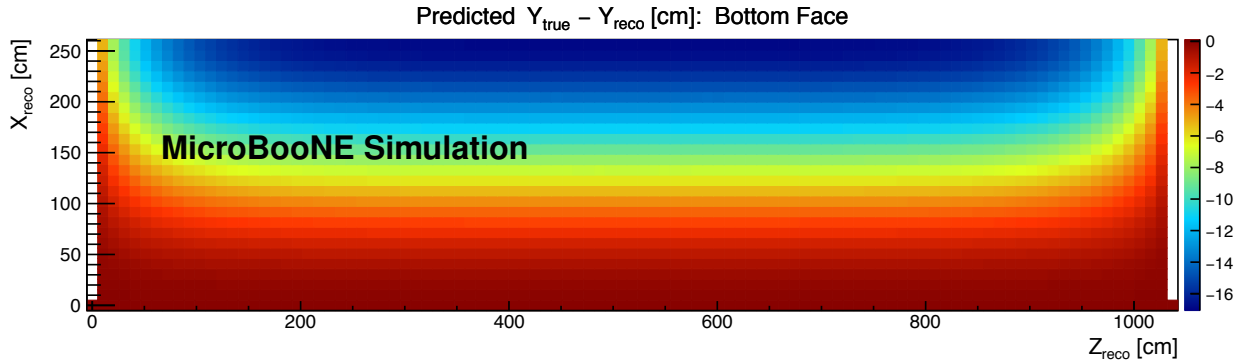

(b)

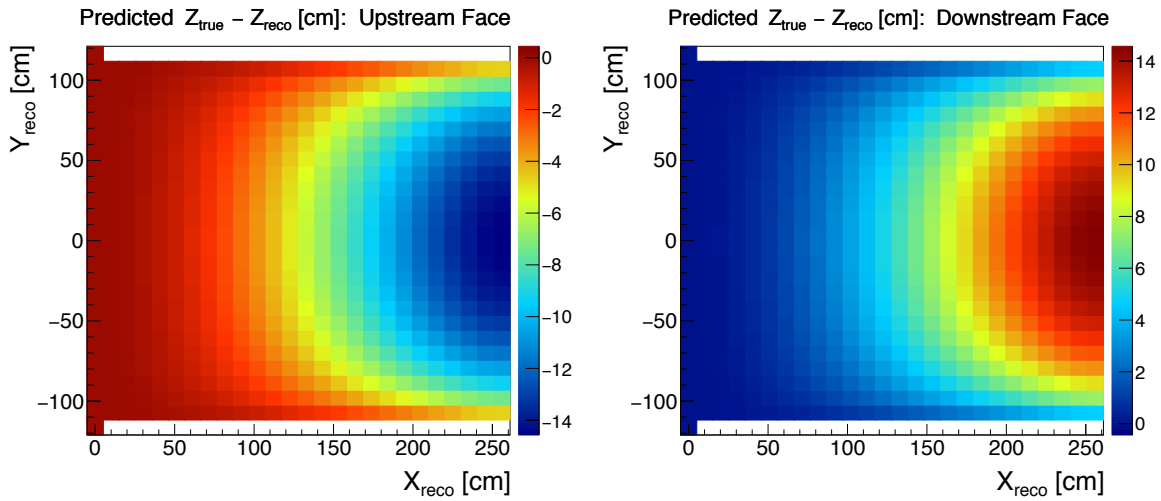

(c) (d)

Figure 7.8: Spatial offsets predicted for SCE at the (a) top of the TPC, (b) bottom of the TPC, (c) upstream end of the TPC, and (d) downstream end of the TPC. The voxels in the heatmaps represent the offsets orthogonal to the TPC face. The gaps at the edges of the maps correspond to places in the detector where charge should not be reconstructed due to the impact of SCE.

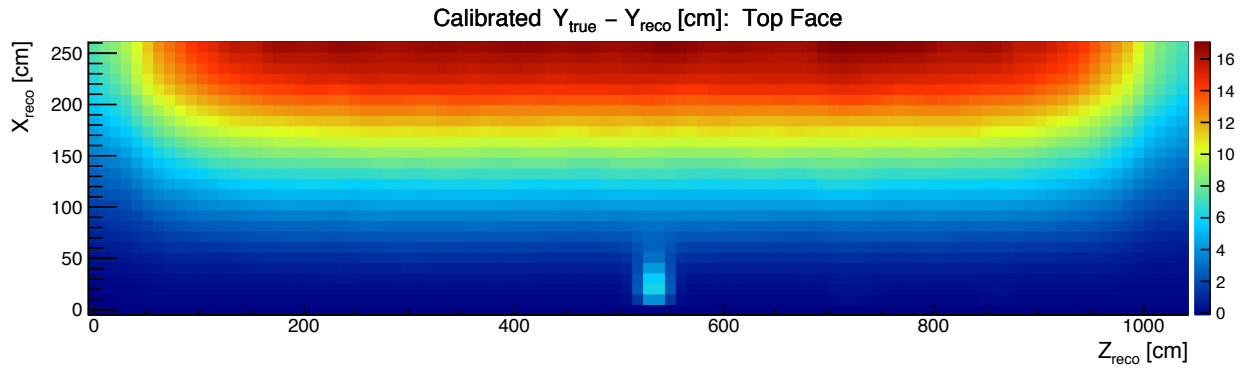

(a)

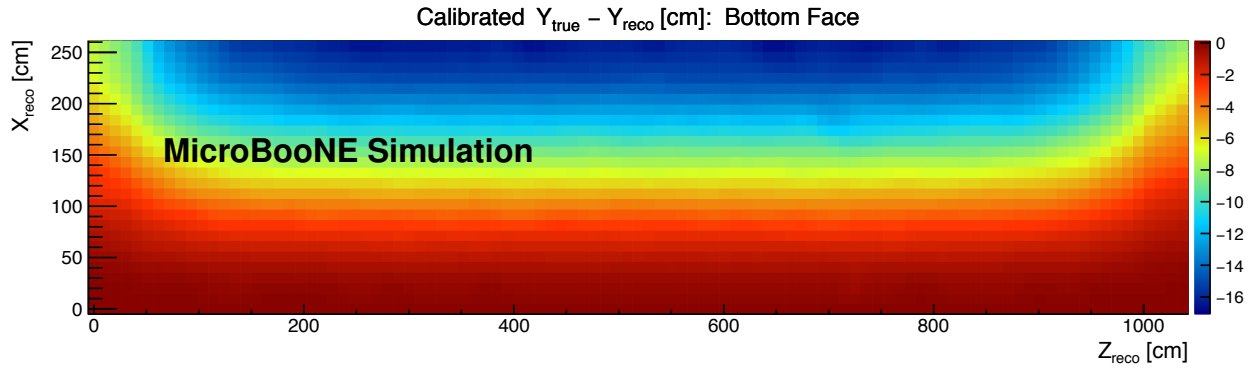

(b)

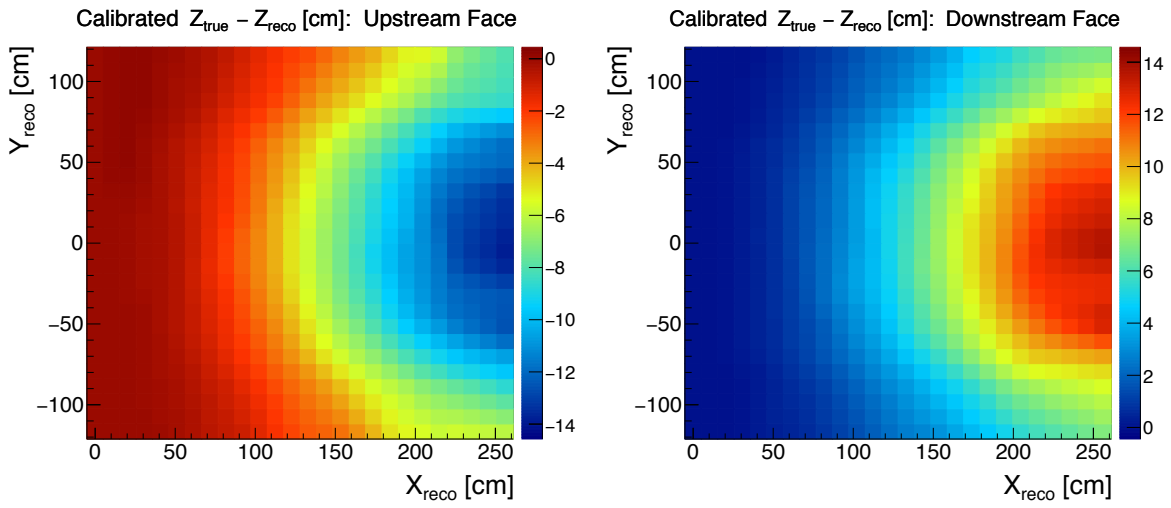

(c) (d)

Figure 7.9: Reconstructed spatial offsets from SCE for MicroBooNE simulated events at the (a) top of the TPC, (b) bottom of the TPC, (c) upstream end of the TPC, and (d) downstream end of the TPC. The voxels in the heatmaps represent the reconstructed offsets orthogonal to the TPC face. A cubic spline is used to fill in the gaps in the spatial offset maps at the edges of the TPC.

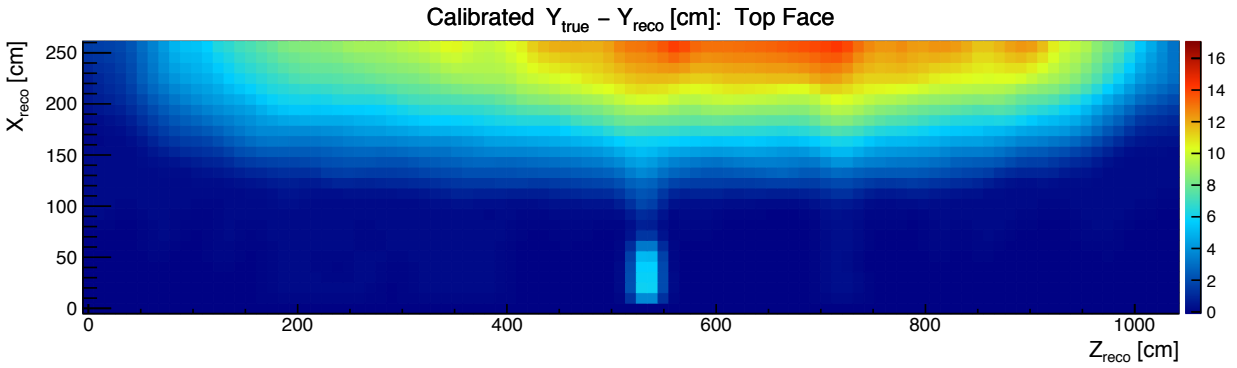

(a)

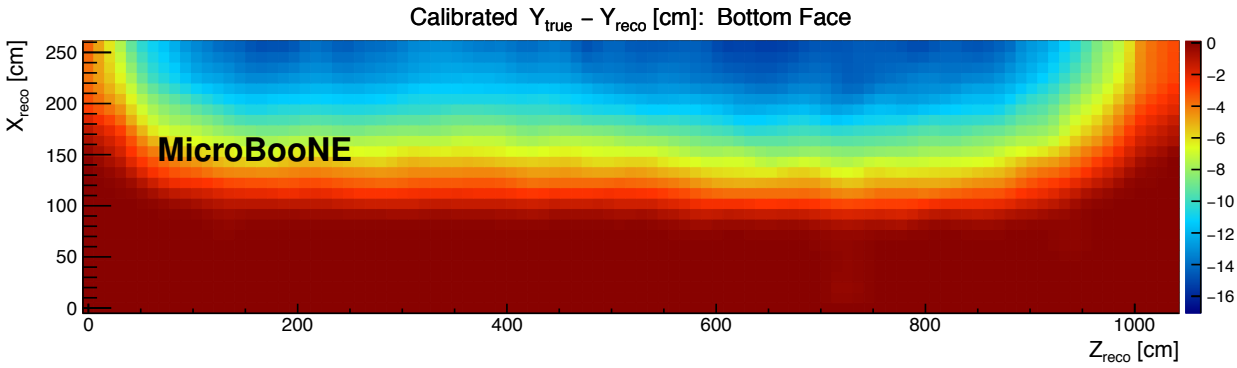

(b)

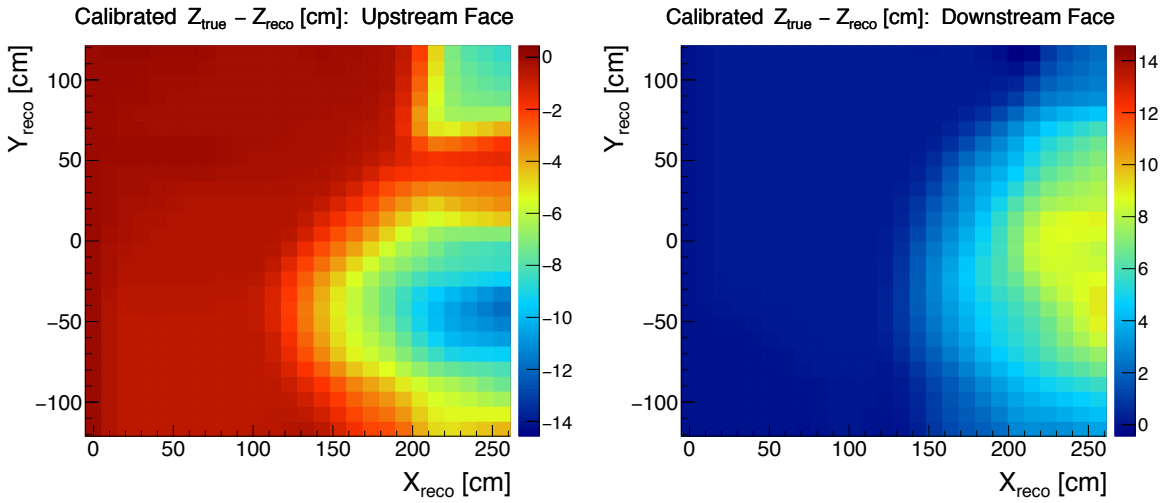

(c) (d)

Figure 7.10: Reconstructed spatial offsets from SCE for MicroBooNE data events at the (a) top of the TPC, (b) bottom of the TPC, (c) upstream end of the TPC, and (d) downstream end of the TPC. The voxels in the heatmaps represent the reconstructed offsets orthogonal to the TPC face. A cubic spline is used to fill in the gaps in the spatial offset maps at the edges of the TPC.

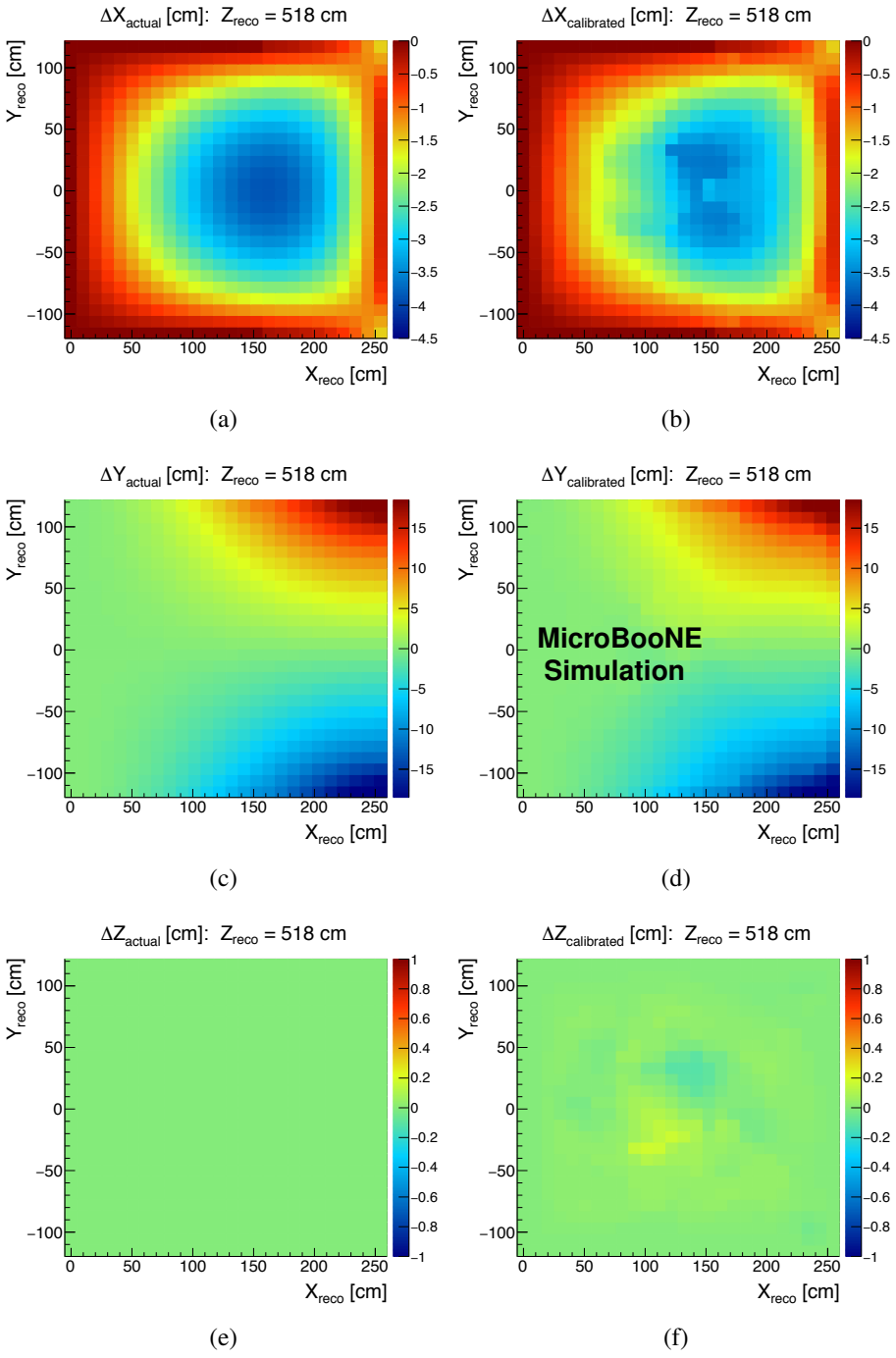

Figure 7.11: Comparison of the (a, c, e) spatial offsets predicted from SCE simulation to (b, d, f) the results of the TPC bulk calibration on Monte Carlo simulation events for a midstream slice of the detector in z. Results are shown for spatial offsets in (a, b) x, (c, d) y, (e, f) z. The distortions in reconstructed ionization electron cluster position are shown in units of cm and are plotted as a function of reconstructed position inside the TPC.

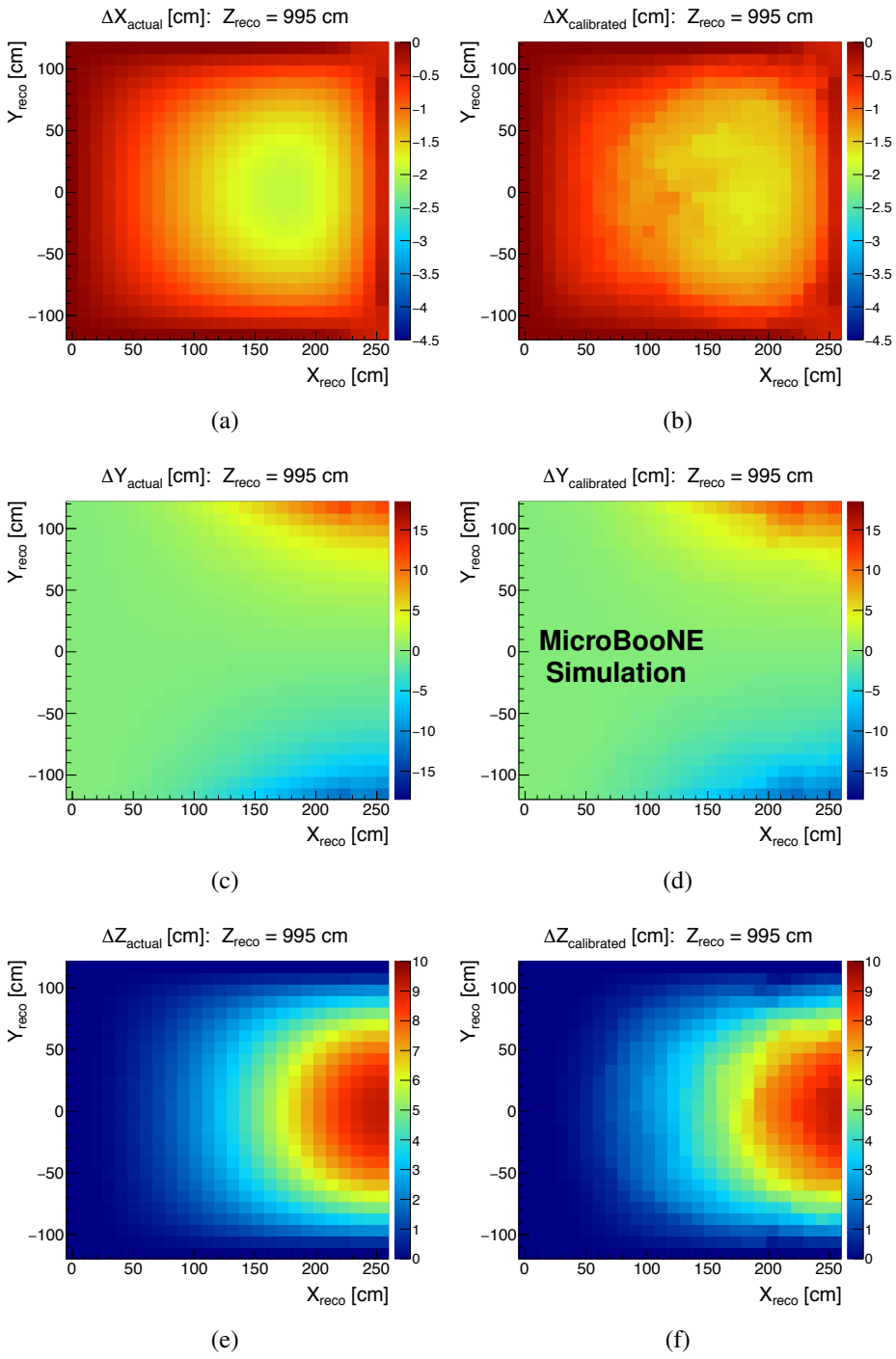

Figure 7.12: Comparison of the (a, c, e) spatial offsets predicted from SCE simulation to (b, d, f) the results of the TPC bulk calibration on Monte Carlo simulation events for a downstream slice of the detector in z. Results are shown for spatial offsets in (a, b) x, (c, d) y, (e, f) z. The distortions in reconstructed ionization electron cluster position are shown in units of cm and are plotted as a function of reconstructed position inside the TPC.

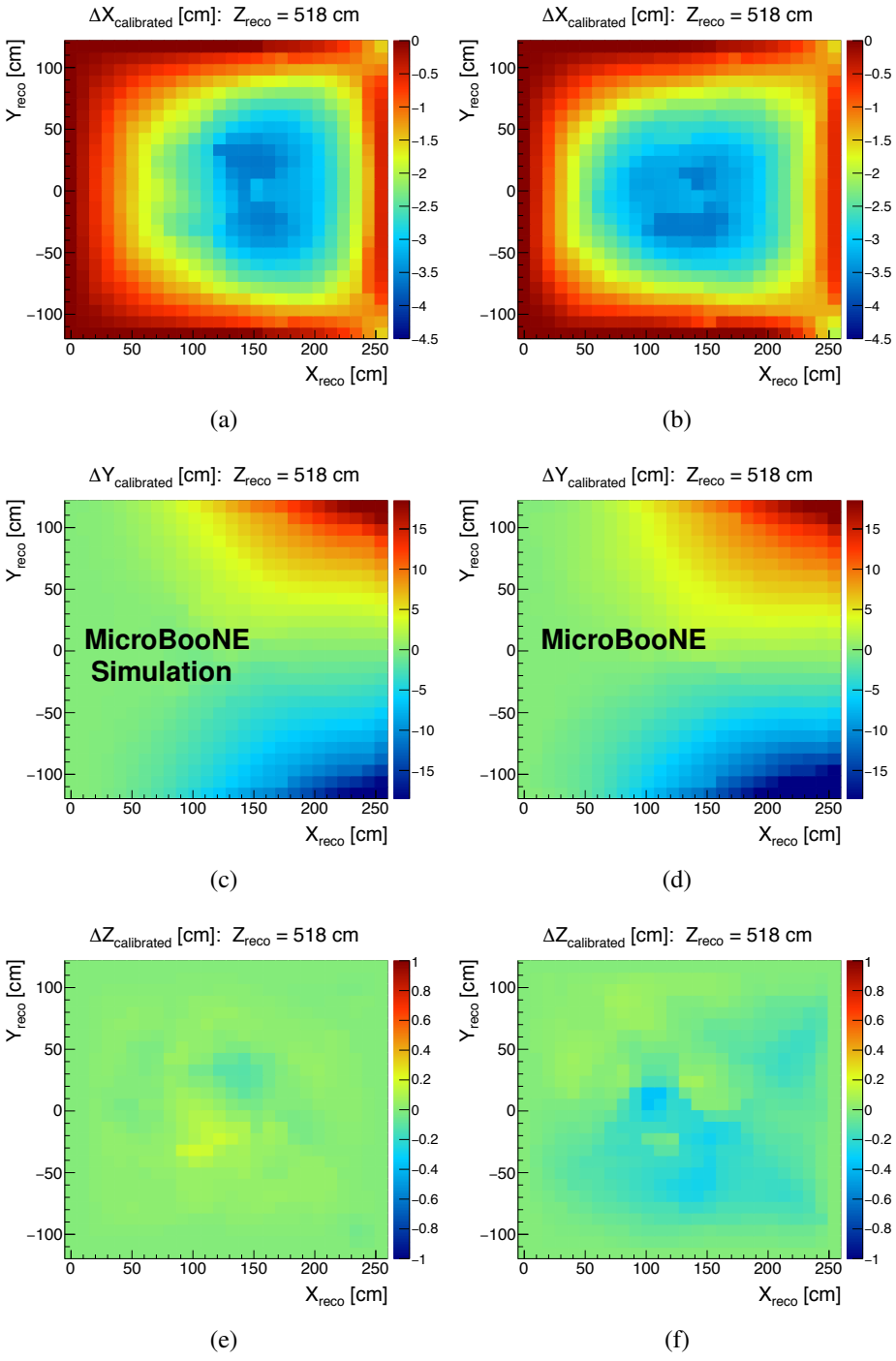

Figure 7.13: Comparison of the (a, c, e) spatial offsets the results of the TPC bulk calibration on Monte Carlo simulation events to (b, d, f) the results of the TPC bulk calibration on data events for a midstream slice of the detector in z. Results are shown for spatial offsets in (a, b) x, (c, d) y, (e, f) z. The distortions in reconstructed ionization electron cluster position are shown in units of cm and are plotted as a function of reconstructed position inside the TPC.

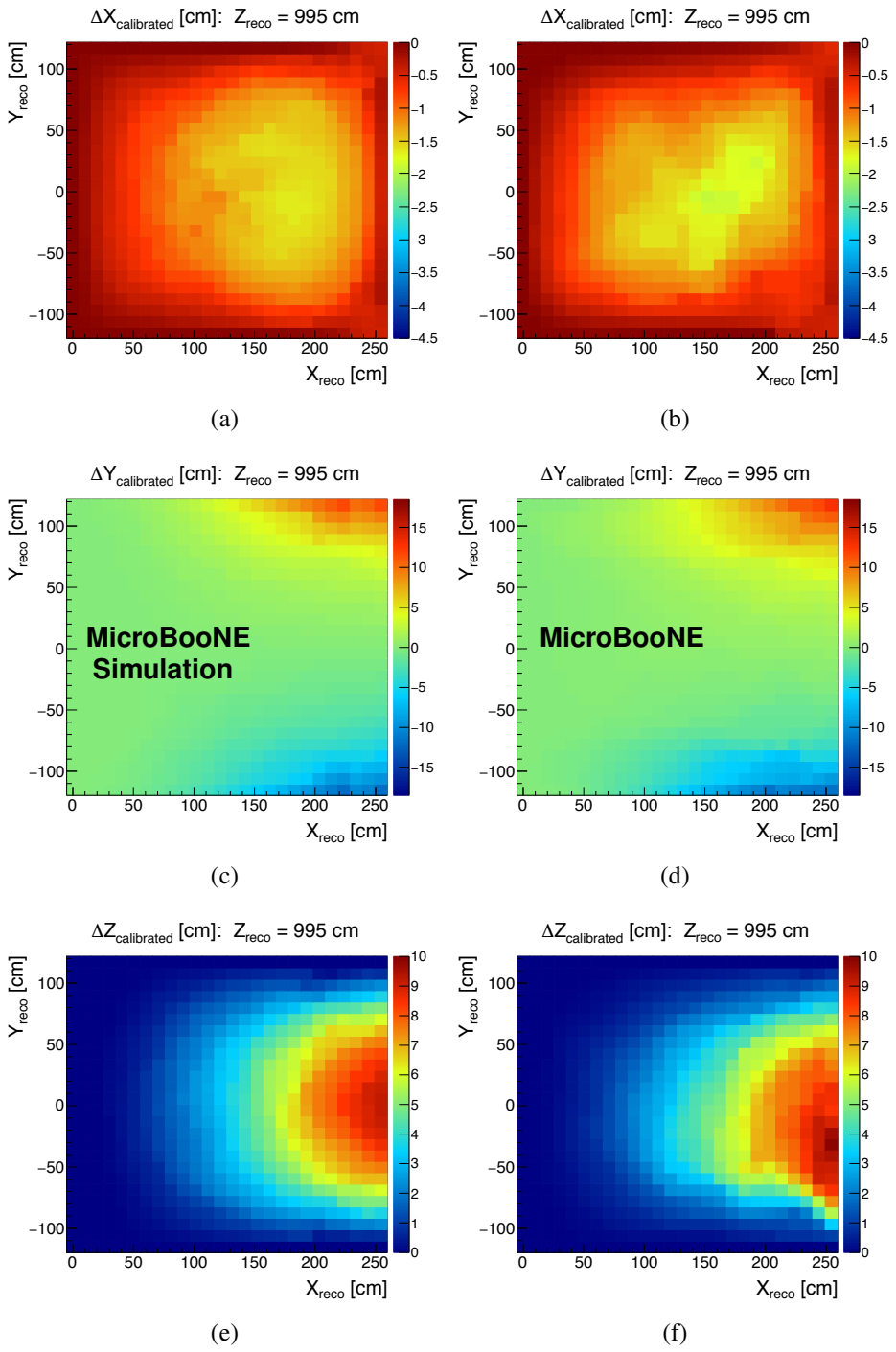

Figure 7.14: Comparison of the (a, c, e) spatial offsets the results of the TPC bulk calibration on Monte Carlo simulation events to (b, d, f) the results of the TPC bulk calibration on data events for a downstream slice of the detector in z. Results are shown for spatial offsets in (a, b) x, (c, d) y, (e, f) z. The distortions in reconstructed ionization electron cluster position are shown in units of cm and are plotted as a function of reconstructed position inside the TPC.

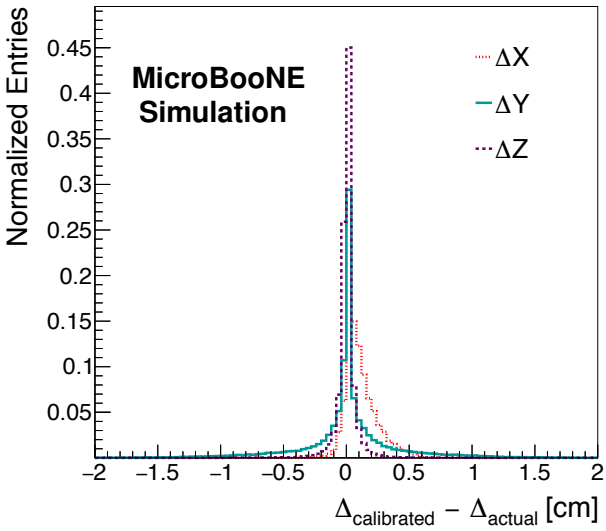

Figure 7.15: The distribution of differences between the TPC bulk calibration used on Monte Carlo simulation and simulated spatial offsets across the entire TPC volume for spatial distortions in x (red), y (blue), and z (green).

The calculated laser track residuals are shown in Figure 7.17 for both MicroBooNE data and simulated laser track events, showing the effect of the SCE calibration. The laser residuals become

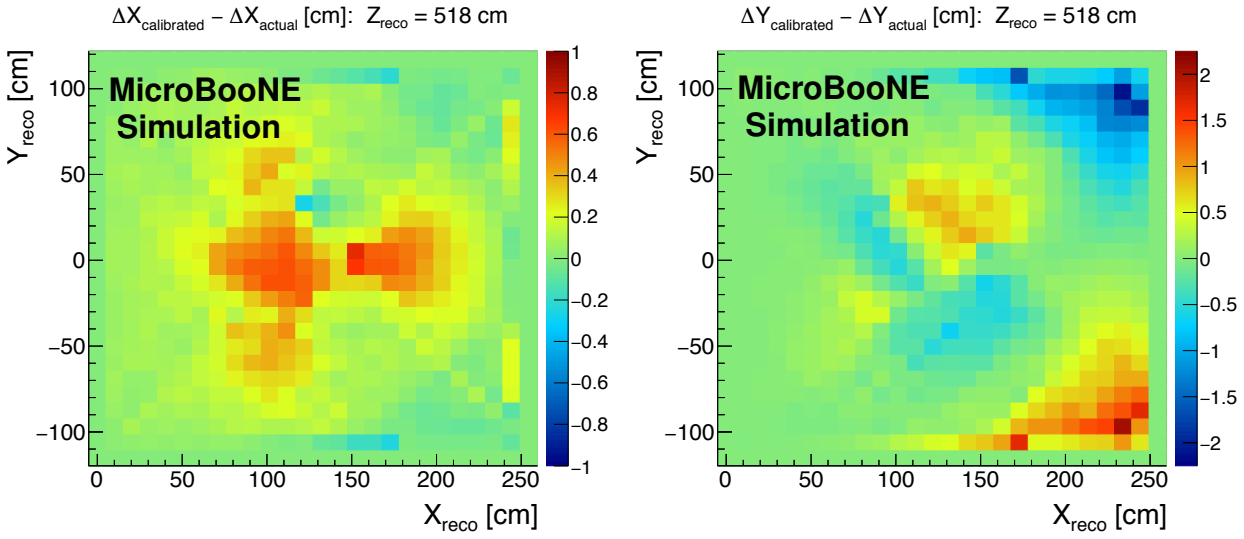

(a) (b)

Figure 7.16: Difference between calibrated spatial offsets in Monte Carlo simulation events and actual spatial offsets obtained from the SCE simulation, showing (a) Δx bias and (b) Δy bias in the x-y plane for a central z slice of the detector.

Measured Offset	Bias [cm]	Resolution [cm]
Δx	0.13	0.09
Δy	0.38	0.01
Δz	0.10	0.00

Table 7.2: The resolution and bias of the calibration, calculated using the standard deviation and mean of the distributions in Figure 7.15.

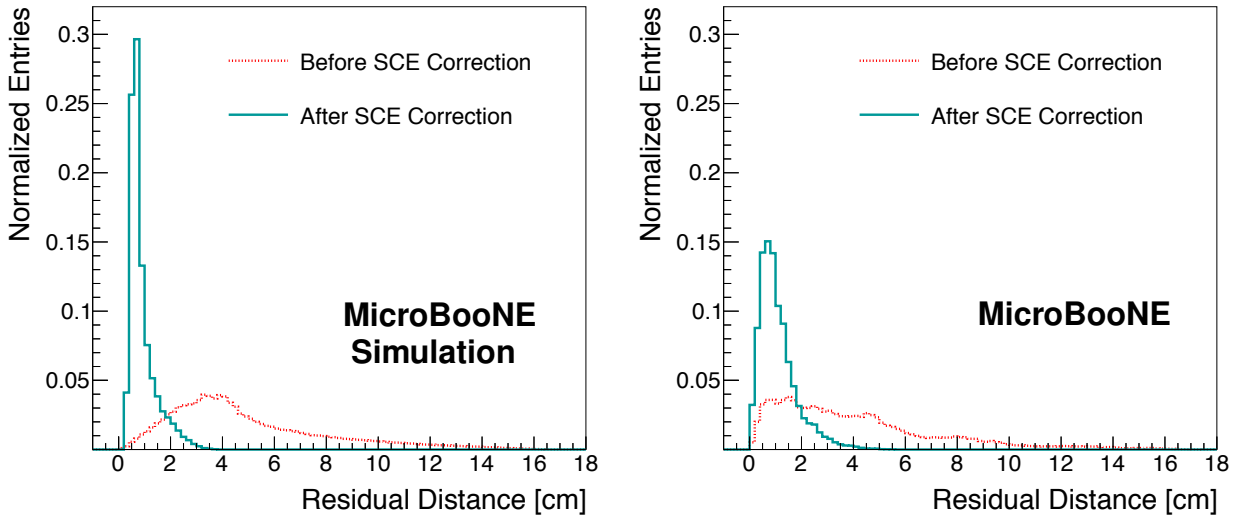

(a) (b)

Figure 7.17: Laser track residuals for (a) Monte Carlo simulation and (b) data events, shown both before and after applying spatial SCE corrections.

significantly smaller and closer to zero after applying the SCE calibration. The performance of the SCE calibration on data events is worse than when it is applied on simulated events, a difference which is found to be roughly 4 mm by applying a Gaussian smearing to the result for simulation until it agrees with the result from data.

7.6.3 Results for the Electric Field Distortion Measurements

With the spatial distortion map throughout the TPC volume, the electric field distortions at each point in the TPC can be calculated. The results of this calculation are shown in Figure 7.18 for simulation and data as a percentage difference from the nominal MicroBooNE electric field value of 273.9 V/cm. It is observed that the general features in the electric field distortion map are consistent when comparing that of simulation to that of data but that there is a small downward shift in the electric field magnitude across the entire TPC in data compared to the simulation.

The electric field varies by no more than 10% across the entire TPC with the greatest percentage differences from the nominal electric field value occuring near the cathode, as expected.

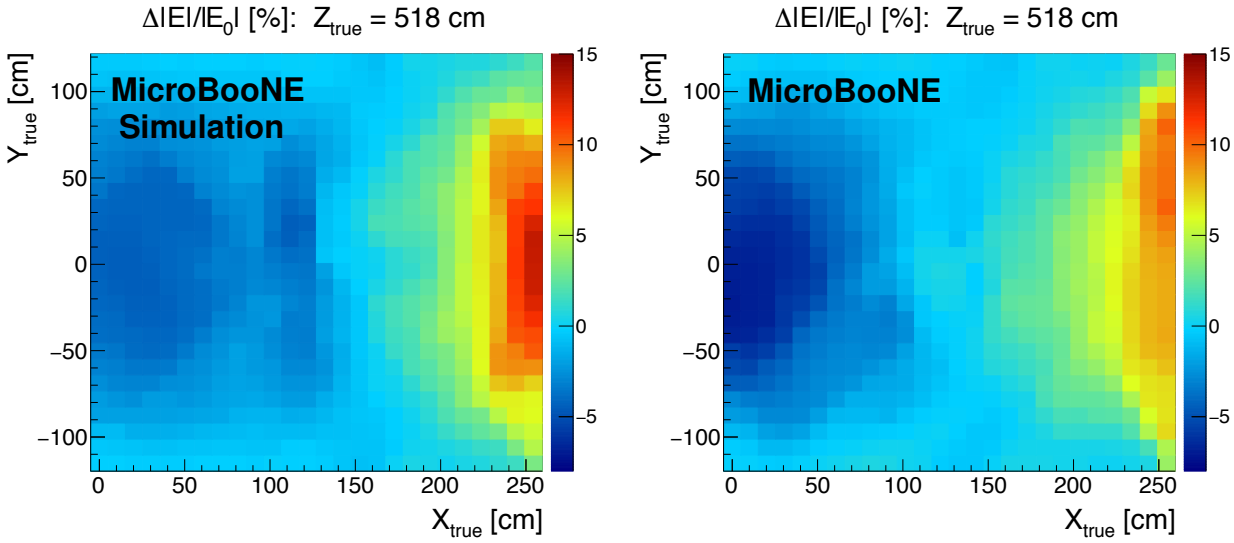

(a) (b)

Figure 7.18: Results of the calculation of the electric field distortion magnitude for a central slice in z, comparing (a) Monte Carlo simulation to (b) data and shown as the percentage change with respect to the nominal MicroBooNE electric field value of 273.9 V/cm.

7.7 Systematic Bias Studies

The results shown in Section 7.6 contain systematic biases which arise from the calibration methodology itself as well as relying on the simulation in the calibration. The laser system is used to derive a data-driven systematic uncertainty on the SCE calibration result. The methodology is described in Section 7.7.1 and the impact on stopping muon dE/dx measurements is presented as a case study in Section 7.7.2.

7.7.1 Systematic Bias Estimation with the Laser System

Used in setting up the systematic uncertainties on the spatial offset calibration are the laser track residuals discussed in Section 7.6.2 due to the role of the laser system providing a secondary handle on the impact of SCE in MicroBooNE data events. The laser track residuals served as an estimator of the bias associated with local spatial offset measurements, which in turn serves as a systematic uncertainty on measurements by using cosmic rays to estimate SCE in the detector. The systematic uncertainty is determined in three dimensions throughout the entire TPC in the following way:

- A loop through all reconstructed laser track points is made, calculating at each point the laser track residual from the three-dimension projection of the reconstructed laser track point to the associated true laser trajectory, defining a three-dimensional vector (the 'projection vector');
- a three-dimensional vector is formed at each reconstructed laser track point using the spatial offset measurements presented in Section 7.6.2, which is rescaled in magnitude so that the component of this vector aligned with the 'projection vector' has the same magnitude as the laser track residual;
- The corrected three-dimensional vector is compared to the original spatial offset vector, with the component-wise differences divided by the original spatial offset vector magnitude resulting in a relative systematic uncertainty for spatial offsets in each of the three dimensions (x, y, and z) at the point in question;
- after the loop over all reconstructed laser track points is complete, another loop through all voxels in the TPC is conducted in order to calculate a systematic uncertainty for spatial offsets in all three dimensions throughout the entire TPC;
- for each voxel in the TPC, another loop through all reconstructed track points is conducted in order to compute a weighted average of relative systematic uncertainties (in each of the three dimensions) for the voxel in question, using weight factors of r^{-2} where r is the distance

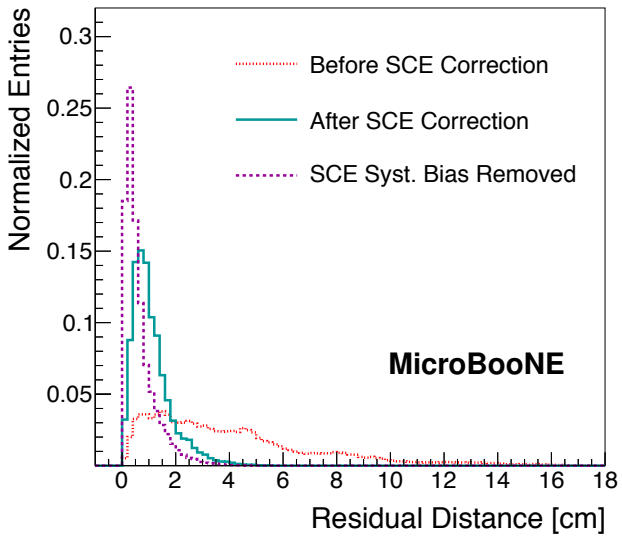

Figure 7.19: Laser track residuals before and after applying the SCE correction, now also shown with the systematic bias from the method removed.

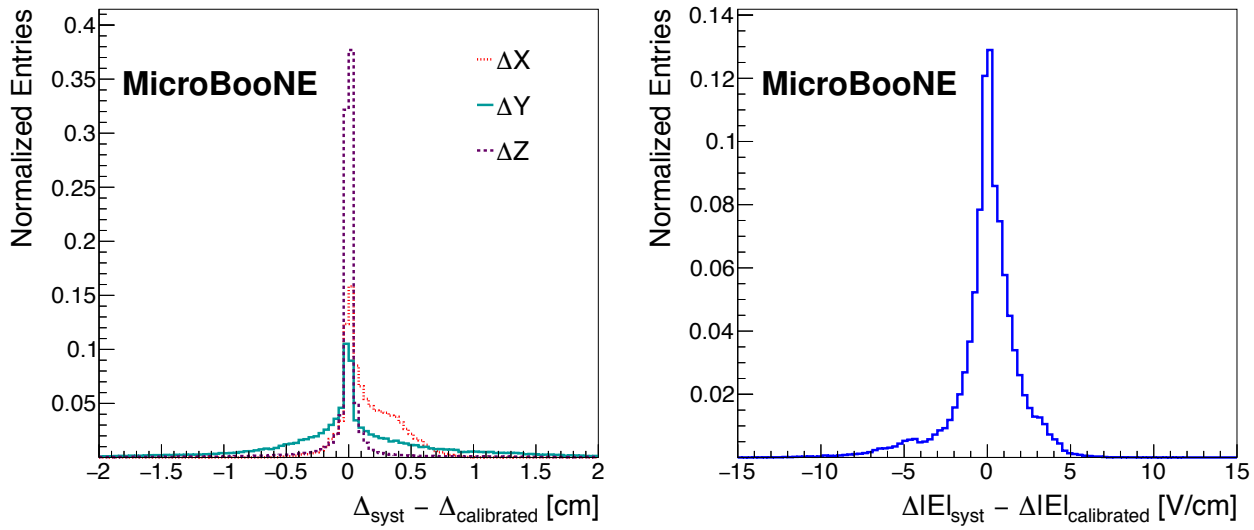

(a) (b)

Figure 7.20: (a) Distribution of systematic bias in the data using the method described in the text; (b) distribution of systematic bias in the electric field offset measurement in data using the same method, in units of V/cm.

between a voxel and a given reconstructed laser track point;

- the distance-weighted relative systematic uncertainty computed in the previous step for each dimension is multiplied by the corresponding spatial offset at that voxel to calculate the absolute systematic uncertainty in the spatial offset measurement; and
- finally, once the loop over all voxels is complete, an absolute systematic uncertainty on the spatial offset measurement is available for all points in the detector for each of the three dimensions.

Because the laser system only has partial coverage throughout the TPC, gaps in coverage are accounted for in the above procedure by extrapolating the calculated relative systematic uncertainties from neighboring regions of the TPC where there is coverage by the laser system, weighted by relative uncertainty.

The systematic uncertainty is an estimated bias which can be corrected on a point-by-point basis throughout the TPC. The results of correcting this bias are shown in Figure 7.19, leading to laser track residuals in data that are much closer to the simulation distribution shown in Figure 7.17. This study is a check to ensure that the calibration is being carried out correctly, as it is expected that the overall magnitude of the laser track residuals decreases given that this information is used in the estimation of the systematic bias. This systematic uncertainty associated with the spatial

offset measurement can be propagated to the electric field calculation as well, which is done by taking the bias-corrected spatial offset map and applying the methodology discussed in Section 7.5.4. The impact of systematic bias with respect to the nominal measurements of spatial offsets and electric field distortions for MicroBooNE data are shown in Figures 7.20 and 7.21 throughout the TPC and in the central z slice of the detector, respectively. These comparisons quantify the performance of the data-driven calibration technique described in Section 7.5.

7.7.2 Impact on Stopping Muon dE/dx Measurements

To capture the impact of SCE on particle energy reconstruction with MicroBooNE, a high-purity selection of contained neutrino-induced stopping muons is utilized. This selection makes use of the following purity-enhancing requirements for the reconstructed muon:

- the reconstructed muon track must be at least 100 cm;
- the length of each reconstructed muon track segment depositing ionization charge on a single TPC wire must be less than 3 cm for all collection plane wires receiving signal from the muon;
- the median measured dE/dx value in the last 10 cm of the reconstructed muon track must be greater than 2.5 MeV/cm; and
- the dE/dx profile of the reconstructed muon track must satisfy $\chi^2_\mu < 4$.

χ^2_μ is calculated by comparing the measured dE/dx profile of the reconstructed muon track to the Bethe-Bloch expectation for a muon in liquid argon using a χ^2 test, normalizing the χ^2 to the number of hits in the reconstructed muon track (which here serves as the number of degrees of freedom in the fit).

The stopping muon dE/dx in the last 100 cm of the reconstructed track, calculated using ionization charge signals from the collection plane, is shown in Figure 7.22 for two data samples: one when the neutrino beam is entering the TPC (an 'on-beam' sample), and another making use of collected events when the neutrino beam was not running (an 'off-beam' sample). In the case of the off-beam sample, the selected muons are cosmic muons, though the selection is performed identically to the case of the on-beam sample. As a result, the off-beam sample is characteristic of cosmogenic background events one would find in studies of CC muon neutrino events at MicroBooNE. The distributions shown in Figure 7.22 demonstrate the high purity of the stopping muon selection, as the energy deposition profile of the selected tracks are largely consistent with that of stopping muons.

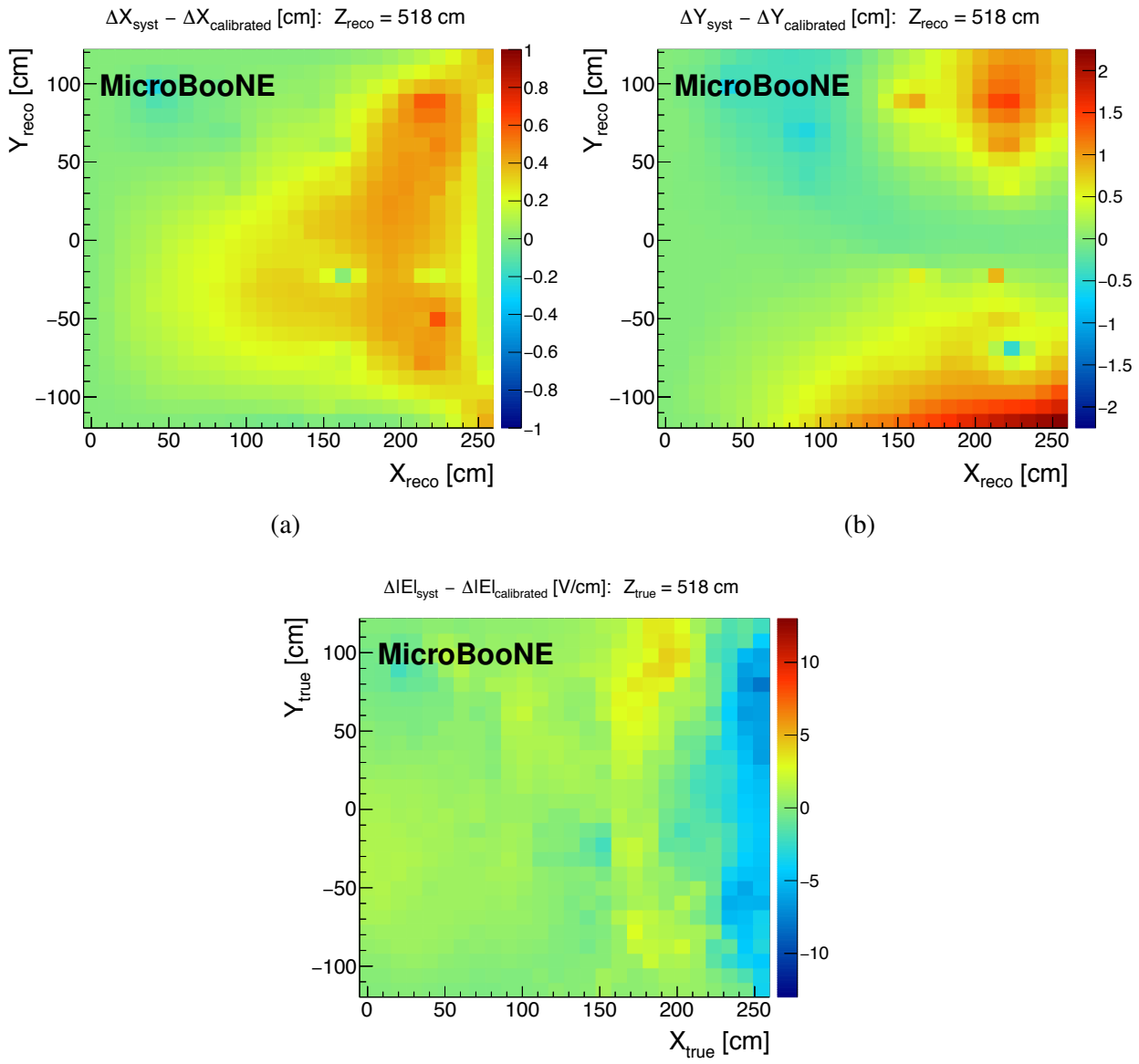

Figure 7.21: Systematic bias in the spatial offset measurement in data using the method described in the text, showing (a) the Δx bias and (b) showing the Δy bias in the x-y plane for the central z slice of the detector; (c) systematic bias in the electric field magnitude offset measurement in data using the same method for the same slice of the detector, in units of V/cm.

Figure 7.23 depicts the effect that an SCE calibration has on stopping muon dE/dx measurements using the collection plane wire signals, including the impact from the systematic bias calculation. Two distinct corrections are applied: the spatial offset correction presented in Section 7.6.2, which accounts for squeezing/stretching of the track and associated bias of the energy deposition per unit length of the reconstructed track, and another correction accounting for variations

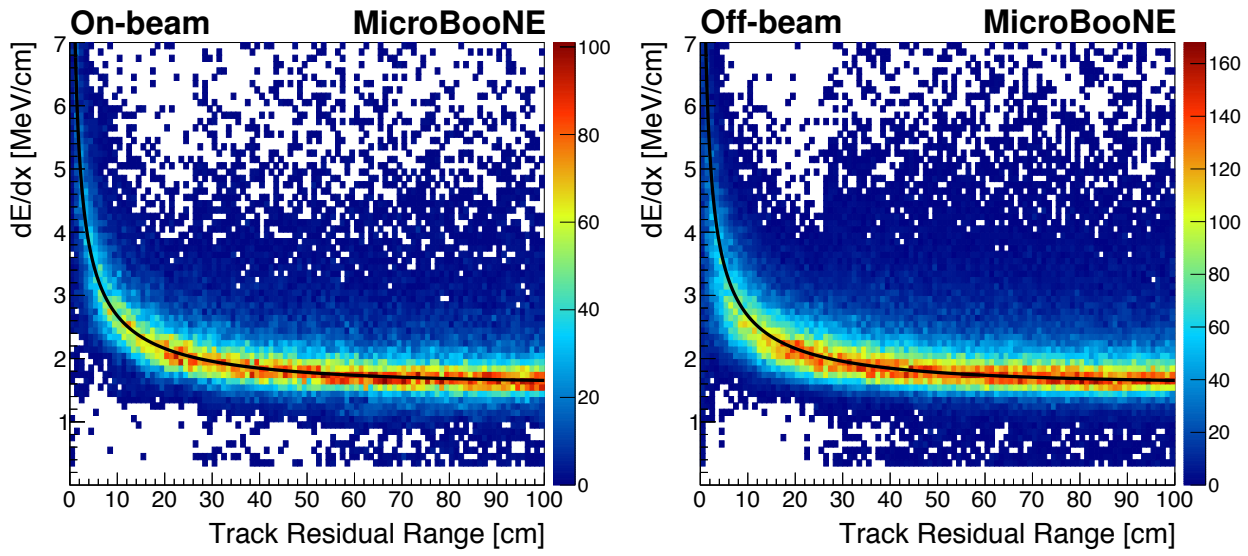

(a) (b)

Figure 7.22: dE/dx as a function of residual range for a pure selection of stopping muons obtained using both (a) on-beam and (b) off-beam events. The dE/dx measurement, shown after application of the SCE dE/dx calibration described in the text, is made using ionization signals from the collection plane of the MicroBooNE TPC. The black curves show the Landau-Vavilov most probable energy loss per unit length associated with a detector thickness of 4.5 mm, the median reconstructed muon track segment length associated with the charge deposition on a single TPC wire.

in electron-ion recombination stemming from electric field distortions changing the local electric field magnitude. The second correction modifies the measured ionization charge at a given point along the reconstructed muon track by a factor that accounts for the electric-field dependence of electron-ion recombination. The recombination correction makes use of the MicroBooNE effective recombination parameters for the modified Box model.

Stopping muons in on-beam events should be less impacted by SCE because they are more likely than not traveling in the direction of the neutrino beam. As a result, they experience less spatial squeezing that shifts dE/dx measurements to larger values (due to dx being smaller on average). Stopping muons in off-beam events are largely downward-going cosmic muons that experience more vertical squeezing in the associated reconstructed track, especially impactful as spatial offsets in the vertical (y) direction are on average largest throughout the MicroBooNE TPC. This suggests that there is an angular dependence of the SCE corrections to dE/dx measurements. Figure 7.23 shows that the nominal SCE dE/dx calibration leads to a shift of 1% (4%) in the mean of the dE/dx distribution for on-beam (off-beam) events. As expected, neutrino-induced stopping muons are less impacted by SCE than cosmogenic stopping muons, primarily a result

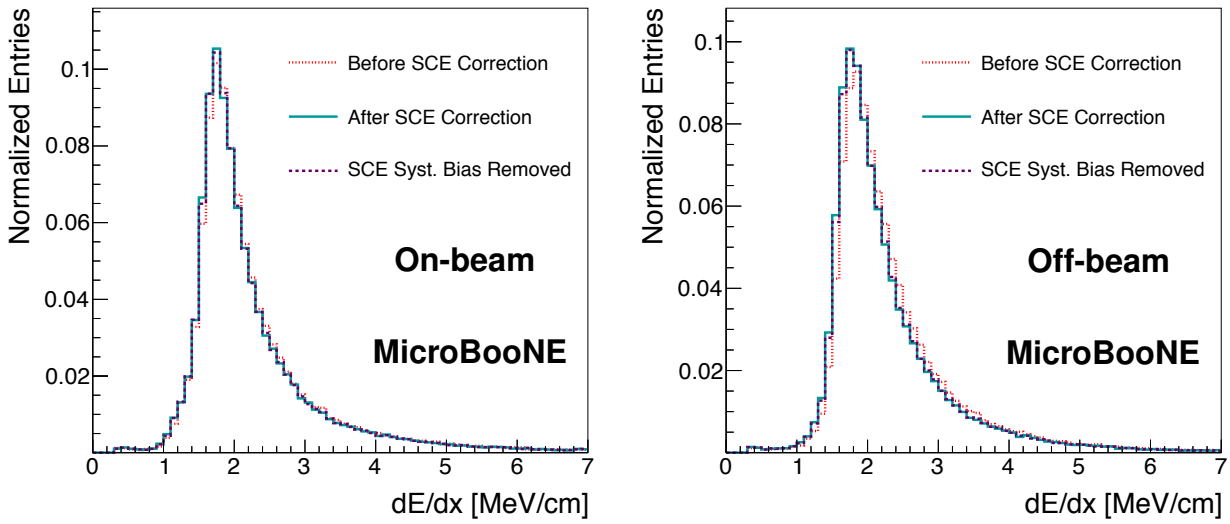

(a) (b)

Figure 7.23: dE/dx distribution for stopping muons in both (a) on-beam and (b) off-beam events, looking both before and after the SCE dE/dx calibration described in the text is applied; these distributions are also shown after accounting for the estimated systematic bias in the measurement.

of different levels of spatial squeezing. The variation in electron-ion recombination throughout the MicroBooNE TPC, due to variation in the electric field magnitude associated with SCE, has a subleading role in biasing dE/dx measurements. As shown in Figure 7.23, the mean dE/dx shift associated with the systematic bias in the SCE dE/dx calibration is much smaller: 0.1% (0.4%) for on-beam (off-beam) events, or one-tenth of the overall systematic dE/dx bias associated with SCE.

7.8 Time-Dependence Study

Another study was carried out to determine if there is significant time-dependence of SCE in MicroBooNE. This is important to the calibration, because unless the calibration is performed frequently with respect to the rate at which underlying changes to the SCE configuration occur, this uncertainty will serve as the lower bound on the level of precision possible with any calibration technique.

Spatial distortions at the faces of the TPC are studied using the entry and exit points of t_0-tagged cosmic ray muon tracks. Because the correction vector is dominated by the variable that is orthogonal to the TPC face, this is the variable that is used here to study time-dependence effects. Only about one hundred tracks are needed to estimate the magnitude of this effect within a relatively small region (roughly 1 m^2) on a TPC face. Four different spots in the TPC are probed

in this way: two at the top face of the TPC and two at the bottom face of the TPC, with different locations in the z direction in both cases, looking at average measured value of the Δy spatial offset from the TPC face in all cases. The study is carried out using off-beam MicroBooNE data collected between February 2016 and September 2018.

The results of the time-dependence study are shown in Figure 7.24; these measurements take into account the 4.5 cm average offset between the field cage and the instrumented TPC volume, described in Section 7.5.1. It is observed that the magnitude of spatial offsets at each of the four probed regions in the TPC varies by no more than 4% over time relative to the total magnitude of

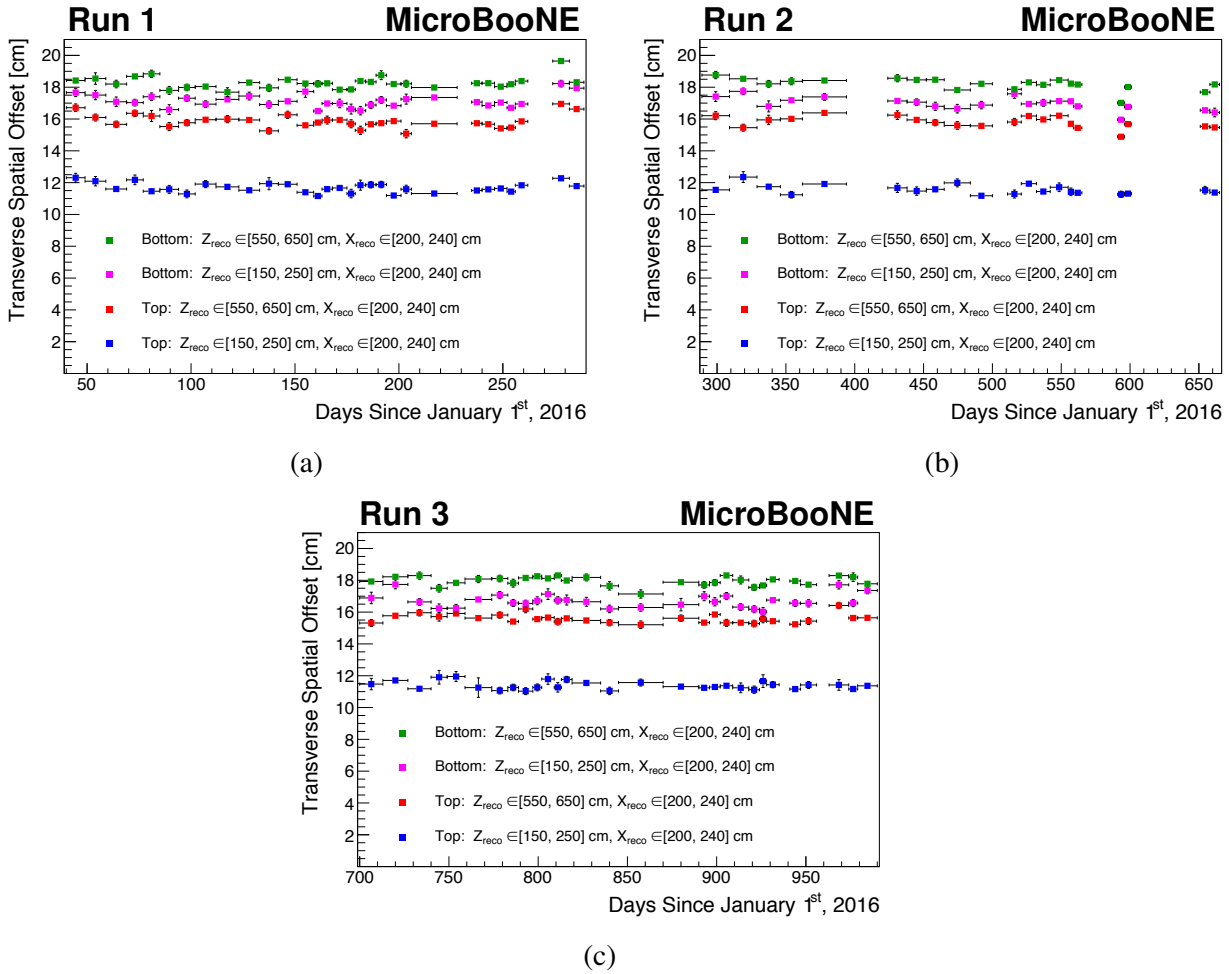

Figure 7.24: Time-dependence of SCE in the MicroBooNE detector; shown are transverse spatial offsets (Δy in this case) at the top and bottom of the detector near two different values of z: one near the upstream part of the detector and another closer to the center of the detector in the beam direction. Distributions are shown for three different time periods: (a) Run 1, (b) Run 2, (c) Run 3, measured in days since January 1^{st}, 2016. Gaps in time are due to detector maintenance. The overall level of variation in spatial offsets is less than 4% across the entire data-taking period.

the effect. An overall decrease in the magnitude of the spatial offsets is also observed over time, included as part of the 4% variation. It is expected that seasonal variations in the cosmic muon rate (which is proportional to the amount of space charge deposited in the detector) should account for no more than 1% of this variation over time, bounded by measurements of seasonal cosmic muon rate variations at the MINOS near detector and noting that the variation should be smaller at the surface, where MicroBooNE operates, due to the lower average cosmic muon energy. One possible explanation for the larger time-dependence of SCE in the detector than expected from seasonal variations in the cosmic muon rate is potential impact from shifting liquid argon flow patterns in the cryostat. This may lead to a change in the space charge configuration in the detector, resulting in temporal variations in observed SCE.

Given the observed long-term time-dependence of SCE, it is reasonable to target a level of precision of roughly 5% or better with respect to measurement of spatial offsets, which is demonstrated to be the case for the methodology discussed in Section 7.5 within the majority of the MicroBooNE TPC, as shown in Section 7.7. In principle, it is possible to improve the accuracy of the SCE calibration by performing the full calibration at different points in time, applying different calibrations to different time periods of the total collected dataset. No study of short-term variations (less than a day) of SCE over time is presented in this chapter, as it is difficult to do with any reasonable precision using cosmic muons given the relatively small cosmic sample available on such timescales. For timescales much shorter than a day, the laser system at MicroBooNE is better equipped to study the time-dependence of SCE. However, techniques using cosmic muons, such as those discussed in this chapter, allow for continuous long-term monitoring of SCE in LArTPC detectors without interrupting data-taking.

7.9 Conclusion

Cosmic muon tracks reconstructed in the MicroBooNE TPC have been shown to be particularly useful in measuring spatial distortions due to underlying electric field non-uniformities throughout the detector. By comparing the results of a data-driven calibration method making use of cosmic tracks with predictions from a dedicated simulation of SCE in the detector, it is shown that the spatial distortions observed in MicroBooNE data are similar in nature to those that would arise from the presence of SCE in the detector. However, the features of the spatial distortion map differ in detail from the predictions of a simulation. This captures the necessity of using a data-driven calibration procedure, such as the one presented here, at large LArTPC detectors (like MicroBooNE) operating near the surface in order to correct for these effects, which can impact the reconstruction of particle trajectories and measured ionization charge per unit length.

Spatial offsets in reconstructed particle trajectories as large as 15 cm have been observed in

MicroBooNE data, associated with underlying electric field distortions as large as 10% with respect to the nominal MicroBooNE electric field of 273.9 V/cm. The calibration methodology presented in this chapter is shown to significantly improve the estimation of particle trajectories, studied in MicroBooNE data using measured track residuals as associated with laser tracks from the laser system before and after the SCE calibration is applied. A data-driven determination of systematic uncertainty on the measurement is also derived by using these laser track residuals, consistent with a spatial smearing of 4 mm after the calibration is applied. The associated uncertainty on the calculated underlying electric field is less than 1% of the nominal MicroBooNE electric field, or 10% of the electric field distortion arising due to SCE in the TPC. The impact of SCE on reconstructed muon dE/dx measurements in the detector varies from 1% to 4%, heavily dependent on the angle of the reconstructed muon tracks, with a relative residual uncertainty of one-tenth of the systematic effect after the SCE dE/dx calibration is carried out. Long-term temporal variations in the underlying space charge profile on the order of 4% have been observed, which cannot be explained by seasonal variation in the cosmic muon rate at MicroBooNE. It is possible that the flow of liquid argon in the detector is responsible for these variations over time.

These calibration methods, developed at MicroBooNE, are forseen to be useful to other running and future large LArTPC detectors. This includes the single-phase and dual-phase ProtoDUNE detectors as well as SBND and ICARUS. While the single-phase far detector and LArTPC near detector of DUNE are expected to experience negligible SCE due to being located deep underground and having a TPC with a short ionization drift length (0.5 m), respectively, the dual-phase far detector of DUNE will have such a long ionization drift length (12 m) that it may still see significant SCE due to positive ion build-up from $^{39}\mathrm{Ar}$ beta decays. The work presented in this chapter should provide a useful starting point for additional study in all of these other experiments.

CHAPTER 8

Isolating Low-Energy Neutrino Interactions

8.1 Introduction

MicroBooNE is capable of producing numerous measurements in both oscillations and cross section physics, yet few of those measurements specifically probe regions of parameter space where low-energy neutrinos dominate. One set of examples, the low-energy excess analyses, rely on measurements of electron neutrino-like interactions in the energy region < 600 MeV to achieve its goals. Few measurements exist in that energy regime, and the ones that do are quite valuable for constraining cross section systematics and informing nuclear physics models. This is the first reason why the measurement of the Kaon Decay-At-Rest (KDAR) muon neutrino differential cross section is such a valuable contribution to the particle physics community. The second reason is that the KDAR neutrino serves as the world's first low-energy, weak interaction-only probe of the nucleus [51]. Finally, the KDAR differential cross section measurement serves as a benchmark of neutrino energy reconstruction. That measurement serves as the motivation for the techniques presented in this chapter.

8.2 Motivation

8.2.1 Cross Section Benchmark

Knowledge of an underlying cross section is important to constrain systematics in neutrino oscillation experiments. Particularly, in experiments studying oscillations, ν_μ is typically used as the signal channel for the disappearance measurement and also as a means of constraining the predictions for the ν_e appearance channel. Knowledge of the cross section is important in these experiments, because the near detector and the far detector inherently are exposed to different neutrino fluxes due to their distance from the neutrino source. While the near detector is subject to neutrinos with

a variety of energies and angles of incidence, the far detector essentially sees a point source of neutrinos with more uniform energy and angle of incidence. Further, systematic differences between the near and far detector, such as size or detection technology, would make rendering an event rate comparison even more difficult. Therefore, the cross section must be known in order to limit the impact these systematic effects have on an oscillation measurement. Examples of current and future experiments that could make use of this cross section are T2K, NOνA, and DUNE.

A measurement of the KDAR cross section will also be useful for MicroBooNE in its capacity as a map between reconstructed neutrino energy and true neutrino energy, relied on by all analyses. The nature of the two-body decay means that the energy of the KDAR muon neutrino is known exactly to be 236 MeV, so measurements of events deemed to be KDAR neutrinos from the NuMI dump can be compared to this value to benchmark neutrino energy reconstruction, which has never been done before with a known-energy neutrino. Neutrino energy is difficult to reconstruct, with the uncertainty on reconstructed energy typically $> 20\%$ at relevant energies (200 MeV - 5 GeV). This metric is particularly useful for MicroBooNE's purposes, because 236 MeV falls in the energy range of the LEE (200 - 475 MeV). For this to use to be realized, neutrino energy must be removed from the analysis selection to avoid a circular measurement. It is included in the studies presented in this chapter to optimize the signal-to-background ratio.

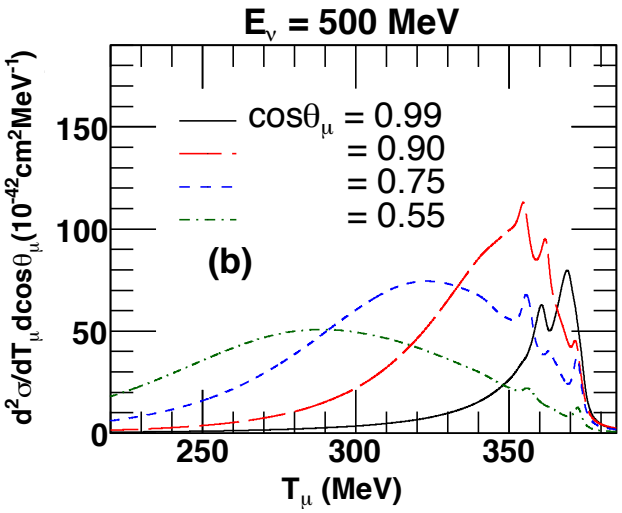

Figure 8.1: A plot of the double differential cross section with respect to muon kinetic energy, T_μ, and muon scattering angle, θ_μ, as a function of muon kinetic energy for E_ν = 500 MeV and several values of θ_μ. The peaks shown for $\mathrm{T}_\mu \geq 350$ MeV represent excitations of the ^{12}C nucleus [17].

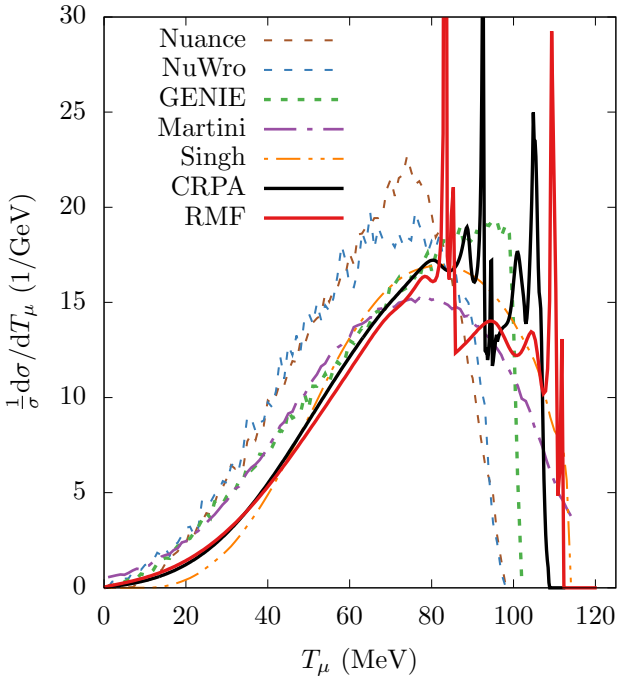

Figure 8.2: A plot showing the prediction for the KDAR shape-only differential cross section in terms of muon kinetic energy for neutrino-carbon scattering [18].

8.2.2 Nuclear Probe

As noted earlier, the KDAR neutrino will serve as the world's first-ever known-energy, weak-interaction-only probe of the nucleus. The energy of the KDAR neutrinos is right between two different regimes in nuclear physics: the neutrino-on-nucleus model and the neutrino-on-nucleon model. At lower energies than 236 MeV, the 'impulse approximation', which assumes that the neutrino interacts with only one nucleon, breaks down. A measurement of the KDAR neutrino cross section will shed light on this regime.

Comparing the KDAR measurement's result for the double differential cross section with respect to muon scattering angle and muon kinetic energy to an identical plot generated by theoretical models can help to confirm or deny those models. Figure 8.1 shows this quantity for ^{12}C in the reaction $\nu_\mu + ^{12}\mathrm{C} \longrightarrow \mu^- + \mathrm{X}$ in which X is an unobserved hadronic final state. This will be the same measurement, but with ^{40}Ar [17].

Nuclear models also differ significantly with respect to their interpretation of the differential cross section of neutrino scattering with respect to quantities related to the muon. Figure 8.2 shows the prediction for the KDAR shape-only differential cross section in terms of muon kinetic energy for neutrino-carbon scattering [18]. With results of the differential KDAR cross section, this measurement with 236 MeV ν_μ charged current events (the signature KDAR energy) with ^{40}Ar

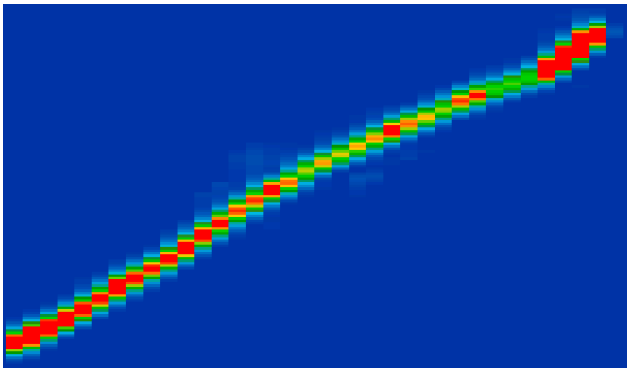

Figure 8.3: A sample collection plane event display from simulation for a KDAR ν_μ CC event. This event exhibits the topology of many of those events: a long muon track of length 13.8 cm with several highly ionizing hits belonging to a proton at the start of the track (at the top righthand corner of the image).

can be replicated.

8.3 Overlay Samples

All of the simulated samples that are used in this chapter and in Chapter 9 are formed by overlaying a true neutrino on a cosmic background (called 'overlay samples'). This is done because the cosmic backgrounds can be predicted perfectly by the off-beam data.

8.4 Signal Definition

In this analysis, the signal is defined as low-energy ν_μ CC events which originate from a kaon parent at the NuMI beam dump. According to NuWro, it is expected that there will be 971 such events in the MicroBooNE active volume for 8.3×10^{20} POT at a neutrino cross section of 1.25×10^{-39} cm^2/neutron at a neutrino energy of 236 MeV. GENIE v3, the neutrino event generator used by the MicroBooNE collaboration, predicts ~30% fewer events than that.

An example collection plane event display from simulation is shown in Figure 8.3. This event display is a typical KDAR ν_μ charged-current topology: a muon track with a short proton at its start (located in the top righthand corner of the image). The relative length of the muon track compared to the proton track is information that is taken advantage of when selecting the muon candidate and reconstructing the energy and direction of the neutrino, presented in Section 8.6.

8.5 Dataset

The total amount of POT used in this analysis, 8.3×10^{20} POT, is split between Run 3b and Run 4 of MicroBooNE data. The breakdown in the amount of POT collected for each epoch is shown in Table 8.5. All of the plots in this chapter are generated using only Run 3b data. Run 3b differs from the first portion of Run 3, Run 3a, in that the CRT was fully operational for all data taken during that epoch.

Dataset	Amount of POT
Run 3b	5.2×10^{20}
Run 4	3.1×10^{20}

The reason for restricting the analysis to these two datasets is that both consist only of antineutrino mode data and use a fully operational CRT. Antineutrino mode is exclusively used because, while KDAR events are present in the dataset in both cases, the total neutrino cross section is less than for neutrino mode, meaning that the backgrounds are ~13% lower than they are for neutrino mode for the part of the neutrino energy spectrum that is most likely to be considered signal (30 MeV - 1 GeV). A functional CRT is needed to reject cosmic rays at the expense of very little signal, which is necessary in the selection in which there are not many signal events to begin with.

8.6 Reconstruction

For use in the KDAR neutrino selection, three tools were developed to reconstruct event quantities independent of the Pandora framework: muon candidate direction, neutrino energy, and neutrino direction. They rely on Pandora to select the part of the event in which the neutrino interacts, a collection of tracks known as the 'neutrino slice' (described in more detail in Section 4.6). The existing tools were designed for higher-energy topologies and performed far worse at lower neutrino energies ($<$ 500 MeV) than they do at higher energies.

8.6.1 Muon Candidate Direction Reconstruction

To reconstruct neutrino direction, calorimetry information of the track is used. This procedure is carried out after the muon candidate is identified, which is done by selecting the longest track associated to the neutrino slice. This procedure picks out the correct muon candidate 97% of the time when comparing to truth information. The tool proceeds in the following manner:

- Use the calorimetry info on a plane if there are more than 20 calorimetry points available.

- Find the median dE/dx value of all the calorimetry points on the plane selected.
- Find the standard deviation on this median using all of the other calorimetry points.
- Remove the points that differ by more than two standard deviations from the median.
- Fit the calorimetry points to a line in both directions. The direction with the greater slope has the vertex at the start.
- Repeat this for all three planes. The direction which is reconstructed for at least two of the planes is chosen as the muon direction. Only planes that have at least 20 calorimetry points are considered in orienting the track to ensure that there is enough information on a plane to reconstruct the direction.

The vertex is placed at the start of the muon track, reconstructed according to this procedure. The tool works with 81% accuracy. Typically the types of events it fails on are those with Landau fluctuations in the calorimetry of points along the track and fewer (< 20) than typical points on the track on one or more planes.

8.6.2 Neutrino Energy Reconstruction

Because the signal for this analysis is monoenergetic, an algorithm was developed to reconstruct the energy of the candidate events in the analysis. Its procedure takes advantage of the typical topology of a KDAR candidate event: a long muon track with a set of highly ionizing proton hits at the start. The specific set of steps used to reconstruct the energy of a neutrino candidate are the following:

- Reconstruct the kinetic energy of the track by using range with the track under the muon assumption using the technique described in Section 2.3.1.
- Look for other tracks that originate within 3 cm of the reconstructed vertex found using the procedure outline in Section 8.6.1. Reconstruct the kinetic energy of these tracks by using range with the track under the proton assumption using the technique described in Section 2.3.1.
- If no track is found in the previous step, then associate high-charge points of charge on each of the three planes close to the vertex with the proton. Include both calorimetry points (points on the reconstructed tracks) and hits close to the vertex in this categorization.
- Fit the points to a 3D line using their coordinates. To obtain coordinates from a 2D hit on one of the planes, match hits across two of the planes.

- Reconstruct the kinetic energy of the track formed by the 3D fit by using range with the track under the proton assumption using the technique described in Section 2.3.1.
- Add the muon kinetic energy and the proton kinetic energy together and add values of 40 MeV for the binding energy of the argon nucleus and 105.7 MeV for the mass of the muon.

8.6.3 Neutrino Direction Reconstruction

The direction of a KDAR neutrino is calculated as the 3D cosine of the angle between the vector pointing from the NuMI beam dump to MicroBooNE and the reconstructed neutrino direction vector. The equation used to find this for two vectors $\overrightarrow{\mathrm{A}}$ and $\overrightarrow{\mathrm{B}}$ is the following:

$$\cos(\theta) = \frac{\overrightarrow{\mathrm{A}} \cdot \overrightarrow{\mathrm{B}}}{\mid \overrightarrow{\mathrm{A}} \mid\mid \overrightarrow{\mathrm{B}} \mid} \tag{8.1}$$

It is found through the following procedure:

- If there is a reconstructed track other than the muon candidate found to originate within 3 cm of the vertex, then skip the next two bullets and orient the track according to its direction with respect to the vertex.
- On each plane, look for high-charge hits (not necessarily associated with the track) in the vicinity of the closest hit to the vertex. Determine the direction in which high-charge hits emanate from the vertex and match the hits across two planes to determine the direction of the proton track.
- Reconstruct the proton track as a 3D line as described in the procedure for reconstructing neutrino energy and use its three components with the directions found in the manner described in the previous bullet.
- Calculate the muon and proton momentum components by multiplying the total momentum by the normalized component of the direction that it traveled in each Cartesian dimension for each track separately. Add them together, forming the reconstructed neutrino direction vector.
- Use Equation 8.1 to find the 3D cosine between the vector pointing from the NuMI beam dump to MicroBooNE and the reconstructed neutrino direction vector.

8.7 Binary Cut Selection

Although there are, relatively speaking, not very many KDAR neutrinos in the dataset under consideration (according to NuWro, 971 such events in the MicroBooNE active volume for 8.3×10^{20} POT at a neutrino cross section of 1.25×10^{-39} cm^2/neutron at a neutrino energy of 236 MeV out of millions on-beam events recorded), the tradeoff is that the signal is quite distinct in terms of the light, charge, and higher-level reconstructed objects that can be calculated from those quantities. As a result, the signal-to-background ratio can be improved drastically by using hard cuts on flash, track, and CRT quantities in the event before employing the machine learning techniques described in Section 8.8. The cuts are chosen to take advantage of physical and reconstruction limits and are intended to be as model-independent as possible.

There are two cuts taken with respect to the CRT. Both rely on the fact that KDAR events are short in extent (the muon track can have a maximum length of ~40 cm) and as such are unlikely to pierce a face of the TPC. One cut, called the 'CRT veto', requires there to be a minimum amount of time, ± 1 μs, between when a flash of light is reconstructed in the beamgate and a CRT hit above an ADC threshold is recorded in one of the CRT panels. The second cut, named the 'CRT distance' cut, requires a minimum distance of 15 cm between a track associated to a CRT hit and the reconstructed neutrino vertex. If either one of these requirements is not met, then it is very likely that the event was either triggered by cosmogenic activity or the neutrino slice is cosmic.

The only hard cut taken with respect to the PMT system is the requirement that the reconstructed flash have a number of photoelectrons in the range [50 PEs, 2000 PEs]. The upper and lower limits are determined by the maximum and minimum amount of PEs that a KDAR neutrino typically induces in the PMTs, respectively.

There is required to be a neutrino slice reconstructed by Pandora in the event which has at least one track associated to it, called the 'neutrino slice' cut. Without it, there is no way to know where in the event the neutrino-induced tracks are located. If there is no track associated to the neutrino slice, then pandora did not reconstruct the slice as belonging to a muon neutrino interaction, which means that it must be cut from the analysis.

There are cuts on containment and the fiducial volume. Containment, which as stated previously is meant to leverage the fact that few KDAR events have outgoing tracks that pierce the boundaries of the detector, requires that no track in the neutrino slice come within 3 cm of a detector boundary after being SCE-corrected, meaning that the distorted track points are placed where they would be located in the absence of SCE. The fiducial volume requirement is meant to eliminate events with cosmic muons, which enter the detector from the outside, and to eliminate from consideration regions of the detector where track distortions due to SCE are largest (close to the boundaries). No reconstructed neutrino vertex can be within 20 cm of any TPC face.

Proton Candidate Track Length [cm]	Muon Candidate Track Length [cm]
1.0	36.0
2.0	28.0
3.0	24.0
4.0	20.0
5.0	11.0
6.0	8.0
7.0	7.0
11.0	-

Table 8.1: A table containing the greatest length that the muon candidate track (the longest track) and the proton candidate track (the second-longest track emanating from the vertex) can have.

The requirements on the tracks are meant to eliminate both impossible topologies which have tracks that are too long and also remove events with track multiplicities that are highly unlikely. No event can have tracks originating from the vertex which sum to > 40 cm, because that would mean that the incoming neutrino had more than 236 MeV of energy. There is also a set of cuts, contained in Table 8.1, which shows the maximum lengths that the muon candidate track and the proton candidate track in a neutrino slice can have. This regime operates under the assumption that the longest track in the neutrino slice is a muon and the second longest track emanating from the vertex is a proton. The percentage of events with two or more tracks emanating from the vertex in which this assumption is not true is rare (~3% of events).

The track multiplicity cut takes advantage of the fact that most KDAR neutrino events consist of, at most, a long muon track, a short proton track, and a Michel electron reconstructed as a track. Most topologies, however, only have one or two tracks, something that can be worked into a selection cut. Because of this, it is required that there be no more than 3 tracks associated to the

Binary Selection Cuts (In Order)
CRT Veto
Flash PE Cut
Neutrino Slice Cut
Fiducial Volume Cut
Track Quality Cuts
Track Multiplicity Cuts
Track Length Cuts
Containment
CRT Distance Cut

Table 8.2: A table containing the binary cuts used in the NuMI KDAR analysis.

neutrino slice and no more than two tracks originating from the vertex.

Finally, there are requirements on the standard deviation of the distance between a track spacepoint and its associated hit and on the fraction of spacepoints with associated hits, called the 'track quality' cuts. These are intended to discard background events, showers which are mistakenly reconstructed as tracks. All of the binary selection cuts are shown in Table 8.2 in the order in which they are applied.

8.8 BDT Selection

In order to further separate signal from background, a Boosted Decision Tree (BDT) is used. This technology combines a series of weakly performing decision trees into one that performs strongly, a technique which is called 'gradient boosting'. The BDT works by taking as input the distributions of signal and background for a set of variables, which it uses to create the strongly performing tree. This tree provides a score in the range [-1,1] for input events, with a lower score corresponding to an event that is more likely to be background and a higher score corresponding to one that is more likely to be signal. A total of 26 variables are fed into the BDT, chosen according to how effectively they assist the BDT in distinguishing signal from background.

Reconstructed neutrino energy and direction, described in Sections 8.6.2 and 8.6.3, are included in the BDT, because they are characteristics that distinguish KDAR neutrinos originating from the NuMI dump from others.

The reconstructed vertex coordinates are included, because KDAR neutrinos are biased to high x and z with respect to cosmic rays, while cosmic rays are biased to higher y because most of them are downwards-going.

The absolute values of the muon's momentum components are included, because cosmic rays typically have larger y components of momentum than KDAR neutrino-induced events and, correspondingly, smaller x and z components.

The difference between the vertex y (z) and the flash's weighted y (z) is included. This difference for z is lesser for KDAR events than it is for cosmic and neutrino background events, and the y difference is biased to higher values for cosmic events than it is for KDAR events.

The truncated mean dQ/dx is included for each plane and as a three-plane sum are fed into the BDT. This is meant to eliminate background NC events, which have a muon candidate that is actually a proton. Therefore, their values of these quantities tend to be higher.

The sum of the neutrino slice associated hits and the three-plane sum are used as well. These variables capture the same difference with NC events that was described in the last paragraph as well as capturing differences with reconstructed hits belonging to cosmic-induced muons.

The difference between the ADC sum of the hits in the vertex vicinity and the neutrino slice

Variables Used in BDT
Neutrino Energy
Neutrino Direction
Vertex Coordinates: x, y, z
Absolute Value of Muon Direction Cosine: x, y, z
Difference Between Vertex y/z and Flash y/z
Truncated Mean dQ/dx For Each Plane Three-Plane Sum
ADC Sum of Neutrino Slice Track Associated Hits For Each Plane Three-Plane Sum
Difference in ADCs Between Hits in Vertex Vicinity and Neutrino Slice-Associated Hits For Each Plane Three-Plane Sum
Number of Hits in Vertex Vicinity For Each Plane Three-Plane Sum

Table 8.3: A table containing the variables fed into the BDT in the NuMI KDAR analysis.

associated hits for all three planes and a three-plane sum eliminate poorly reconstructed, higher-energy background events. These capture charge that is deposited in the vicinity of the reconstruced vertex that is not associated to the neutrino slice, important if a higher-energy background neutrino interaction passes the binary cut selection.

The number of hits in the vertex vicinity and the three-plane sum is just the unweighted form of the quantity used in the difference described two paragraphs prior. It serves the same purpose but does not include the ADC sum of the hits in calculating these quantities.

Table 8.3 includes all of the quantities that are used in the BDT.

8.9 Track Length Sideband Region

There are two sideband regions for this analysis. First, one is generated by turning off the track length cuts in the binary selection cut stage (sum of track lengths $<$ 40 cm and two-track length selection) and requiring that the muon candidate (the longest track associated to the neutrino slice) has a length of at least 50 cm. This completely blinds the signal region because no KDAR neutrino would induce a track of length as great or greater than 50 cm and allows for the study of data-simulation agreement in this region. The second sideband region involves results from the BDT and is discussed in Section 8.12.

The results for the sideband region are shown for the track length in Figure 8.4 for the muon candidate track length, in Figure 8.5 for the Y plane truncated dQ/dx, and in Figure 8.6 for the

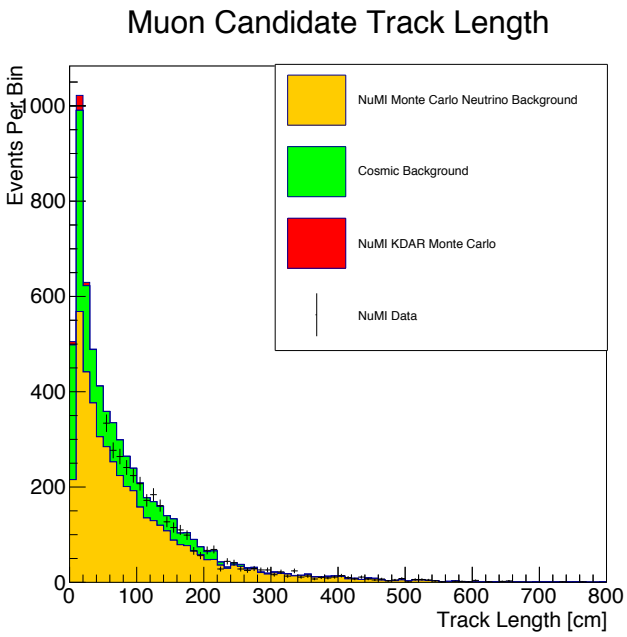

Figure 8.4: Muon candidate track length with the track length cuts turned off and a $>$ 50 cm requirement on the muon candidate for the data sample. In the two other plots in this section, the $>$ 50 cm muon candidate length requirement is applied to the samples. The error bars correspond to the statistical uncertainty only.

PEs of the in-time flash. Figure 8.6 is the only one for which agreement is not close, and this can be almost fully explained by including the light yield, attenuation, and Rayleigh length systematic samples in generating the stacked histogram. Also, artificially decreasing the light yield by 40% causes a greater amount of agreement than what is currently seen.

8.10 Binary Selection Cut Results

The results of the binary cut selection are shown in Table 8.4 in terms of the percentage of each sample left after enacting each of the cuts in the order presented. The first row shows 100% for each of the samples to indicate that none of the events have been removed before the first cut. The KDAR events are affected particularly strongly by the neutrino slice requirement, which is one of the outputs of the pandora reconstruction framework. The NuMI EXT events are almost entirely removed by the flash and neutrino slice requirements. Most of the cuts in the second half of the table are aimed at removing higher-energy neutrino background events with more complex topologies (i.e., more tracks) so that the BDT can take as input events that can possibly be a KDAR event given physical and reconstruction limits. The NuMI On-Beam data most closely resembles the NuMI EXT sample, because the majority of the On-Beam sample is cosmic itself. The number

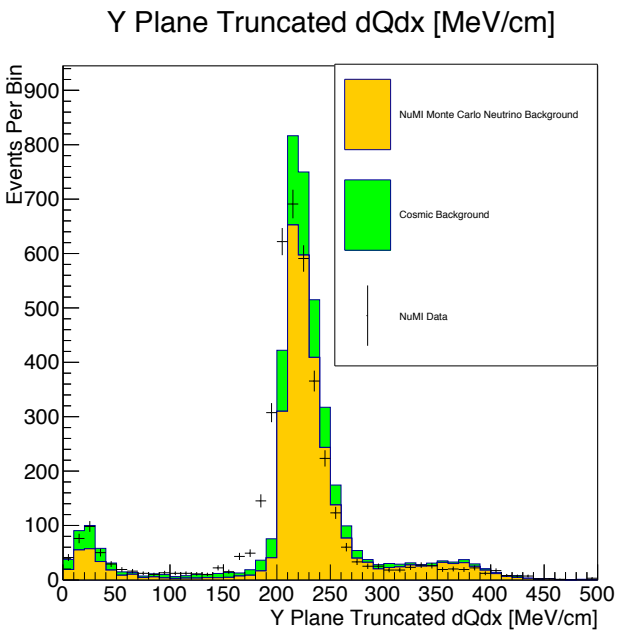

Figure 8.5: The Y plane truncated mean dQ/dx for the muon track length sideband sample. Other than a slight offset between the data points and the stacked histograms, agreement is quite good. The error bars correspond to the statistical uncertainty only.

of surviving events shown in the bottom row is normalized to 2.05×10^{20} POT, which is 24.6% of the POT in the entire dataset. These events constitute a signal-to-background ratio of 1:44.

8.11 BDT Selection Results

The BDT selection takes advantages of shape differences between the signal and background in the variables described in Section 8.8 to further improve the signal-to-background ratio. The BDT score cut distribution is shown in Figure 8.7. The low-score region of the plot is background-enhanced and the high-score region of the plot is signal-enhanced. There is an excess of events observed in the high-score region of the plot, exactly where KDAR events are expected to be observed. The background rejection as a function of signal efficiency for the BDT is shown in Figure 8.8. Table 8.5 displays the numbers of signal and background events passing a number of BDT score cuts. The first row shows 100% for each of the samples to indicate that none of the events have been removed before the first cut. This only considers events passing the binary cut selection in the BDT.

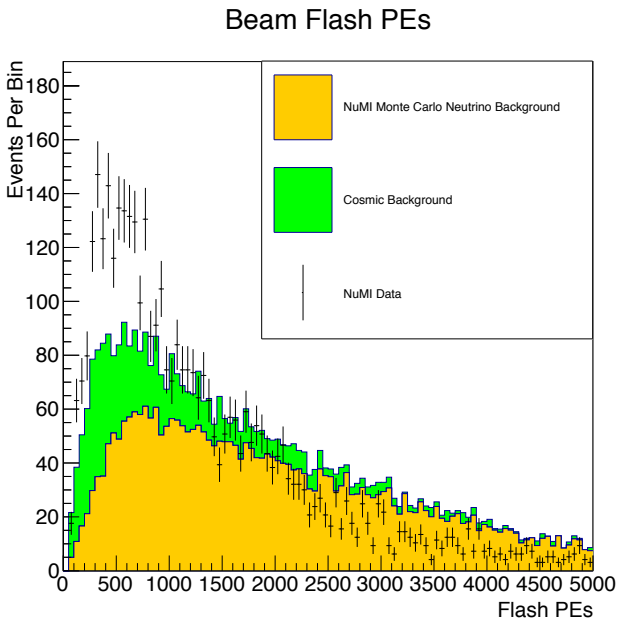

Figure 8.6: The beam flash PEs for the muon track length sideband sample. This is the only sideband of all of the quantities being fed into the BDT for which agreement is not close. This can be almost fully explained by including the light yield, attenuation, and Rayleigh length systematic samples in generating the stacked histogram. Artificially decreasing the light yield by 40% also causes the two distributions to agree much better. The error bars correspond to the statistical uncertainty only.

8.12 BDT Sideband Region

With the BDT score distribution presented in Section 8.11, the background-enhanced region allows for another set of sideband comparisons. This region offers the opportunity for sideband comparisons for neutrino energy and neutrino direction (in the form of the 3D cosine of the angle between the vector pointing from the NuMI beam dump to MicroBooNE and the reconstructed neutrino direction vector) because the algorithms are designed for events passing the binary selection cuts. Figures 8.9, 8.10, and 8.11 show the values of neutrino energy, neutrino direction, and muon candidate track length for this region, respectively. The agreement is quite good for all of them.

8.13 Output Variable Distributions From BDT Selection

The output variable distributions for neutrino energy, neutrino direction, and muon candidate track length are shown for a BDT score cut value of 0.5 in Figures 8.12, 8.13, and 8.14, respectively.

Cut/Sample	KDAR	Background	Off-Beam	On-Beam
No Cut	100%	100%	100%	100%
CRT Veto	94.9%	77.9%	68.8%	67.6%
Flash Cut	88.4%	40.2%	17.0%	21.7%
No Neutrino Slice	39.9%	14.9%	2.6%	4.9%
Fiducial Volume	32.8%	13.7%	2.3%	4.4%
> 0 Tracks in Neutrino Slice	32.3%	13.5%	2.2%	4.4%
Track Quality	31.8%	13.3%	2.2%	4.2%
Two-Track Length Cut	31.1%	13.1%	2.2%	4.2%
Containment	25.5%	4.3%	0.5%	1.2%
Track Lengths From Vertex	24.5%	2.1%	0.3%	0.7%
Sum of Track Lengths	24.5%	2.1%	0.3%	0.7%
Number of Tracks in Neutrino Slice	24.5%	2.0%	0.3%	0.7%
Number of Tracks Originating From Vertex	24.4%	1.9%	0.3%	0.6%
CRT Distance Cut	23.5%	1.4%	0.2%	0.4%
Final Pre-BDT Efficiency	23.5%	1.4%	0.2%	0.4%
Surviving Events	44	1075	839	2277

Table 8.4: A table containing the efficiencies for each sample using the binary cuts applied in the NuMI KDAR analysis.

Score Cut/Metric	Background Eff.	Signal Eff.	Signal	Background	S:B
-1.0	100%	100%	44	1919	1:43.6
-0.5	31%	94%	42	572	1:13.6
0.0	15%	86%	39	308	1:7.9
0.5	8%	74%	32	142	1:4.4
0.9	1%	24%	11	21	1:1.9

Table 8.5: A table containing the efficiencies for the sample entering the BDT used in the NuMI KDAR analysis. The efficiency is set to 100% starting from the end of the binary selection (the input to the BDT).

There is an excess of events shown in data in comparison to the stacked histograms in the neutrino energy and muon candidate track length distributions (which include signal events), specifically where KDAR events are expected to be observed according to the Monte Carlo. The reconstructed neutrino energy spectrum in Figure 8.12 includes an offset of ~15 MeV from the true neutrino energy of 236 MeV, perhaps due to the fact that hits belonging to the proton also contribute to the extent of the muon candidate, increasing its reconstructed kinetic energy.

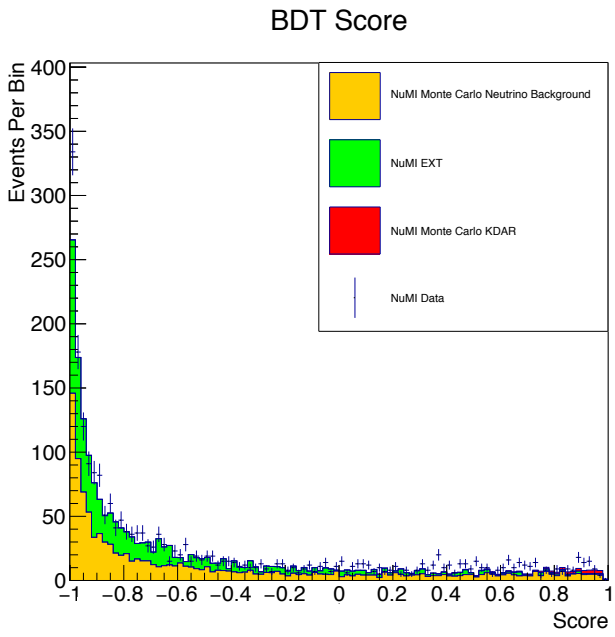

Figure 8.7: The normalized BDT score distribution. The low-score region of the plot is background-enhanced and the high-score region of the plot is signal-enhanced. There is an excess of events observed in the high-score region of the plot, exactly where KDAR events are expected to be observed according to the Monte Carlo. The error bars correspond to the statistical uncertainty only.

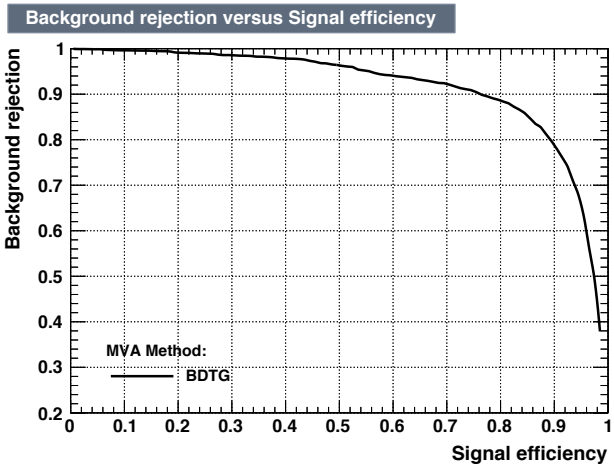

Figure 8.8: The background rejection vs. signal efficiency of the BDT.

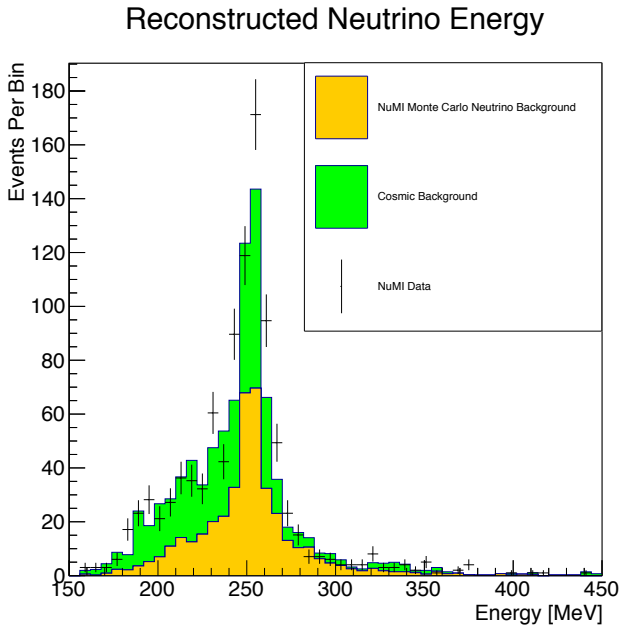

Figure 8.9: The neutrino energy distribution for the BDT score sideband. The error bars correspond to the statistical uncertainty only.

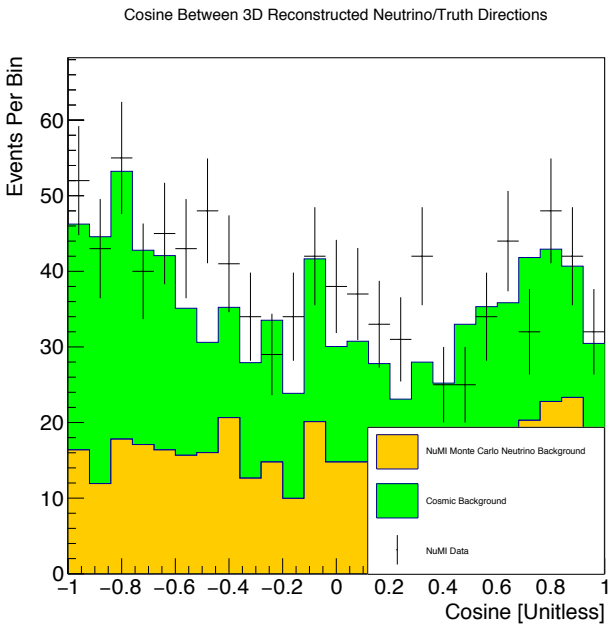

Figure 8.10: The neutrino direction distribution for the BDT score sideband. The error bars correspond to the statistical uncertainty only.

8.14 Cross Section and Flux Systematics

When the cross section and flux systematics are tabulated, the flux and cross section systematics are 21% and 13% of the central value number of KDAR events in a single bin, respectively, at a BDT

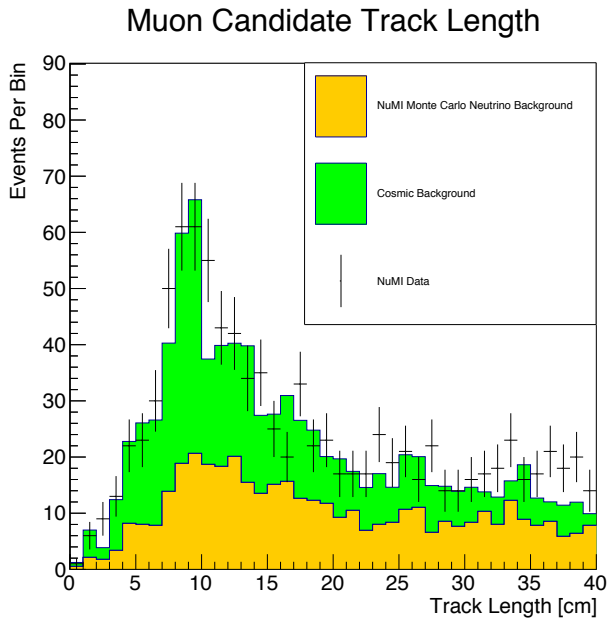

Figure 8.11: The muon candidate length distribution for the BDT score sideband. The error bars correspond to the statistical uncertainty only.

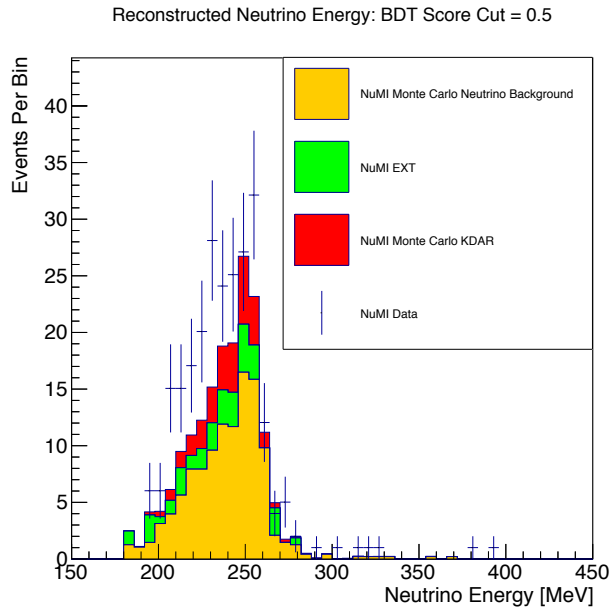

Figure 8.12: The neutrino energy distribution for a BDT score cut of > 0.5. The error bars correspond to the statistical uncertainty only.

score cut value of 0.5. The specifics of these systematics will be discussed more thoroughly in the Chapter 9. The data-only statistical uncertainty is 8% of the central value. As a result, there is very

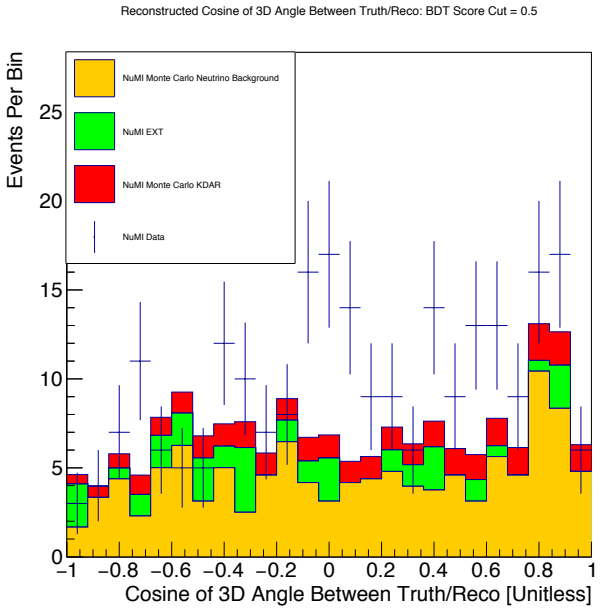

Figure 8.13: The neutrino direction distribution for a BDT score cut of > 0.5. The error bars correspond to the statistical uncertainty only.

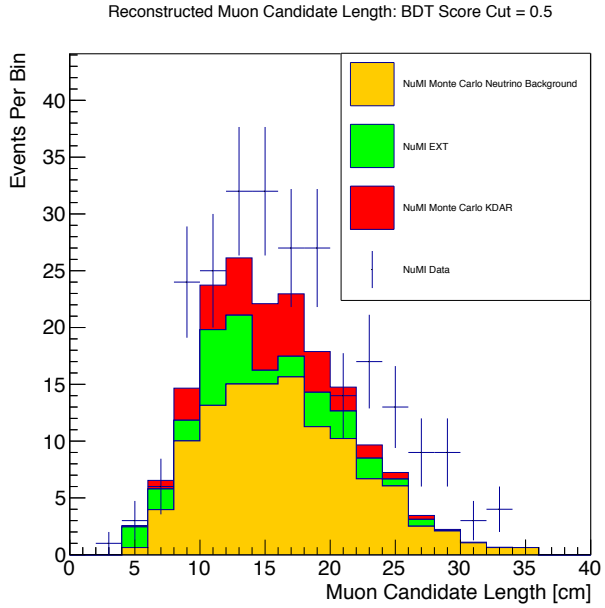

Figure 8.14: The muon candidate length distribution for a BDT score cut of > 0.5. The error bars correspond to the statistical uncertainty only.

little sensitivity to the KDAR signal in this selection and the analysis is impossible to do at this time. It is estimated that the reconstruction (both a framework like Pandora and neutrino direction

reconstruction) would have to improve signal-to-background by a factor of ~4 with enough signal events passing the selection for this analysis to be possible.

CHAPTER 9

Cross Section Measurements and the NuMI NuMuCCInclusive Analysis

A cross section measurement, with dimension of area, can be thought of as an interaction probability between two sets of targets, a flux and a fixed entity, at a microscopic level. It can be expressed as a function of a kinematic variable in a quantity called a differential cross section. It is calculated by means of the following formula:

$$\frac{\mathrm{d}\sigma}{\mathrm{d}u} = \frac{N_{\mathrm{measured},i} - N_{\mathrm{background},i}}{\Delta u_i \epsilon_i N_{\mathrm{targ}} \Phi} \tag{9.1}$$

Here, σ is the cross section in units of area, u is the kinematic variable that the differential cross section is expressed in terms of, $N_{\mathrm{measured},i}$ is the number of events reconstructed in data in a bin, $N_{\mathrm{background},i}$ is the number of predicted background events (primarily cosmic ray muon events and neutral-current events) in a bin, N_{targ} is the number of targets (argon nuclei, in the case of this measurement), ϵ_i is the efficiency of truth signal events in the selection in a bin, and Φ is the flux value in dimension of area^{-1}.

9.1 The NuMI NuMuCCInclusive Analysis

The NuMI beamline at Fermilab operated in neutrino mode (described in Section 4.9) for all MicroBooNE data collected from 2015 to June 2016. This created a neutrino beam of primarily ν_μ content (60% for the energy and angular range under study in this chapter and the next two) to study differential cross sections as functions of muon kinematics.

The signal under study in this analysis consists of ν_μ and $\overline{\nu}_\mu$ neutrinos that interact via the charged-current (CC) channel. As described in Chapter 1, this means that the neutrino interacts with an atomic nucleus, producing a muon and perhaps ejecting hadronic particles (protons and neutrons, the latter of which are undetectable) from the nucleus as well. This result can help

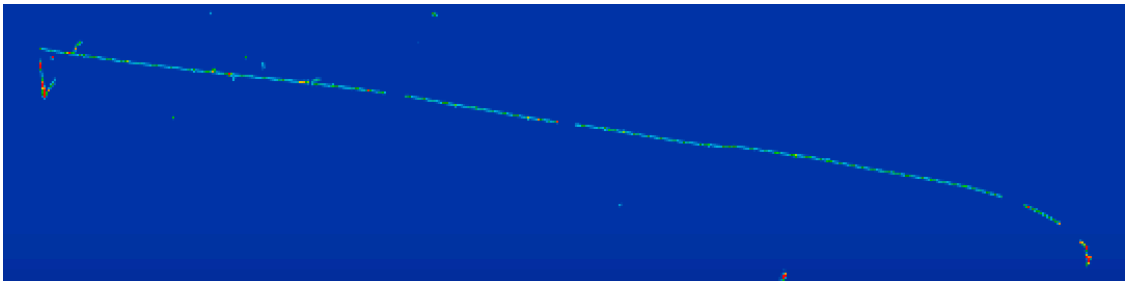

Figure 9.1: A simulated event from a ν_μ in the MicroBooNE detector. The vertex is located close to the top lefthand corner of the image. This muon is contained in the detector (meaning it does not exit) and has length 2.6 m.

describe the neutrino-nucleus interaction as well as provide information about the kinematics of the outgoing muon in the interactions. In order to resolve the direction of the muon with respect to the neutrino direction, only neutrinos from the NuMI target are considered. A simulated signal event is shown in Figure 9.1.

9.1.1 Differential Cross Section Quantities

The differential cross section is expressed in terms of the direction and kinetic energy of the muon candidate. This section describes how those quantities are defined, calculated, and reconstructed.

9.1.1.1 Calculation of Neutrino Angle and Muon Candidate Angle

The muon candidate direction is expressed in terms of the cosine of the angle between the muon candidate's trajectory and the trajectory of the mean direction of a neutrino passing the selection given by GENIE. To account for the existing flux resources described in Section 9.1.3 which include all of the neutrinos originating from within 10 degrees of the target within the same bin, all of the neutrinos within 156 m of the target are considered signal in the analysis. Approximately 91% of all signal NuMI muon neutrinos (without any requirement on their origin along NuMI beamline) originate from within this distance from the beam target. A plot showing where $\nu_\mu/\overline{\nu}_\mu$ charged-current events passing all signal requirements but the angular requirement originate from NuMI is shown in Figure 9.2. The fractional resolution is defined by the following equation:

$$\text{Fractional Difference} = \frac{\text{Truth Quantity} - \text{Reconstructed Quantity}}{\text{Truth Quantity}} \tag{9.2}$$

A plot of this quantity for the cosine variable is shown in Figure 9.3, and the resolution (the Gaussian standard deviation of the distribution) is 1.4%.

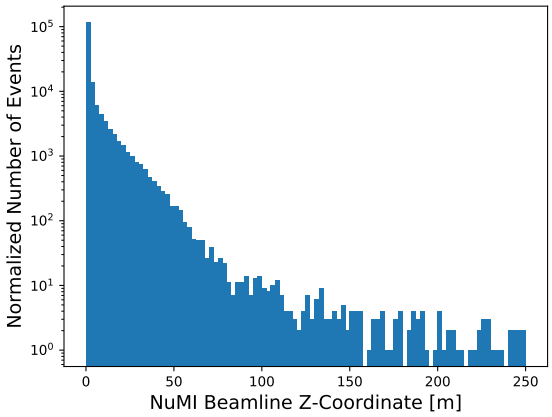

Figure 9.2: A plot showing where $\nu_\mu/\overline{\nu}_\mu$ charged-current events passing all signal requirements but the angular requirement originate from the NuMI beamline. Approximately 91% of events originate from within 10 degrees of the NuMI target ($<$ 156 m along the NuMI beamline in z), which is the requirement for an event to be considered signal. This histogram is normalized to 2.187×10^{20} POT.

9.1.1.2 Muon Candidate Kinetic Energy Reconstruction

The muon candidate kinetic energy is calculated based on the distance that the muon candidate track travels in the detector before stopping or being captured by an argon ion using the technique described in Section 2.3.1. A plot of the fractional resolution for this variable as defined by Equation 9.2 is shown in Figure 9.4, and the resolution (the Gaussian standard deviation of the distribution) is 5.7%.

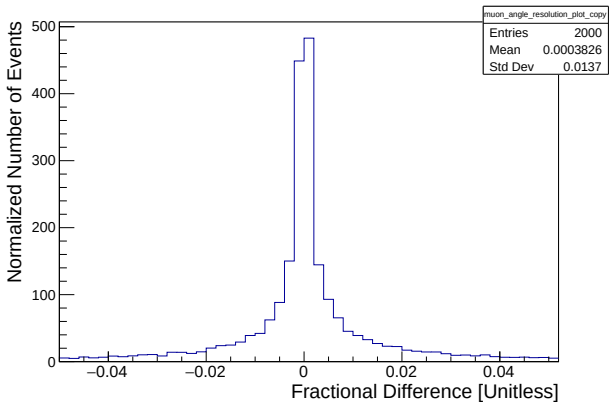

Figure 9.3: A plot showing the fractional difference of the cosine of the angle between the muon candidate direction and the neutrino direction. The resolution is 1.4%.

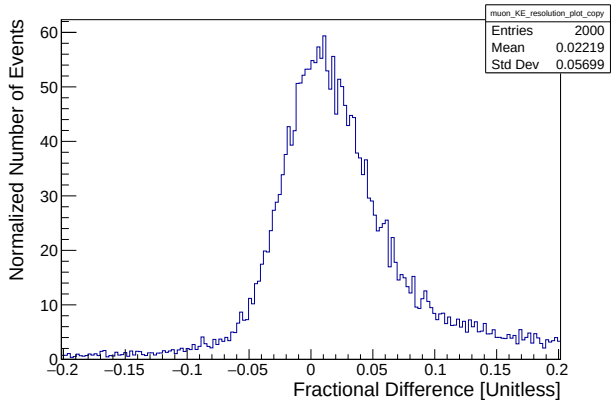

Figure 9.4: A plot showing the fractional difference of muon candidate kinetic energy. The resolution is 5.7%.

9.1.2 Dataset

The dataset under study is the total amount of Run 1 forward horn current on-beam data taken by MicroBooNE between February and June 2016 that passes beam, detector, and DAQ quality cuts. This altogether amounts to approximately 2.187×10^{20} POT. The off-beam dataset consists of NuMI EXT-triggered data taken between February (starting on the same run as the on-beam data) and September 2016. The Monte Carlo on-beam sample consists of 3.21×10^{21} POT of neutrino interactions simulated with GENIE overlaid on EXT-Unbiased events, totaling approximately 1.2M events before any selection requirements. There is a sample corresponding to each detector systematic for the same set of events with some minor differences between samples due to production job failures. The Monte Carlo dirt sample consists of 1.59×10^{20} POT of neutrino events that interact outside of the cryostat, totaling approximately 540k events before any selection requirements.

9.1.3 Flux

The flux model for the NuMI beamline determines the weight of a given neutrino event as a function of the location weight (the point where the neutrino's parent particle decayed in the NuMI beamline), the muon polarization weight (the fact that a muon that decays in flight does not do so isotropically), the importance weight (applied to decays with high statistics to limit the number of them in the files applying the flux model to reduce the required amount of storage space), the tilt weight (takes into account the technique of measuring the neutrino flux with respect to the detector), and the area weight (normalizing by the area of the unit circle used to calculate the location weight). The product of these weights determines the total weight used to calculate a neutrino flux.

Systematic Abbreviation	Description
$pC \rightarrow KX$	Protons incident on a carbon target producing a final state with kaons.
$pC \rightarrow \pi X$	Protons incident on a carbon target producing a final state with pions.
$pC \rightarrow$ Nucleon$X$	Protons incident on a carbon target producing a final state with nucleons.
$nC \rightarrow \pi X$	Neutrons incident on a carbon target producing a final state with pions.
Nucleon-A	Nucleons interacting with a non-carbon material in the beamline.
TotAbsorp.	Absorption that occurs in the interaction chain, in the decay volume or pipe.
Other	Additional interactions not covered by the other categories.
Meson Incident	Mesons that interact with any material in the beamline.
TargetAtten.	The attenuation of all particles passing through the beamline components.
All	A combination of all of the uncertainties into a single weight applied to an event.

Table 9.1: A table containing all of the hadron production uncertainties.

The Package to Predict the FluX (PPFX) implements constraints on the hadron production modeling and uses these constraints for the particular case of the NuMI beamline. It includes corrections pertaining to the attenuation of particles, the thickness of the beam's target, and uncertainties for which there is no measurement to provide a constraint. There are systematics calculated for protons interacting with a carbon target, neutrons interacting with a carbon target, and nucleons interacting with materials in the beamline which are not carbon. Table 9.1 contains all of the hadron production uncertainty systematics. Modifications to these parameters form the basis for some of the NuMI flux systematic uncertainties, which are described in more detail in Section 9.9.2.

The simulation for the NuMI beamline in MicroBooNE applies default configurations for parameters associated with the beam, like the horn current. The uncertainties associated with these quantities are independent of PPFX, and they are generated by tweaking these parameters. They are varied by amounts corresponding to their $\pm 1\sigma$ uncertainty. Figure 9.5 contains all of the parameters, the central values, and the modes used to evaluate beamline uncertainties in the NOνA detector, with which the NuMI flux model was validated.

The plots in Figure 9.6 show the ν_μ and $\overline{\nu}_\mu$ fluxes originating from within 10 degrees, or within 156 m, of the NuMI beam target as a function of neutrino energy. Plots of these fluxes overlaid onto the flux from the full NuMI beamline are shown in Figure 9.7. The values in these plots have to be scaled by the amount of POT available for the analysis, which is 2.187×10^{20}, to yield a

Bin Range [GeV]	CV [10^{-7} $\mathrm{POT}^{-1}\mathrm{m}^{-2}$]	HP/Beamline/Total Frac. Uncertainty [Unitless]
[0.24, 0.50]	11.6	0.14/0.03/0.14
[0.50, 0.75]	3.2	0.13/0.04/0.13
[0.75, 1.0]	1.9	0.13/0.03/0.13
[1.0, 1.50]	2.9	0.10/0.04/0.11
[1.50, 2.0]	1.8	0.10/0.05/0.11
[2.0, 3.0]	1.1	0.10/0.05/0.11
[3.0, 5.0]	0.4	0.11/0.05/0.12
[5.0, 10.0]	0.006	0.13/0.11/0.17

Table 9.2: A table containing the information pertaining to the ν_μ flux. 'CV' refers to the central value in the bin and 'HP' refers to the fractional hadron production uncertainty.

total of 8.29×10^{14} neutrinos per m^2. It was required that the signal ν_μ CC events originate from the target so that the muon angle could be calculated with respect to the mean direction of passing signal events from the simulation. The existing flux resources had resolution of 10 degrees on the angle from the target, which is the motivation for using that value. This is to apply a truth neutrino energy cut of 240 MeV. There are no events with energy less than 175 MeV that pass the selection, and a cut of 240 MeV also excludes the KDAR signal at 236 MeV. The KDAR signal is highly uncertain, so those events are removed to limit the flux systematic uncertainties in the analysis.

Table 9.2 and Table 9.3 contains the range of each bin, the central-value flux (in units of 10^{-7} $\mathrm{POT}^{-1}\mathrm{m}^{-2}$), the fractional uncertainty due to the beamline variations, and the fractional uncertainty due to hadron production uncertainties for the ν_μ and $\overline{\nu}_\mu$ fluxes, respectively. Figures 9.8 and 9.9 show the fractional uncertainties for the hadron production and beamline systematics, respectively.

Variation	**Central Value**	**Modes**
Horn Current	200 kA	$\pm$2 kA
x Horn 1 Position	0 mm	$\pm$3 mm
y Horn 1 Position	0 mm	$\pm$3 mm
Beam Spot Size	1.3 mm	$\pm$0.2 mm
x Horn 2 Position	0 mm	$\pm$3 mm
y Horn 2 Position	0 mm	$\pm$3 mm
Water on Horns	1 mm	$\pm$1 mm
Beam Shift x Position	0 mm	$\pm$1 mm
Beam Shift y Position	0 mm	$\pm$1 mm
Target z Position	-143.3 cm	$\pm$7 mm
Old Horn 1	OFF	ON
B Field in Decay Pipe	OFF	ON
Refined Horn 1	ON	OFF
54 mrad divergence	-	-

Figure 9.5: The NuMI beamline uncertainties, their central values, and their modes.

Bin Range [GeV]	CV [10^{-7} $\mathrm{POT}^{-1}\mathrm{m}^{-2}$]	HP/Beamline/Total Frac. Uncertainty [Unitless]
[0.24, 0.50]	5.7	0.14/0.02/0.15
[0.50, 0.75]	2.8	0.11/0.03/0.12
[0.75, 1.0]	1.9	0.10/0.04/0.11
[1.0, 1.50]	2.2	0.09/0.03/0.10
[1.50, 2.0]	1.0	0.11/0.04/0.11
[2.0, 3.0]	0.7	0.10/0.04/0.11
[3.0, 5.0]	0.5	0.09/0.05/0.10
[5.0, 10.0]	0.1	0.11/0.09/0.14

Table 9.3: A table containing the information pertaining to the $\overline{\nu}_\mu$ flux. 'CV' refers to the central value in the bin and 'HP' refers to the fractional hadron production uncertainty.

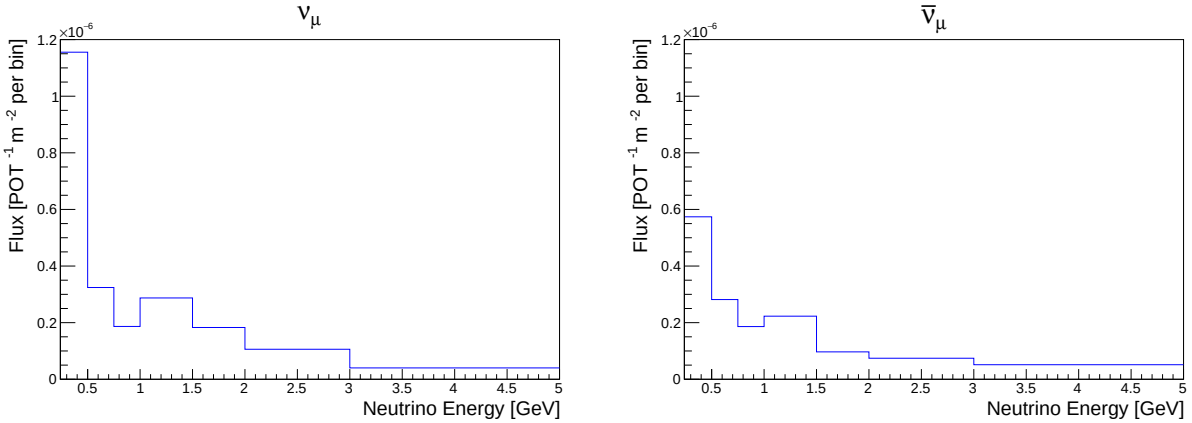

Figure 9.6: A plot of the ν_μ and $\overline{\nu}_\mu$ fluxes as a function of neutrino energy. These bins closer to lower energy are more populated in these plots because there is more phase space with which to produce neutrinos in this region of the kinematic space. The sum of the integrals of these two plots scaled by the amount of POT available for the analysis (2.187×10^{20}) is used as the flux in the differential cross section equation.

9.1.4 Cross Section

The cross section model used by MicroBooNE is GENIE, which is a comprehensive set of physics models which describe neutrino interactions. It is produced by a collaboration which upkeeps a set of software products commonly used by the high-energy physics community. It has been validated against bubble chamber experiments and a CC0π result from MiniBooNE [53]. The models for cross sections, central values for parameters, and uncertainties are chosen based on available neutrino scattering data. In cases where cross sections are not measured, theoretically-motivated uncertainties that provide sufficient coverage are chosen instead.

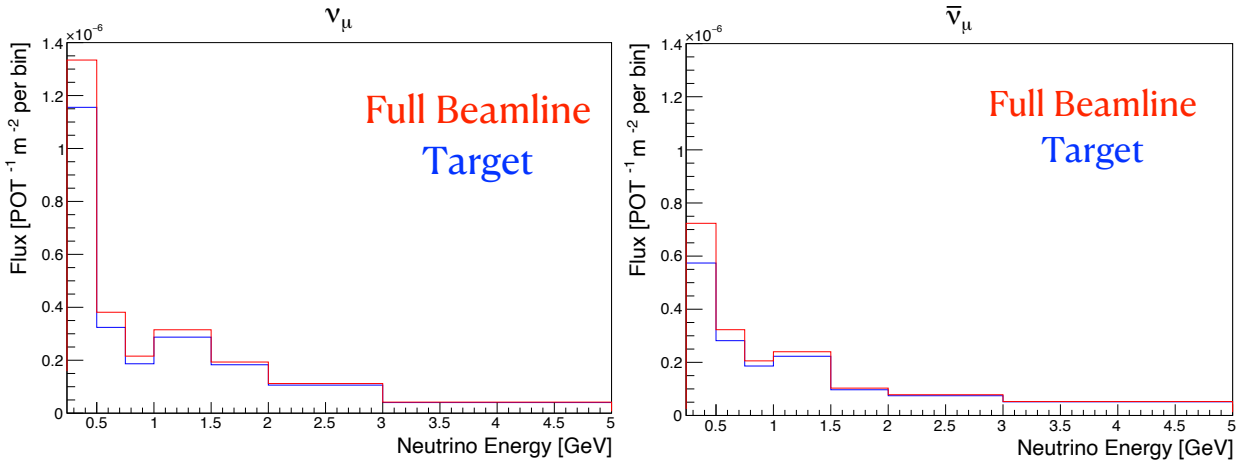

Figure 9.7: A plot of the ν_μ (left) and $\overline{\nu}_\mu$ (right) fluxes from the full NuMI beamline (red) and from the target only (blue).

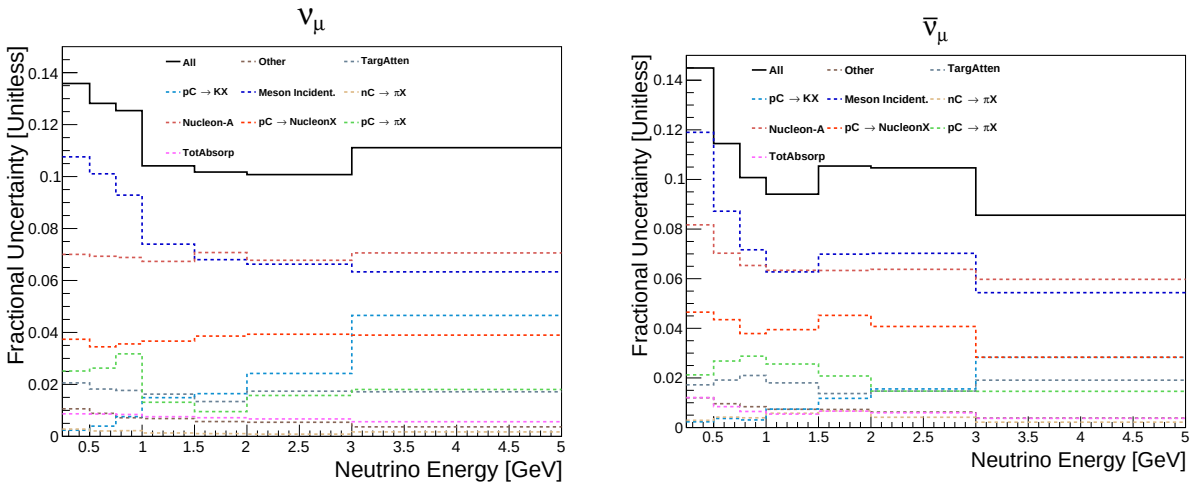

Figure 9.8: A plot of the ν_μ (left) and $\overline{\nu}_\mu$ (right) hadronic production uncertainties, expressed as a fraction of the central value flux. The 'All' systematic combines the contributions from the nine individual sources, but it is not a quadrature sum because of correlations between them.

9.1.5 Number of Targets

For this analysis, 'target' is defined as the number of target argon nuclei, which is calculated by means of the following equation:

$$N_{targ} = \frac{\rho_{Ar} \times V \times N_A}{m_{mol}} \tag{9.3}$$

The variables in this equation have the following values:

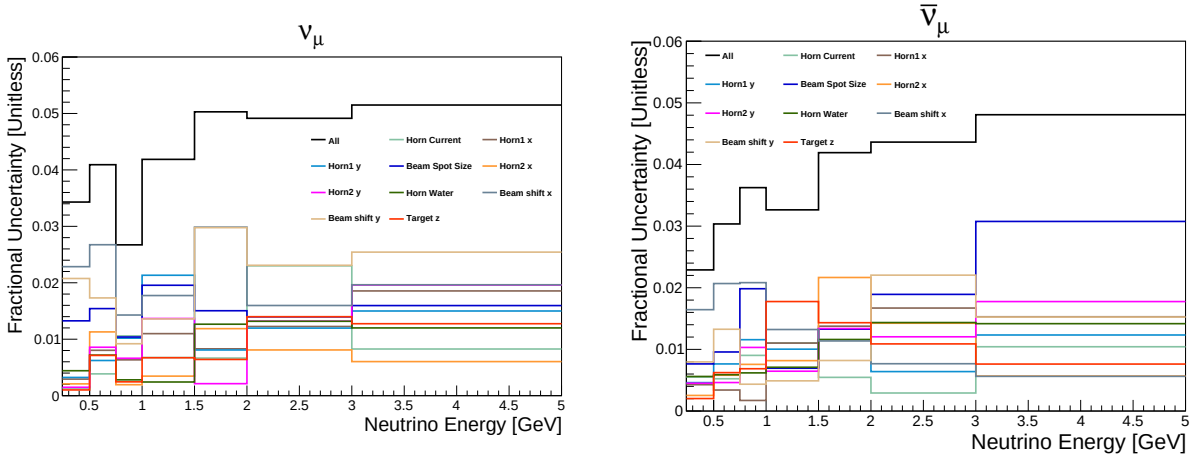

Figure 9.9: A plot of the ν_μ (left) and $\overline{\nu}_\mu$ (right) beamline uncertainties, expressed as a fraction of the central value flux. The 'All' systematic is the quadrature sum of the ten individual sources of beamline uncertainty.

ρ_{Ar}	1.3836 g/cm^3
V	4.1622×10^7 cm^3
N_A	6.022×10^{23} molecule/mol
m_{mol}	39.95 g/mol

Table 9.4: A table of the values that the variables in the equation for the number of target nuclei.

The volume is calculated by using a fiducial volume of 20 cm from each face of the TPC, which is the fiducial volume requirement used in the analysis. This value is not efficiency-corrected, meaning that it is the same for every bin of the differential cross section measurements and for every part of the target volume (the fiducial volume). When these values are used in the equation, the total number of argon nuclei is 8.68×10^{29}.

9.1.6 Backgrounds

There are three dominant types of backgrounds in the NuMI NuMuCCInclusive analysis: NC events, cosmic ray events, and CC ν_μ events that either do not originate from the NuMI target or interact outside of the analysis's fiducial volume. There is a small ($< 1\%$) contamination from ν_e and $\overline{\nu}_e$ events. The neutral-current events are present in the analysis because a proton is mistakenly identified as a muon. The cosmic ray events are included when they are not flagged as entering the detector from the outside, they are identified as being associated to a neutrino vertex by Pandora, and they are identified as neutrino-like by the particle identification tools. The ν_μ events that interact outside of the fiducial volume have a misreconstructed vertex, and those which do not originate

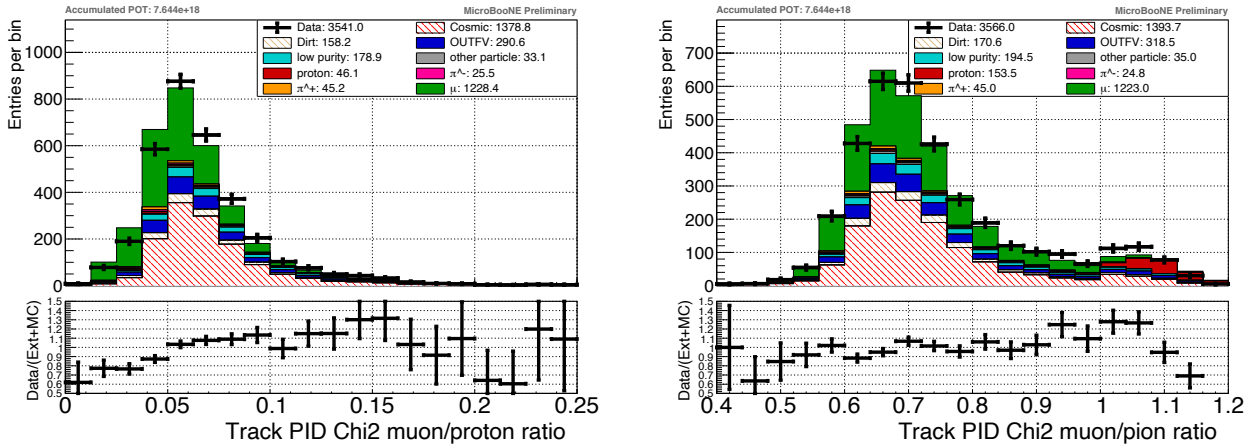

Figure 9.10: Plots of (left) the ratio of the muon likelihood to the proton likelihood and of (right) the ratio of the muon likelihood to the pion likelihood. The requirement for a track to be considered a muon candidate is < 0.168 for the lefthand plot and < 1.06 for the righthand plot [19].

from the NuMI beam target are an irreducible background (they are identical to the signal except for neutrino direction, which is less straightforward to reconstruct for this analysis, unlike for the KDAR ν_μ analysis described in Chapter 8). There is also a minimum requirement on neutrino energy (> 240 MeV), which is in line with the requirement placed on the neutrino flux described in Section 9.1.3. The full breakdown of the backgrounds, prior to any selection requirements, are shown below in Table 9.5.

Cosmic Rays	86%
ν_e	<1%
Neutral Current ν_μ	4%
ν_μ from NuMI Beamline	<1%
ν_μ Outside Fiducial Volume	6%
Dirt	4%
ν_μ with Energy < 240 MeV	<1%

Table 9.5: The backgrounds of the NuMI NuMuCCInclusive analysis from the NuMI beam target prior to any event selection.

9.2 Particle Identification

There are two stages in the particle identification process for the NuMI NuMuCCInclusive Analysis: selecting the muon candidate and then making event-level selection requirements based on

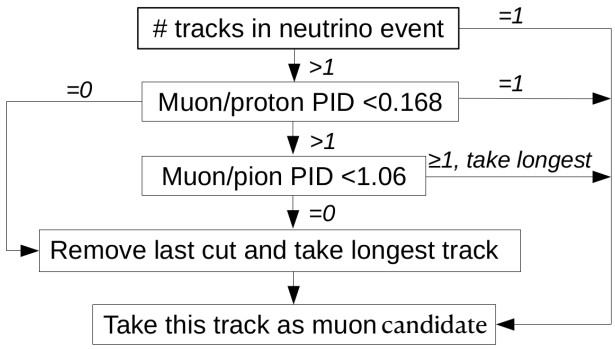

Figure 9.11: The procedure for selecting the muon candidate from the neutrino slice in the event.

its characteristics. For the muon candidate selection, there is a χ^2 fit that is performed for a track under the assumption that it is a muon, a proton, and a pion. The χ^2 likelihood values are normalized to the number of hits in the reconstructed track, which serves as the number of degrees of freedom in the fit. The lower the likelihood from a fit is, the more likely the track is to be that kind of particle. First it is required that the ratio of the muon likelihood to the proton likelihood is less than 0.168, and then it is required that the ratio of the muon likelihood to the pion likelihood is less than 1.06. If there is only one track remaining after the first requirement, then that track is chosen as the muon candidate. If there are no tracks left after either one of these stages, the longest track is considered the muon candidate (because muons deposit less energy per unit length along their trajectory than the other particle species and will travel further in the detector than other particles of the same energy). If there is more than one track remaining after both of these stages, the longest track is considered the muon candidate. By using a truth-to-reconstruction comparison, this procedure picks out the correct muon candidate 84% of the time. These quantities as used in the Run 3 BNB NuMuCCInclusive analysis are shown in Figure 9.10 [19]. The procedure is described in the diagram in Figure 9.11.

Once a muon candidate is selected, it is required that the track have a proton likelihood (Particle IDentification, or PID) value > 78. This is meant to reject NC events, which contain protons that could be mistaken as the muon candidate. It is required that the muon candidate have a Muon Track Score value, which measures if the track is sufficiently track-like, > 0.8. This is meant to reject shower events. Finally, it is required that the muon candidate track have a NuScore value, the output from a Support Vector Machine, > 0.1. This determines if the track is neutrino-induced vs. cosmic-induced. If any of these conditions are not met for the muon candidate track, the event fails the selection. Plots of these quantities are shown in Figures 9.12, 9.13, and 9.14.

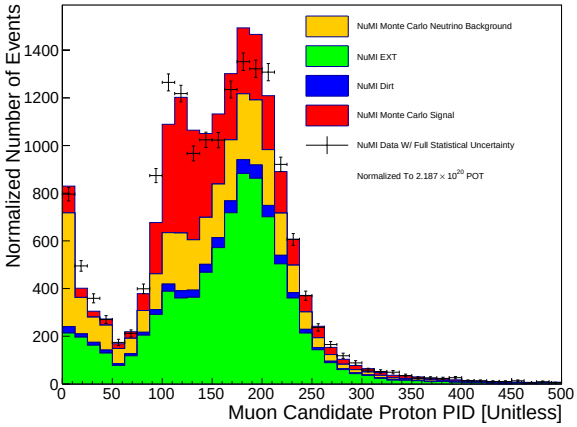

Figure 9.12: A plot of the Proton PID. The requirement for an event to pass is that this quantity is $>$ 78 for the muon candidate track.

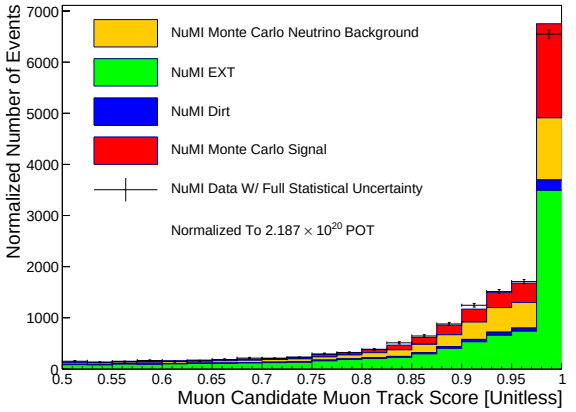

Figure 9.13: A plot of the Muon Track Score. The requirement for an event to pass is that this quantity is $>$ 0.8 for the muon candidate track.

9.3 Vertex Reconstruction

The vertex reconstruction used in this analysis is identical to the vertex reconstruction used in the NuMI KDAR analysis (Section 8.6.1) with one difference: for tracks of greater length than 150 cm associated to neutrino slices with more than one other track, the vertex is determined to be located at the endpoint of the muon candidate track with more tracks located closer to it. In the event that there are an equal number of tracks close to each endpoint of the muon candidate track, the endpoint corresponding to the greater average track length of the tracks other than the muon

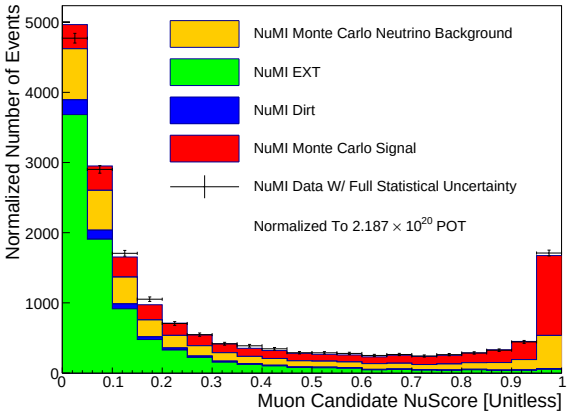

Figure 9.14: A plot of the NuScore. The requirement for an event to pass is that this quantity is $>$ 0.1 for the muon candidate track.

candidate is determined to be the start. The track length cutoff was chosen to be 150 cm because the vertex reconstruction described in Section 8.6.1 works better than Pandora when including all tracks up to that length. Including this adjustment, this vertex reconstruction algorithm correctly reconstructs the direction of the muon candidate tracks for 87% of events compared to 83% of events for Pandora.

9.4 Selection

The neutrino selection for this analysis takes advantage of the fact that the muon neutrino interactions produce track-like particles that are minimum ionizing until the end of their trajectory. The selection is simple, requiring a flash of a minimum of 50 photoelectrons and a neutrino slice with at least one track. The reconstructed vertex has to be contained within a fidicial volume of 20 cm from each TPC face, and the track has to be determined to be sufficiently neutrino muon-like instead of proton-like, shower-like, or cosmic muon-like based on the PID variables in Section 9.2. Finally, the track is required to be contained, meaning that its endpoint does not come within 3 cm of any TPC face after being SCE-corrected (the same containment requirement as the analysis in Chapter 8 used), because of biases with the track momentum calculator for non-contained tracks. The requirements are all contained in Table 9.6.

9.5 Selection Effect on Each Sample

The effect of the selection on each sample in the analysis is shown in Table 9.7. The signal is affected most strongly by the containment requirement, while the other samples all fall below 10% efficiency with the flash, neutrino slice/track, and fiducial volume requirements. Following this selection, for the amount of POT used in the analysis (2.187×10^{20}), there are 3194 passing signal events, 1593 passing neutrino background events, 175 passing dirt events, 1969 passing off-beam events, and 7189 passing on-beam events. Among the signal events, the ν_μ content increases to 86% after the selection from 82% prior to it. This is due to the containment requirement having a greater impact on the $\overline{\nu}_\mu$ events than on the ν_μ events.

9.6 Truth Variable Distributions Pre-Selection

The truth muon candidate kinetic energy and directional cosine distributions are shown in Figures 9.15 and 9.16, respectively. In the kinetic energy distribution, the greatest number of events are present in the bins with the least kinetic energy. The directional cosine distribution shows the greatest number of events in the most forward-going bin (the one most in the neutrino direction contained in the interval [0.8, 1.0]) of cosine space.

9.7 Variable Distributions Post-Selection

Stacked plots of the muon candidate kinetic energy and muon candidate directional cosine are shown in Figure 9.17 and 9.18, respectively. These plots are used to make the background-subtracted distributions that are contained in Chapter 10. The muon candidate length distribution is shown in Figure 9.19 as well. The kinetic energy range calculation described in Section 2.3.1

One Flash of $>$ 50 photoelectrons
A Neutrino Slice With At Least One Track
PID Requirements
Reconstructed Vertex Within Fiducial Volume
Track is Contained

Table 9.6: The selection of the NuMI NuMuCCInclusive analysis from the NuMI beam target.

Cut/Sample	Signal	Neutrino Background	Dirt	Off-Beam
Flash Cuts	99%	74%	73%	55%
Neutrino Slice/Track Cut	78%	27%	24%	10%
Fiducial Volume Cut	68%	9%	9%	3%
PID Cuts	56%	4%	2%	<1%
Containment Cut	21%	2%	<1%	<1%

Table 9.7: A table containing the accumulative efficiencies (with the cuts enacted from the top of the table to the bottom) for each sample using the requirements of the NuMI NuMuCCInclusive analysis.

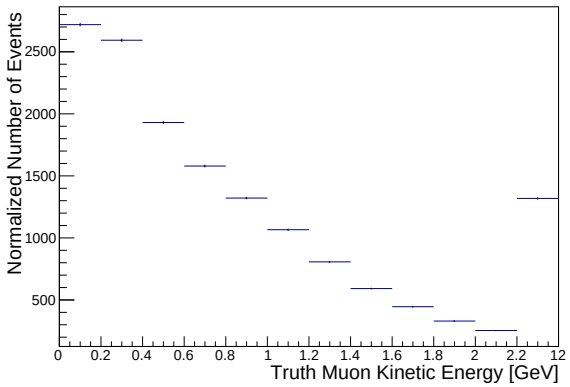

Figure 9.15: The truth muon candidate kinetic energy distribution of signal events before the event selection. The error bars correspond to the statistical error only. This histogram is normalized to 2.187×10^{20} POT.

uses the muon candidate length as input, thereby serving as a 'map' between this quantity and the kinetic energy.

The truth neutrino energy of selected signal events is shown in Figure 9.20. Because of the requirement that the muon candidate must be contained, more than 90% of the passing signal events contain a neutrino with energy < 2.24 GeV.

9.8 Backgrounds Post-Selection

After the selection, the composition for the backgrounds changes from what it is before the selection. Cosmic backgrounds (from the off-beam, from events in which the incorrect vertex is found, and from neutrino interactions outside the cryostat, the last of which is shown in a different category) are the easiest to eliminate, because they are the most likely to not contain a flash of light and to not contain activity in the TPC that looks like it was caused by a muon neutrino. The signal-

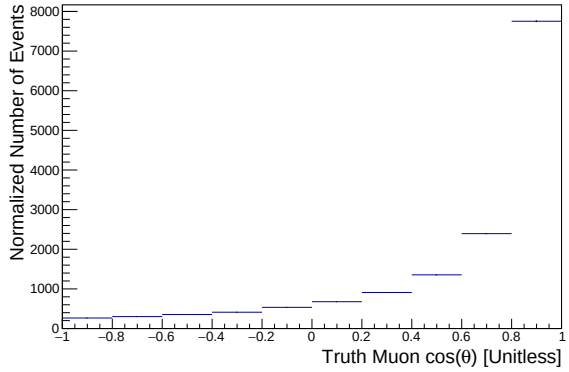

Figure 9.16: The truth muon candidate directional cosine distribution of signal events before the event selection. The error bars correspond to the statistical error only. This histogram is normalized to 2.187×10^{20} POT.

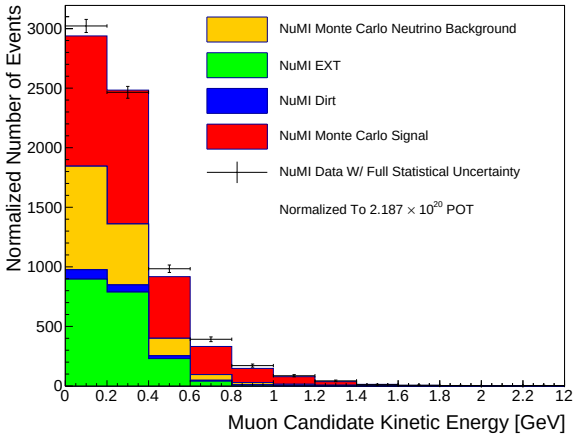

Figure 9.17: A stacked plot of the muon candidate kinetic energy distributions with data overlaid.

to-background ratio after the selection is 0.85. The breakdown of the backgrounds following the selection is shown in Table 9.8.

9.9 Systematics

There are three categories of systematics used in this analysis: detector, flux, and cross section.

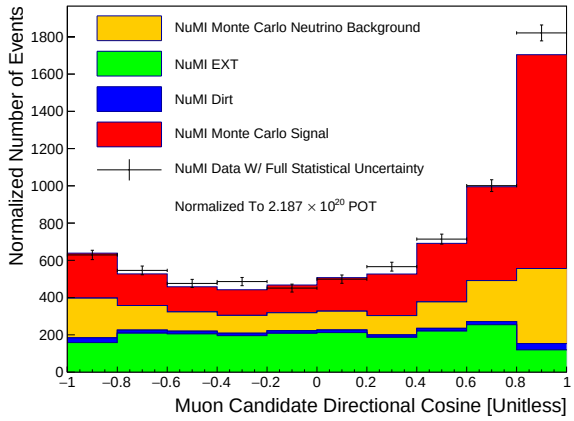

Figure 9.18: A stacked plot of the muon candidate directional cosine distributions with data overlaid.

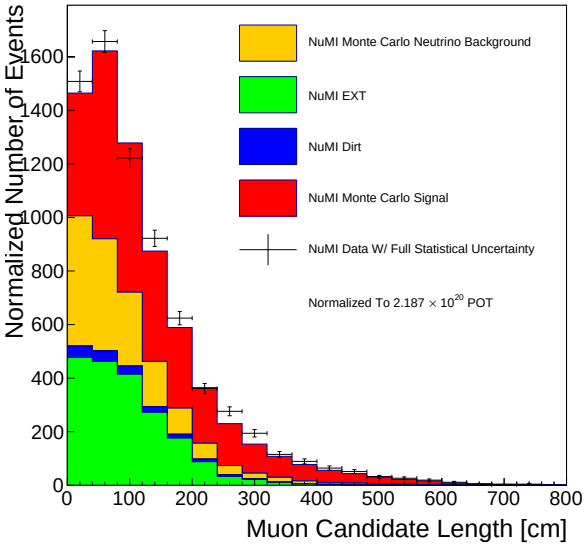

Figure 9.19: A stacked plot of the muon candidate length distributions with data overlaid.

9.9.1 Detector Systematics

There are three classes of detector systematics in MicroBooNE: TPC systematics, light systematics, and Wire Modified (WireMod) systematics. They represent the associated uncertainties of performing a differential cross section measurement of a charged-current $\nu_\mu/\overline{\nu}_\mu$ signal.

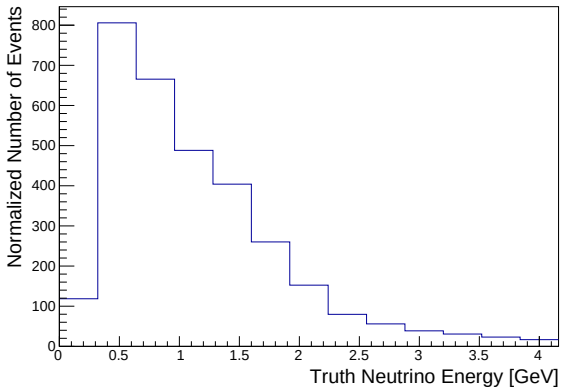

Figure 9.20: The truth neutrino energy distribution for passing charged-current $\nu_\mu/\overline{\nu}_\mu$ signal events. This histogram is normalized to 2.187×10^{20} POT.

Cosmic Rays	72%
ν_e	<1%
Neutral Current ν_μ	8%
ν_μ from NuMI Beamline	11%
ν_μ Outside Fiducial Volume	4%
Dirt	5%
ν_μ with energy $<$ 240 MeV	<1%

Table 9.8: The backgrounds of the NuMI NuMuCCInclusive analysis from the NuMI beam target after the event selection.

9.9.1.1 TPC Effect Systematics

The TPC systematics capture the uncertainty associated with the space charge effect (SCE) and recombination. The SCE calibration is used to make an electric field distortion map (described in Chapter 7), so a different SCE map is used to generate an alternate sample. In the center of the detector, where laser data is plentiful, the laser track residual is used to determine the uncertainty. Because there is not laser information in every voxel, the average of the neighboring voxels is taken to calculate the bias. For the recombination sample, the modified box model (described by Equation 4.3) was used with different parameters to calculate the systematic. The equation is updated by changing the value of β_P to $\beta_P - d\beta$ in the simulation.

9.9.1.2 Light Systematics

The light systematics come in two varieties: the reduced light yield sample and the modified Rayleigh length sample. The amount of light collected comes from the total amount of prompt and

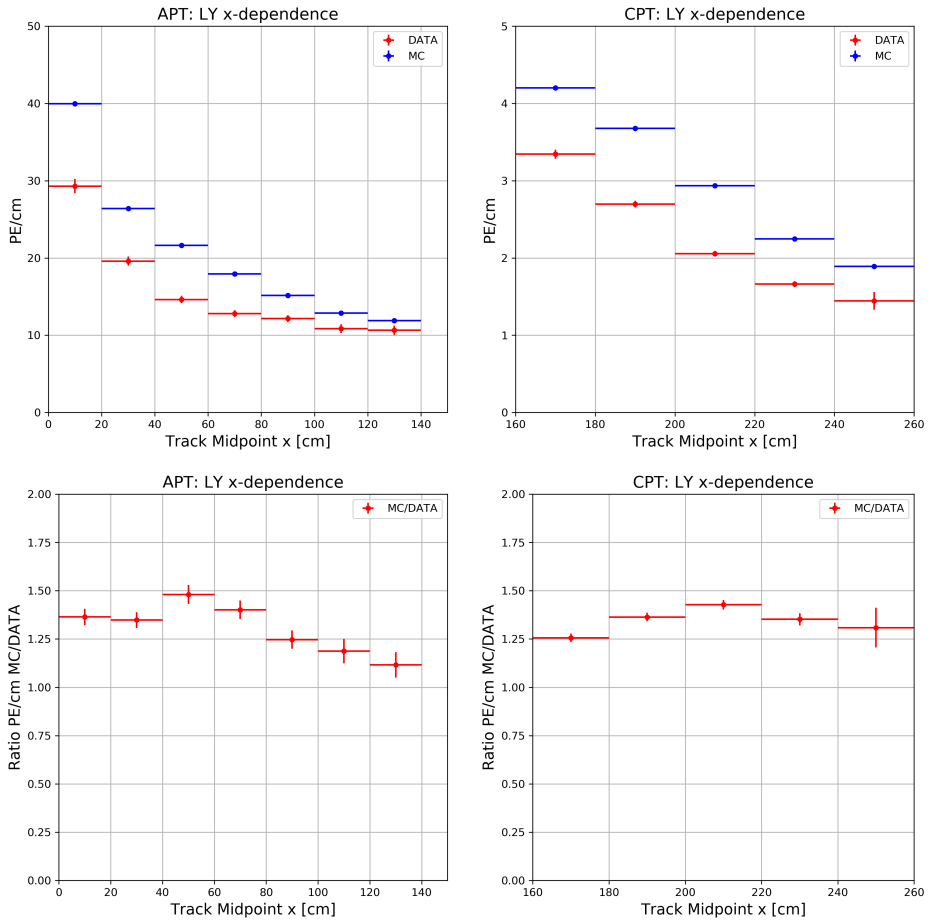

Figure 9.21: The ratio of the light in Monte Carlo vs. data ACPT t_0-tagged tracks plotted separately (top) and as a ratio (bottom) for the anode-piercing tracks (left) and the cathode-piercing tracks (right). The ratio between the two samples is ~25% as shown in the ratio distributions in the bottom row.

late light in the detector collected by the PMTs for flashes in the beamspill window. The total light yield in the detector is scaled down by 25% of its nominal value in the simulation. Plots in Figure 9.21 generated using ACPT t_0-tagged tracks reveal a ratio of light in the Monte Carlo to the data of ~25%. The Rayleigh scattering length used in MicroBooNE simulation is 60 cm while several measurements are more in line with 90 cm. Studies of a position-dependent light yield variation as a function of Rayleigh scattering exists for a MicroBooNE-like geometry, and that is used to scale up the amount of visibility for each voxel in the detector by the ratio between the simulation with the 120 cm Rayleigh length vs. the current 60 cm length. That is used to generate the Rayleigh length variation sample. The light yield decline that is described in Section 4.4.4 is not included in a systematic because this is Run 1 data that was collected before that became an effect.

9.9.1.3 WireMod Systematics

The last class of detector systematics, the WireMod Systematics, are based on data-driven variations between the data and the Monte Carlo which are included in physics analyses by modifying the wire waveforms after deconvolution in the simulated events. The effects of each waveform are described in terms of its integrated charge Q and its width σ. The way in which this works is that these two properties are measured as a function of each of the relevant variables for both data and simulation and then the ratio between data and simulation is found to form a smooth function. The simulated waveforms in Monte Carlo are modified according to these ratios.

There are several advantages to this approach. The first is that it captures effects that cannot be fully described by simulation; because the method is data-driven, the full impact of the data itself is included in the modifications to the simulation. Second, it is computationally efficient; the most computationally intensive parts of preparing simulation for analysis are the charge drift simulation and the wire waveform deconvolution. Because this procedure uses the deconvolved waveforms, these two stages do not have to be run as part of running each of the variations.

The five variables that are used in this technique are x, (y,z), θ_{XZ}, θ_{YZ}, and dE/dx. The coordinates transverse to the drift direction are used in the same variable because the behavior is driven largely by the state of the wires, which extend in both Cartesian directions. Several angular bases were considered for this technique, but the angles θ_{XZ} and θ_{YZ} that were chosen represent true detector effects. They are defined differently for each of the planes. Finally, the dE/dx variable is chosen because it is affected by recombination and whatever changes the relationship between the dQ/dx in a given region of the detector and the resulting dQ/dx. The hit charge and hit width splines, taken as ratio between Monte Carlo are data, for the x variable are shown in Figure 9.22.

This technique was first designed for the BNB, and it was modified for the NuMI systematics

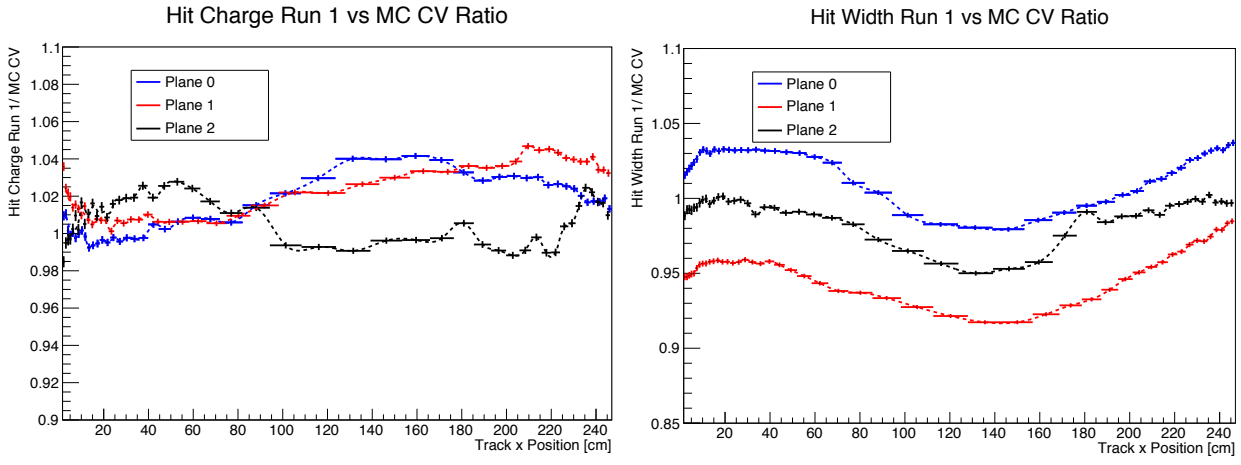

Figure 9.22: The splines for (left) hit charge and (right) hit width for the x variable.

for two reasons: the diffusion value used for NuMI is ~40% lower than it is for the BNB and the processes of identifying the simulated energy deposit belonging to a neutrino-induced track depends on the length of the readout window, which is six times greater for NuMI than it is for BNB. Also, there is a hit σ spline that is used to generate the θ_{YZ} spline for NuMI, for which a minor dependence as observed, but not for BNB, for which no dependence was observed. With these changes, the same procedure described in the beginning of this section was used to generate the WireMod systematics for NuMI in the same manner they were for the BNB.

9.9.2 Flux Systematics

The flux systematic uncertainty consist of a two sets of modifications: the beamline uncertainties and the application of 600 multisim weights that represent the hadron production uncertainties from PPFX. For the latter, these weights constitute the flux in different 'universes', or deviations from the central value universe. The modifications are applied by picking a random number from a multivariable Gaussian distribution formed by the distribution of quantities contained in Table 9.1 which are expressed as a function of neutrino energy and neutrino angle. To find the uncertainties due to these variations, the 2D flux histograms from the variations like the one in Figure 9.23 are first recast as 1D histograms with single bin indices, which are defined according to Figure 9.24. Note that the binning here is different than the binning used for the flux in Section 9.1.3; the binning used in that section was chosen to reduce statistical uncertainties in individual bins of the flux.

The uncertainties were formed from a covariance matrix, which is defined by the following equation, where x^{CV} is the central value measurement and x^s is a measurement in a systematic universe. N is equal to the number of universes, 600:

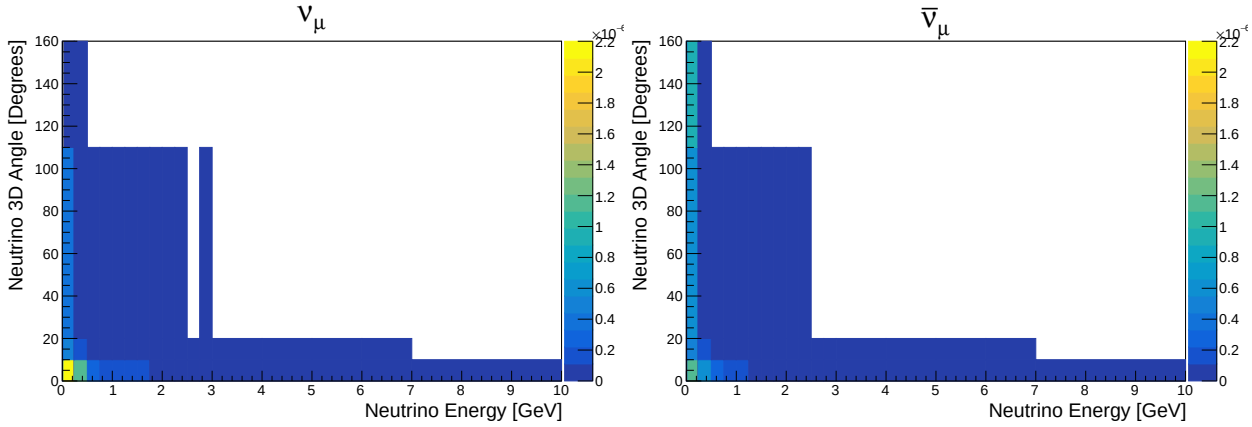

Figure 9.23: The (left) ν_μ and (right) $\overline{\nu}_\mu$ fluxes expressed in terms of 3D angle to MicroBooNE with respect to the NuMI beamline vs. neutrino energy.

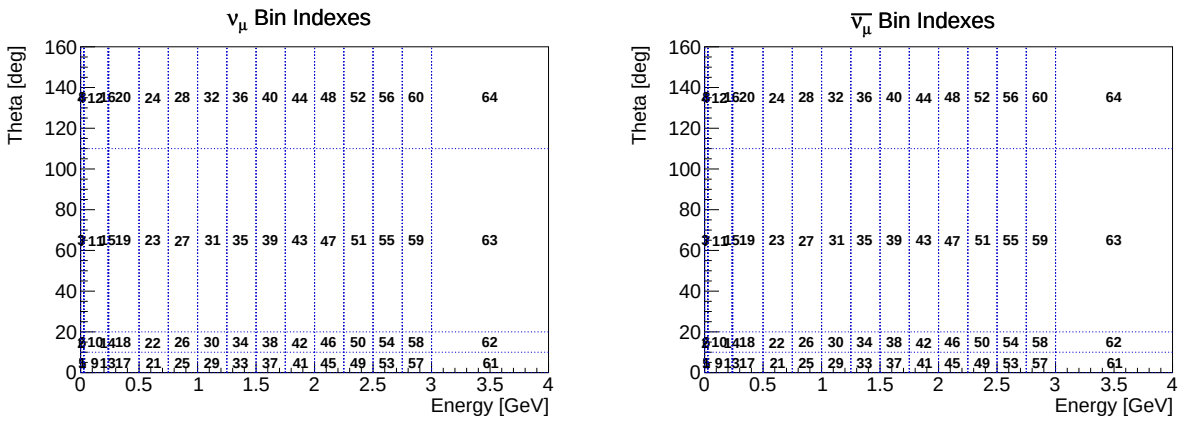

Figure 9.24: The indices for recasting the 2D flux histogram in Figure 9.23 as a 1D histogram for (left) the ν_μ distibution and (right) the $\overline{\nu}_\mu$ distribution. Bins 65-80 are located in the analogous locations to where they are in the interval from 3 GeV - 4 GeV for the 1 GeV bin intervals from 4 GeV - 8 GeV and for the 3 GeV bin interval from 7 GeV - 10 GeV.

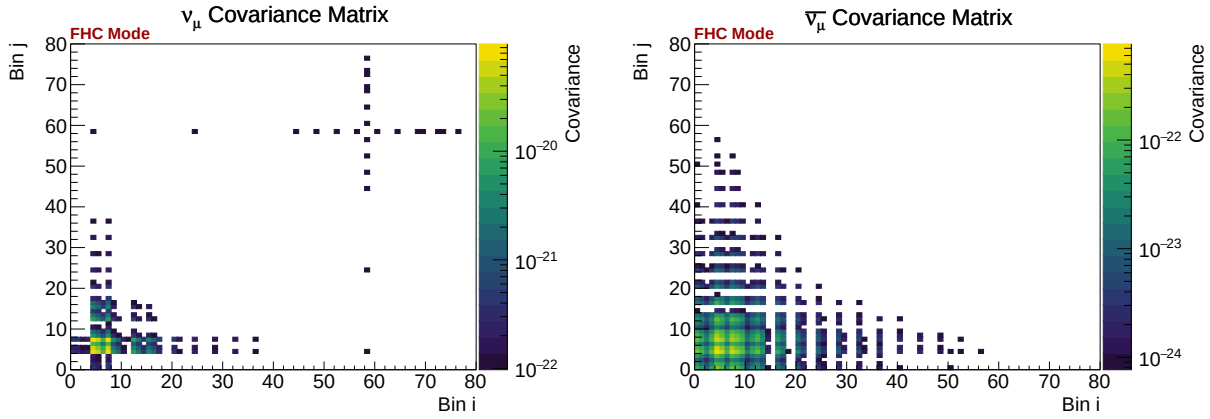

Figure 9.25: The covariance matrices generated from the flux systematic universes for (left) the ν_μ distibution and (right) the $\overline{\nu}_\mu$ distribution.

$$E_{ij} = \frac{1}{N}\sum_{s=0}^{N}(x_i^s - x_i^{CV})(x_j^s - x_j^{CV}) \tag{9.4}$$

The covariance matrices resulting from this equation are shown in Figure 9.25.

The fractional covariance matrix is described by the following equation:

$$F_{ij} = \frac{E_{ij}}{x_i^{CV} x_j^{CV}} \tag{9.5}$$

Those values are shown in Figure 9.26 in the 1D binning scheme that describes the 2D flux distribution.

The root-mean-square values of the uncertainties of the different universes constitute the sys-

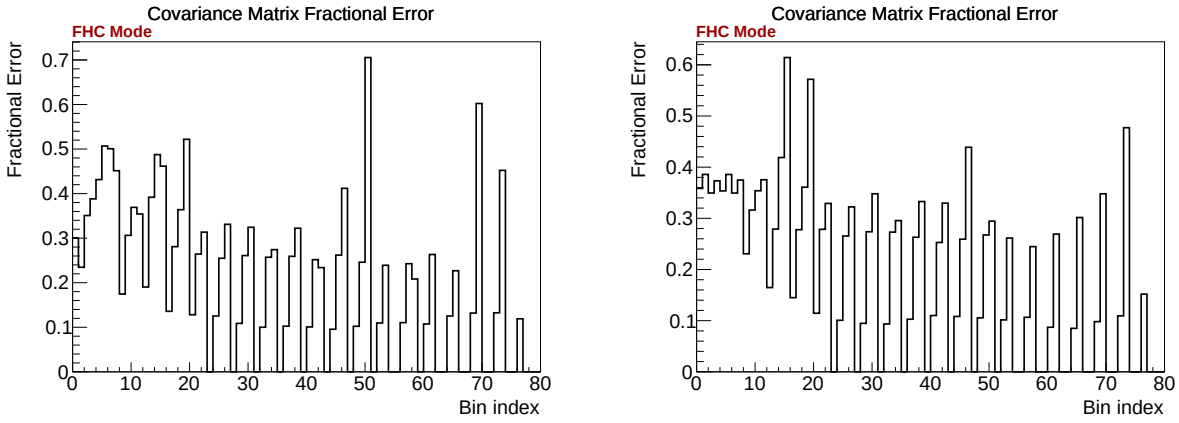

Figure 9.26: The fractional covariance uncertainties for the flux systematic universes, shown in the 1D binning scheme that describes the 2D flux for (left) the ν_μ distibution and (right) the $\overline{\nu}_\mu$ distribution.

tematic flux uncertainty in each bin of the differential cross section measurements shown in Chapter 10.

To apply the beamline uncertainties, there is a unisim 2D flux histogram like the one in Figure 9.23 that was formed by changing the input parameters to the Monte Carlo according to the $\pm 1\sigma$ deviations shown in Figure 9.5. The ratio of this histogram to the central value histogram is taken and applied to the central value PPFX weight for each event to find the new backgrounds and efficiency for that particular beamline systematic. The data-extracted cross section is then calculated using the new backgrounds and efficiency. There are two variations for each beamline systematic. The root-mean-square value for the two variations constitute the systematic flux uncertainty in each bin of the differential cross section measurements shown in Chapter 10.

9.9.3 Cross Section Systematics

There are four sources of cross section systematic uncertainties that are used in the analysis. The first item varies the multisim variables, which are modified at the same time as other systematic uncertainties, and the second varies the unisim variables, which are modified independently from the others because they affect other uncertainties when they are modified. Like the flux systematics, the magnitudes of their respective uncertainties are determined by considering the root-mean-square values of the uncertainties of each of the variations. The individual cross section systematic uncertainties are described in more detail below:

- 600 'universes' (in the same concept as the flux) that modify the parameters of the cross section model simultaneously by randomly varying them according to individual Gaussian distributions centered on their respective central values. Over 40 parameters, corresponding

to different models, are varied as multisims within each universe. A full list of the parameters and their meaning is included in Appendix A.

- The parametrization of the nucleon axial form factor in two variations.
- The parameter that changes the strength of the Nieves RPA correction to the CCQE cross section, from the full Nieves correction to no cross section in two variations.
- The parameter that changes the cross section to the shape predicted by GENIE's empirical MEC model in two variations.

CHAPTER 10

Result

When publishing a physics measurement, it is important to express the result in a way that it is most understandable and useful to the theorists who will use it to improve their models of the process under study. Unfolding, the process of taking a measurement in reconstructed space and translating it to truth space, does exactly that. The numerical result of a χ^2 fit is provided with a covariance matrix to explain how well the provided model agrees with the data. The measurement is provided with associated statistical and systematic uncertainties which describe the $\pm 1\sigma$ spread of the central value in each bin.

10.1 Unfolding

To express the differential cross section, the D'Agostini unfolding technique is used [54]. It is an iterative technique which uses the truth information of the Monte Carlo events passing the selection as a prior prediction, using a χ^2 fit between the number of truth events in a bin before and after each iteration. The purpose of the unfolding is to find the number of truth events in each bin, given the knowledge of the reconstructed spectrum and of the smearing matrix relating truth information to reconstructed information across different bins.

D'Agostini unfolding is based on Bayes Theorem, which describes how conditional probabilities for two separate effects A and B are related to one another and is given by the following equation:

$$P(A|B) = \frac{P(B|A) \cdot P(A)}{P(B)} \tag{10.1}$$

This can be used to find a matrix that translates results in reconstructed space to truth space, the opposite of what the smearing matrix does. It requires the reconstructed background-subtracted data distribution and the smearing matrix.

The smearing matrix represents the probability that an event is reconstructed in one bin given that it is in another in truth:

$$S_{ij} = P(r_i|t_j) \tag{10.2}$$

The probability that an event is reconstructed in a truth bin is given by:

$$P(t_i) = \frac{N_{t_i}}{\sum_{\alpha}^{\text{truth bins}} N_{t_a}} \tag{10.3}$$

The number of reconstructed events in a bin i is given by:

$$N_{r_i} = \sum_{\alpha}^{\text{truth bins}} P(r_i|t_\alpha) \cdot N_{t_\alpha} \tag{10.4}$$

Using the previous two equations, the probability that an event is reconstructed in a reconstructed bin is given by:

$$P(r_i) = \sum_{\alpha}^{\text{truth bins}} P(r_i|t_\alpha) \cdot P(t_\alpha) = \frac{N_{r_i}}{\sum_{\alpha}^{\text{truth bins}} N_{t_a}} \tag{10.5}$$

Bayes' Theorem can then be used to give the opposite of the smearing matrix:

$$P(t_j|r_i) = \frac{P(r_i|t_j) \cdot P(t_j)}{P(r_i)} \tag{10.6}$$

Using this and the expression for the efficiency for a truth bin, ϵ_j,

$$\epsilon_j = \sum_{\alpha}^{\text{reco bins}} P(r_\alpha|t_j) \tag{10.7}$$

one can find an expression for an estimate of the number of events in a truth bin:

$$N_{t_j}^{\text{unfolded}} = \frac{1}{\epsilon_j} \sum_i P(t_j|r_i) \cdot (N_{r_i} - B_{r_i}) \tag{10.8}$$

This gives an updated prediction for the predicted number of events in a truth bin, $P(t_i)$, which can be reinserted into Equation 10.3 for the truth number of unfolded events to get another prediction for the truth spectrum. This process can be performed iteratively so that the data trains the unfolding, continuing until there is only a limited difference in the unfolded event spectrum between iterations. The amount of statistical uncertainty increases between iterations so its minimization also is considered in deciding when to stop the procedure, meaning that fewer iterations when there is little change in the output event distribution is better than more.

	Kinetic Energy	Directional Cosine
1 - 2 iterations	0.65%	0.54%
2 - 3 iterations	0.47%	0.32%
3 - 4 iterations	0.37%	0.20%

Table 10.1: The average bin-by-bin variation between unfolding iterations.

The number of iterations used for the unfolding was picked based on the average variation in each bin between iterations in a fake data study. Once the average variation fell below 0.5%, the procedure was terminated. Table 10.1 shows the average bin-by-bin variation between unfolding iterations for the kinetic energy and directional cosine distributions for the single-differential cross section measurements. Based on the information in the table, three iterations were chosen for this measurement.

10.2 Statistical Uncertainties

10.2.1 Data

The data statistical uncertainties are provided by the package used to do the unfolding, the `RooUnfold` package of the `ROOT` analysis framework. They are approximately equal to the square root of the entry in each bin, but they increase with each unfolding iteration applied (described in Section 10.1). The data statistical uncertainties are equal to the square root of the diagonal entries of the covariance matrix provided by the unfolding (described in more detail in Section 10.3).

10.2.2 Monte Carlo

The Monte Carlo statistical uncertainties are generated by the Poisson-sampling technique. This operates by modeling the number of unweighted Monte Carlo neutrino overlay and dirt overlay events in each bin as a Poisson distribution with a mean equal to the number of events in that bin. For 400 throws, a random number is generated from this Poisson distribution, and the normalized number of overlay events in that bin is varied by the percentage difference that the new number of unweighted events in that bin varies from the nominal number of unweighted events. The new normalized number of events is used to generate a new smearing matrix which is input into the unfolding (described in Section 10.1) and a new normalized number of dirt and neutrino backgrounds which are subtracted off the selected on-beam data distribution. The number of iterations was arbitrarily chosen but 400 is plenty to get an accurate estimate for the amount of Monte Carlo statistical error in each bin.

10.3 Single-Differential Cross Section Measurements

The single-differential cross section measurements are formed by dividing the unfolded event distributions by the efficiency distributions. The unfolded event distributions are formed by feeding the background-subtracted event distribution (the selected neutrino background, dirt background, and NuMI EXT distributions subtracted from the selected on-beam data distribution) and a smearing matrix (a column-normalized matrix of the reconstructed signal distribution on the y-axis plotted vs. the corresponding truth distribution on the x-axis) into the unfolding procedure. The unfolded distributions are formed after three iterations of using the algorithm described above.

The covariance matrix has to be constructed to compare the measurement to the model. This expresses the difference between the central value measurement and the model prediction in two separate bins as a product which is the entry in a two-dimensional matrix. Because the covariance matrix contains variances, the individual ones from separate statistical and systematic uncertainties add to form the full covariance matrix.

In comparing the measurement to the model in the simulation in a χ^2 fit, the following equation is used with x representing the measurement, μ representing the Monte Carlo, and V_{ij} representing the covariance matrix (the number of degrees of freedom equal to the number of bins in the differential cross section):

$$\chi^2(x) = \sum_{ij}^{\text{All Bins}} (x_i - \mu_i) \cdot V_{ij}^{-1} \cdot (x_j - \mu_j) \tag{10.9}$$

10.3.1 Kinetic Energy

The kinetic energy background-subtracted and unfolded data distributions are shown in Figure 10.1. The unfolding has the effect of increasing the number of entries in bins of higher kinetic energy to bins greater than 1.8 GeV.

The smearing matrix in Figure 10.2, which is input to the unfolding procedure, shows the migration of events in truth bins (x-axis) to different reconstructed bins (y-axis). The excess of events at high truth kinetic energy and low reconstructed kinetic energy is almost entirely due to cosmic contamination: events in which the reconstructed vertex is placed on a cosmic. The unfolding matrix in Figure 10.3, which is output from the unfolding procedure, translates the background-subtracted data distribution (red) to the unfolded event distribution (blue), both shown in Figure 10.1. The background-subtracted data distribution can be compared to the truth (red) and reconstructed (blue) kinetic energy distributions of signal events after the selection, shown in Figure 10.4.

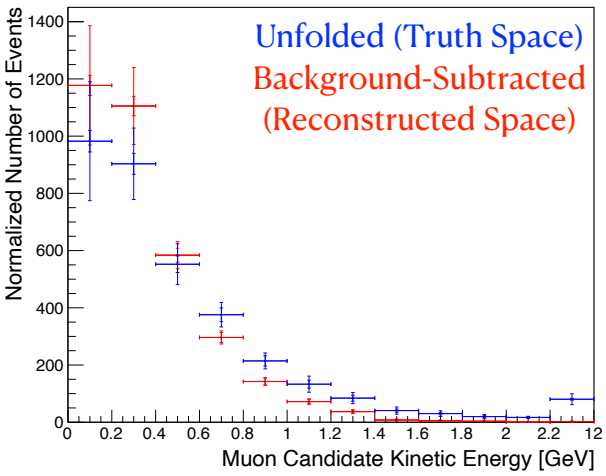

Figure 10.1: The muon candidate kinetic energy background-subtracted (red) and unfolded (blue) data spectra. The unfolded data spectrum was produced by using D'Agostini unfolding with three iterations. The inner error bars correspond to the statistical error and the outer error bars correspond to the total error. These histograms are normalized to 2.187×10^{20} POT.

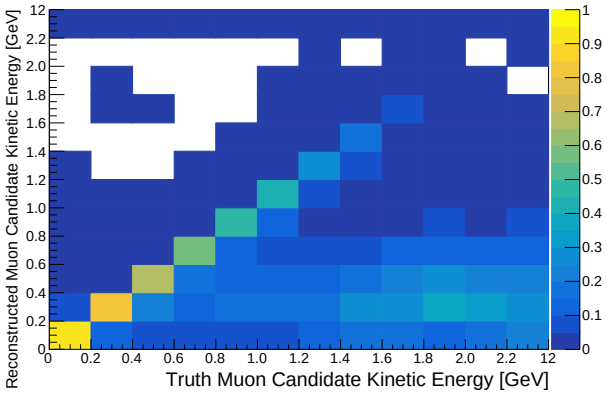

Figure 10.2: The muon candidate kinetic energy smearing matrix. This plot shows the migration of events in truth bins (x-axis) to different reconstructed bins (y-axis). Each of the columns of the plot are normalized to unity.

The single-differential cross section distribution for kinetic energy is shown in Figure 10.6. The measurement is shown in blue and the Monte Carlo is shown in red. This is formed by dividing the unfolded event distribution (blue) in Figure 10.1 by the efficiency spectrum in Figure 10.5. The efficiency is lower in the first bin than in the second because muon candidates with length in the interval [0 MeV, 200 MeV] are the least likely to be reconstructed. The muon candidates in the second bin are the most likely to be both reconstructed and contained, and the efficiency decreases

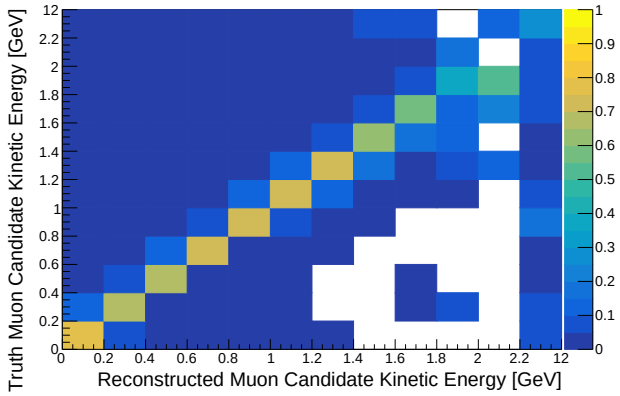

Figure 10.3: The muon candidate kinetic energy unfolding matrix. This translates the background-subtracted data distribution (red) to the unfolded event distribution (blue), both shown in Figure 10.1.

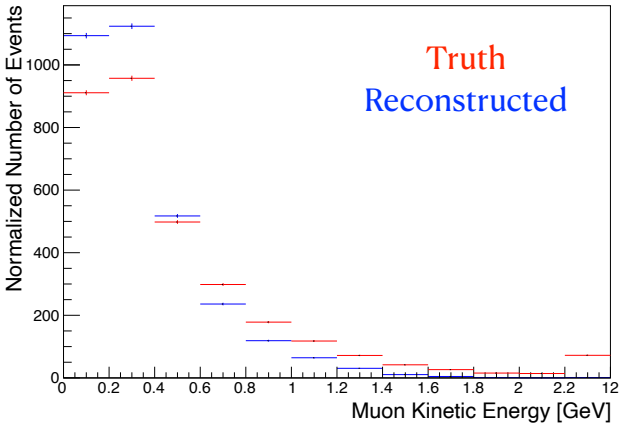

Figure 10.4: The truth (red) and reconstructed (blue) muon candidate kinetic energy distributions of signal events after the event selection. The error bars correspond to the statistical error only. These histograms are normalized to 2.187×10^{20} POT.

with increasing kinetic energy throughout the rest of the spectrum because of the containment requirement. The central value of the measurement shows greater values than the model in all bins but two ([0.2 GeV, 0.4 GeV] and [1.4 GeV, 1.6 GeV]). Unit-normalized distributions of the single differential cross section for both the measurement and the model are shown in Figure 10.7, and they reveal that the disagreement between the two stems from both the shape and normalization of the two distributions.

Using Equation 10.9 gives a χ^2 value of 5.8 (12 d.o.f.). The χ^2 contribution from each combination of two bins is shown in Figure 10.8, which shows that the χ^2 value is increased by positive

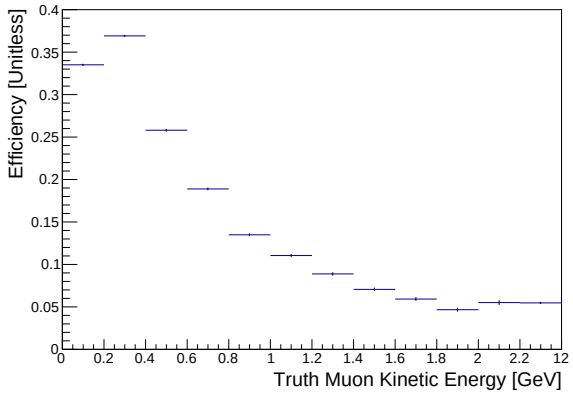

Figure 10.5: The muon candidate kinetic energy efficiency. This plot was producing by dividing the normalized number of signal events passing the selection in each bin by the total number of normalized signal events in that same bin before any selection cuts. The error bars correspond to the statistical uncertainty only.

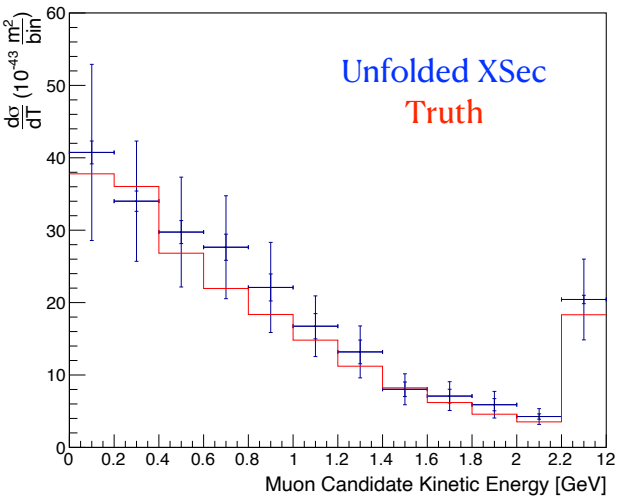

Figure 10.6: The muon candidate kinetic energy single-differential cross section, shown for the measurement (blue) and the Monte Carlo (red). For the measurement, the plot was formed by dividing the unfolded data spectrum, shown in blue in Figure 10.1 by the efficiency in Figure 10.5. For the measurement, the inner error bars correspond to the statistical error and the outer error bars correspond to the total error. These histograms are made using 2.187×10^{20} POT of on-beam data, and the Monte Carlo and off-beam data are normalized to that amount of exposure.

components along the diagonal and decreased by off-diagonal negative components. The covariance matrix used in Equation 10.9 is shown in Figure 10.9 for the kinetic energy distribution. The greatest values are located in the same places where the differential cross section is the highest

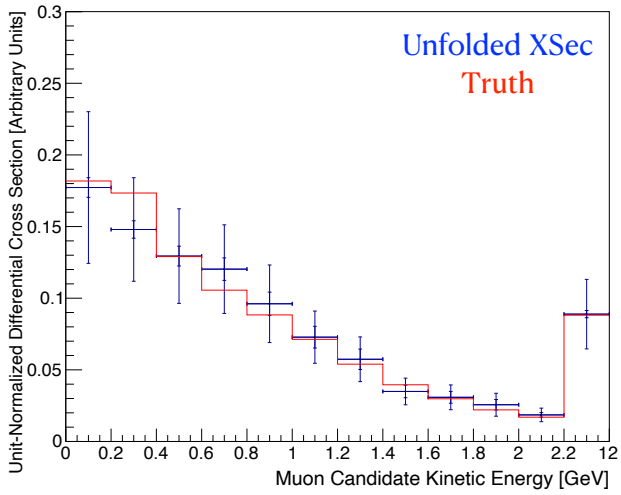

Figure 10.7: The unit-normalized muon candidate kinetic energy single-differential cross section, shown for the measurement (blue) and the Monte Carlo (red). For the measurement, the inner error bars correspond to the statistical error and the outer error bars correspond to the total error.

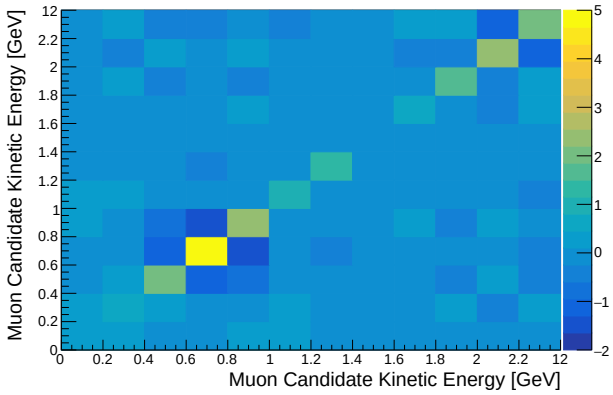

Figure 10.8: The contributions to the muon candidate kinetic energy χ^2 value from each combination of two bins in the spectrum.

(close to lower kinetic energy values).

10.3.2 Directional Cosine

The directional cosine background-subtracted and unfolded data distributions are shown in Figure 10.10. The unfolding has the effect of removing events reconstructed in the bins at the least cosine values and moving them to the bins with the greatest values. This accounts for events which have a misreconstructed direction and belong in the most forward-going bin, which is where most of the

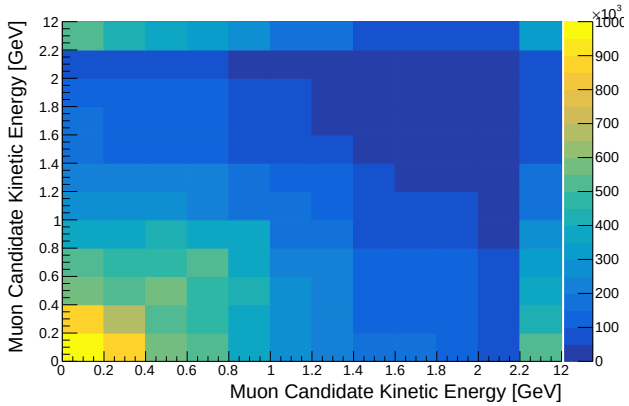

Figure 10.9: The covariance matrix for the muon candidate kinetic energy measurement. The variances from each source of systematic and statistical uncertainty in the measurement are added to form this matrix.

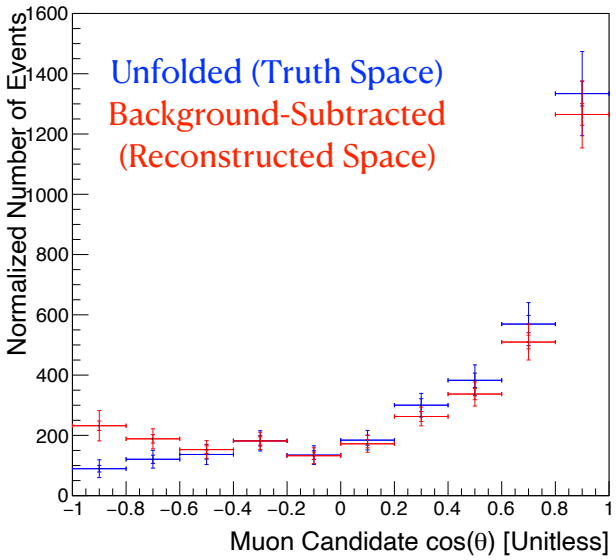

Figure 10.10: The muon candidate directional cosine background-subtracted (red) and unfolded (blue) data spectra. The unfolded data spectrum was produced by using D'Agostini unfolding with three iterations. The inner error bars correspond to the statistical error and the outer error bars correspond to the total error. These histograms are normalized to 2.187×10^{20} POT.

events are located.

The smearing matrix in Figure 10.11, which is input to the unfolding procedure, shows the migration of events in truth bins (x-axis) to different reconstructed bins (y-axis). The unfolding matrix in Figure 10.12, which is output from the unfolding procedure, translates the background-subtracted data distribution (red) to the unfolded event distribution (blue), both shown in Figure

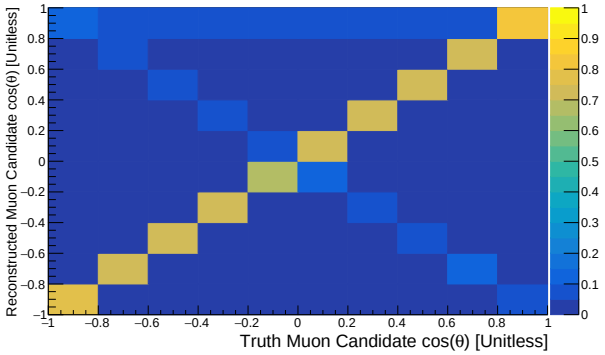

Figure 10.11: The muon candidate directional cosine smearing matrix. This plot shows the migration of events in truth bins (x-axis) to different reconstructed bins (y-axis). Each of the columns of the plot are normalized to unity.

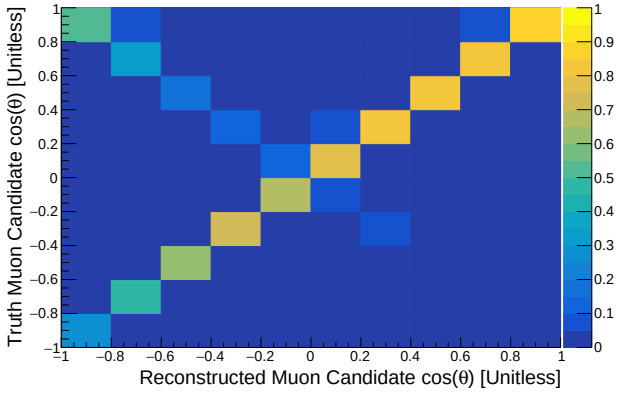

Figure 10.12: The muon candidate directional cosine unfolding matrix. This translates the background-subtracted data distribution (red) to the unfolded event distribution (blue), both shown in Figure 10.10.

10.10. The background-subtracted data distribution can be compared to the truth (red) and reconstructed (blue) directional cosine distributions of signal events after the selection, shown in Figure 10.13. The uptick in bin values in the lowest directional cosine bins of the background-subtracted data distribution corresponds to events in which the muon candidate direction is misreconstructed. In truth, these events are much more parallel to the neutrino direction and belong in one of the bins most along the neutrino direction (one of the greatest directional cosine bins), which is corrected in the unfolded distribution.

The efficiency distribution is shown in Figure 10.14. The efficiency is lower for more forward-going muons than for more background-going ones because forward-going muons are more likely

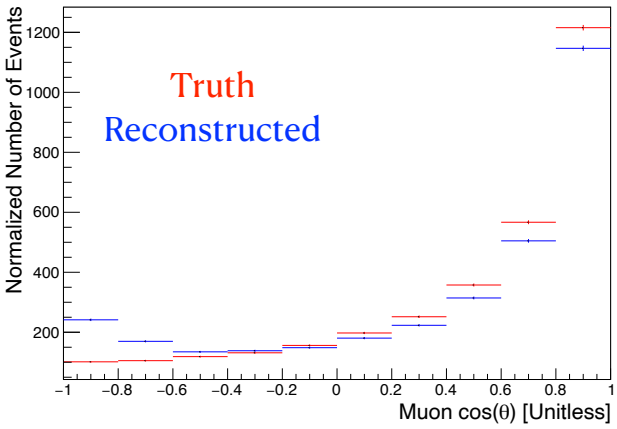

Figure 10.13: The truth (red) and reconstructed (blue) muon candidate directional cosine distributions of signal events after the event selection. The error bars correspond to the statistical error only. These histograms are normalized to 2.187×10^{20} POT.

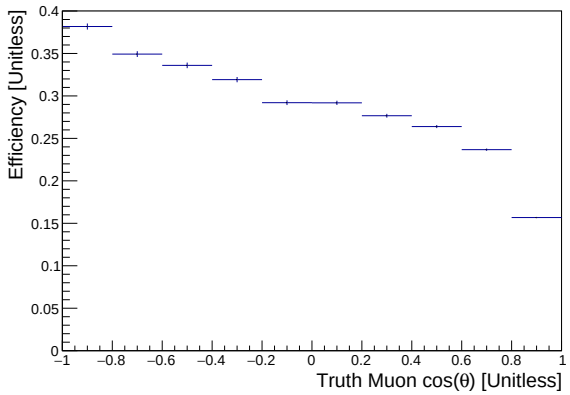

Figure 10.14: The muon candidate directional cosine efficiency. This plot was producing by dividing the normalized number of signal events passing the selection in each bin by the total number of normalized signal events in that same bin before any selection cuts. The error bars correspond to the statistical uncertainty only.

to have greater kinetic energy and therefore less likely to be contained in the detector. This means that they are more likely to be removed by the selection than more backward-going ones are. A plot of the efficiency as a function of truth neutrino energy is shown in Figure 10.15. This distribution peaks at ~500 MeV.

The differential cross section distribution is shown in Figure 10.16. The measurement is shown in blue and the Monte Carlo is shown in red. This is formed by dividing the unfolded event distribution (blue) in Figure 10.10 by the efficiency spectrum in Figure 10.14. There is an excess

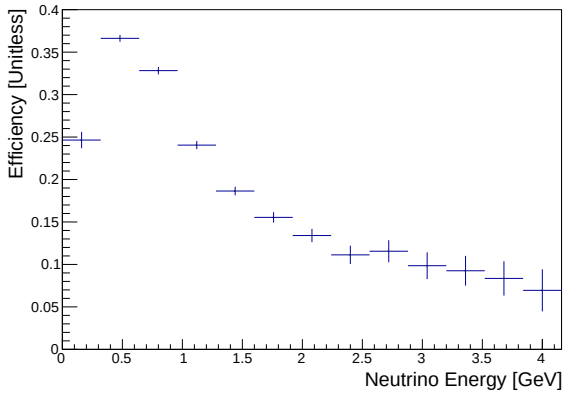

Figure 10.15: The selection efficiency plotted vs. truth neutrino energy. The error bars correspond to the statistical uncertainty only.

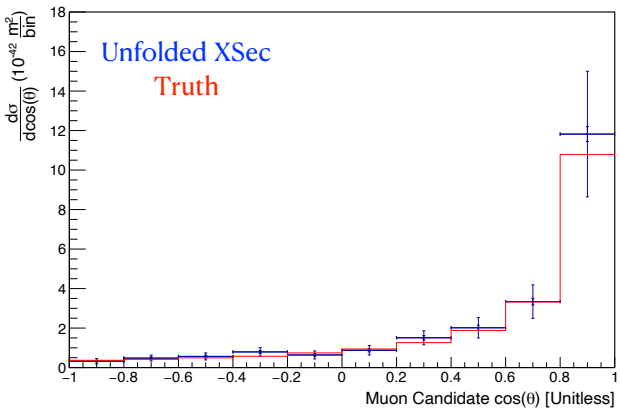

Figure 10.16: The muon candidate directional cosine single-differential cross section, shown for the measurement (blue) and the Monte Carlo (red). For the measurement, the plot was formed by dividing the unfolded data spectrum, shown in blue in Figure 10.10, by the efficiency in Figure 10.14. For the measurement, the inner error bars correspond to the statistical error and the outer error bars correspond to the total error. These histograms are made using 2.187×10^{20} POT of on-beam data, and the Monte Carlo and off-beam data are normalized to that amount of exposure.

of data seen in the most forward-going bin and deficits seen in the bins at the least and intermediate cosine values, but these are within the range of the uncertainties. Unit-normalized distributions of the single differential cross section for both the measurement and the model are shown in Figure 10.17, and they reveal that the disagreement between the two is primarily rooted in normalization.

Using Equation 10.9 gives a χ^2 value of 11.4 (10 d.o.f.). The χ^2 contribution from each combination of two bins is shown in Figure 10.18, which shows that the χ^2 value is increased by positive components along the diagonal, particularly in the fourth and seventh bins, and decreased by off-

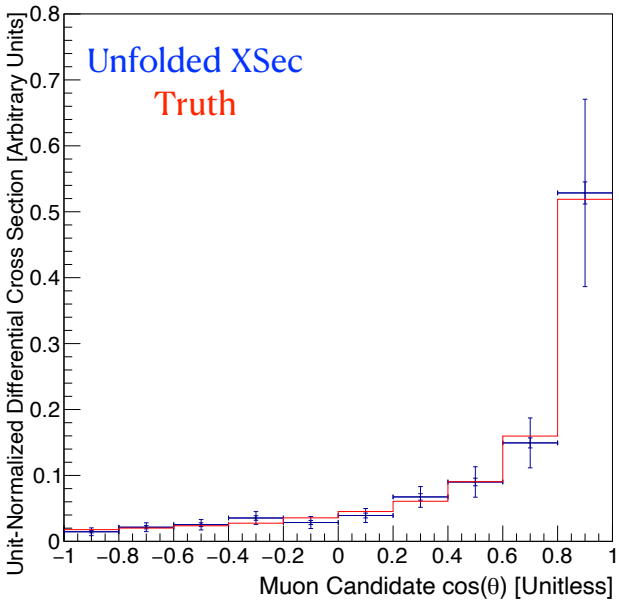

Figure 10.17: The unit-normalized muon candidate directional cosine single-differential cross section, shown for the measurement (blue) and the Monte Carlo (red). For the measurement, the inner error bars correspond to the statistical error and the outer error bars correspond to the total error.

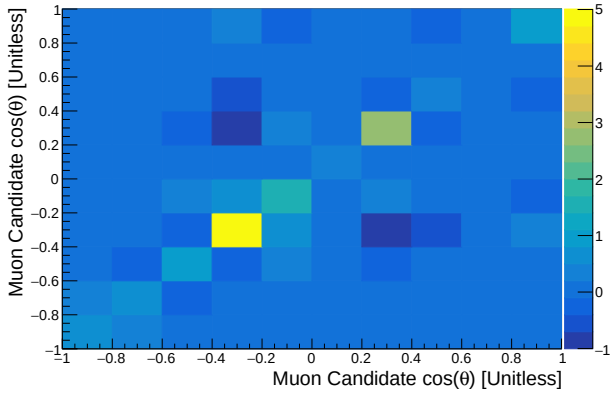

Figure 10.18: The contributions to the muon candidate directional cosine χ^2 value from each combination of two bins in the spectrum.

diagonal negative components. The covariance matrix used in Equation 10.9 is shown in Figure 10.19 for the directional cosine distribution. The greatest values are located in the same places where the differential cross section is the highest (close to greater directional cosine values).

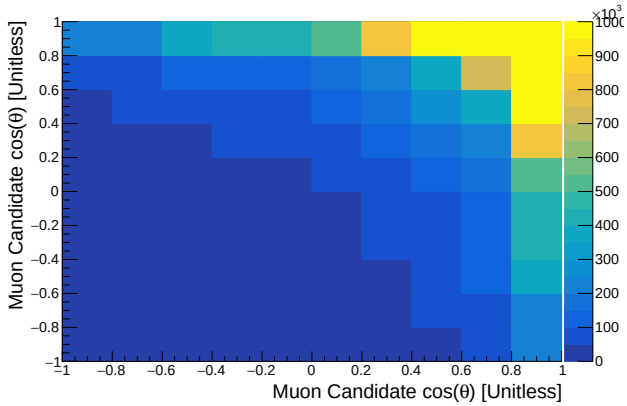

Figure 10.19: The covariance matrix for the muon candidate directional cosine measurement. The variances from each source of systematic and statistical uncertainty in the measurement are added to form this matrix.

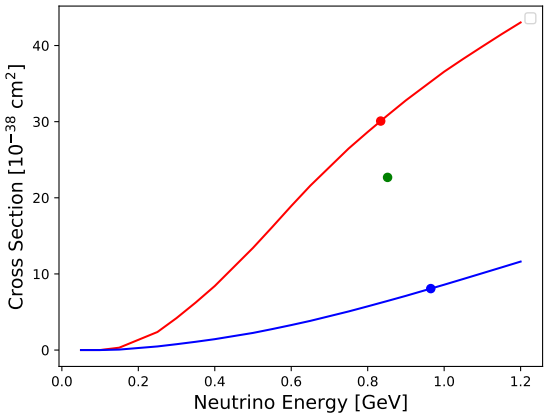

Figure 10.20: The total ν_μ (red) and $\overline{\nu}_\mu$ (blue) cross sections with their mean energies, 834 MeV and 965 MeV, respectively, denoted by points. The mean of the total cross section from the two measurements (green) is plotted at the neutrino energy weighted according to the relative ν_μ and $\overline{\nu}_\mu$ compositions of the sample, 852 MeV.

10.4 Total Cross Section

The total cross section for the kinetic energy and the directional cosine distributions expressed with statistical uncertainty only are $(23.0 \pm 0.6) \times 10^{-38}$ cm^2/nucleon and $(22.4 \pm 0.6) \times 10^{-38}$ cm^2/nucleon, respectively. These values differ from one another after the processes of subtracting the predicted backgrounds from the passing on-beam data events and the unfolding. The shortcomings of the Monte Carlo in describing the data manifest themselves in differences between the total

Type of Uncertainty	% of Central Value
Hadron Production Multisim Variation	20.2%
Horn Current	0.4%
Horn 1 x	0.4%
Horn 1 y	0.9%
Beam Spot Size	1.4%
Horn 2 x	0.4%
Horn 2 y	0.2%
Horn Water	0.2%
Beam Shift x	2.4%
Beam Shift y	1.7%
Target z	0.2%
Total Flux	20.5%

Table 10.2: The sources of flux uncertainty in the analysis, expressed as a percentage of the central value in a single bin.

cross sections of the kinetic energy and directional cosine distributions after those two processes. This corresponds to ν_μ and $\overline{\nu}_\mu$ values of 2.29×10^{-10} cm^{-2} per POT and 1.50×10^{-10} cm^{-2} per POT, respectively. The neutrino flux distribution expressed in terms of neutrino energy is shown in Figure 9.6.

As a visual, the total ν_μ (red) and $\overline{\nu}_\mu$ (blue) cross sections are plotted in Figure 10.20 with their mean energies, 834 MeV and 965 MeV, respectively, denoted by points of the corresponding color. The mean of the total cross section central value from the two measurements, 22.7×10^{-38} cm^2/nucleon, (green) is plotted at the energy of the weighted ν_μ and $\overline{\nu}_\mu$ composition of the sample, 852 MeV.

10.5 Measurement Uncertainties

If you include all of the entries in the plot in a single bin, you can study the impact of each source of uncertainty independent of the unfolding. The sources of flux systematic uncertainty are contained in Table 10.2, the sources of cross section systematic uncertainty are contained in Table 10.3, the sources of detector systematic uncertainty are contained in Table 10.4, and the sources of statistical uncertainty are contained in Table 10.5. The total amount of each type of uncertainty and the total uncertainty are contained in Table 10.6.

Type of Uncertainty	% of Central Value
Multisim Variation	7.5%
AxialFF	0.2%
RPACCQE	2.8%
XSecShape	0.3%
Total Cross Section	8.0%

Table 10.3: The sources of cross section uncertainty in the analysis, expressed as a percentage of the central value in a single bin.

Type of Uncertainty	% of Central Value
Light Yield - Rayleigh	0.5%
Light Yield - Reduction	0.4%
SCE	7.3%
Recombination	6.9%
WireModX	0.7%
WireModYZ	0.5%
WireModAngleXZ	$< 0.1\%$
WireModAngleYZ	1.0%
WireModdEdX	3.5%
Total Detector	10.7%

Table 10.4: The sources of detector uncertainty in the analysis, expressed as a percentage of the central value in a single bin. As shown in this table, the largest detector systematic uncertainty is SCE.

Type of Uncertainty	% of Central Value
Data Statistical	2.5%
Background Statistical	1.1%
Total Statistical	2.7%

Table 10.5: The sources of statistical uncertainty in the analysis, expressed as a percentage of the central value in a single bin.

Type of Uncertainty	% of Central Value
Total Statistical	2.7%
Flux	20.5%
Cross Section	8.0%
Detector	10.7%
Total Systematic	24.5%
Total Uncertainty	24.6%

Table 10.6: The sources of uncertainty in the analysis, expressed as a percentage of the central value in a single bin.

CHAPTER 11

Discussion

11.1 Interpretation of Result

This result presents the first-ever muon neutrino on liquid argon differential cross sections with an off-axis beam. In addition to this distinction, this result adds to the on-axis BNB result because the neutrino flux is from a different beam and is therefore quite different as a function of neutrino energy as shown in Figure 11.1 [14].

There is also an excess seen in the central value of the data in all bins of the kinetic energy differential cross section distribution but two ([0.2 GeV, 0.4 GeV] and [1.4 GeV, 1.6 GeV]) of the measurement (Figure 10.6), but this is within the range of the uncertainties. The muon candidate direction differential cross section indicates that there is an excess of data in the most forward-going direction (the one most in the mean passing neutrino direction) in comparison to the model in the simulation (Figure 10.16), and this is also within the range of the uncertainties.

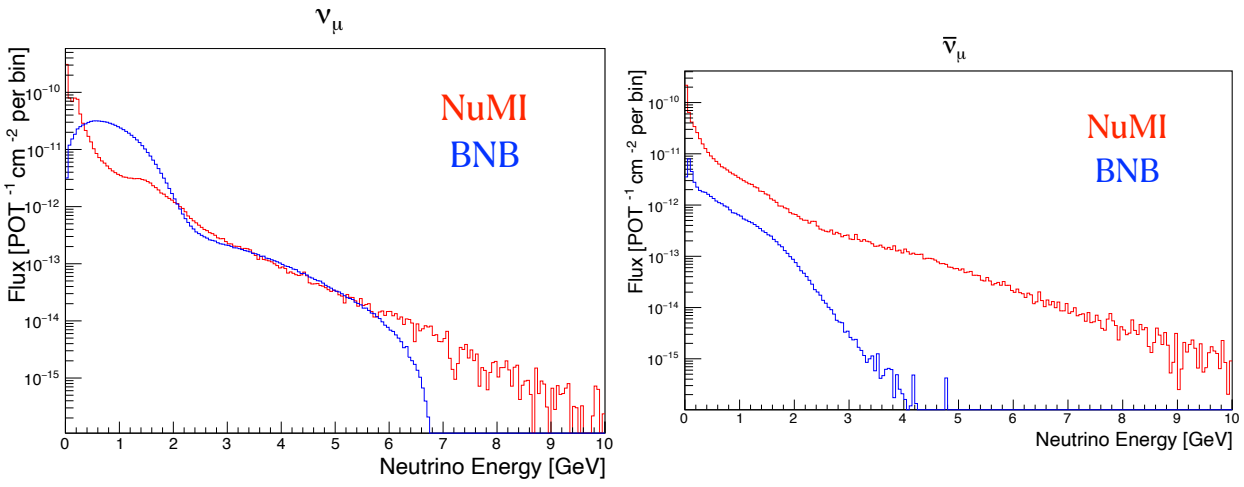

Figure 11.1: Plots of the ν_μ (left) and $\overline{\nu}_\mu$ (right) fluxes for the NuMI and BNB datastreams.

In spite of this excess, the data and the simulation are consistent within the uncertainties. This result indicates that for the ν_μ and $\overline{\nu}_\mu$ energies covered by this measurement (primarily in the energy range [0-3] GeV), the simulation's prediction for the muon kinematics can be trusted. This is essential information for oscillation experiments, including DUNE.

11.2 Context of Result

Future work on this experiment starts with expressing the two single-differential cross section measurements in terms of a double-differential measurement. That would first involve picking binning for the measurement which would minimize the data statistical uncertainty. Next, a method for the Monte Carlo statistical uncertainty would have to be selected that does not induce large uncertainties in any single bin. The method laid out in Section 10.2.2 may not work because the Monte Carlo statistical uncertainty would grow artificially large in bins with low statistics, so another method (perhaps varying the entire unweighted number of Monte Carlo events according to a Poisson variation and multiplying the number of events in each bin according to the percentage change of the entire unweighted number in a given throw) may have to be used instead.

An interesting follow-up measurement would be to find a proxy for reconstructed neutrino direction and measure the neutrino energy for high-energy $\nu_\mu/\overline{\nu}_\mu$ events. Comparing the relationship between neutrino direction and neutrino energy in a double-differential cross section to the histograms shown in Figure 9.23 could help constrain the neutrino flux. It was demonstrated that reconstructing neutrino direction is difficult for low-energy ν_μ events like the KDAR signal in Chapter 8 (Figure 8.13), but it may be easier to do this at higher neutrino energies.

APPENDIX A

List of Cross Section Multisim Systematic Variables

The following variables, referred to as 'multisim' variables, are modified as part of the 600 cross section universe systematic variations:

- MACCQE: Mass parameter for CCQE dipole axial form factor.
- CoulombCCQE: Value of Coulomb potential used in corrections for CCQE.
- MaNCEL: Axial mass for neutral-current elastic events.
- EtaNCEL: Strange axial form factor parameter for neutral-current elastic event.
- NormCCMEC: scales the total CCMEC cross section by a constant factor.
- NormNCMEC: scales the total NCMEC cross section by a constant factor.
- FracPN_CCMEC: varies the fraction of initial nucleon pairs that are proton/neutron.
- FracDelta_CCMEC: varies the relative contribution of the Δ diagrams to the total cross section.
- MaCCRES: CCRES axial mass.
- MvCCRES: CCRES vector mass.
- MaNCRES: NCRES axial mass.
- MvNCRES: NCRES vector mass.
- NonRESBGvpCC1pi, NonRESBGvpCC2pi, NonRESBGvpNC1pi, NonRESBGvpNC2pi, NonRESBGvnCC1pi, NonRESBGvnCC2pi, NonRESBGvnNC1pi, NonRESBGvnNC2pi, NonRESBGvbarpCC1pi, NonRESBGvbarpCC2pi, NonRESBGvbarpNC1pi, NonRESBGvbarpNC2pi, NonRESBGvbarnCC1pi, NonRESBGvbarnCC2pi,

NonRESBGvbarnNC1pi, NonRESBGvbarnNC2pi: Normalization parameters for various non-resonant background final states.

- AhtBY: Bodek-Yang Model A_{HT} higher-twist parameter.
- BhtBY: Bodek-Yang Model B_{HT} higher-twist parameter.
- CV1uBY: C_{V1u} u valence GRV98 PDG correction parameter for the Bodek-Yang model.
- CV2uBY: C_{V2u} u valence GRV98 PDG correction parameter for the Bodek-Yang model.
- AGKYxF1pi, AGKYpT1pi: control the Andreopoulos-Gallagher-Kehayias-Yang (AGKY) hadronization model.
- MFP_pi: Pion mean free path.
- MFP_N: Nucleon mean free path.
- FrCEx_pi: Nucleon charge exchange probability.
- FrInel_pi: Pion inelastic reaction probability.
- FrAbs_pi: Pion absorption probability.
- FrCEx_N: Nucleon charge exchange probability.
- FrInel_N: Nucleon inelastic reaction probability.
- FrAbs_N: Nucleon absorption probability.
- RDecBR1gamma: Branching ratio for radiative Δ decays.
- RDecBR1eta: Branching ratio for Δ decays to $N + \eta$

BIBLIOGRAPHY

[1] "A fresh look for the standard model," http://theoryandpractice.org/2013/08/a-fresh-look-for-the-standard-model/#.YFzmki1h1N0, Accessed: 2021-03-25.

[2] "History of the Neutrino: Experimental Discovery," https://neutrino-history.in2p3.fr/experimental-discovery, Accessed: 2021-02-11.

[3] Joseph Formaggio and G.P. Zeller, "From eV to EeV: Neutrino Cross-Sections Across Energy Scales," *Rev. Mod. Physics*, Vol. 84, 2012.

[4] Qian, X. and Vogel, P., "Neutrino Mass Hierarchy," https://arxiv.org/abs/1505.01891, Accessed: 2021-06-21.

[5] Aguilar-Arevalo, A. A. et al., "Updated MiniBooNE neutrino oscillation results with increased data and new background studies," *Phys. Rev. D.*, Vol. 103, 2021.

[6] Aguilar, A. et al., "Evidence for neutrino oscillations from the observation of ν_e appearance in a ν_μ beam," *Phys. Rev. D.*, Vol. 64, 2001.

[7] Williams, Z., Private Communication.

[8] Caratelli, D., Private Communication.

[9] P. Abratenko and others, "Measurement of the Flux-Averaged Inclusive Charged-Current Electron Neutrino and Antineutrino Cross Section on Argon using the NuMI Beam and the MicroBooNE Detector," 2021.

[10] Machado, A. et al., "The X-ARAPUCA: An improvement of the ARAPUCA device," https://arxiv.org/abs/1804.01407, Accessed: 2021-06-21.

[11] The MicroBooNE Collaboration, "Study of Space Charge Effects in MicroBooNE," 2016.

[12] Acciari, R. et al., "The Pandora multi-algorithm approach to automated pattern recognition of cosmic-ray muon and neutrino events in the MicroBooNE detector," *European Physical Journal C*, Vol. 78, 2017.

[13] The MicroBooNE Collaboration, "First Measurement of Muon Neutrino Charged Current Neutral Pion Production on Argon with the MicroBooNE LArTPC," *Physical Rev. D.*, Vol. 99, 2019.

[14] The MicroBooNE Collaboration, "First Measurement of Inclusive Muon Neutrino Charged Current Differential Cross Sections on Argon at E_ν ~0.8 GeV with the MicroBooNE Detector," *Physical Rev. Letters*, Vol. 123, 2019.

[15] The MicroBooNE Collaboration, "First Measurement of Differential Charged Current Quasielastic-like ν_μ-Argon Scattering Cross Sections with the MicroBooNE Detector," *Physical Rev. Letters*, Vol. 125, 2020.

[16] The MicroBooNE Collaboration, "Measurement of Differential Cross Sections for Muon Neutrino Charged Current Interactions on Argon with Protons and No Pions in the Final State with the MicroBooNE Detector," *Physical Rev. D.*, Vol. 102, 2020.

[17] V. Pandey and others, "Low-energy excitations and quasielastic contribution to electron-nuclues and neutrino-nucleus scattering in the continuum random-phase approximation," *Phys. Rev. C*, Vol. 92, 2015.

[18] A. Nikolakopoulos and others, "Modeling quasielastic interactions of monoenergetic kaon decay-at-rest neutrinos," *Phys. Rev. C.*, Vol. 103, 2021.

[19] The MicroBooNE Collaboration, "Single differential ν_μ charged-current cross section with the MicroBooNE detector using the Cosmic Ray Tagger," 2020.

[20] "All About Neutrinos," https://icecube.wisc.edu/info/neutrinos, Accessed: 2021-01-05.

[21] The MicroBooNE Collaboration, "Establishing a Pure Sample of Side-Piercing Through-Going Cosmic-Ray Muons for LArTPC Calibration in MicroBooNE," 2017.

[22] The MicroBooNE Collaboration, "Ionization electron signal processing in single phase LArTPCs. Part II. Data/simulation comparison and performance in MicroBooNE," *JINST*, Vol. 13, 2018.

[23] The MicroBooNE Collaboration, "Measurement of Space Charge Effects in the MicroBooNE LArTPC Using Cosmic Muons," *JINST*, Vol. 15, 2020.

[24] "Neutrino mass disovered," https://physicsworld.com/a/neutrino-mass-discovered, Accessed: 2021-12-31.

[25] "Katrin sets first limit on neutrino mass," https://cerncourier.com/a/katrin-sets-first-limit-on-neutrino-mass, Accessed: 2021-01-21.

[26] "Neutrino Physics," https://www.slac.stanford.edu/econf/C040802/papers/L004.PDF, Accessed: 2020-12-12.

[27] Giganti, C. et al., "Neutrino oscillations: the rise of the PMNS paradigm," 2017.

[28] Tanabashi, M. et al., "Review of Particle Physics," *Phys. Rev. D*, Vol. 98, 2018.

[29] Mills, G. B., "Neutrino Oscillation Results From LSND," Vol. 66, 1998.

[30] Lasserre, T., "Neutrino Oscillations - The Double Chooz Experiment," Vol. 38, 2007.

[31] F.P. An and others, "Independent Measurement of the Neutrino Mixing Angle θ_{13} via Neutron Capture on Hydrogen at Daya Bay," *Phys. Rev. D*, Vol. 90, 2014.

[32] "An improved measurement of θ_{13} from Daya Bay," https://cerncourier.com/a/an-improved-measurement-of-13-from-daya-bay/, Accessed: 2021-07-27.

[33] "The T2K Experiment: About T2K," https://t2k-experiment.org/t2k, Accessed: 2021-01-17.

[34] M.A. Acero and others, "First measurement of neutrino oscillation parameters using neutrinos and antineutrinos by NOvA," *Phys. Rev. Letters*, Vol. 123, 2019.

[35] "Mu2e: Research Goals," https://mu2e.fnal.gov/research_goals.shtml, Accessed: 2021-05-02.

[36] "Deep Underground Neutrino Experiment," https://www.dunescience.org, Accessed: 2021-05-02.

[37] "Earth's Atmosphere: Composition, Climate Weather," https://www.space.com/17683-earth-atmosphere.html, Accessed: 2020-07-03.

[38] R. Acciarri and others, "Liquid Argon Dielectric Breakdown Studies with the MicroBooNE Purification System," *JINST*, Vol. 9, 2014.

[39] C. Adams and others, "Design and construction of the MicroBooNE cosmic ray tagger system," *JINST*, Vol. 14, 2019.

[40] PDG, "Table 289: Muons in Liquid Argon," https://pdg.lbl.gov/2012/AtomicNuclearProperties/MUON_ELOSS_TABLES/muonloss_289.pdf.

[41] NIST, "Stopping Power and Range Table For Protons," https://physics.nist.gov/PhysRefData/Star/Text/PSTAR.html.

[42] P. Abratenko and others, "Determination of muon momentum in the MicroBooNE LArTPC using an improved model of multiple Coulomb scattering," *JINST*, Vol. 12, 2017.

[43] "The NuMI Technical Design Handbook," 2002.

[44] The MicroBooNE Collaboration, "A Measurement of the Attenuation of Drifting Electrons in the MicroBooNE LArTPC," 2017.

[45] Unlisted, "A* search algorithm," https://en.wikipedia.org/wiki/A*_search_algorithm, Accessed: 2021-06-26.

[46] A. A. Aguilar-Arevalo and others, "First Measurement of Monoenergetic Muon Neutrino Charged Current Interactions," *Phys. Rev. Letters*, Vol. 120, 2018.

[47] The MicroBooNE Collaboration, "Proton Track Identification in MicroBooNE Simulation for Neutral Current Elastic Events," 2017.

[48] R. Acciarri and others, "Noise Characterization and Filtering in the MicroBooNE Liquid Argon TPC," *JINST*, Vol. 12, 2017.

[49] C. Adams and others, "Calibration of the charge and energy loss per unit length of the MicroBooNE liquid argon time projection chamber using muons and protons," *JINST*, Vol. 15, 2020.

[50] R. Acciarri and others, "Michel Electron Reconstruction Using Cosmic-Ray Data from the MicroBooNE LArTPC," *JINST*, Vol. 12, 2017.

[51] Joshua Spitz, "Cross Section Measurements with Monoenergetic Muon Neutrinos," *Phys. Rev. D*, Vol. 89, 2014.

[52] S. Amaruso and others, "Analysis of the liquid argon purity in the ICARUS T600 TPC," *Nucl. Instrum. Methods A*, Vol. 516, 2004.

[53] Aguilar-Arevalo, A. A. et al., "First measurement of the muon neutrino charged current quasielastic double differential cross section," *Phys. Rev. D*, Vol. 81, 2018.

[54] D'Agostini, G., "A Multidimensional unfolding method based on Bayes' theorem," *Nucl. Instrum. Meth. A*, Vol. 362, 1995.